Downscaling of future meteorology for land-surface modelling in the glacierised Amu Darya headwaters

GEO 511 Master's Thesis

Author
Pascal Wyss
16-214-777

Supervised by
Stefan Fugger (PhD) (stefan.fugger@wsl.ch)
Prof. Dr. Francesca Pellicciotti (francesca.pellicciotti@wsl.ch)

Faculty representative
Prof. Dr. Andreas Vieli

31.01.2024
Department of Geography, University of Zurich

Abstract

The impact of climate change on hydrological regimes and the associated water availability in Central Asia is currently understudied. Due to the Amu Darya's important role in providing fresh water in the region, particularly the future of its glacier-melt and snow-melt dominated headwaters under continued climate change requires more detailed investigation.

This thesis therefore addresses this understudied impact of climate change on the Amu Darya's headwaters by providing a first state-of-the-art dataset for land surface modelling, comprising six spatially and temporally downscaled CMIP6 model chains with a climate-length historical reference period and all Tier1 future scenario projection reaching until the end of the 21th century. This is achieved by using the previously published empirical–statistical TopoCLIM scheme. The ability of this dataset to reproduce spatial snow pack dynamics with T&C is demonstrated with a scene-by-scene evaluation of simulated snow cover against remote-sensing derived Landsat-7/Landsat-8 snow maps, which exhibited average DSC of 0.74 in Kyzylsu and 0.73 in Sangvor.

Further, this thesis conducts a comparative evaluation of the two topography-based downscaling methods HIMAL-method and TopoPyScale, aiming to generate a spatially downscaled reanalysis dataset with highest possible quality. To do so, both methods are applied for the hydrological year 2022 and further evaluated against in-situ observations of recently established monitoring networks in two valuable, remote catchments in the northern Pamir mountains.

Moreover, the efficacy of an additional bias correction step with in-situ observations is assessed, highlighting its potential and its importance for accurate downscaling, especially for complex or bias-prone meteorological variables such as wind speed and precipitation. By discussing limitations of such bias correction, the relevance of a continued monitoring network that provides reliable ground measurements in the region is empathised.

Finally, the importance of future land surface modelling that investigates the impact of climate change on the region's water regimes is empathised by providing a summary of the climate change signals present in the downscaled future projections: they essentially predict a significant increase in air temperature (e.g in Kyzylsu up to +4.45°C until the end of the century) and a seasonal shift in precipitation (with more precipitation during winter months and early spring, and less at the end of the hydrological year).

Acknowledgements

First, I would like like to express my gratitude to Prof. Dr. Andreas Vieli[1] and Prof. Dr. Francesca Pellicciotti[2,3] for making this Master's Thesis with an external supervision possible.

Second, I extend my thanks to the Swiss Polar Institute Flagship Programme PAMIR, SPI-FLAG-2021-001, for funding the Kyzylsu fieldwork campaign in September 2023.

Further, my appreciation goes to Evan Miles[3], Thomas Shaw[2,3] and Achille Jouberton[2,3] for co-supervising this thesis and providing valuable inputs and feedback. Their perspectives and insights have greatly enhanced this work

Last but not least, I would like to especially thank Stefan Fugger[2,3] for his close and thorough supervision. His profound expertise and didactic competence have not only helped to shape this thesis but have also significantly contributed to my academic growth.

---

[1] Department of Geography, University of Zurich, Switzerland

[2] Institute of Science and Technology Austria, ISTA, Klosterneuburg, Austria

[3] Swiss Federal Research Institute WSL, Birmensdorf, Switzerland

Contents

Figures

Tables

1 Introduction

As the largest river in the Aral Sea Basin, the Amu Darya constitutes a crucial freshwater source for Central Asia, a region predominated by a semiarid to arid climate (Abdolvand et al., 2015; J. Huang et al., 2022; Immerzeel et al., 2019; Wang et al., 2016). While receiving very little precipitation (<300mm/year; Pohl et al., 2017) downstream of the Pamir and Hindu Kush mountains, the river's major water source originates from upstream high mountain headwaters (J. Huang et al., 2022; Pohl et al., 2017). Therefore, the cryosphere of the Pamir mountains is representing a crucial water storage and -buffer in the Amu Darya River basin, making snow and ice reserves a critical element for sustaining seasonal water availability in Central Asia (Armstrong et al., 2019; Barandun et al., 2020; J. Huang et al., 2022; Immerzeel et al., 2009; Pohl et al., 2017; Wang et al., 2016).

With Pamir glaciers exhibiting near neutral mass balance in the recent decades, the region has been regarded as an extension of the Karakoram Anomaly (Farinotti et al., 2020; Hugonnet et al., 2021; Miles et al., 2021). However, recent evidence suggests that the region might shift towards overall negative mass balances (Hugonnet et al., 2021). Additionally, reduced mountain snowfall related to warming temperatures has been observed in the region over recent decades (Sorg et al., 2012). With future climate projections predicting a further increase in mean air temperatures and shifting precipitation regimes in the region (Jiang Jie et al., 2020; Reyer et al., 2017; White et al., 2014), the region's cryosphere is expected to further change (Barandun et al., 2020; Chen et al., 2016), which in turn is likely to affect the seasonality and magnitude of runoff (Adam et al., 2009; White et al., 2014) and affecting a large population downstream (J. Huang et al., 2022; Immerzeel et al., 2019; Yao et al., 2020).

Therefore, given the region's heavy reliance on water released from the Pamir mountain's cryosphere for both drinking and irrigation, it is essential to understand the impacts of climate change on runoff regimes and seasonal water availability in a more detailed manner. Hence, it is crucial to investigate the response of the snowmelt dominated and glacier-melt dominated headwaters to increasing air temperatures and seasonal precipitation shifts under continued climate change. In the Pamir domain, this subject has seen little investigation to date. Existing research on this topic consists of observation-based studies examining the impact under recent climate change (e.g. Chen et al., 2016; Normatov and Normatov, 2020; White et al., 2014), and studies investigating the impact under future climate projections with large-scale conceptual models (e.g. Chen et al., 2016; White et al., 2014), large-scale process-based models (e.g. Luo et al., 2018) or catchment-scale conceptual models (e.g. Hagg et al., 2013). However, these efforts rely on temporal, spatial and process-related simplifications, which can obscure relevant mechanisms and hinder the investigation of individual processes of water balance components (Mastrotheodoros et al., 2019; van Tiel et al., 2020). Therefore, physical-based approaches, representing all relevant processes of land-surface interaction by incorporating vegetational, cryospheric and hydrological processes in high temporal and spatial detail, are required to adequately capture energy and mass budgets in mountainous terrain with high topographical variability Fan et al., 2019. However, such physical-based modelling that investigates the impact of future climate change projections on catchment-scale hydrology in high-elevation catchments of the Pamir region remains undone.

To fill this research gap in the complex, mountainous terrain of the Pamir mountains, climate projections with a high spatial (∼100m) and temporal (hourly) resolution are required (Fan et al., 2019; Fiddes et al., 2022). In most cases however, neither of these requirements are fulfilled by available regional (RCM) or global (GCM) climate models and therefore careful downscaling of climate model outputs to high resolution is required (Fiddes et al., 2022) to account for detailed topographic effects, spatial gradients and feedback.

Therefore, this thesis aims to provide a downscaled meteorological forcing dataset of future climate projections for physical-based land-surface-modelling. While various downscaling methods exist within the field of dynamical and statistical downscaling, they are often constrained by accuracy, spatio-temporal scalability and data availability (see e.g. Ekström et al., 2015; Fiddes et al., 2022; Hong and Kanamitsu, 2014; Michel et al., 2021; Tapiador et al., 2020). However, a recently developed empirical-statistical downscaling scheme named TopoCLIM (Fiddes et al., 2022) specifically addresses these limitations and enables topography-aware hillslope-scale downscaling for land-surface modelling over complex terrain. Hence, CMIP6 climate projections are downscaled in this thesis by following the TopoCLIM scheme (Fiddes et al., 2022). However, prior to applying, the scheme requires a spatially downscaled reanalysis dataset, upon which the quality of the final product strongly depends, making its preparation a key factor for providing a high quality forcing dataset. For this purpose, the scheme suggests to use TopoSCALE (Fiddes & Gruber, 2014) coupled with TopoSUB (Fiddes & Gruber, 2012). While these tools have been initially tested over Switzerland (Fiddes & Gruber, 2012, 2014) and been extensively applied in diverse environments around the globe (e.g. Fiddes et al., 2015; Fiddes et al., 2019; Obu et al., 2019, 2020; Schuler and Østby, 2020; Westermann et al., 2015), the efficacy for an application in high-elevation catchments of the Pamir mountains has not been tested yet. Furthermore, an alternative method has been recently applied for downscaling a reanalysis dataset in the Pamir region (Fugger et al., 2024).

Since, up to now, an evaluation and comparison of such possible methods to generate a downscaled reanalysis dataset for the Pamir headwaters remains undone, the thesis further aims to assess the efficacy of these simplified, statistical downscaling approaches in a critical, yet understudies mountain region of Central Asia. Consequently, the thesis starts by comparing two possible methods, namely TopoPySCALE and the HIMAL-method, in two high-elevation catchments with newly established measurement networks in the Pamir mountains. This comparison intends to answer the following two questions:

(i) Which method is the most suitable for downscaling meteorological reanalysis time series in order to generate climate-length meteorological fields at the catchment scale in the Pamir mountains?

(ii) Does an additional bias-correcting step with short-term in-situ data improve the downscaled meteorological fields?

After identifying the most suitable method, the method is applied to finally generate the required downscaled, climate-length reanalysis dataset, which is further used to spatially downscale and temporally disaggregate the CMIP6 future climate projections. Eventually, the final product is evaluated in terms of its ability to reproduce catchment-wide snowpack dynamics with the land-surface model T&C, and the climate change signals at mid-century and end-century are presented.

2 Study sites and data

2.1 Domain

Two glacierised catchments on the northernmost slopes of the Pamir mountains in Tajikistan are building the study domain for this thesis: the Kyzylsu catchment and the Sangvor catchment Figure 1.Both sites are located in the headwaters of the Amu Darya river basin, making its cryosphere a crucial water storage and -buffer for the region (Pohl et al., 2017).

The Kyzylsu catchment (168.2 km^2) has an elevation range of almost 3800 metres (2076-5853 m.a.s.l.) and its glacierised area makes up slightly more than a fifth (20.8%) of the total catchment area with more than a third of it debris-covered. About half (50.4%) of the basin is vegetated, consisting of only grass. Further, 28.7% are rocky surfaces, particularly in higher elevations of the catchment or where slopes are steep.

The Sangvor catchment (37.4 km^2) is - concerning the basin area - four and a half times smaller than the Kyzylsu catchment and has approx. 500 vertical metres less on both sides of the elevation range (2518-5305 m.a.s.l.). Almost half of the catchment (49.1%) are bare, rocky surfaces. The other half consists of grass (26.8%) in the lower altitudes and glaciers (24.1%) in the higher altitudes.

An overview of the two catchments is provided in Figure 1, including their horizontal (map) and vertical (hypsometry) cover distribution. Further the general climate in the study region is presented in Figure 2. A continental climate prevails at both sites with cold winters and warmer summers. Most of the precipitation falls in winter and spring, with less precipitation towards the end of the hydrological year. Hence, the portion of annual precipitation falling as snow is high (e.g. 74% in Kyzylsu; Fugger et al., 2024). Overall, glacier mass balance in the region is dominated by a winter/spring accumulation regime (L. Huang et al., 2022).

2.2 Geodata

2.2.1 Topography

Two digital elevation models (DEMs) are used in this thesis: one with a spatial resolution of 100 metre (hillshade background in Figure 1) and one with 2 metre spatial resolution. The former is derived by resampling the ALOS PRISM stereo images derived ALOS World 3D-30 digital elevation model from a 30 metre resolution (Takaku et al., 2014) to the intended spatial resolution of 100 metres, using the nearest neighbour method. The latter is derived by processing Pleiades optical stereo images, using the NASA Ames Stereo Pipeline (ASP; Beyer et al., 2018). The Pleiades images were acquired in September 2022 (snow-free) for each study site, but existing data gaps were filled using images acquired similarly in the early summer of the same year.

The 100m-DEMs are used to provide topographical features for downscaling (section 3.2.1, section 3.2.2 and section 3.3) and land surface modelling (section 3.4). The higher resolute 2m-DEM are used to estimate slope and aspect for plot-scale land surface modelling (section 3.4)

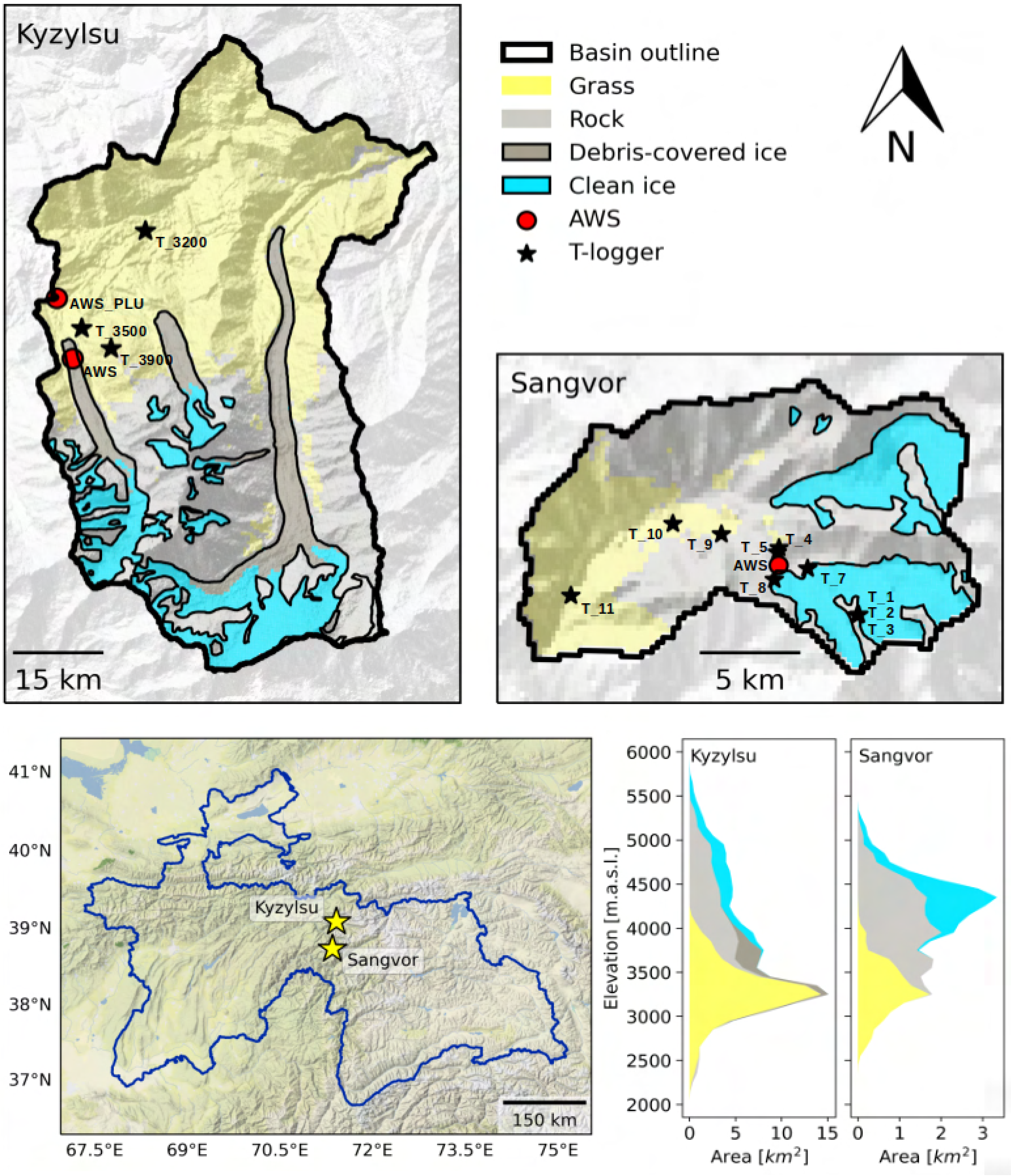

Figure 1: Map of Tajikistan showing the study sites (lower left), along with the vertical distribution (hypsometry) of land cover within the catchment (lower right) and maps showing the spatial distribution of land cover and glaciers within the catchments, including locations and names of the automatic weather stations and temperature loggers used (top).

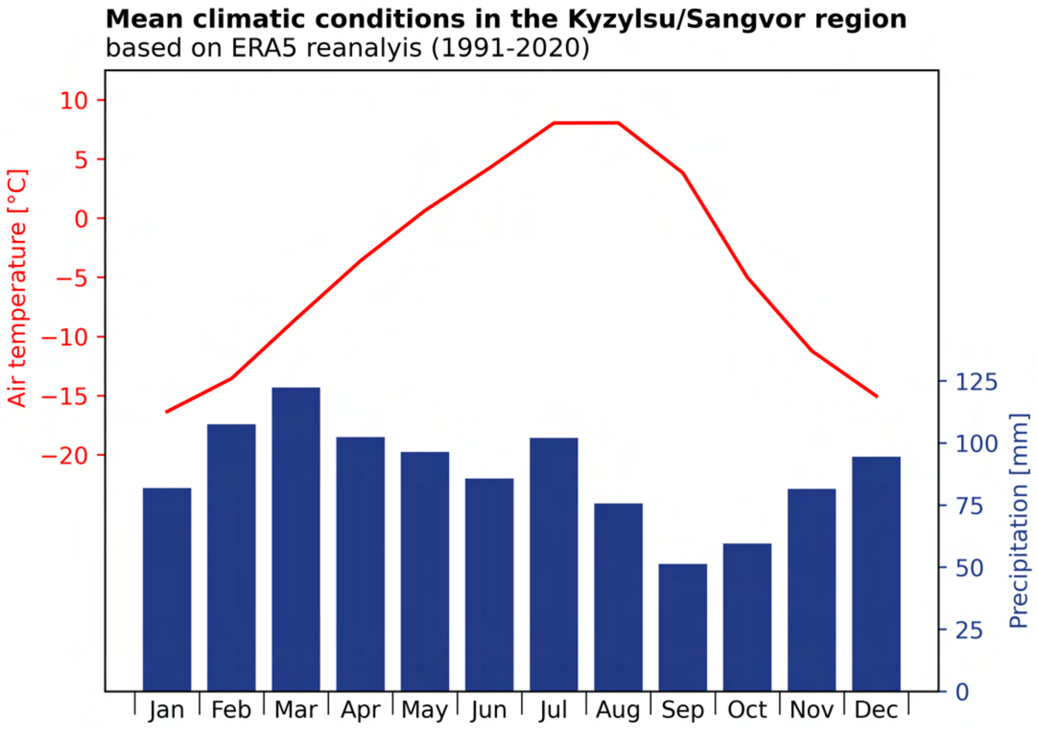

Figure 2: General climate conditions in the region of the two study sites based on climate-length ERA5 reanalysis data from 1991 to 2020. Mean 2m air temperature is indicated with a red line and mean monthly precipitation sum with blue bars.

Table 1: Overview of hydro-meteorological variables, including their abbreviations, usual units and long names. Variables used as input for land surface modelling with T&C are indicated in bold font and variables that are simulated by T&C in italic font.

Short name	Unit	Long name
Ta	°C	Near-surface air temperature (usually 2m above surface)
Rh	%	Near-surface relative humidity (usually 2m above surface)
Pr	mm	Precipitation
Ps	hPa	Surface air pressure
Sw↓	W/m^2	Downwelling shortwave radiation
Sw↑	W/m^2	Upwelling shortwave radiation
Lw↓	W/m^2	Downwelling longwave radiation
Lw↑	W/m^2	Upwelling longwave radiation
Ws	m/s	Wind speed (at reference height)
Wdir	°	Wind direction
Ts	°C	Surface temperature
Tdeb	°C	Debris temperature at given depth
Sd	cm	Snow depth / snow height

2.2.2 Glacier maps and debris maps

Glacier outlines of RGI 6.0 (RGI Consortium, 2017; see Figure 1) are used to derive the glacierised area within the catchments. Further, debris-covered glacier area (Figure 1) is extracted using outlines by Scherler et al. (2018) and finally, debris thickness is empirically derived as a function of velocity, as described in Buri et al. (2023).

2.2.3 Land cover maps

Land Cover maps with a spatial resolution of 100 metre are derived by aggregating the vegetated area from the 2019 land cover product of PROBA-V satellite imagery (Buchhorn et al., 2020) to forest, shrubs and grassland, whereas in both catchments the vegetated area consists of only grassland. However, it should be noted that these are generalisations and in reality sub-grid heterogenities are likely.

2.2.4 Snow lines and snow maps

Snowlines are derived from the MODIS product MOD10A1.v6 (Hall & Riggs, 2021), using the RSLE method (Krajčí et al., 2014). Further, snow cover maps are derived as following: Landsat-7 surface reflectance from Landsat Collection 2 Level-2 (USGS EROS Archive, 2020) and Landsat-8 surface reflectance from the Harmonized Landsat Sentinel-2 project (HLS; Masek et al., 2021) are used to compute the Normalised Difference Snow Index (NDSI) and surface albedo, following Liang (2001). Outside of clean-ice areas, a critical NDSI threshold is computed using the Otsu method (Otsu, 1979) and further used to classify pixels as snow-free or snow-covered. On clean-ice areas, in order to avoid misclassifying bare-ice as snow, a surface albedo threshold, computed using the Otsu method, is used to distinguish bare-ice and snow. This albedo threshold is bounded by 0.25 and 0.55 following Naegeli et al. (2019). Due to difficulties encountered when using albedo to distinguish snow and ice in shaded areas, these areas were excluded from the analysis by computing the shadow-affected areas from the sun azimuth angle, the sun zenith angle and the DEM.

2.3 Observations

2.3.1 Kyzylsu

The monitoring of the Kyzylsu catchment started in June 2021 and is geared towards glacio-hydrological modelling (Fugger et al., 2024)). The network includes two automatic weather stations (AWS) and three additional air temperature loggers. One AWS (KYZ_AWS; Figure 3) is located on the lower part of the Kyzylsu Glacier ablation zone over a surface of mixed cobbles and sand. The other one (KYZ_AWS_PLU) is on a small plateau approximately 1km to the north of the Kyzylsu Glacier snout, intended to represent off-glacier meteorological conditions. The available measured or measurement-derived hydro-meteorological variables include air temperature (Ta), relative humidity (Rh), precipitation (Pr), surface air pressure (Ps), downwelling and upwelling shortwave and longwave radiation (Sw↓, Sw↑, Lw↓, Lw↑), wind speed (Ws), wind direction (Wdir), snow height (Sd) and debris temperature (Tdeb). A definition of the measured variables is given in Table 1, and an overview of the monitoring network in Figure 1 (locations) and Table 2 (measurement details).

At this point it should be mentioned that in September 2023 the author of this thesis was part of a field work campaign, contributing in maintaining the monitoring network in this valuable, remote catchment. In turn, the author gained a more profound understanding of the monitoring network, including its local conditions and challenges.
The observations from October 2021 until September 2022 include a full hydrological cycle and are used in this thesis as in-situ data for the observational period of the Kyzylsu catchment. The exact available and used time span is indicated for each variable and location in Table A.1.

For each measured variable a thorough examination, selection, and whenever needed processing, is carried out and described in this paragraph.
The pressure sensor of the AWS on Kyzylsu-glacier (KYZ_AWS) didn't work correctly and is therefore not used in this thesis. Furthermore, the automatic weather station KYZ_AWS_PLU is not equipped with a pressure sensor itself and the pressure data from the nearby stream gauging station KZY_GAUG, located 500 metres southeast at a similar altitude, is used as a representative for the station instead.
Debris temperature at the KYZ_AWS was measured by two installed temperature sensors. Since debris temperature is strongly influenced by the debris thickness (Östrem, 1959), the measurements of the debris-covered logger closest to the modelled debris thickness of 22.4cm is used, which is the thermistor located directly at the UDG (Thermistor2).
Concerning near-surface air temperature (Ta), near-surface relative humidity (Rh) and wind speed (WS), the sensor nearest to 2 metres above the surface is used at locations where multiple sensors at different heights are present. Excluding wind speed, differences to 2 metres above surface level are considered negligible. For wind speed, the corresponding value at 2 metres above the surface is calculated from the measured wind speed at the sensor height, applying the logarithm law Equation 1. The relative roughness is thereby estimated as 0.1 for both measurement locations.
Additionally, following the correction method proposed by Masuda et al. (2019), a catch ratio based on the wind speed at gauge level is used to address and correct the wind-induced precipitation undercatch. The wind speed at gauge level is calculated according to the logarithm law as well.
Finally, in order to obtain a dataset at an hourly resolution, the measurements are aggregated from the logged 15 minute intervals by calculating the hourly mean value, except for precipitation where the hourly sum is calculated, and show depth, where only daily values are available.

$$U = U_{\text{obs}} \frac{\ln(z_1 - z_0)}{\ln(z_2 - z_0)}, \tag{1}$$

where

- z_1 = height of interest [m] = 2m or height of rain gauge
- z_2 = height of anemometer [m]
- z_0 = relative roughness element [0-1]

Table 2: Available measurement locations in the Kyzylsu catchment with their unique names and used hydro-meteorological parameters. One additional pressure transducer at KYZ_AWS is not listed, since it didn't work properly. At KYZ_T_3200 data is only available from 21th June 2022 onwards. Measured variables that are not used in the thesis are written in grey font.

Location name	Altitude [m.a.s.l]	Type	Sensor	Senosr height [m.a.g.l]	Measured variable(s)
KYZ_AWS	3579	AWS	Anemometer	2.78	Ws, Wdir
			Radiometer	2	Sw↓, Sw↑, Lw↓, Lw↑
			Aspirated T/RH	2	Ta, Rh
			Ultrasonic distance sensor		Sd
			Thermistor 1	-0.15	Tdeb
			Thermistor 2	-0.21	Tdeb
KYZ_AWS_PLU	3369	AWS	Wind monitor (propeller)	4.49	Ws, Wdir
			T/RH	4.04	Ta, Rh
			Sonic distance sensor	3.89	Sd
			Rain gauge	2.31	Pr
KZY_GAUG	3366	Logger	Pressure	0	Ps
KYZ_T_3200	3186	Logger	Temperature	2	Ta
KYZ_T_3500	3529	Logger	Temperature	2	Ta
KYZ_T_3900	3899	Logger	Temperature	2	Ta

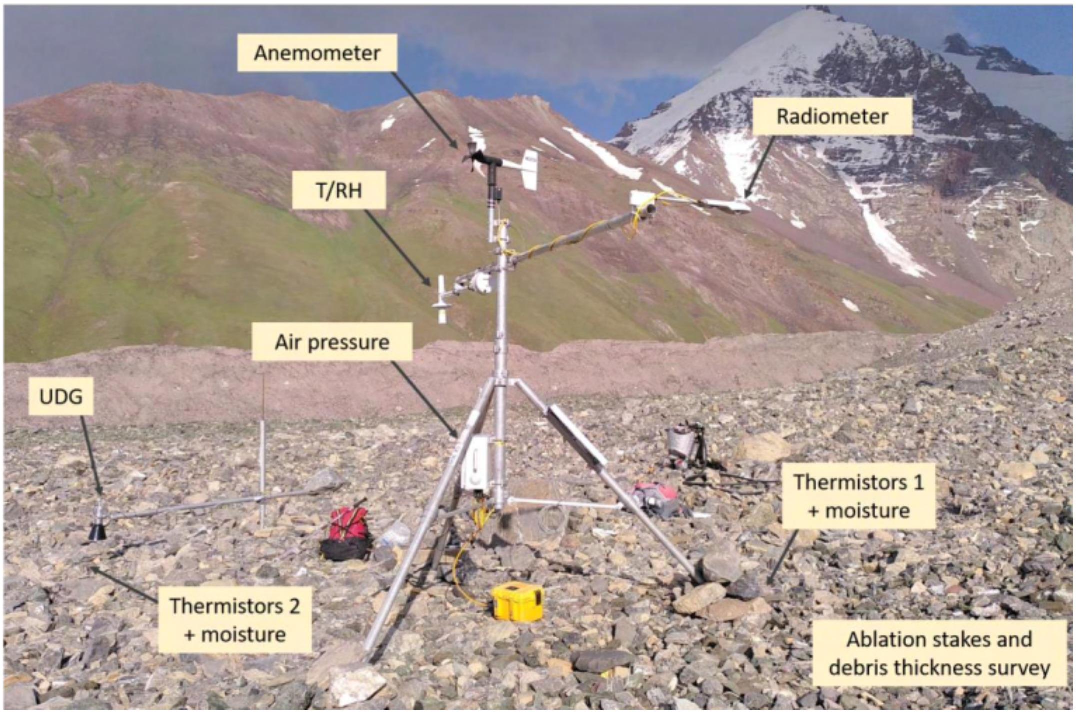

Figure 3: On-glacier AWS KYZ_AWS as an example for an automatic weather station in the Kyzylsu catchment. Source: Pamir field report 2021

2.3.2 Sangvor

The monitoring network for the Sangvor catchment was set up in September 2021 and consists of an automatic weather station Figure 4 and twelve additional surface temperature loggers. The installed AWS is situated in a moderately exposed location on a small rise above the proglacial plain. Except for precipitation (Pr), surface pressure (Ps), and debris temperature(Tdeb), the monitoring of the catchment provides measurements for the same hydro-meteorological variables as in the Kyzylsu catchment, but with additional surface temperature (Ts) measurements. An overview of the monitoring network and its sensors is given in Figure 1 (locations) and Table 3 (measurement details).

The earliest available time series starts on 19. September 2021 and includes almost one full year (except for the last three days). Data available for the hydrological year 2022 is used in this thesis for the observational period. The exact available time span used is indicated for each variable and location in Table A.1. For bias correcting within the HIMAL-method, the whole dataset is used, maximising the covered period.

Same as for the Kyzylsu catchment, the sensor nearest to 2 metre above surface is used for near-surface air temperature (Ta), near-surface relative humidity (Rh) and wind speed (WS). Differences to the 2 metre above surface level are considered as negligible, except for wind speed where wind speed at sensor height is transformed to wind speed 2 metres above the surface by applying the logarithm law Equation 1 with an estimated relative roughness of 0.1. Further, it is important to mention that the installed surface temperature (Ts) loggers are located at the ground and could therefore be covered with snow. Finally, all measurements are aggregated from the logged intervals to an hourly resolution.

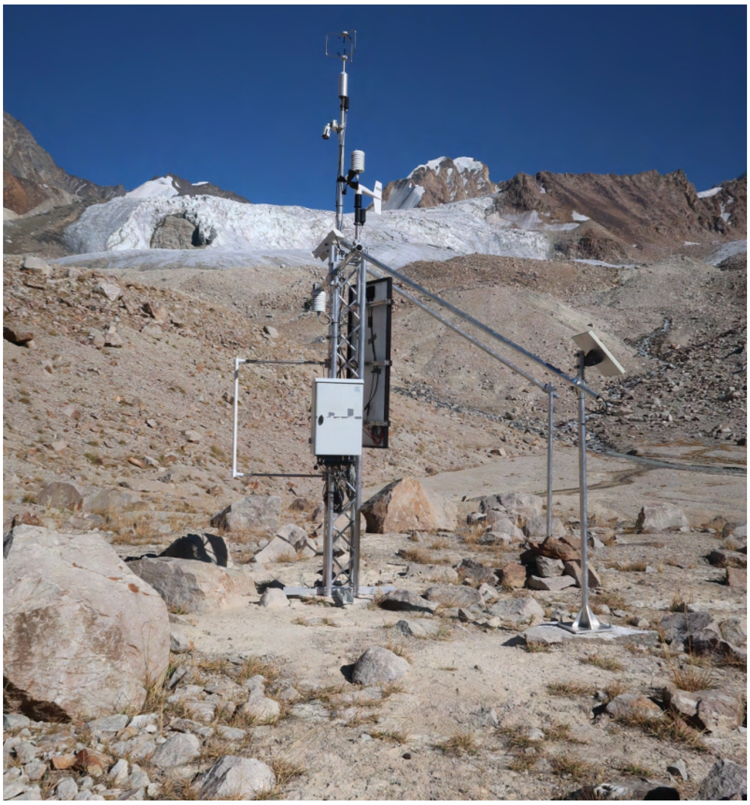

Figure 4: AWS SANG_AWS in the Sangvor catchment. Source: Nissai fact-sheet 2021

Table 3: Available measurement locations in the Sangvor catchment with their unique names and used hydro-meteorological parameters. Two additionally installed surface temperature loggers (SANG_T_6 at 4616 m.a.s.l. and SANG_T_12 at 2431 m.a.s.l.) are not listed for this thesis, since the former had no data available and the latter is located outside of the catchment outline used for this thesis. Measured variables that are not used in the thesis are written in grey font.

Location name	Altitude [m.a.s.l]	Type	Sensor	Senosr height [m.a.g.l]	Measured variable(s)
SANG_AWS	3909	AWS	Anemometer	4.43	Ws, Wdir
			T/RH	3.73	Ta, Rh
			Wind monitor (propeller)	3.13	Ws, Wdir
			Radiation sensor	2.73	Sw↓, Sw↑, Lw↓, Lw↑
			Infrared sensor	2.73	Ts
			Sonic distance sensor	2.73	Sd
			T/RH	2.43	Ta, Rh
SANG_T_1	4389	Logger	Temperature	0	Ts
SANG_T_2	4404	Logger	Temperature	0	Ts
SANG_T_3	4412	Logger	Temperature	0	Ts
SANG_T_4	3942	Logger	Temperature	0	Ts
SANG_T_5	3938	Logger	Temperature	0	Ts
SANG_T_7	4002	Logger	Temperature	0	Ts
SANG_T_8	3951	Logger	Temperature	0	Ts
SANG_T_9	3591	Logger	Temperature	0	Ts
SANG_T_10	3236	Logger	Temperature	0	Ts
SANG_T_11	2800	Logger	Temperature	0	Ts

2.4 Reanalysis data

2.4.1 ERA5

ECMWF Reanalysis v5 (ERA5) is the fifth generation of ECMWF atmospheric reanalysis for the global climate and weather. ERA5 is based on the Integrated Forecasting System (IFS) Cy41r2 and available at hourly temporal resolutions from 1940-present with a spatial resolution of 0.25°x0.25° ($\sim$31 km). Inddition to the meteorological variables at surface level it provides a vertical resolution of the atmosphere at 137 different pressure levels from 1000hPa to 1hPa. As Successor of ERA-Interim it therefore extends the temporal as well as the horizontal and vertical resolution. (Hersbach et al., 2023a, 2023b; Hersbach et al., 2020).
In this thesis, ERA5 reanalysis of the hydrological year 2022 is used for the observational period (section 3.2.2 and Figure 6), and downscaled ERA5 reanalysis from 1985 to 2014 as a climate reference period for downscaling the future climatology (section 3.3 and Figure 6).

2.4.2 ERA5-Land

ERA5-Land is driven by the downscaled meteorological forcing from ERA5 climate reanalysis and therefore a sub-product of ERA5. An enhanced spatial resolution of 9 km (0.1°x0.1°) is one of the main advantages of this product. The temporal resolution remains hourly with data available from 1950 to present. The earth's surface is represented in ERA5-Land with 4 surface levels. (Muñoz-Sabater, 2019; Muñoz-Sabater et al., 2021)
The reanalysis product ERA5-Land of the hydrological year 2022 is used in this thesis for the observational period (section 3.2.1 and Figure 6).

2.4.3 NHM-SMAP

Niwano et al. (2018) introduced the high-resolution regional climate model NHM-SMAP (Non-Hydrostatic atmospheric Model–Snow Metamorphism and Albedo Process) with a horizontal resolution of 5km. The coupled model combines the Japan Meteorological Agency Non-Hydrostatic atmospheric Model (NHM) and the Snow Metamorphism and Albedo Process model (SMAP) and is forced by the Japanese 55-year reanalysis (JRA-55). Taking advantage of both short-term detailed weather forecast models and long-term computationally stable climate models, it outputs hourly values of surface meteorological properties including precipitation. (Niwano et al., 2018)
NHM-SMAP data from 2017 to February 2022 is used in this thesis to derive vertical temperature and precipitation gradients within the HIMAl-method section 3.2.1

2.5 Climate scenarios

The basic future climate projections used in this thesis come from the Coupled Model Intercomparison Project Phase 6 (CMIP6), which is organised within the World Climate Research Programme's (WCRP) Working Group on Coupled Modelling (WGCM) (Eyring et al., 2016). CMIP6 integrates both socioeconomic and radiative forcing scenarios, utilising the ScenarioMIP framework. This framework structures CMIP6 scenarios in a matrix, with Shared Socioeconomic Pathways (SSPs) and the forcing levels of Representative Concentration Pathways (RCPs) forming its axes (Eyring et al., 2016; O'Neill et al., 2016). Such a coupled approach is advantageous as it allows to represent various combinations of socioeconomic challenges related to mitigation and adaptation by incorporating SSPs (O'Neill et al., 2016, 2017), while maintaining compatibility with CMIP6's predecessors and other RCP-based climate models through the concurrent use of RCPs (Eyring et al., 2016).

With ScenarioMIP's experimental design suggesting participating modelling groups to run at least all four 21st century top priority scenarios, grouped in the so called *Tier1* (O'Neill et al., 2016), the highest number of model runs is to be expected within this group. Therefore, this thesis focuses on Tier 1, consisting of the low end (SSP1-2.6), medium end (SSP2-4.5), medium to high end (SSP3-7.0) and high end (SSP-5.85) range of future pathways (O'Neill et al., 2016), with future projections starting in 2015. A more detailed description of these CMIP6 scenarios is further given in O'Neill et al. (2016).

The standardised outputs of CMIP6 are accessible through the Earth System Grid Federation, as noted by Eyring et al. (2016). Model chains are selected based on the variant with the most extensive set of model runs available, specifically the r1i1p1f1 variant. Further, they are only used if they provide gapless datasets at a daily resolution for all meteorological variables over the historical reference period as well as across all four Tier 1 future scenario projections. Thereby, the historical reference period is defined to cover a standard climate-length (30 years; Arguez and Vose, 2011) from 1985 up to and including 2014, and future projections are retrieved from their onset in 2015 through to the end of 2099. The six retrieved and complete model chains used in this thesis are presented in Table 4. A full description of all used CMIP6 variables is given in Table 6, and CMIP6's scenario matrix is shown in Figure 5, including the scenario's priority within ScenarioMIP.

Table 4: Retrieved CMIP6 model chains and their spatial resolution. For all model chains a historical reference period and the Tier1 future projections are retrieved for the variant r1i1p1f1 at daily temporal resolution.

Scenario	Timestep	Variant	Model	Spatial resolution (lat x lon)
Historical SSP1-2.6 SSP2-4.5 SSP3-7.0 SSP5-8.5	daily	r1i1p1f1	GFDL-ESM4	1.00° x 1.25°
			IPSL-CM6A-LR	~1.27° x 2.50°
			MIROC6	~1.401° x ~1.406°
			MPI-ESM1-2-HR	~0.935° x ~0.938°
			MPI-ESM1-2-LR	~1.865° x 1.875°
			MRI-ESM2-0	~1.121° x 1.125°

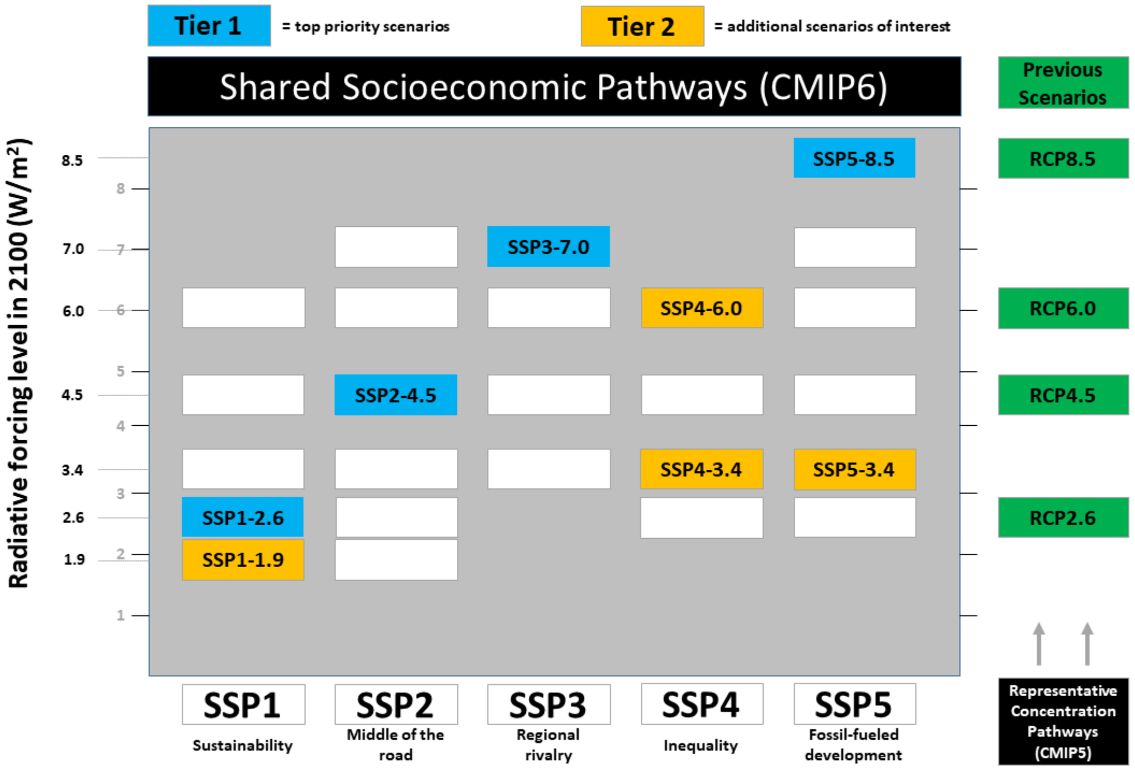

Figure 5: ScenarioMIP's scenario matrix consisting of Shared Socioeconomic Pathways and year 2100 radiative forcing combinations used in CMIP6, Including an overview of the scenario priority defined in O'Neill et al. (2016). Source: based on Fig.2 of O'Neill et al. (2016), and retrieved from https://climate-scenarios.canada.ca/?page=cmip6-overview-notes

3 Methods

3.1 Overview

Following the four step procedure presented in Figure 6, a suitable method for downscaling meteorological reanalysis data in the study domain is identified in a first step (i) and subsequently (ii) applied to downscale ERA5 reanalysis for the historical reference period of CMIP6. This downscaled reanalysis product further serves (iii) as pseudo-observations for downscaling Tier 1 future climate scenarios of the general circulation model CMIP6 to 100m spatial resolution and hourly temporal resolution, following the TopoCLIM scheme of Fiddes et al. (2022) with minor adjustments. Eventually, (iv) the land surface model *Thetys-Chloris* (T&C; Fatichi et al., 2012a, 2012b) is forced in a semi-distributed manner to evaluate whether the spatial dynamics of observed snow cover are well reproduced with the downscaled CMIP6 forcings of the historical period.

3.2 Spatial downscaling of reanalysis data

Bias-correcting-based downscaling of future climate scenarios (step3; Figure 6) requires a climate-scale time series reference dataset (Fiddes et al., 2022). Due to insufficient in-situ data in the study domain, this reference dataset is derived by downscaling global reanalysis for the historical reference period (step2; Figure 6), upon which the quality of the final product strongly depends. Therefore, an appropriate downscaling method, suited for the study domain, is required. To address this, two potential downscaling methods are applied and compared for the observational period (step1; Figure 6): *TopoPyScale*, based on the work of Fiddes and Gruber (2012, 2014) and implemented in the eponymous open-source Python tool TopoPyScale (Filhol et al., 2023), and the *HIMAL-method*, described by Machguth et al. (2009) and previously employed by this thesis's supervising research group (e.g., Fugger et al., 2024). The observational period is thereby defined as the hydrological year 2022. Thus, after spatially downscaling ERA5 and ERA5-Land using TopoPyScale and the HIMAL-method, respectively, the downscaled reanalysis forcings are evaluated against meteorological observations of the hydrological year 2022 in both catchments. It is important to empathise that this comparison serves to identify the more suitable downscaling method, and only one of the presented methods (TopoPyScale) is finally applied for the historical reference period in order to generate a climate-length, downscaled reanalysis reference period further used for quantile mapping CMIP6 scenarios. Additionally, the ability to reproduce surface temperature, snowpack dynamics and debris temperature within T&C is assessed at plot-scale.

Furthermore, the added value of bias correction with short-term in-situ data is investigated by additionally extending and evaluating the HIMAL-method with a bias correction step. However, it is important to clarify that this thesis does not consider to apply an additional bias correction step in downscaling the full historical reference period, since observations are only available over one year, which is seen as insufficient to reflect average climatic conditions for bias correcting a standard climatic period of thirty years. Therefore, the examination of the bias correction's added value is confined to the observational period, aiming to provide a basis for further research, for instance for short-term application or when more ground data is available.

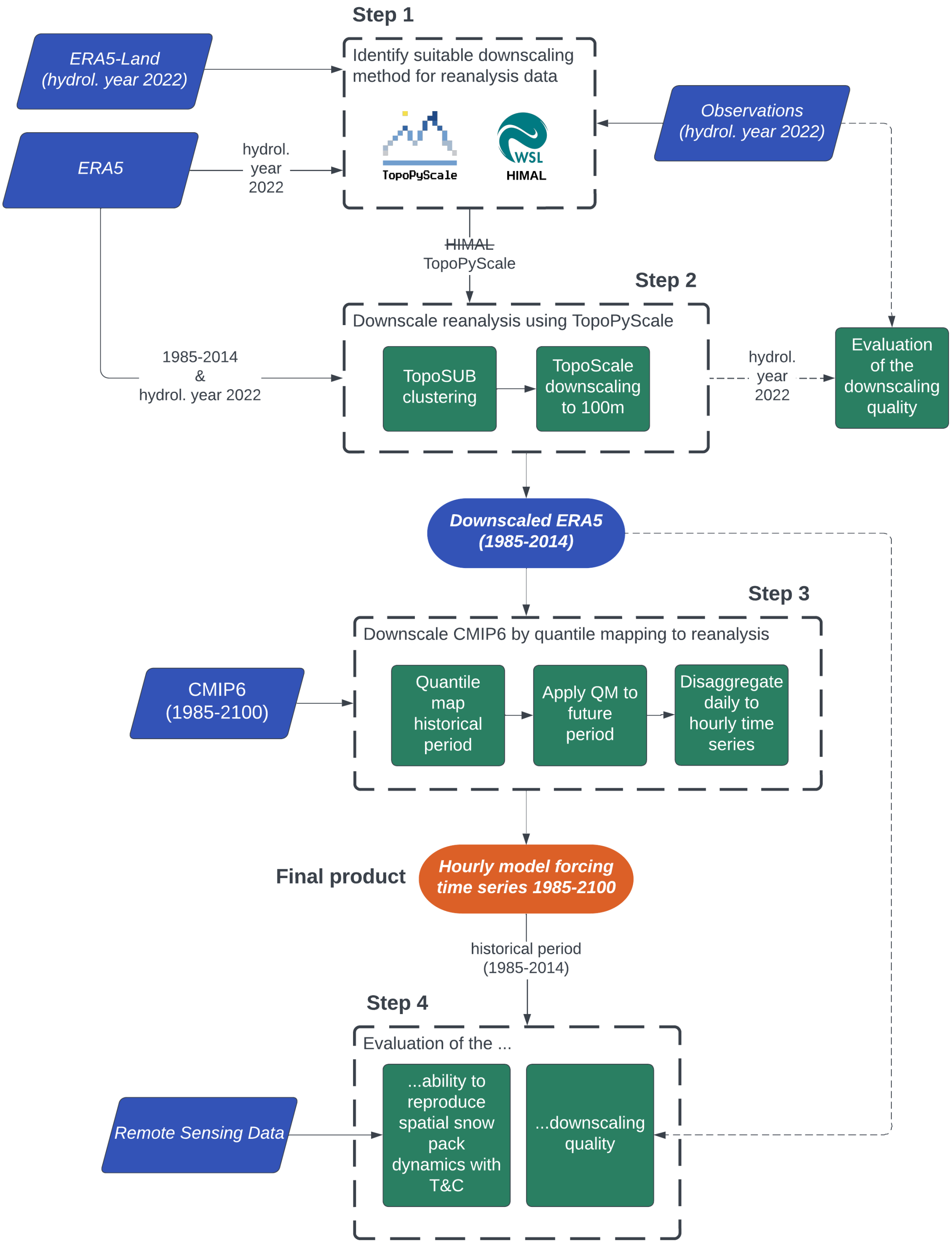

Figure 6: Schematic overview of the main processes and experimental setup of this thesis.

3.2.1 HIMAL-method

The HIMAL-method is geared towards catchment scale land-surface modelling and follows the general method of Machguth et al. (2009) to generate statistically downscaled hourly ERA5-Land forcings from coarse grid cells (approx. 9 km) to the 100 metre spatial resolution Fugger et al. (2024) of the input DEM (section 2.2.1). Again, it is mentioned hereby that this method is only applied for the observational period.

For most meteorological variables, such as air temperature (Ta), relative humidity (Rh), precipitation (Pr) and incoming shortwave and longwave radiation (Sw↓, Lw↓), a vertical gradient (lapse rate) is applied to the coarse grid in order to produce a new grid on a normalised 0 m.a.s.l. reference plane where the horizontal gradients remain. Subsequently, the normalised grids are spatially interpolated for each timestep to the desired 100m grid resolution by employing a thin-plate spline interpolation. Finally, the interpolated grid cells on the 0 m.a.s.l. reference plane are mapped to the altitude of the provided fine grid DEM using the same vertical gradients as before. A schematic overview of the described approach is presented in Figure B.1.

Vertical temperature gradients are derived for each catchment based upon the availability of in-situ data. In the case of the Kyzylsu catchment, air temperature records were available on different elevations (Table 2) and therefore used to generate a mean hourly-monthly temperature gradient following Shaw et al. (2022). However, it should be noted that these gradients may be over-fitted to lower elevations, since the higher altitude ranges of the catchment remain ungauged. In the Sangvor catchment, not enough air temperature measurements are available in order to derive a vertical gradient. Therefore, mean hourly-monthly temperature gradients are derived for this catchment from the higher resolved NHM-SMAP (Niwano et al., 2018), recently developed over High Mountain Asia (unpublished). Compared to the raw ERA5-Land gridded data, the 5km grids of NHM-SMAP are deemed to represent a greater sub-grid variability of temperature against elevation.

As relative humidity (Rh) depends on air temperature, dew point temperature from ERA5-Land grids is first downscaled using the same lapse rates as described above for air temperature and subsequently converted into relative humidity by following the calculation of saturated vapour pressure from Murphy and Koop (2005) and using the already downscaled air temperature and air pressure.

For precipitation (Pr), a substantial gradient was witnessed from field visits and deemed to be appropriately explained by an hourly-monthly mean vertical gradient (Fugger et al., 2024). It is assumed to be similar for the Sangvor catchment, since both catchments are rather small, have a similar elevation range and are spatially close to each other. Given the insufficient amount of precipitation gauges in the Kyzylsu catchment, and the complete absence of such gauges in the Sangvor catchment, vertical precipitation gradients are derived from NHM-SMAP as well. Further, interpolated values below 0.05 mm are set to zero and finally, regions of the catchment with no precipitation in the coarser ERA5-Land grids are set to zero as well, preserving the original discontinuities of ERA5-Land precipitation fields (Figure B.2).

Incoming short- and longwave radiation (Sw↓, Lw↓) are provided with small vertical gradients based upon the work of Marty et al. (2002) who derived vertical radiation gradients from observations across the Alps. For incoming shortwave radiation, the vertical gradient is +1.3 Wm^2 / 100m and for incoming longwave radiation -2.9 Wm^2 / 100m. It should be noted that the interpolation does not account for the potential relationship with topography due to e.g. cloud formation, for it can be accounted for within T&C. However, it is additionally accounted for when comparing to TopoPyScale, since the latter inherently accounts for topography.

Finally, air pressure (Ps) and wind speed (Ws) are downscaled with different methods than the above mentioned variables: surface air pressure is downscaled simply using its known relationship to elevation and wind speed is calculated from the u- and v-components from the closest ERA5-Land grid cell using the diagnostic WINDSmodel as described by Burlando et al. (2007) and Peleg et al. (2017). While the latter method accounts for topographic sheltering of winds and for the exposed nature of valley ridges, it does not account for wind regimes affected by density driven flows (e.g. glacier katabatic winds) or by valley heating (slope winds).

The data source(es) used to derive the vertical distribution (as described above) is indicated for each variable and catchment in Table 5.

To additionally evaluate the added value of an additional bias correcting step with short-term in-situ station data, the above described procedure is extended with the commonly used empirical quantile mapping function (EQM) (e.g. Fiddes et al., 2022; Rye et al., 2010; Themeßl et al., 2012. This method is further referred to in this thesis as *HIMAL-BC*. Provided station coordinates are used to extract the corresponding pixel of the downscaled variable for the total period over which observations are available and subsequently derive monthly variable bias-correction coefficient series. To do so, the downscaled hourly data is compared against the hourly observations and an additive or multiplicative (precipitation) correction factor based upon the cumulative distribution function with n numbers of quantiles is defined. Seasonal biases are accounted for by using monthly bias-correction coefficients. The number of quantiles used was empirically derived through optimisation and set to 300, as increasing this value did not result in additional improvement of performance (Fugger et al., 2024).

Dealing with precipitation, multiplicative EQM coefficients are derived based upon daily sums of observations and downscaled grid points (Themeßl et al., 2011; Wilcke et al., 2013). Dry-day frequency underestimation caused by high frequency light precipitation ('drizzling effect'; e.g Gutowski et al., 2003) is known to be an issue in ERA5 products (e.g. Lavers et al., 2022) and therefore addressed by setting daily precipitation values below 0.1 mm to zero. Subsequently, the above-described EQM scheme is applied and the bias corrected daily values are temporally disaggregated back to hourly intervals. To do the latter, the temporal distribution from the initial ERA5-Land dataset is applied, ensuring consistency with other forcing variables (e.g., avoiding coincidences of high solar radiation values and high precipitation rates).

Ground data used for bias correction is selected by a manual interpretation of the available data's adequacy. However, monitoring meteorological conditions in remote, high elevation regions is challenging: station failures, dysfunctional sensors or data gaps affect the overall time series and thus possible choices are sometimes limited. The selected measurement locations used for bias correcting are presented for each variable and catchment in Table 5, whereby only locations covering at least a certain percentage of the bias correcting period are used. While data availability in the Kyzylsu catchment allows setting this threshold to 95%, the threshold in Sangvor was set to 89%, allowing the use of every measured variable. Bias-correction coefficients derived based upon one single reference location are assumed to be representative for the whole catchment and thus applied to bias-correct all grid cells. If multiple locations with sufficient data are used, a spline interpolation is used to distribute the bias correction coefficients

in three dimensional space. In order to avoid extrapolation issues towards areas with no stations (e.g. in ungauged high elevation regions), mapping coefficients are kept equal to the nearest station when moving beyond the geographical limits of the used stations.
However, it is important to mention, that only one year of station data (hydrological year 2022 for Kyzylsu, and full dataset for Sangvor) is used to quantile map downscaled reanalysis data and thus seasonal biases could occur (e.g. if the year included had an extraordinarily hot summer). Furthermore, for variables where many (or all) available measurement locations are already included in bias correction, additional in-situ measurements are missing in order to be able to perform an independent evaluation of bias correction.

Table 5: Treatment of each ERA5-Land variable within the HIMAL-method and HIMAL-BC, including the data source(s) for deriving vertical gradients, and stations used for bias correction in HIMAL-BC.

	Kyzylsu		Sangvor	
Variable	Vertical gradient	Station(s) for EQM	Vertical gradient	Station(s) for EQM
Ta	KYZ_AWS KYZ_T_3500 KYZ_T_3900	KYZ_AWS KYZ_T_3500 KYZ_T_3900	NHM-SMAP	SANG_AWS
Rh	Same as Ta	KYZ_AWS	NHM-SMAP	SANG_AWS
Pr	NHM-SMAP	KYZ_AWS_PLU	NHM-SMAP	-
Ps	Correlation with altitude	KZY_GAUG	Correlation with altitude	-
Sw↓	Literature (fixed)	KYZ_AWS	Literature (fixed)	SANG_AWS
Lw↓	Literature (fixed)	KYZ_AWS	Literature (fixed)	SANG_AWS
Ws	ERA5-Land	KYZ_AWS	ERA5-Land	SANG_AWS

3.2.2 TopoPyScale

TopoPyScale (Filhol et al., 2023) is an open-source python package for downscaling ERA5 reanalysis and is based on an adapted version of the downscaling scheme TopoSCALE (Fiddes & Gruber, 2014), including an option to couple the sub-grid scheme TopoSUB (Fiddes & Gruber, 2012). Spatial downscaling can therefore be run either at plot-scale for predefined points of interests by providing their coordinates (e.g. locations of weather stations) or in a semi-distributed manner by coupling the clustering routine TopoSUB to the downscaling routine TopoSCALE.

The Topographic SUBgrid tool (TopoSUB; Fiddes and Gruber, 2012) uses the K-means clustering algorithm (Hartigan & Wong, 1979) to cluster fine resolution DEM grid cells based on their geographical and topological features, such as location, elevation, slope, aspect and sky view factor. Subsequently, cluster centroids (points) representing the mean geographical and topological features of the cluster are generated. These centroids can be seen as ‘virtual points’, as they do not exist in reality (e.g. they have a different elevation than the same coordinates of the initial provided DEM). Cluster centroids can subsequently be used for computational-efficient semi-distributed downscaling, as they efficiently describe sub-grid behaviour and allow a post-downscaling disaggregation of downscaled values back to the initial grid. To do so, each grid cell of a cluster is assigned the same downscaled value from its representing centroid.

TopoSCALE (Fiddes & Gruber, 2014) is an extensively tested (e.g. Fiddes et al., 2015; Fiddes et al., 2019; Obu et al., 2019, 2020; Schuler and Østby, 2020; Westermann et al., 2015 quasi-physical topography-based downscaling scheme used in TopoPyScale as routine for spatially downscaling ERA5 reanalysis from coarse grid cells (approx. 30 km) to points of interests (either provided coordinates or TopoSUB cluster centroids) based on their topological features derived from the input DEM (in this thesis a 100m DEM; section 2.2.1). Air temperature (Ta), relative humidity (Rh), surface air pressure (Ps) and wind speed (Ws) are downscaled directly from ERA5 pressure levels by a three dimensional interpolation, inherently accounting for time varying vertical gradients. As downscaled wind speed is at 10m above surface, 2m wind speed used for comparison against the HIMAL-method is calculated based on Equation 1. Precipitation (Pr) is downscaled from the ERA5 surface grid using a non-linear lapse rate based on Liston and Elder (2006) and radiative fluxes (Sw↓ and Lw↓) are topographically corrected, including an elevation correction. A more detailed description of the involved downscaling processes is presented by Fiddes and Gruber (2014). In contrast to the HIMAL-method, the routine does not rely on additionally provided lapse rates, as all vertical gradients are already implemented.

In order to compare the implemented downscaling routine against the HIMAL-method for the observational period, TopoPyScale is applied at plot-scale. Further, the TopoSUB-coupled version is applied for the historical reference period to derive a reference dataset for downscaling future CMIP6 scenarios, as described in section 3.3

Table 6: CMIP6 variables used in this study, together with the Climate and Forecast Conventions (CF) standard names and the used disaggregation method. Tasmin and tasmax are only used to disaggregate near-surface air temperature (tas). Near-surface wind speed (sfcWind) is derived from the eastward (uas) and northward (vas) components of near-surface wind, and wind direction is not analysed in this thesis.

CMIP6 variable name	Unit	Timestep	CF long name	Disaggregation method
tas	K	daily	Near-surface air temperature	Melodist: sine mean
tasmin	K	daily	Daily maximum near-surface air temperature	
tasmax	K	daily	Daily minimum near-surface air temperature	
pr	kg/m^2s	daily	Precipitation	Station derived (KYZ_AWS_PLU)
ps	Pa	daily	Surface air pressure	Linear interpolation
hurs	%	daily	Near-surface relative humidity	Melodist: equal
rsds	W/m^2	daily	Surface downwelling shortwave radiation	Melodist: pod rad
rlds	W/m^2	daily	Surface downwelling longwave radiation	Relationship to Ta
sfcWind	m/s	daily	Near-surface wind speed (10m)	Melodist: random

3.3 Downscaling future meteorology

While both TopoPyScale and the fully gridded HIMAL-method exhibit comparable performance for many meteorological variables throughout the observation period (section 4.1.1), TopoPyScale demonstrates a slight superiority in reproducing certain variables such as air temperature (Ta), surface air pressure (Ps) and incoming shortwave radiation (Sw↓). Additionally, it offers extra benefits, making it a more suitable choice for generating downscaled reanalysis forcings of the reference period. The main advantage of the chosen method is the already built-in possibility for semi-distributed downscaling (by coupling TopoSUB), drastically reducing both computational resources required as well as storage demand. To leverage this advantage, ERA5 reanalysis is downscaled for the historical reference period using the TopoSCALE routine coupled with prior TopoSUB clustering (step 2; Figure 6). For this purpose, the clustering method implemented is enhanced by incorporating an algorithm that considers land cover within the catchment during clustering. To do so, the clustering routine is executed separately for each land cover type, ensuring all cluster members share the same land cover type. The number of clusters per land cover is determined by the relative area covered within the catchment. Decimal numbers are rounded up to the next integer, ensuring the total number of clusters does not decline (thus in most cases the total number of clusters slightly increases). Following the demonstration (Fiddes & Gruber, 2012) of stable performance at 128 clusters in all tested cases, the total number of clusters is set to 128, resulting in 132 clusters for Kyzylsu and 129 clusters for Sangvor.

This approach eventually provides a climate length time series of ERA5 pseudo-observations while still accounting for the main topographic effects on atmospheric forcing (Fiddes et al., 2022). The downscaled reanalysis series further serves as reference data for statistical downscaling CMIP6 scenario outputs (step 3; Figure 6) using the quantile mapping bias correction method (Gudmundsson et al., 2012). Seasonal varying biases are addressed through monthly quantile mapping. A detailed description of the applied quantile mapping is provided by Fiddes et al. (2022) and therefore not repeated here. Furthermore, the spatially downscaled CMIP6 climate scenarios remain at daily resolution and thus a temporal downscaling to sub-daily fields (hourly resolution) is required. To address this, the meteorological variables are disaggregated with the methods listed in Table 6. For most variables the open-source melodist package (Förster et al., 2016) is used, further following the TopoCLIM scheme. Surface air pressure (Ps) is disaggregated using linear interpolation and incoming longwave radiation by its relationship to air temperature (Ta) for which Fiddes et al. (2022) provide a detailed description. For precipitation (Pr) a different method is used: monthly diurnal disaggregation patterns are derived using in-situ observations of the station KYZ_AWS_PLU. Specifically, days with recorded precipitation are used to identify the monthly mean number of hours per day where precipitation occurs (n). If this monthly average is below two hours per day, n is set to 2 instead. Subsequently, the mean precipitation for all hours is ranked by magnitude and precipitation occurring in hours ranked lower than n (rank<n) is equally redistributed to the n-highest ranks. Finally, the resulting monthly diurnal precipitation patterns are applied to the downscaled CMIP6 time series. The same diurnal patterns are applied for Sangvor, where no precipitation gauge is available, assuming the patterns are representative due to the geographical closeness of the two catchments. It should be mentioned that although these patterns deem to appropriately represent the the variability of occurring precipitation in the study domain, it still is a simplified treatment of temporal precipitation disaggregation, which remains a persistent challenge within the scientific community (e.g. Acharya et al., 2022; Scher and Peßenteiner, 2021).

3.4 The land surface model Thetys-Chloris (T&C)

Surface temperature (Ts), debris temperature (Tdeb) and snowpack dynamics are simulated in this thesis by applying the ecohydrological model Thetys-Chloris (T&C; Botter et al., 2021; Buri et al., 2023; Fatichi et al., 2012a, 2012b; Manoli et al., 2018; Mastrotheodoros et al., 2019; Paschalis et al., 2022. This state-of-the-art physical land surface model has been widely used in mountainous regions (e.g. Botter et al., 2021; Buri et al., 2023; Fugger et al., 2022, 2024; Fyffe et al., 2021; Mastrotheodoros et al., 2020; Shaw et al., 2022 and can simulate all essential components of the hydrological cycle by resolving, the mass and energy balances at hourly scale (Fatichi et al., 2012a) for any type of land cover, including bare ground, vegetated land, rock, snow, glaciers, supraglacial debris and surface water (Fugger et al., 2024). The main fluxes included in resolving surface energy balance are net radiation, sensible and latent heat, heat exchange with the subsurface, as well as the heat consumed by photosynthesis. Additionally, the model resolves infiltration and exfiltration, deep percolation and soil moisture dynamics in the unsaturated zone, including root water uptake. Further, depending on the local and dynamic conditions, the surface and subsurface layers can comprise snow, ice and supraglacial debris and therefore the melt and accumulation of ice and snow are explicitly simulated in the model (Fugger et al., 2022). A schematic overview of the model framework is presented in Figure 7.

For the Kyzylsu catchment, the model setup of Fugger et al. (2024) is used and for Sangvor the model is set up in the same manner. Topology (100m DEM), glaciers, debris cover and land cover are derived as described in section 2.2, and model parameters requiring adjustment either estimated from literature or derived through optimisation (Fugger et al., 2024). A single-layered ice pack is used to represent glacier ice. The implemented ice and ice-under-debris mass balance models are described by Fyffe et al. (2021) and Fugger et al. (2022). Snow however, is represented in the model by a multi-layer snowpack model, within which a 3mm thick surface skin-layer exchanges energy with the overlying atmosphere and transfers heat into the underlying snowpack (Fugger et al., 2024). Snowpack dynamics are hereby simulated by using an iterative numerical approach to solve the energy balance of the surface skin-layer while concurrently solving the mass balance of the whole snowpack (Fatichi et al., 2012a; Fugger et al., 2024). The implemented energy and mass balance models for snow, including a sensitivity analysis of the individual energy and mass fluxes, are described in more detail by Fyffe et al. (2021) and Fugger et al. (2022) and include heat flux due to precipitation, freezing of liquid water in the snowpack and the accumulation (including interception), melting and sublimation of snow. Although model uncertainties of this specific setup were not explicitly quantified, the ability to replicate the necessary physical processes is tested and confirmed by Buri et al. (2023) and Fugger et al. (2022, 2024).

For the observational period the model is applied at plot-scale to simulate surface temperature and snow height at the in-situ measurement locations. The general topography is represented in the model by a 100m DEM (section 2.2.1). For enhanced accuracy, slope and aspect at the measurement locations are determined either from field measurements (if available) or by employing a Pléiades 2m DEM (section 2.2.1). Land-cover, glaciers and debris-cover however, are derived from a 100m grid as well, and may therefore not correctly represent the local conditions as they aim to represent the average over the whole grid-cell.

For the historical reference period, the model is forced in a semi-distributed manner, taking advantage of the TopoSUB clustering method. To do so, each TopoSUB-derived cluster centroid is associated with the cluster member grid cell that shares the same land cover and the most topological characteristics, determined by minimising the squared distance of the predictors. Subsequently the model is forced at plot-scale for each of these assigned grid cells, representing the cluster centroid and thus representing multiple grid cells. A map of the cluster centroids used is presented in Figure B.4. After simulating each centroid, the model output is spatialised by assigning each grid cell the same model output from its representing cluster centroid. Although uncertainties resulting from this TopoSUB-based approach are not quantified for this study domain, an analysis in another catchment (Figure B.3) suggests that this approach is able to simulate spatial snow pack dynamics similarly well as a fully distributed model approach. But with much more efficiency. Nevertheless, it should be mentioned that lateral mass fluxes (lateral water flows on the surface and subsurface, wind drift, avalanches, etc.) are not simulated by this approach.

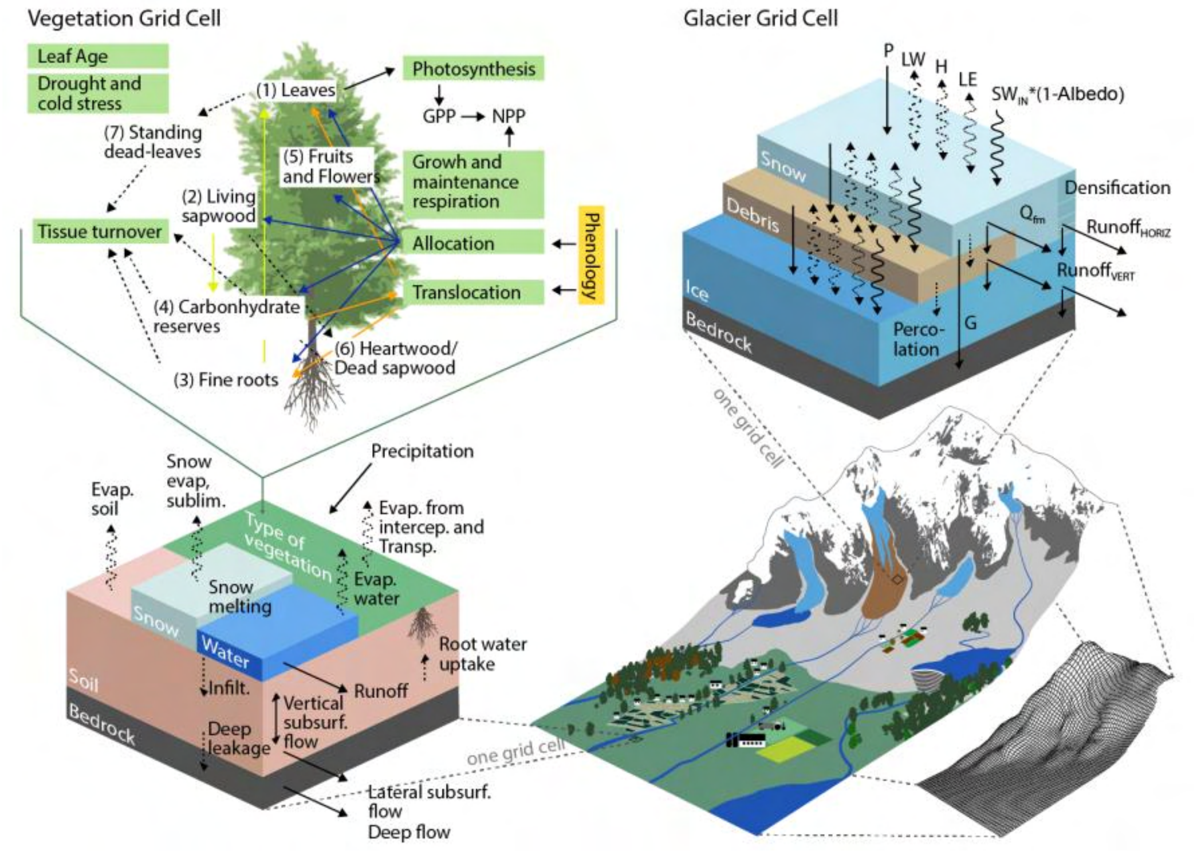

Figure 7: T&C model framework: hydrosphere, cryosphere and biosphere components together with energy balance components. Lateral processes are only simulated within a distributed model run. Source: Fugger et al. (2024)

3.5 Evaluation

3.5.1 Downscaling reanalysis

To evaluate the performance of each downscaling approach (step 1; Figure 6), the downscaled meteorological reanalysis forcings are compared against in-situ observations. The comparison consists of a quantitative assessment by calculating performance measures and a visual interpretation of different plots, such as temporal evolution, scatter, cumulative distribution function and diurnal cycle. For this evaluation the following performance measures are chosen: Pearson correlation coefficient (R), root mean squared error (RMSE), bias (BIAS) and for some variables additionally the percentage bias (PBIAS). This allows to assess how well the downscaled data captures the variability and trends present in the observed data (R), measure the accuracy of the downscaled data by understanding the typical size of discrepancies between downscaled and observed values (RMSE) and finally to assess the overall tendency of the downscaling method to overpredict or underpredict (BIAS/PBIAS). Figure 8 presents an example of such evaluation for the case of 2m air temperature at the station KZY_AWS. Such a comparative evaluation is carried out for all downscaled meteorological variables at each in-situ location where ground measurements of the specific variable are available Table A.1. To further evaluate the ability of T&C to reproduce surface temperature (Ts), local snowpack dynamics (Sd) and debris temperature (Tdeb) at plot scale with the downscaled forcings, model outputs (Ts, Sd, Tdeb) are evaluated in the same manner.

For Precipitation (Pr) and snow height (Sd) the comparison is done at daily scale by using daily sums instead of hourly values, whereby biases in precipitation were calculated using the monthly sums. Further, surface temperature (Ts) is treated differently, since in T&C surface temperature refers to the temperature between the uppermost ground layer and the atmosphere and consequently, loggers that may be covered with snow only correspond to it in snow-free conditions. Thus, the performance measure is separately conducted for August (Ts_{Aug}), a month with presumably snowfree conditions at all logger locations. The only location where performance measures of surface temperature are designated for the whole year is SANG_AWS, since the installed infrared sensor is above ground and measures the surface layer interacting with the atmosphere over the whole year. Moreover, the locations SANG_T_1 and SANG_T_8 are excluded from evaluation due to a discrepancy between the model's representation and their actual topographic characteristics: T&C, using average characteristics of a 100 metre grid, inaccurately represents these sites as glaciated instead of bare rock, making comparisons with observed data unfeasible. While it is possible to adjust this within the model set up, such modifications were not implemented for the scope of this thesis. This decision is justified by the close spatial proximity of one of these loggers to other sites (Figure C.36) and the sufficient number of alternative locations available for analysis (Table A.1). Notably, despite their exclusion from the primary evaluation, detailed figures related to these locations are still included in appendix C.2.2.

All supplementary figures not included in the main body of the thesis are in appendix C, encompassing evaluational details for all variables across all locations. Further, a comprehensive summary of the performance measures across all locations is presented in Table 7, with further interpretation provided in the results section. However, it is important to note that the observation time span of some variables varies across different locations Table A.1. For instance, data at SANG_AWS Sangvor is only available from mid October 2021 up to the beginning of September 2022. Though discrepancies in observation periods could potentially impact comparability between locations, they are not further discussed in this thesis as they concern rather short periods compared to the whole observational period, and it is likely that resulting uncertainties are exceeded by other uncertainty sources discussed in section 5.

Further, it is important to mention that due to a lack of long term in-situ observations not all observations used for the comparison are independent from downscaling processes that include a bias correction step or use certain stations to derive vertical gradients (Table 5). Nevertheless, for TopoPyScale and the HIMAL-method (without bias correction) all observations are independent, except for the HIMAL-method in Kyzylsu where air temperature is indirectly used to derive vertical temperature gradients. Finally, it is worth mentioning that the in-situ observations used here are not assimilated by ERA5 nor its subproduct ERA5-Land.

3.5.2 Downscaled CMIP6

The efficacy of the applied TopoCLIM scheme in removing biases is assessed (right part of step 4; Figure 6) by comparing the downscaled CMIP6 forcings against the downscaled ERA reference dataset of the historical period for the two most important meteorological forcing variables for hydrological modelling, namely air temperature (Ta) and precipitation (Pr). Further the quality of the downscaled ERA5 reference dataset itself is evaluated against observations for these same meteorological variables, aiming to assess the capability of the used TopoSUB-coupled mode of TopoPyScale.

Eventually, the quality of the final product is analysed in terms of its implications for land surface modelling with T&C, specifically focusing on the ability to reproduce spatial snowpack dynamics (left part of step 4; Figure 6). Thus, the T&C model is forced in a semi-distributed manner for the historical reference period of the final product, as previously described (section 3.4). The model was run from October 1999 to the end of the historical reference period (December 2014), with October 1999 to September 2000 as spin-up period. Subsequently, simulated catchment-wide snowline elevation as well as simulated snow cover are compared against independent remote sensing data (MODIS, Landsat-7 and Landsat-8; section 2.2.4). The ability to reproduce snowline elevation is thereby quantified by the coefficient of determination (R^2) and the accuracy of simulated snow cover with the Sørensen–Dice similarity coefficient (DSC; Dice, 1945; Sorensen, 1948). whereby the higher- resolution binary snowmaps (0=no snow; 1=snow) derived from remote sensing images were resampled to the 100m grid of the input DEM by linear interpolation. Since resampling leads to values in between 0 and 1, the maps are transformed back to binary values by setting cells with an average of 0.5 or higher to 1 and all other cells to 0.

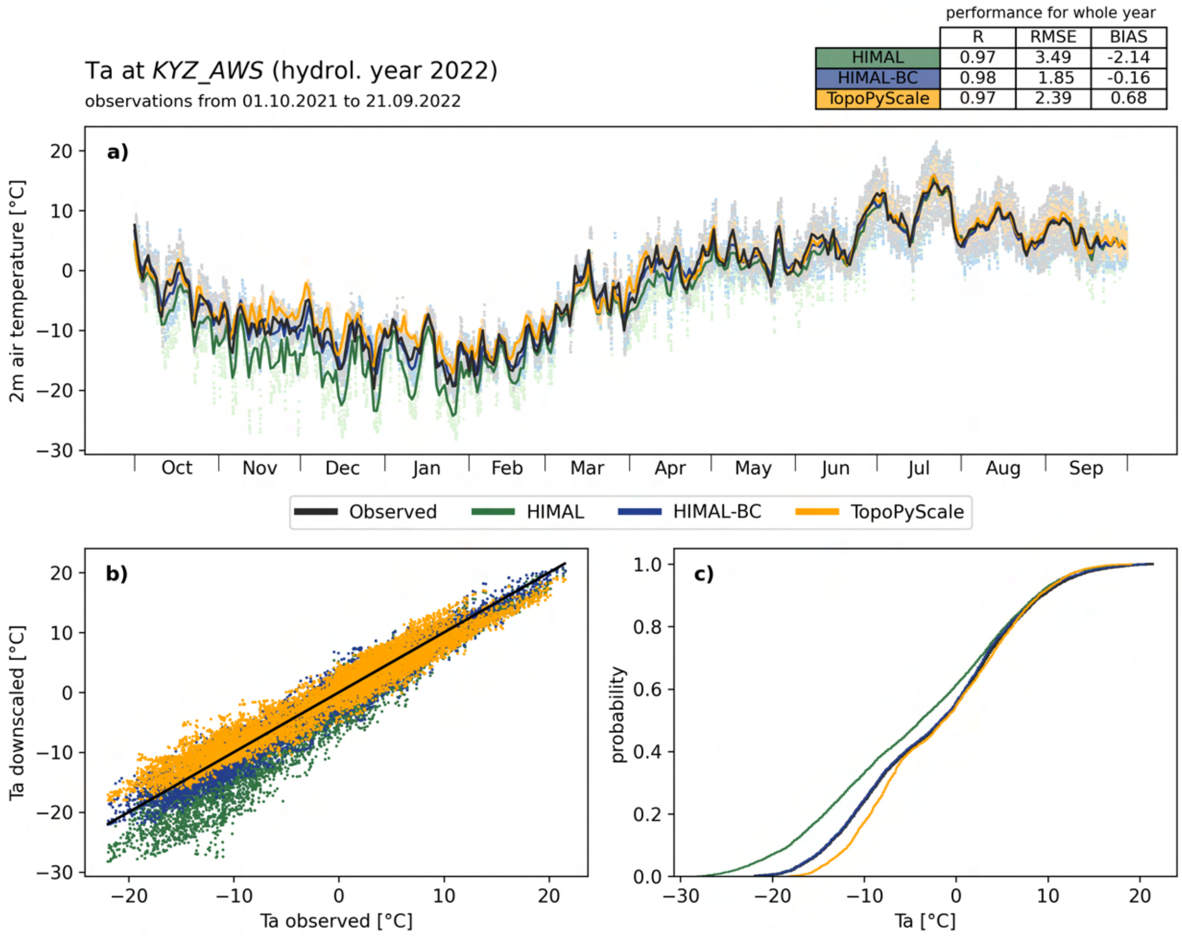

Figure 8: Evaluation of the downscaling methods - exemplary figure for the case of 2m air temperature at the KYZ_AWS station. a) temporal evolution of the daily mean as solid lines and the hourly values as bright points, together with b) a scatter plot showing the correlation between downscaled and observed hourly values, and c) a cumulative distribution (CDF) of the hourly values. Additionally, the performance is evaluated in quantitative terms by three performance measures: the Pearson correlation coefficient (R), root mean squared error (RMSE) and bias (BIAS). These measures are presented in the table to the upper right of the figure. The temporal evolution is always plotted for the whole hydrological year. The period over which the performance measures are calculated, and over which the scatter plot and the CDF are plotted, is indicated to the top of the performance-table, whereby only days with complete observations are used, ensuring consistency.

4 Results

4.1 Downscaled reanalysis

4.1.1 Evaluation of meteorological forcings

A comprehensive summary of the downscaling performance across all locations for each downscaling approach and meteorological forcing variable is presented in Table 7. The analysis reveals that the HIMAL-method and TopoPyScale overall exhibit comparable levels of performance. However, in the case of certain meteorological variables, TopoPyScale demonstrates a marginally superior performance. Further, an additional application of bias correction for HIMAL-BC is observed to generally enhance the accuracy of the downscaled variables. In this section, the performance of the different downscaling methods is further discussed in more detail for each meteorological forcing variable.

Concerning air temperature (Ta), both TopoPyScale and the HIMAL-method exhibit a strong correlation (R=0.95 in both methods) with in-situ observations. However, TopoPyScale shows enhanced accuracy with a lower RMSE (2.5) and less bias (-0.33) compared to the HIMAL-method. The latter tends to underestimate air temperature (BIAS=-2.12), particularly for low temperatures (e.g Figure C.1: subfigures b-c or wintermonths in subfigure a). Bias correction within HIMAL-BC is able to correct this and generally improves performance, reaching a correlation of 0.96, lower RMSE (2.31), and reduced bias (-0.54). It should be noted though that the demonstrated performance of TopoPyScale is comparable with the one of bias-corrected HIMAL-BC.

Concerning relative humidity (Rh), TopoPyScale exhibits a stronger tendency to underestimate (bias of -11.5) and shows a slightly higher RMSE (18.41) compared to the HIMAL-method (RME=16.48; BIAS=-3.88), while both methods demonstrate a similar correlation (HIMAL=0.75; TopoPyScale= 0.78) with in-situ observations. However, given the inherent dependency of relative humidity on air temperature, performance measures must be interpreted carefully. For instance, the HIMAL-method's seemingly superior performance may be linked to its tendency to underestimate air temperature, as lower temperatures results in higher relative humidity for constant specific humidity. The noteworthy temporal correspondence between the period where the HIMAL-method predominantly exhibits lower performance for air temperature (e.g. winter) and the period where it outperforms for relative humidity (e.g. Figure C.1) suggests that this may indeed be the case - especially as, like for air temperature, the correspondence during summer months are comparable for both methods. Concerning bias correction, a slightly improved correlation (0.77) and reduced RMSE (15.22) and bias (-0.61) indicate beneficial impact on downscaling relative humidity. This positive effect extends even to stations not included in the bias correction process (Figure C.2).

Both TopoPyScale and the HIMAL-method overestimate monthly precipitation sums (Pr) on average by about 25% (PBIAS of 23.8% in TopoPyScale and 28.6% the in HIMAL-method) with a similar RMSE of almost 4 and low temporal correlation (TopoPyScale=0.5; HIMAL-method=0.53) (Figure C.10). While this tendency is present in most months (Aug-Mar), a notable deviation is observed during late spring to early summer (Apr-Jul), where both methods temporarily underestimate precipitation. Further, dry-day frequency is underestimated by both methods (Figure C.10: subfigure b-c). The moderate performance, likely associated with existing biases in ERA5 and ERA5-Land (section 5.1.1), can be successfully enhanced with additional bias correction as shown for the HIMAL-method where bias could be reduced to 4%. However, although monthly and annual precipitation sums could be adjusted and the underestimation of dry days reduced by specifically addressing the issue within bias correction (section 3.2.1), the temporal correlation slightly deteriorates (0.49) and dry-day frequency still is underestimated. Both indicate that the replication of temporal precipitation distribution remains challenging.

An interesting observation about atmospheric surface pressure (Ps) is that it is differently reproduced by the HIMAL-method and TopoPyScale (Figure C.11). While the former succeeds in capturing the daily and sub-daily variability (R=0.94), TopoPyScale represents pressure fluctuations solely at specific step sizes, resulting in a lower correlation of 0.86. However, TopoPyScale exhibits a lower RMSE (2.23) and minimal bias (1.69). The higher RMSE (12.04) of the HIMAL-method is largely affected by the systematic bias (-11.95). Both clearly can be reduced by applying bias correction within HIMAL-BC, although an overcorrection of higher pressure values is evident. As, apart from small fluctuations, TopoPyScale outperforms the HIMAL-method in reproducing atmospheric surface pressure and is therefore considered as more suitable for this specific variable and application.

Further, all downscaling approaches effectively capture the main pattern of the average diurnal cycle of incoming shortwave radiation (Sw↓) and thus achieve strong correlations with the observed data (Figure C.12 and Figure C.13), resulting in an average R-value between 0.92 and 0.94 (Table 7). However, both TopoPyScale and the HIMAL-method exhibit discrepancies to hourly observations, as reflected in their average RMSE values of 123.98 (TopoPyScale) and 113.66 (HIMAL-method). It is further interesting that both tend to overestimate average peak radiation, which is evident in the average diurnal cycle. Although this may partially explain discrepancies and biases, additional underlying factors may be present. This is indicated by HIMAL-BC: while the additional bias correction adjusts the cumulative distribution and reduces bias to 0.07% on average, discrepancies and the tendency to overestimate peak radiation still remain. The spread in the scatter plots, predominantly at lower radiation values, and the shape of the cumulative distributions, suggest that there may be an additional temporal shift (e.g. in the evening) contributing to the observed discrepancies. It should be mentioned at this point that no persistent seasonal pattern in temporal shifts across sites is observed (Figure C.14 to Figure C.17) and thus it is not further investigated in the scope of this thesis. Nevertheless, while it is advisable to keep the noted discrepancies in mind, both methods are regarded as suited for downscaling Sw↓, since the main patterns of the average diurnal cycle and the mean daily radiation are largely captured by the downscaling methods. Further, due to its smaller bias, TopoPyScale is regarded as slightly more accurate than the HIMAL-method.

Regarding incoming longwave radiation (Lw↓), the HIMAL-method and TopoPyScale both demonstrate robust temporal correlation with observations, as indicated by average R-values of 0.86 (HIMAL-method) and 0.83 (TopoPyScale) and by supporting figures (Figure C.18 and Figure C.19). Yet, both methods have discrepancies (RMSE of 33.2 in HIMAL-method and 33.96 in TopoPyScale) and tend to underestimate incoming longwave radiation, as indicated by an average bias of -21.87 (HIMAL-method) and -17.88 (TopoPyScale). While the HIMAL-method tends to underestimate rather lower values, TopoPyscale is more likely to underestimates high radiation. These tendencies are discernible in the scatter plots and the cumulative distribution functions and particularly pronounced in temporal evolution during

specific periods, such as winter or summer months. Bias correction in HIMAL-BC is able to enhance performance by reducing the average RMSE to 25.21 and bias to -0.62.
Ultimately, the assessment of downscaled wind speed (Ws) reveals that both the HIMAL-method and TopoPyScale are unable to accurately reproduce observed wind speed dynamics(Table 7 and supporting figures Figure C.20 to Figure C.22). This is especially evident in low R-values and considerable negative biases, with an average PBIAS of -85.24% for the HIMAL-method and -58.16% for TopoPyScale. The pronounced underestimation of wind speeds is further revealed in the cumulative distribution functions and scatter plots, which show a consistent shortfall in capturing the magnitude of higher wind speeds. However, it is noteworthy that, despite the overall underperformance, TopoPyScale exhibits a markedly smaller bias compared to the HIMAL-method. Concerning bias correction, the alignment of CDFs to observed values is markedly improved for stations included in bias correction (Figure C.20 and Figure C.22) and hence biases are lowered. Yet, the correction is not equally effective for all locations, as indicated at the station KYZ_AWS_PLU by an only partially reduced bias and persistent underestimation of high wind speeds (Figure C.21). This indicates that biases observed at one station are unlikely representative for the entire catchment and thus, catchment-wide bias correction with only one station has limited effectiveness. Further, the overall temporal correlation remains modest (0.25) and sub-daily divergence still exhibits an average RMSE of 2.24. This suggests that while bias correction can adjust the overall tendency to underestimate wind speed, it cannot fully reconcile the temporal misalignments. To summarise, downscaling wind speed has inherent challenges of spatial and temporal variability. Despite this, bias correction within HIMAL-BC can clearly enhance performance by increasing wind speed magnitudes and thus reducing the average bias to -11.97%.

Table 7: Mean performance (R, RMSE and BIAS) of the different downscaling methods for each variable over all locations. The number of locations with observations is indicated inside the brackets next to the variable name. Performance measures are at hourly scale, except for variables marked with a '*' where the daily sum was used. Surface temperature is additionally summarised for the month of August (Ts_{Aug}), ensuring snowfree conditions. PBIAS is additionally provided for variables where a percentage bias is useful.

		Downscaling (meteorological forcing variables)							T&C at plot-scale (simulations)			
	Statistic	Ta (6)	Rh (3)	*Pr (1)	Ps (1)	SW↓ (2)	LW↓ (2)	WS (3)	Tdeb (1)	Ts (1)	Ts_{Aug} (9)	*Sd (3)
HIMAL	R	0.95	0.75	0.50	0.94	0.93	0.86	0.19	0.60	0.84	0.80	0.88
	RMSE	3.69	16.48	3.98	12.04	113.69	33.20	3.25	7.83	13.15	13.27	29.55
	BIAS	−2.12	−3.90	0.41	−11.95	24.33	−21.87	−2.62	−6.05	0.10	11.13	16.35
	PBIAS			23.77		12.38		−85.24				44.73
TopoPyScale	R	0.95	0.78	0.53	0.86	0.92	0.83	0.37	0.48	0.81	0.69	0.81
	RMSE	2.50	18.43	3.87	2.45	124.00	33.96	2.62	8.20	8.71	10.58	35.57
	BIAS	−0.33	−11.51	0.50	−1.46	7.29	−17.88	−1.87	−6.28	−3.39	−3.75	20.51
	PBIAS			28.63		3.73		−58.15				52.13
HIMAL-BC	R	0.96	0.77	0.49	0.94	0.94	0.86	0.25	0.79	0.84	0.81	0.75
	RMSE	2.31	15.22	4.28	2.22	107.44	25.22	2.24	4.64	9.48	10.84	26.27
	BIAS	−0.54	−0.61	0.07	1.68	0.15	−0.63	−0.49	−1.08	0.20	4.44	−12.93
	PBIAS			4.07		0.07		−11.97				−37.50

4.1.2 Evaluation of T&C model outputs at plot-scale

Simulated surface temperature (Ts) at the automatic weather station in Sangvor (Figure C.23) notably correlates to observed conditions, as depicted in the scatter plot and evidenced by an average R-value of 0.83 across all three downscaled forcing datasets. Despite this correlation, there is a notable overestimation of the temperature span, accompanied by an evident tendency to underestimate lower temperatures and overestimate higher temperatures. Both are particularly pronounced in the HIMAL-based simulation. Although this can be partly linked to the quality of downscaled forcings (e.g. Ta of the HIMAL-method in January and December exhibits similar underestimation patterns as its Ts simulations; Figure C.24), it may indicate model limitations (see section 5.3).A further interesting observation is that the simulated snowmelt period is clearly discernible from April to June, or July for TopoPyScale-based simulations, as evidenced by modelled surface temperature remaining around 0°C. In August too, simulated surface temperature indicates snowmelt for HIMAL-BC and particularly TopoPyScale simulations (Figure C.25). Notably, the same can be observed at other locations, but with varying degrees of prominence: it is less evident in lower altitudes (e.g. SANG_T10 or SANG_T11; Figure C.32 and Figure C.33) and more pronounced at higher altitudes (e.g. SANG_T_2 or SANG_T_3; Figure C.26 and Figure C.27). In such cases, strong but temporally limited deviations to observed values are apparent. Apart from these, temporal trends in modelled surface temperature of August (Ts_{Aug}) largely align with observed temperature, though exhibiting bias (Figure C.25 to Figure C.33). Yet here too, a consistent overestimation of the total range of surface temperatures is evident across sites. Further, a general tendency to overestimate surface temperature at higher elevations and underestimate at lower elevations is present.

In the context of simulating snowpack dynamics (Sd), the temporal pattern of snowpack accumulation is generally well-captured (Figure C.38 to Figure C.40). Yet, simulations tend to slightly delay the onset of the sustained melting phase, leading to a general overestimation of the maximum snowpack size, except for HIMAL-BC-based simulations in the Kyzylsu catchment where snowpack size is underestimated (Figure C.38 and Figure C.39). While melting rates are largely consistent with observations, these prevalent delays in the onset of the sustained melting phase further lead to a prolonged snowmelt period. Consequently, in the majority of the simulations, the complete melting of the snowpack occurs later than observed. It is further interesting that while both TopoPyScale-based and HIMAL-based simulations generally lead to similar snowpack dynamics, similarities at SANG_AWS end mid-April when the TopoPyScale-based simulation exhibits stronger re-accumulation, followed by an extended snowmelt period Figure C.40. This indicates the sensitivity of snowmelt dynamics to input forcings and the magnitude of short-scale snow re-accumulations and its resulting changes in albedo, as furhter discussed in section 5.2.

The evaluation of simulated debris temperature (Tdeb) at KYZ_AWS (Figure C.41) indicates varied levels of accuracy across seasons: during winter and spring, the simulations tend to underestimate debris temperature, while the accuracy of the simulations is evidently improved in summer, closely aligning with observed temperatures. However, as glacier melting primarily occurs from late spring to the end of the hydrological year, the accurate reproduction of debris temperature becomes particularly essential for predicting glacial melt during this period. Therefore, the evaluation suggests a reliable simulation during this important period.

4.2 Downscaled CMIP6

4.2.1 Evaluation of meteorological forcings

The evaluation of the CMIP6 downscaling process for air temperature (Ta) and precipitation (Pr) in the Kyzylsu catchment (Figure 9) shows that the TopoCLIM scheme effectively removes systematic biases inherent in the CMIP6 forcing scenarios (subfigures a-d), while retaining the variability across different model outputs (subfigures a-b). The efficacy of monthly applied bias correction within the TopoCLIM scheme is thereby evident by no remaining biases for downscaled air temperature (BIAS =0) and precipitation (PBIAS=0%) on annual as well as on daily (Ta) or monthly (Pr) scale. Therefore, concerning the historical reference period, the average inter-annual temperature cycle and precipitation distribution of the downscaled CMIP6 forcings align with the ones present in the downscaled ERA5 reference dataset. However, bias correction methods in general cannot correct every single value and thus temporal deviations still remain, as shown by the provided RMSE values. Further, subfigures e) and d) demonstrate that the TopoSUB coupled mode of TopoPyScale exhibits similar performance as the previously evaluated (section 4.1.1) non-coupled mode. However, it should be mentioned that biases present in the downscaled ERA5 dataset (e.g. precipitation as shown in subfigure d) are adopted by CMIP6 during bias correction. Since the evaluation in the Sangvor catchment shows similar results, it is not further discussed here. Though, its equivalent figure can be found in appendix D.1 (Figure D.1).

4.2.2 Evaluation of spatial snow pack dynamics

Modelled snowlines in the Kyzylsu catchment correspond well with remote sensing observations (R^2=0.65), and are often within the uncertainty range of the observed snowlines (Figure 10). Though, simulated snowline elevation tends to be underestimated (BIAS=-281.5m). In the Sangvor catchment however, differences between observed and simulated snowline elevations frequently exceed the uncertainty range of MODIS observations and thus exhibit larger negative bias (-462.06m) and low model performance (R^2=0.19). This is especially evident in the mid-range of observed SLE (e.g. 3000m-4000m), as visible in the scatter plot. The temporal evolution (left plot) suggests that the duration of periods with high snow cover (low SLE) seem to be overestimated, while underestimating the duration of periods with low snow cover (high SLE).

Nevertheless, the scene-by-scene evaluation of spatial snow cover distribution against Landsat-7/Landsat-8 (Figure 11) reveals that in both catchments modelled snow cover agrees well with Landsat-7/Landsat-8 scenes, with average DSC of 0.74 (Kyzylsu) and 0.73 (Sangvor). Further, higher performance during periods with more extensive snow cover and lower performance during periods with less snow cover are apparent, with a noteworthy similarity in the seasonal patterns between the two catchments, indicating a seasonal cycle in model performance. It is further interesting that during periods with low or modest snow cover the variability between different model chains is apparently higher (e.g. Figure D.2 or Figure D.3).

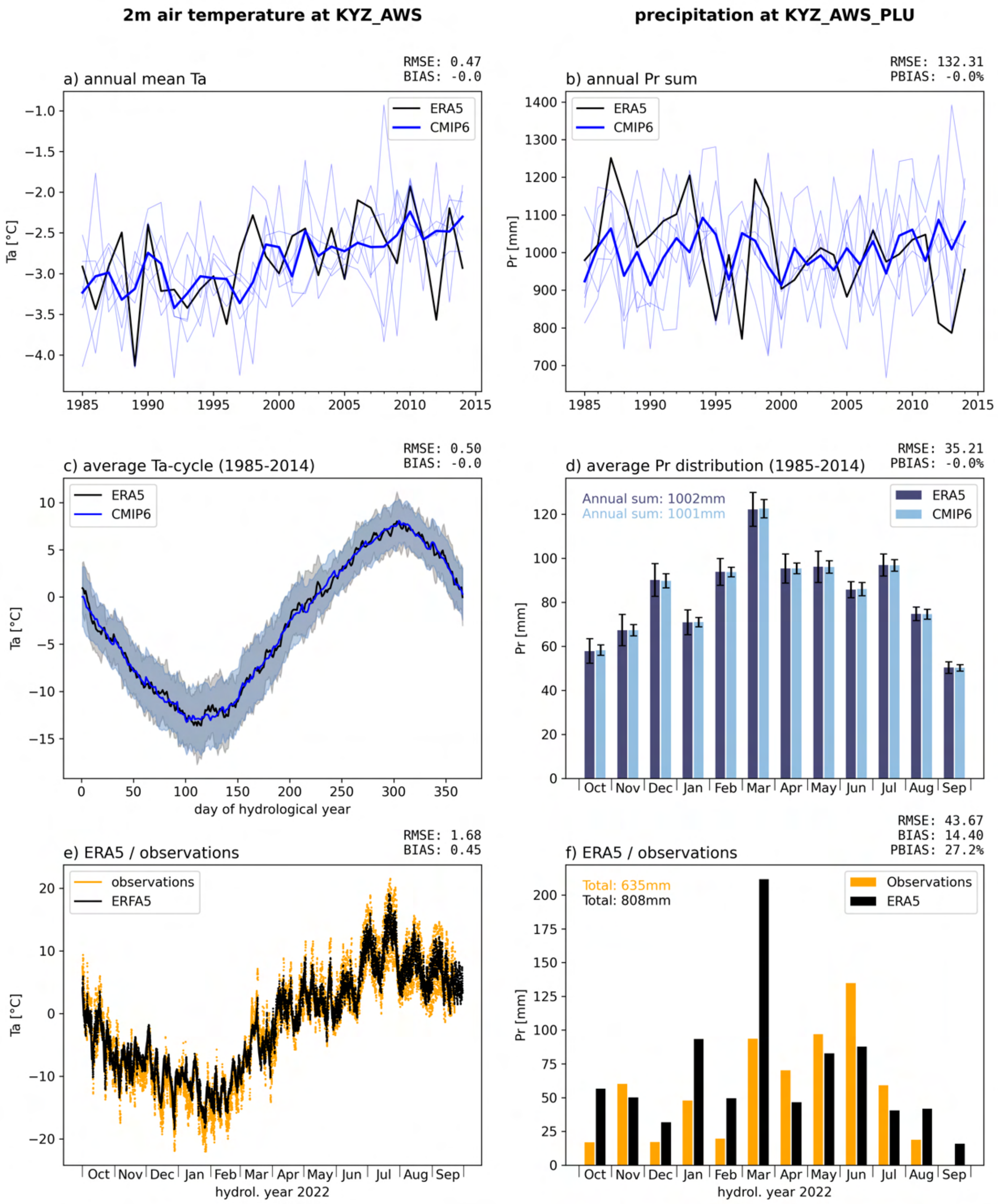

Figure 9: Evaluation of the CMIP6-downscaling process for 2m air temperature (Ta) and precipitation (Pr) in the Kyzylsu catchment. Ta at KYZ_AWS is presented in the left column and Pr at KYZ_AWS_PLU in the right column. a) and b) show the temporal evolution over the historical reference period (1985-2014) of annual mean temperature and annual precipitation sum, respectively. Thereby, the CMIP6 ensemble mean is indicated by a blue line, while its individual model chains are shown in light blue. The average annual temperature cycle and precipitation distribution (monthly sum) during the historical reference period are further presented in c) and d), respectively. In the former, the mean is indicated by solid lines and the standard deviation by the shading. In the latter subplot, the mean is indicated by bars and the standard errors by error-bars. e) (hourly temporal scale) and f) present a comparison between observations and TopoPyScale-downscaled ERA5 for the hydrological year 2022. Since the historical reference period of CMIP6 does not overlap with observations, it cannot be included here. For each subplot RMSE and BIAS (PBIAS for precipitation) are indicated at the presented temporal scale.

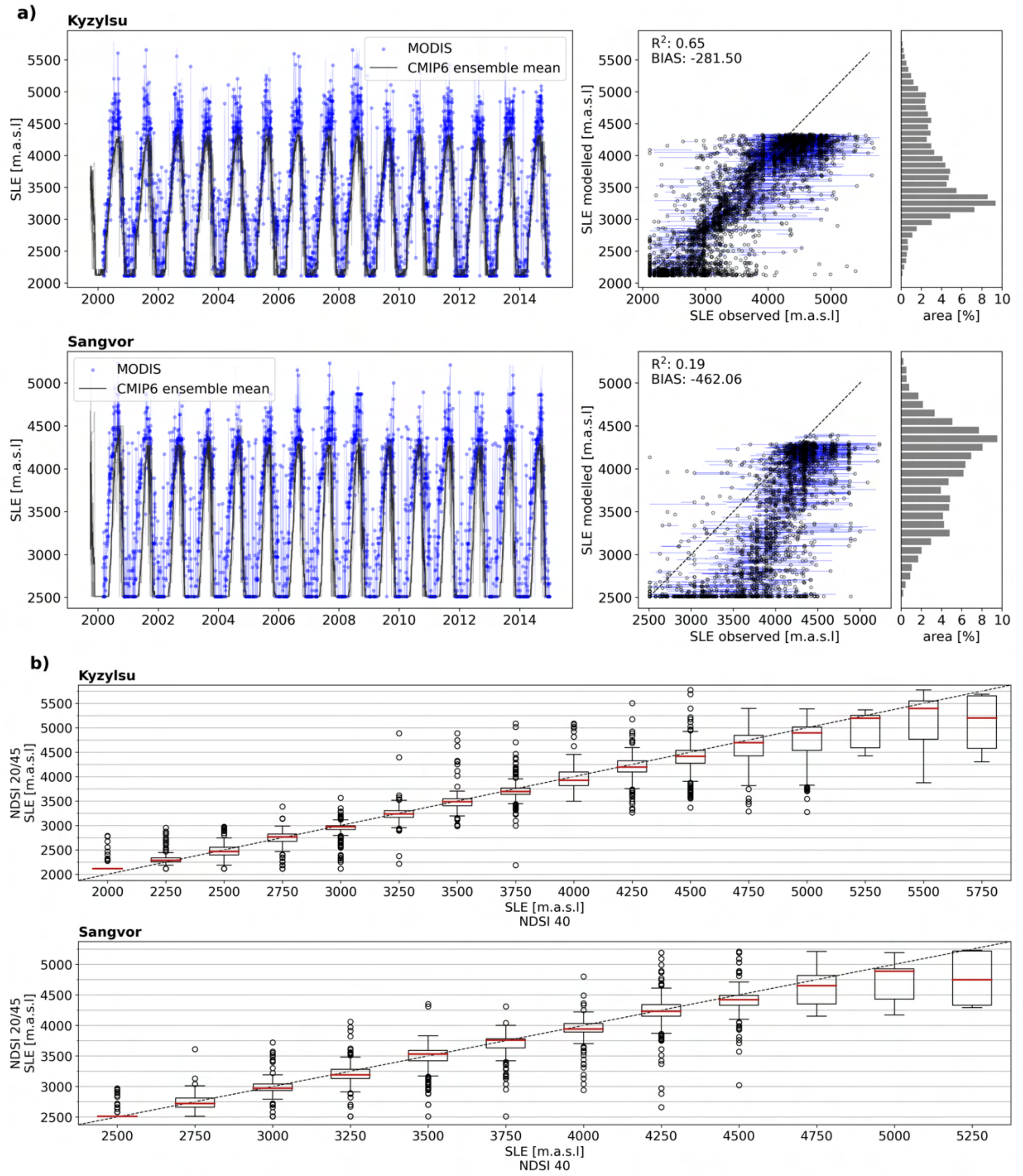

Figure 10: a) Snow cover evaluation against catchment-wide snowline elevation derived from MODIS Terra snow cover product (MOD10A1) in Kyzylsu and Sangvor (ensemble members are additionally plotted in light grey), together with scatter plots and catchment hypsometry. MODIS-SLE derived with the NDSI threshold 0.4 is used as the observed reference, while blue uncertainty bars indicate the range of different NDSI thresholds (0.2, 0.4, 0.45). Further, b) an uncertainty estimation of the MODIS product is presented by showing the SLE-range of SLE derived witht hese NDSI thresholds (0.2, 0.4, 0.45) at 250m elevation band.

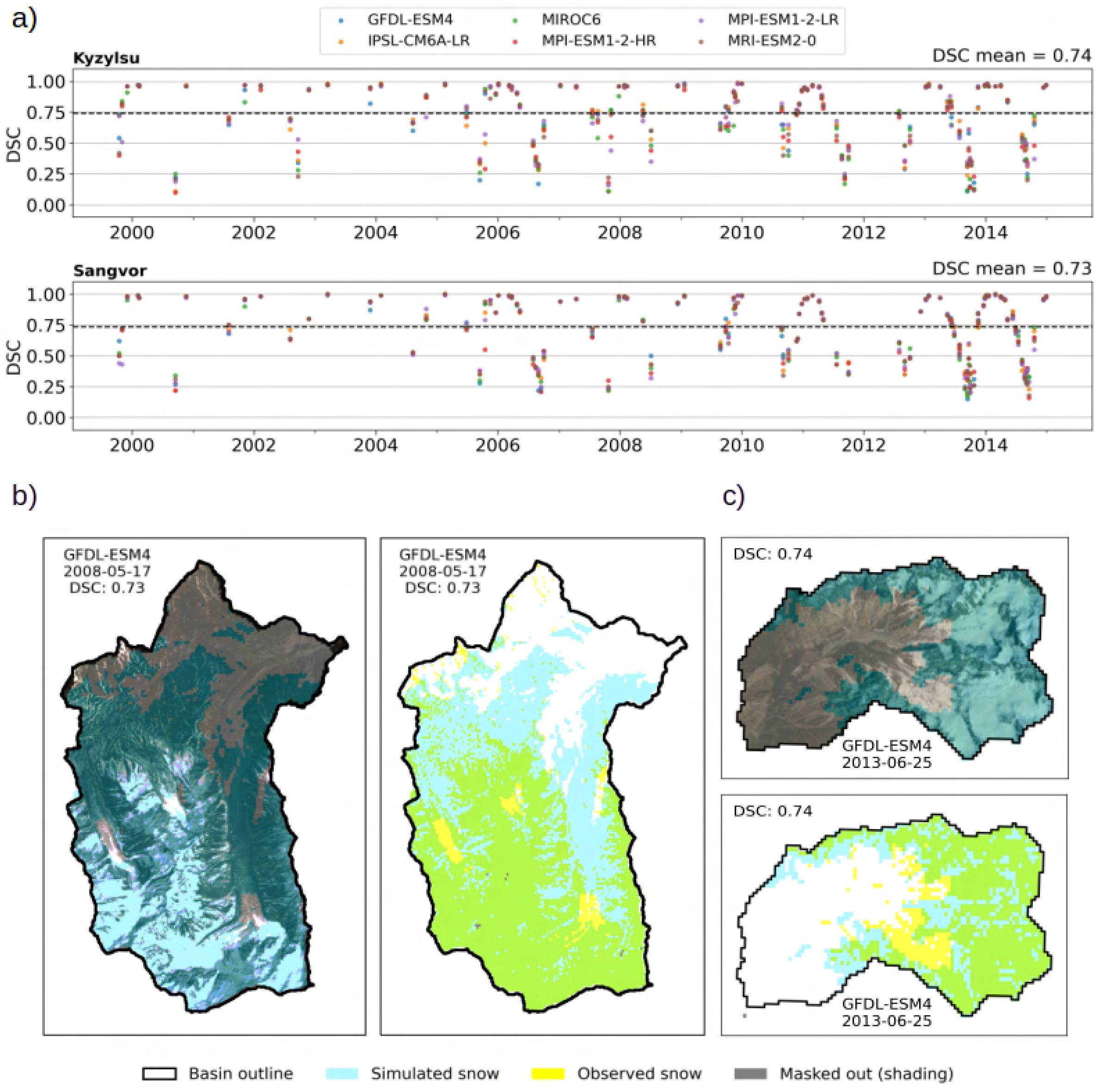

Figure 11: a) Sørensen–Dice coefficients of scene-by-scene evaluation against Landsat-7/Landsat-8 for each CMIP6 model chain, together with example scenes in true colour and as binary snow cover information (derived from NDSI and albedo) at each site (b=Kyzylsu; c=Sangvor), whereby scenes with average DSC performance are chosen.

4.2.3 Climate change signal

To assess whether meteorological variables of CMIP6 projections exhibit a significant trend to increase or decrease under future climate, the Mann-Kendall test (Kendall, 1975; Mann, 1945) is applied until mid-century (end of 2049) and end-century (end of 2099) for every future projection scenario. Thereby, a trend is considered as significant if its confidence interval is at least 95%. Further, since the Mann-Kendall test does not assess the magnitude of change, the average change of the ensemble mean and the change of the lowest and most upper ensemble member is quantified for the two periods of interest in order to provide insights into potential magnitude and range of the detected trends. Thereby, the average climatic conditions during the preceding climatic period (mid-century=2020-2049; end-century=2070-2099) are compared against the historical reference (1985-2014). The trend and change analysis are conducted for both catchments at the automatic weather stations KYZ_AWS and SANG_AWS, respectively. Since the analysis reveals similar future trends in both catchments, the results for the Kyzylsu catchment are further presented as representative for both catchments, while including the summary table and plots of the Sangvor catchment in appendix E.

A summary of the future climatic trends at mid-century and end-century at the station KYZ_AWS in the Kyzylsu catchment is presented in Table 8. The analysis reveals that in all CMIP6 projections the ensemble mean of air temperature (Ta) significantly increases, ranging between +0.98 (+1.24) °C until the mid (end) century under SSP1-2.6 and +1.27 (+4.45) °C under SSP5-8.5. In incoming longwave radiation (Lw↓) an increase is evident as well, ranging between + 4.05 (+4.28) W/m^2 until the mid (end) century under SSP1-2.6 and + 5.46 (+17.37) W/m^2 under SSP5-8.5. Further, relative humidity (Rh) significantly decreases towards the end of the century, ranging between -1.7% under SSP1-2.6 and -4.18% under SSP5-8.5. Moreover, slightly more precipitation (Pr) occurs at the end of the century under SSP3-7.0 (+65.14 mm/year) and SSP5-8.5 (+80.6 mm/year), with high inter-annual variability between different model chains (Figure 14).

Trends in other forcing variables are either not significant (Sw↓ and Ws) or do not have a magnitude relevant for land surface modelling within T&C (Ps). The temporal evolution of the relevant trends apparent in air temperature, relative humidity and precipitation are presented in Figure 12 to Figure 14. Similar plots for other variables are included in appendix E.1, including incoming longwave radiation (Figure E.6), since its trends are consistent with elevated radiative forcing of the CMIP6-scenarios.

Moreover, the additional analysis of average annual precipitation distribution under the different future scenarios further reveals that there is an additional shift in temporal precipitation occurrences toward the end of the century under SSP2-4.5, SSP3-7.0 and SSP5-8.0 scenarios: compared to the historical reference period, there is significant more precipitation during winter months and early spring (November to April), and less at the end of the hydrological year (July, August and September). This shift is exemplary illustrated for the scenario where it is most evident, namely in the SSP5-8.0 scenario (Figure 15). Plots for all other scenarios are in appendix E.1.1. However, given the fact that there is no significant change in overall precipitation under the SSP2-4.5 scenario, it is especially interesting that the temporal shift in precipitation is nevertheless evident within this scenario.

Table 8: Overview of the Mann-Kendall trend analysis for all downscaled meteorological CMIP6 variables in the Kyzylsu catchment. The trend analysis is carried out for all Tier 1 Scenarios at mid century and end century. Significant trends are indicated in the column *trend* of the corresponding period, whereby a ’$-$’ indicates a negative trend and ’$+$’ a positive trend. A trend is considered as significant at the confidence interval of 95% and higher. The significance level of the observed trend is further indicated by stars with the following confident intervals: *>=95% / **>=99% / ***>=99.9%. Further, the average change of the ensemble mean is indicated, as well as the lowest and highest trend of its members (model chains). All units refer to the yearly mean (sum for precipitation) and are relative to the historical reference period.

				Mid-century (2020-2049)				End-century (2070-2099)			
Variable	Unit	Station	Scenario	Trend	Avg. change	Lower bound	Upper bound	Trend	Avg. change	Lower bound	Upper bound
Ta	°C	KYZ_AWS	SSP1-2.6	$+^{**}$	+0.98	+0.79	+1.30	$+^{***}$	+1.24	+0.93	+1.85
			SSP2-4.5	$+^{***}$	+1.11	+0.86	+1.58	$+^{***}$	+2.36	+1.97	+2.96
			SSP3-7.0	$+^{***}$	+1.11	+0.94	+1.24	$+^{***}$	+3.50	+3.17	+3.93
			SSP5-8.5	$+^{***}$	+1.27	+0.88	+1.60	$+^{***}$	+4.45	+3.80	+5.36
Rh	%	KYZ_AWS	SSP1-2.6		-0.89	-1.62	+0.17	$-^{**}$	-1.70	-6.13	+0.34
			SSP2-4.5		-0.98	-4.41	+0.62	$-^{***}$	-2.62	-7.56	+0.03
			SSP3-7.0		-0.93	-2.83	+0.27	$-^{***}$	-3.07	-6.85	-0.94
			SSP5-8.5	$-^{*}$	-1.13	-3.61	+0.86	$-^{***}$	-4.18	-11.41	-0.66
Pr	mm	KYZ_AWS	SSP1-2.6		+33.60	-20.09	+94.98		+18.28	-50.64	+110.87
			SSP2-4.5		+33.39	-12.29	+83.70		+32.92	-46.88	+174.32
			SSP3-7.0		+19.30	-20.06	+68.19	$+^{*}$	+65.14	-86.40	+178.39
			SSP5-8.5		+35.30	-11.24	+140.91	$+^{*}$	+80.60	-67.15	+254.65
Ps	hPa	KYZ_AWS	SSP1-2.6	$+^{***}$	+0.87	+0.63	+1.22	$+^{***}$	+1.04	+0.77	+1.29
			SSP2-4.5	$+^{***}$	+0.94	+0.65	+1.16	$+^{***}$	+2.01	+1.67	+2.50
			SSP3-7.0	$+^{***}$	+0.96	+0.69	+1.17	$+^{***}$	+2.87	+2.30	+3.70
			SSP5-8.5	$+^{***}$	+1.07	+0.76	+1.37	$+^{***}$	+3.51	+2.92	+4.77
Sw↓	W/m^2	KYZ_AWS	SSP1-2.6		-0.84	-2.11	+1.33		+0.39	-1.39	+2.54
			SSP2-4.5		-1.99	-3.03	-1.09		-2.30	-4.98	-1.07
			SSP3-7.0		-2.82	-3.32	-2.38	$-^{*}$	-5.75	-6.95	-5.03
			SSP5-8.5		-2.32	-3.90	-0.90		-4.66	-7.81	-1.17
Lw↓	W/m^2	KYZ_AWS	SSP1-2.6	$+^{***}$	+4.05	+3.48	+4.96	$+^{***}$	+4.28	+3.44	+5.42
			SSP2-4.5	$+^{***}$	+4.81	+4.20	+5.69	$+^{***}$	+9.10	+8.02	+10.17
			SSP3-7.0	$+^{***}$	+4.98	+4.36	+5.67	$+^{***}$	+14.32	+12.13	+16.12
			SSP5-8.5	$+^{***}$	+5.46	+4.65	+7.11	$+^{***}$	+17.37	+14.16	+21.49
Ws	m/s	KYZ_AWS	SSP1-2.6		-0.03	-0.05	-0.01		-0.02	-0.06	+0.01
			SSP2-4.5		-0.02	-0.05	+0.00		-0.01	-0.06	+0.01
			SSP3-7.0		-0.03	-0.07	+0.00		-0.03	-0.08	+0.05
			SSP5-8.5		-0.02	-0.04	+0.01		-0.03	-0.09	+0.05

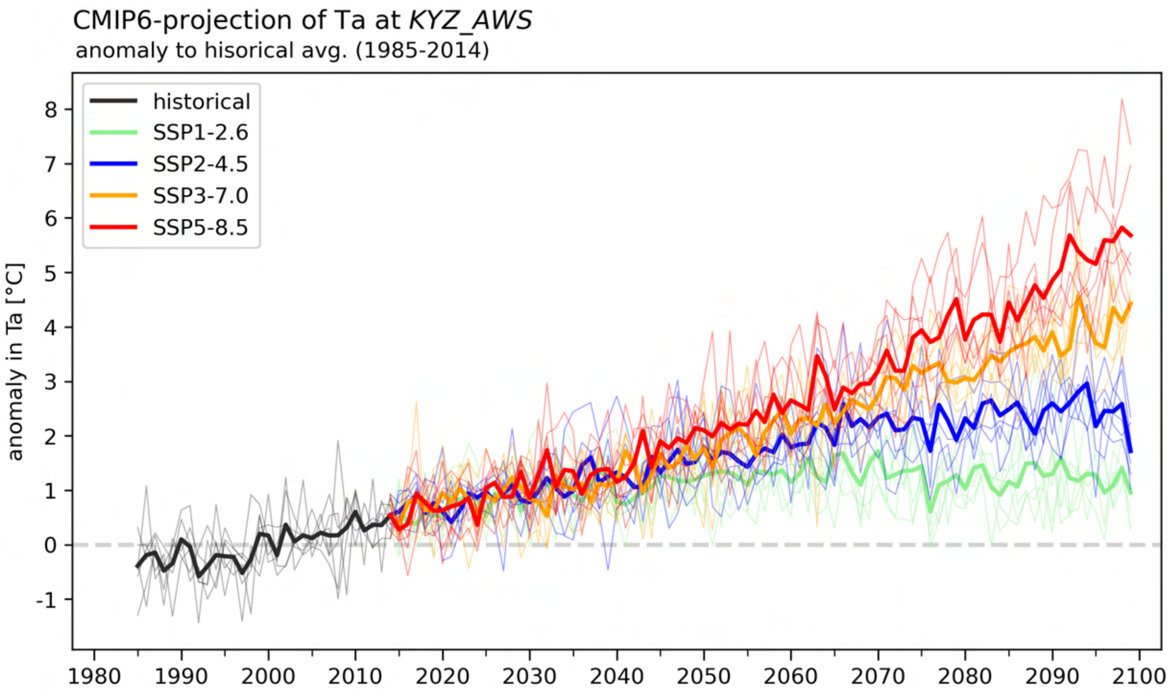

Figure 12: Anomaly in 2m air temperature in CMIP6-projections to historical average at KYZ_AWS. The average of the historical reference period (1985-2014) is thereby indicated as a grey, dashed line, representing zero-change. The CMIP6 ensemble means are plotted in the colours presented in the legend, with its individual members (model chains) indicated by thinner lines in the same colour.

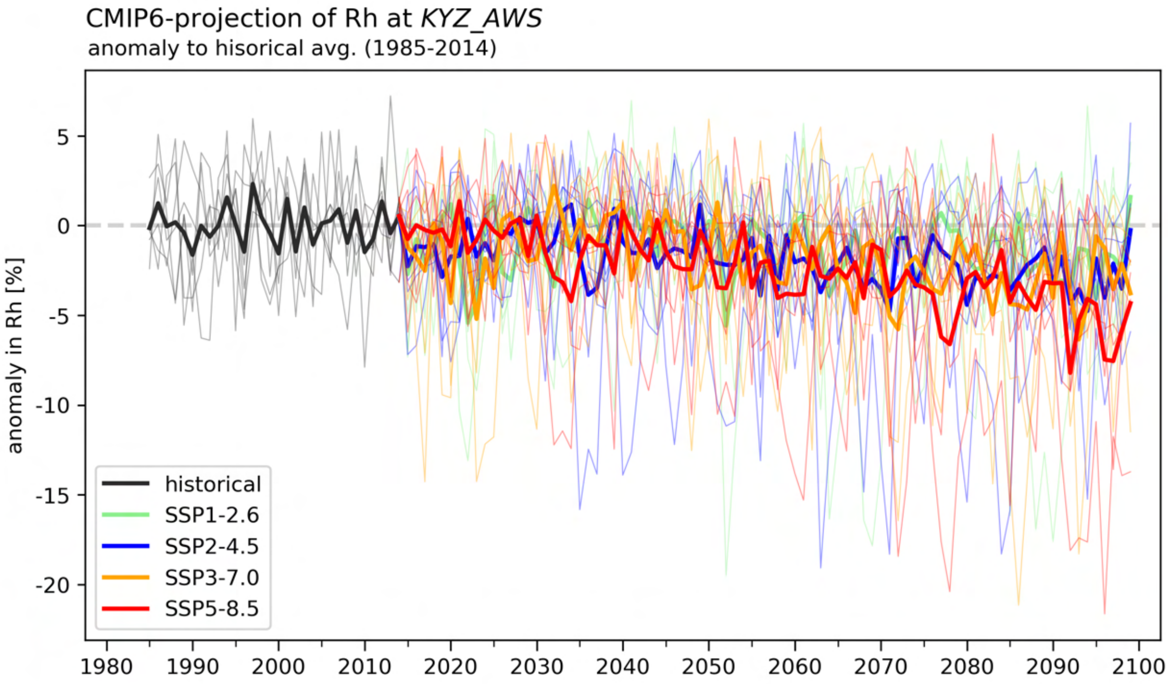

Figure 13: Anomaly in relative humidity in CMIP6-projections to historical average at KYZ_AWS. The average of the historical reference period (1985-2014) is thereby indicated as a grey, dashed line, representing zero-change. The CMIP6 ensemble means are plotted in the colours presented in the legend, with its individual members (model chains) indicated by thinner lines in the same colour.

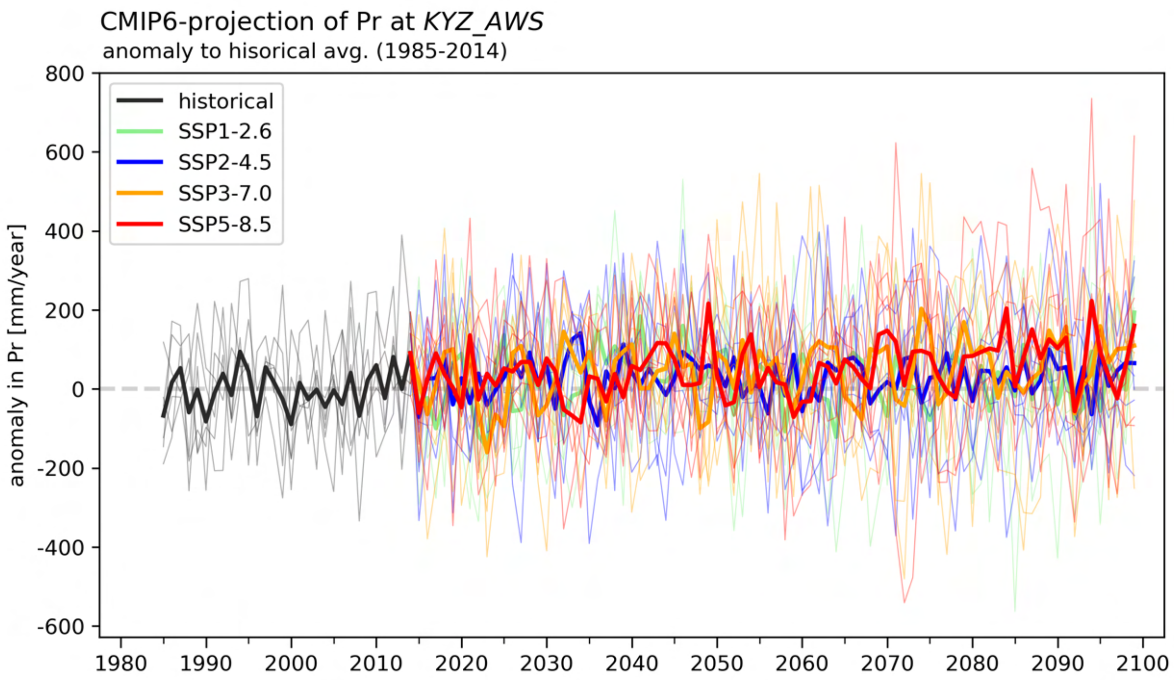

Figure 14: Anomaly in precipitation in CMIP6-projections to historical average at KYZ_AWS. The average of the historical reference period (1985-2014) is thereby indicated as a grey, dashed line, representing zero-change. The CMIP6 ensemble means are plotted in the colours presented in the legend, with its individual members (model chains) indicated by thinner lines in the same colour.

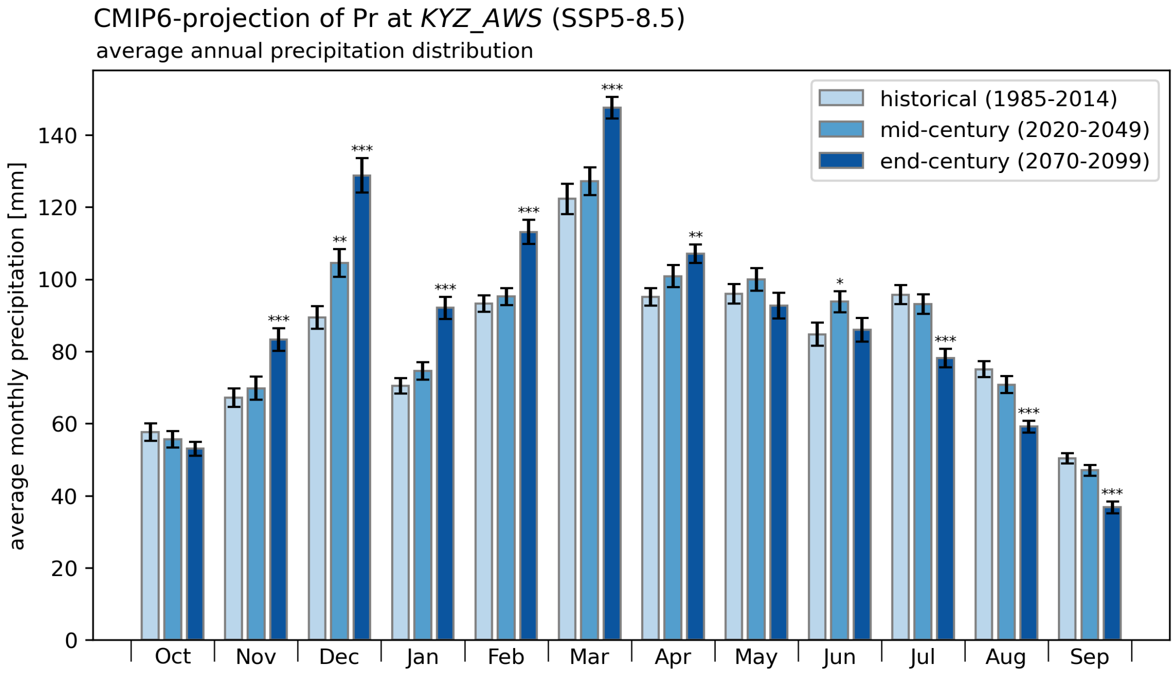

Figure 15: Average annual precipitation distribution during the historical reference period (1985-2014), mid-century (2020-2049) and end-century (2070-2099) of SSP5-8.5 CMIP6-projections at KYZ_AWS. The significance of change in a certain month is calculated with a T-test and indicated by stars, whereby a change is regarded as significant if it has a confidence interval of at least 95%. The following labels are used for significant changes: *>=95% / **>=99% / ***>=99.9%.

5 Discussion

5.1 Downscaling process

5.1.1 Downscaling reanalysis

The evaluation of the two downscaling methods TopoPyScale and the HIMAL-method (non-bias-corrected) reveals similar performance of both methods in downscaling meteorological fields. Nevertheless, TopoPyscale is chosen as the more suitable method for downscaling the reanalysis reference dataset in this thesis, due to its slightly better performance in downscaling air temperature (Ta), surface air pressure (Ps) and incoming shortwave radiation (Sw↓), its computational efficacy, and its built-in clustering method (TopoSUB), which reduces storage demand and further facilitates to force T&C in a semi-distributed manner. While an additional bias correction step within HIMAL-BC enhances downscaling performance for the observational period, bias correction was not tested in combination with TopoPyScale. This could potentially be done in future research, as bias correction could further improve downscaling performance, especially for variables like wind speed where the downscaling does not perform well (e.g. Table 7, or precipitation where clear biases exist (e.g Figure C.10). However, bias correction in remote, data-sparse catchments has limitations directly linked to the spatio-temporal availability of observations: bias coefficients of a certain period at one or few locations are not necessarily valid in periods outside the observed time range or at other locations. Of course, this clearly limits the field of possible applications.
Another aspect related to the scarcity of in-situ data is the limited temporal and spatial scale of the evaluation in this thesis. Only one year of station data (at one or few locations per catchment) was available and thus the current evaluation does not capture the inter-annual variability of local conditions nor their extremes. Therefore, a more comprehensive dataset including continuous monitoring over many years is required to appropriately represent the expected distribution of near-surface meteorology. To capture vertical variability within the catchment, such an extended dataset should include high elevation observations. Once such a dataset is available, future applicants would benefit from a repeated evaluation with extended spatial and temporal scale, offering a more robust and generalising understanding of the downscaling performance. Further, concerning the evaluation of bias correction, not all data used for the evaluation are independent from the bias correction process (HIMAL-BC), due to its use as reference data for bias correction (Table 5). Therefore, not using bias correction for generating the full reanalysis reference product brings the advantage of being able to independently evaluate the downscaling approach used.

The evaluation of the downscaling approaches further reveals that, without bias correction, downscaled ERA5 and ERA5-Land both have notable precipitation biases (section 4.1.1). While the presented statistical downscaling methods are certainly subject to simplifications, such biases are consistent with the known presence of precipitation biases in ERA5 products (Hersbach et al., 2020; Lavers et al., 2022; Muñoz-Sabater et al., 2021; Wang et al., 2021): although data assimilation in ERA5 strongly improved compared to its predecessor ERA-Interim), ERA5 products continue to exhibit substantial precipitation biases (Hersbach et al., 2020; Lavers et al., 2022; Muñoz-Sabater et al., 2021), evident as a wet bias primarily linked to an underestimation of dry-day frequency (Lavers et al., 2022).

This thesis specifically addresses these known precipitation biases by applying and evaluating bias-correction within HIMAL-BC. It is demonstrated that monthly precipitation sums are effectively corrected and annual bias significantly reduced. Further, while the underestimation of dry-day frequency partially remains, the notable reduction in wet days marks a clear improvement over the non-bias corrected product. Therefore, the importance and potential benefits of bias correction is highlighted. Yet, despite it being promising, the practical application remains constrained by the availability of observational data, as previously discussed. However, the recently published bias-adjusted ERA5 dataset (WFDE5; Cucchi et al., 2020; Cucchi M. et al., 2022), which also addresses the noted biases and demonstrates the added value of bias correction in hydrological modelling, could serve as an alternative to in-situ-based bias correction limited by available observations. Unfortunately, this dataset does not (yet) overlap with observational data for the study domain of this thesis and thus its use as a reference dataset was not feasible due to the inability to perform a corresponding evaluation. Though, this potentially can change and thus future applications could consider to evaluate and potentially use this bias-corrected dataset too. This could further be advantageous for other forcing variables too, since biases inherent in ERA5 are corrected for other meteorological variables relevant for hydrological modelling with T&C as well.

5.1.2 Downscaling future meteorology

The future climate scenario projections from CMIP6 are spatially and temporally downscaled from a daily resolution at coarse grid scale to the desired 100m spatial resolution and hourly temporal resolution, using a reference dataset of the historical reference period. While an ideal reference dataset for this purpose would comprise in-situ observations, the lack of comprehensive ground data precludes this option and thus the downscaled ERA5 forcings are used instead. Although reanalyses are not observations in the strict sense (Parker, 2016), they are considered to offer the most dense information about the recent climate in data-sparse regions while being physically consistent (Dee et al., 2014). As further pointed out by Fiddes et al. (2022), this physical consistency is expected to enable the TopoCLIM scheme to yield a physically coherent downscaled product, despite the scheme's univariate nature. However, it should be noted that biases inherent in the reanalysis dataset, such as those observed in precipitation, are likely to be reflected in the final downscaled product as well, due to their adoption during bias correction within the TopoCLIM scheme.

Furthermore, the ability of ERA5 to reproduce short-timescale local weather patterns introduces a layer of uncertainty into the temporal disaggregation of the spatially downscaled CMIP6 forcings to sub-daily fields (Fiddes et al., 2022). Therefore, the precipitation disaggregation routine, based on observed precipitation magnitudes in the Kyzylsu catchment and newly implemented for this thesis (section 3.3), is regarded as a clear improvement for disaggregating precipitation. Compared to the alternative equal-distribution-method, this routine avoids continuous drizzling and constitutes realistic sub-daily precipitation magnitudes, which is important to accurately represent water and energy fluxes in hydrological modelling (Fatichi et al., 2012a, 2012b; Y. Huang et al., 2019).

Eventually, it should be noted that by applying bias correction within the TopoCLIM scheme, climate change signals (CSS) of future projections can be modified (Gobiet et al., 2015; Ivanov et al., 2018; Themeßl et al., 2012). However, an analytical analysis by Gobiet et al. (2015) reveals that non-bias corrected CSS are affected by intensity-dependent model errors and thus quantile mapping can even potentially lead to an improved CCS by removing these errors.

5.2 Evaluation

5.2.1 Observational uncertainties

Although difficult to quantify, it is important to acknowledge sources of uncertainties linked to observations. In both the Kyzylsu and the Sangvor catchment, available observations are temporally and spatially limited, reflecting the challenging nature of monitoring remote high mountain catchments. This can lead to evaluational uncertainties, if for instance the observation period is meteorological atypical or if the measurement locations do not adequately represent its surrounding area. The latter is particularly important for snow depth measurements, which are more prone to uncertainty due to the high spatial variability of snow depth and snow cover, even over short distances (Armstrong & Brun, 2008; Buchmann et al., 2021; Clark et al., 2011; Grünewald et al., 2010). Additionally, local factors can introduce further uncertainties. For instance, the accuracy of surface temperature loggers can be affected by micro-topographical features, their specific placement, or exposure to environmental elements like air flows between rocks.
Moreover, it should be noted that remote sensing derived snow maps are not true observations and their quality depends on the correct processing, whereby cloud cover constitutes the main challenge. Uncertainties of MODIS-derived snow line elevations are estimated by using different NDSI thresholds, and uncertainties in Landsat-7/Landsat-8 derived snow maps reduced by using scene-based NDSI thresholds (Otsu, 1979) and excluding shaded areas. Further, it is mentioned that despite the inherent uncertainties in remote sensing derived snow maps they are regarded as suited for catchment-wide snow evaluation, since they are able to represent the spatial and temporal variability of snow cover (Crawford et al., 2013; Donmez et al., 2021; Immerzeel et al., 2009).

5.2.2 Land surface modelling: uncertainties and limitations

Of course, in hydrological modelling, model-inherent uncertainties and limitations exist (Beven, 2012). Some sources of uncertainty, as well as some limitations, are discussed in this section. However, it should be mentioned that although some discussions refer to the applied model, the uncertainties and limitations discussed should not be seen as a model-specific critique, but rather as a general discussion of challenges in land surface modelling, intending to enable a critical assessment of their impacts on the evaluations presented in this thesis.

One potential limitation and source of uncertainty worth mentioning is the representation of the land cover and its thermal properties, which plays a crucial role in solving the surface energy balance (Fatichi et al., 2012a, 2012b; Marty et al., 2002). While in the model setup one certain type of land-cover was defined for an entire grid-cell, local conditions may be very heterogene. For instance at the station SANG_AWS, the surface layer is composed of a mix of rock and sand, while the model's representation consists of bare rock. Since the former is expected to absorb and retain less heat, the model is likely to overestimate surface-temperature in snowfree conditions, as it is indeed observed (section 4.1.2; e.g Figure C.25). Of course, every topological property defined on grid-level is a simplification, as it always

represents averages. However, accounting for sub-grid heterogeneity is often not feasible as it depends on accurate measurement techniques over large scales (Beven, 2012).
Moreover, although soils can freeze up within model simulations, the used model setup does not currently represent any layer of initial permafrost. Since the presence of permafrost can have a strong impact on energy fluxes and local hydrology (Ahmed et al., 2022; W. Li et al., 2023; Melton et al., 2019; Yao et al., 2020; Yokohata et al., 2020), the absence of such a layer is seen as a model limitation. However, it should be noted that, although research in this field is progressing, a reliable detection of permafrost remains challenging (Buckel et al., 2021; Haeberli et al., 2010; Jiang et al., 2020; X. Li et al., 2023; Zhang et al., 2022). Therefore, such an implementation would be challenging, and it is not known at which locations and to what extent this limitation impacts the quality of the model outputs in this thesis.

Concerning snowpack simulations, accurately reproducing snowmelt dynamics remains generally challenging in land surface modelling (DeBeer & Pomeroy, 2017; Essery et al., 2013). This difficulty largely arises due to the sensitivity of snowmelt to various factors, such as snow density, storage and refreezing of liquid water within the snow, turbulent fluxes, and snow albedo (DeBeer & Pomeroy, 2017). Particularly the latter plays a crucial role in surface energy budgets and snowmelt dynamics, since it strongly influences the shortwave radiation budget and thus snowmelt reacts highly sensitive to changes in albedo, as pointed out in several studies (e.g. Armstrong and Brun, 2008; Brock et al., 2000; Doherty et al., 2010; Dumont et al., 2012; Gabbi et al., 2015; Johnson and Rupper, 2020; Naegeli and Huss, 2017. Within T&C too, snowmelt is sensitive to albedo-changes (Fugger et al., 2022; Fyffe et al., 2021), which consequently means that small changes in input forcings that lead to short-scale snow re-accumulation can have a big impact on modelled melt dynamics. However, while albedo dynamics are very complex in reality, the T&C model has an albedo parameterisation developed from observation (Fugger et al., 2024), and therefore its accuracy is limited like any albedo-scheme (Gardner & Sharp, 2010). The accurate simulation of snowmelt dynamics is further complicated by the complexity of real-world processes that cannot be depicted by models. This includes factors like the deposition of aerosols, the exact metamorphosis of the snowpack, and external influences that alter albedo. The latter for instance includes the occurrence of the dust storms common in Tajikistan (Abdullaev & Sokolik, 2019), which deposit dust on the snowpack and thus strongly influences melting dynamics by reducing the snowpack's albedo. Additionally, wind drift and avalanches are not accounted for by the applied model setups. Yet, the redistribution of snow by both wind and avalanches can strongly affect the spatial variability of snow cover, thereby impacting the timing and magnitude of snowmelt (Freudiger et al., 2017; Mott et al., 2011). While an analysis against fully distributed model outputs (where avalanches are specifically modelled) in another catchment (Figure B.3) indicates that omitting avalanches does not notably impair the model's ability to simulate catchment-wide snow cover, the impact of a missing module for simulating wind drifts remains unquantified. Given the low accuracy of downscaled wind speed magnitudes (section 4.1.1) however, it is questionable if such an implementation would enhance accuracy rather than induce additional uncertainty.

5.2.3 Implications on evaluation

The evaluation of downscaled meteorological forcings against in-situ observations is only affected by uncertainties related to the observational spatio-temporal scale and inherent inaccuracies in the measurement process. Despite a limited temporal scale and the consequent inability to capture inter-annual variability, it is important to note that the observational period encompasses a complete hydrological cycle, ensuring that the full range of variability within the observed year is represented. Additionally, uncertainties associated with the spatial scale are mitigated by including two distinct catchments and, where possible, multiple measurement locations into the evaluation process. Furthermore, given the overall data-scarcity in the region, it is empathised that the available in-situ data is highly valuable, enabling an evaluation in the first place. Therefore, while feature research could re-evaluate against a more comprehensive dataset, the comparative evaluation of different downscaling methods (section 4.1.1) presents an important first overview of the feasible quality of downscaled meteorological fields in the region.

Concerning the evaluation of land surface modelling outputs, multifactorial uncertainty sources and model limitations, as discussed in the preceding sections, introduce a layer of complexity, making it challenging to distinguish between observational uncertainties, forcing data quality, and model limitations (Evin et al., 2024; Fatichi, Vivoni, et al., 2016; Reichert et al., 2021; Renard et al., 2010; van Tiel et al., 2020).
However, it is important to distinguish between the two applied spatial scales: the plot-scale and the catchment-scale. Although for modelling at both scales the applied land surface model solves the energy and mass budgets at a certain location (station or representing centroid), different objectives are pursued. While plot-scale modelling focuses on detailed outputs evaluated at specific locations, semi-distributed modelling aims to represent the entire catchment and thus its model output is re-gridded before evaluation. Therefore, the discussed sources of uncertainty are likely to have greater impact on plot-scale evaluation, where model-outputs are compared to local observations, than on catchment-scale evaluation, where model-outputs are compared to grid-cell averages and thus uncertainties may be diminished.
Hence, although plot-scale evaluation does expose certain inaccuracies in simulations, such as in solving the surface mass budgets and reproducing snowmelt dynamics during snowmelt periods, their origin can be manyfold. And while the model could be fine-tuned until it almost perfectly represents observed local conditions, catchment-scale reliability is often considered as more important for cryosphere focused hydrological modelling (van Tiel et al., 2020) and therefore more expressive to effectively estimate the quality of the input forcings in interplay with the hydrological model. This also applies for the aim of this thesis, as the final product intends to serve as an input dataset for catchment-scale modelling, and therefore catchment-wide evaluation is more suited.
Considering this, the plot-scale evaluation in this thesis can be seen as a brief sanity check on local scale, acknowledging the associated uncertainties and limitations. Therefore, it is empathised that (i) overall simulated surface temperature correlates well to observed conditions, (ii) the temporal pattern of snowpack accumulation is generally well-captured, and (ii) debris temperature is reliably simulated during the primarily essential glacier-melt season.

Eventually, the catchment-wide evaluation of the final product (section 4.2.1) revealed that in general spatial snow cover is well reproduced in both catchments. In the Kyzylsu catchment, average performance as well as its seasonal variability are comparable with the ones demonstrated by Fugger et al. (2024). This is especially remarkable, as no bias correction was involved in generating the final reanalysis reference product.

5.3 Implications on land surface modelling

The evaluation of the downscaled CMIP6 product for the historical reference period revealed a notable variability in performance between the different model chains used, especially evident during periods with low or modest observed snow cover. This indicates the potential benefits of ensemble modelling in mitigating forcing uncertainties and reducing model uncertainty. While in this thesis only six complete model chains are downscaled, additional 12 model chains, with only surface pressure missing, are available and could be downscaled for future applications. However, a total amount of 18 models is still not a lot for ensemble modelling, especially given the high stochastic uncertainties related to precipitation (Fatichi, Ivanov, et al., 2016). Therefore, it would be very helpful for future research if more modelling groups would deliver all variables needed for energy-balance based land surface modelling - ideally for all four 21st century top priority scenarios (Tier 1), as already proposed by the ScenarioMIP's experimental design of CMIP6 (O'Neill et al., 2016).

5.4 Future recommendations

Currently, the spatial and temporal availability of in-situ data in the Kyzylsu and Sangvor catchment is growing. At the time of writing, for instance, there is already a second year of station data available in both catchments, and even one year of measurements at an additional automatic weather station (at 3900 m.a.s.l) in the Kyzylsu catchment. The reanalysis downscaling approaches could thus be reapplied and evaluated with extended observations, enabling a more robust evaluation of the downscaling performance and providing valuable insights into the performance of bias-correction outside the temporal and spatial scale of used observations. This highlights the importance of continuous observations in the region. Hence, after recent efforts have improved data availability in the region after there was an observational gap after the collapse of the soviet union, it would be very important for future studies in the region that the Sangvor and Kyzylsu monitoring are being continued for many years to come, since it's otherwise a data-sparse area. As Barandun and Pohl (2023) recently pointed out, such monitoring networks are essential to understand the changing cryosphere at regional scale and to assess future water availability in the region.

Moreover, as no bias correction is applied for the final ERA5 downscaling with TopoPyScale, the TopoPyScale downscaling routine should also be extended with an additional bias correction step and evaluated against observations. However, where bias correction with in-situ data is too limited or not possible, downscaling the already bias-corrected WFDE5 dataset can be considered in future applications, as it provides all near-surface meteorological variables necessary for hydrological modelling with T&C. Yet, to enable an evaluation, this requires the WFDE5 dataset to be extended to overlap with observations. In the meantime, TopoPyScale is a suited tool for downscaling reanalysis reference datasets in the Pamir domain, as it (i) performs already well without bias correction, (ii) it can be easily used in bigger catchments as well due to its scalability and (iii) together with TopoCLIM it builds a semi-automatic pipeline. Finally, (iv) it is an easy-to-use open source package with a steadily growing community and can thus be expected to be constantly improved by the research community. Nevertheless, this thesis demonstrated some specific limitations of the downscaling scheme that could be improved. For instance, wind speed dynamics could not be accurately reproduced (section 4.1.1) and therefore implementing a topography based, wind-specific downscaling technique (e.g. (Dujardin & Lehning, 2022; Reynolds et al., 2023; Winstral et al., 2017) would be an important implementation for capturing fine-scale heterogeneities. This would further enhance the accuracy of potential future wind-drift aware applications.

Given the high importance of high-elevation regions in Central Asia in providing fresh water for downstream regions (Armstrong et al., 2019; Barandun et al., 2020; J. Huang et al., 2022; Immerzeel et al., 2019; Pohl et al., 2017; Wang et al., 2016), and given the climate change signals present in the downscaled CMIP6 forcings (section 4.2.3), the final product of this thesis should be definitely used to force land surface models in order to investigate how hydrological regimes change under different future climate projections. The importance of such research is especially pronounced through increased air temperature (all scenarios) and a seasonal shift in precipitation occurrences (SSP2-4.5, SSP-7.0 and SSP5-8.0), which both can affect runoff regimes and seasonal water availability.

Further, extending the discussion about potential benefits of ensemble modelling, it is advisable for future research to downscale and include as many model chains in hydrological modelling as availability and computational resources allow. This approach would attenuate uncertainties in model outputs related to forcing uncertainties. The method of clustering grid cells with TopoSUB is hereby further advantageous as storage demand does not (or only partially) limit the number of model chains that can be included. Further, the semi-distributed modelling with T&C allows to perform multiple model runs in a short time, facilitating ensemble modelling. Eventually, when fully distributed model runs are necessary, for instance to include lateral mass fluxes, the semi-distributed model could be used pre-modelling to identify model chains that reproduce observed conditions the best.

However, as ensemble-modelling is strongly dependent on the availability of regional or global climate models, it is very important that future research tries to maximise the available model chains. Therefore, climate modelling groups are reminded of the importance of providing all Tier 1 scenario outputs (O'Neill et al., 2016) for all important variables of land surface modelling. Further, given the importance of the high-elevation regions in Central Asia, higher-resolute regional climate models at daily scale are required to further enhance future research investigating the impacts of climate change on water availability.

6 Conclusions

The final product of this thesis comprises six spatially and temporally downscaled CMIP6 model chains with a climate-length historical reference period and all Tier1 future scenario projections reaching until the end of the century. Its mean properties of the historical reference period align well with those in the downscaled ERA5 dataset (BIAS=0 in Ta; PPBIAS=0% in Pr), which in turn corresponds well to observational data. Further, the catchment-wide evaluation of this product demonstrates a good performance in reproducing spatial snow cover distribution (avg. DSC: 0.74 in Kyzylsu; 0.73 in Sangvor), with seasonal fluctuations in performance. Variability between model chains indicates the potential of ensemble modelling and suggests that future research would benefit from additional model chains. Considering the high spatial heterogeneity of meteorological variables in mountainous regions and the constraints imposed by available observations, high-resolution climate models and methodological approaches, the final product of this study is regarded as high-quality and state-of-the-art contribution, upon which future research can build.
For instance, an important next step is to use the future projections of the final product in land surface modelling to investigate the impact of climate change on hydrological regimes and the associated water availability in the region. The relevance of such a research is particularly highlighted by the climate change signals present in the final product, which essentially predict higher temperatures (e.g. in the Kyzylsu catchment between +1.24°C under SSP1-2.6 and +4.45°C under SSP5-8.5 until the end of the century), and a seasonal shift in the precipitation regime.

This thesis further presents a comparative analysis of TopoPyScale and the HIMAL-method, two methods for generating spatially downscaled reanalysis forcings. Both were compared for the hydrological year 2022 in two high-elevation catchments of the northern Pamir mountains. The HIMAL-method and TopoPyScale have demonstrated comparable downscaling performance across various meteorological variables. However, TopoPyScale is identified as more suitable as it demonstrates a higher accuracy for certain variables (Ta, Ps, Sw↓) and offers additional advantages in terms of computational efficiency. Its clustering and spatialising functions are particularly beneficial and showcase a potential for further application in larger catchments as well.
The incorporation of an additional bias correction step in HIMAL-BC has been further shown to effectively mitigate systematic biases in downscaling meteorological reanalysis. This highlights the potential of bias correction with in-situ data, especially for bias-prone variables such as precipitation. However, the spatio-temporal availability of reliable ground measurements is a limiting factor in remote, data sparse catchments. Therefore alternatives are required, especially for long-term application.

Code and data availability

The folowing GitHub repositories of used code are available:

- HIMAL-method (on request): https://github.com/ElTombre/HIMAL_Downscaling
- TopoPyScale: https://github.com/ArcticSnow/TopoPyScale
- Thetys-Chloris (T&C): https://github.com/simonefatichi/TeC_Source_Code

Additional code used in the thesis, as well as the downscaled CMIP6 forcing dataset is available on request.

References

Abdolvand, B., Mez, L., Winter, K., Mirsaeedi-Gloßner, S., Schütt, B., Rost, K. T., & Bar, J. (2015). The dimension of water in Central Asia: security concerns and the long road of capacity building. *Environmental Earth Sciences*, *73*(2), 897–912. https://doi.org/10.1007/S12665-014-3579-9/TABLES/1

Abdullaev, S. F., & Sokolik, I. N. (2019). Main Characteristics of Dust Storm sand Their Radiative Impacts: With a Focuson Tajikistan. *Journal of Atmospheric Science Research*, *2*(2), 1–21. https://doi.org/10.30564/JASR.V2I2.352

Acharya, S. C., Nathan, R., Wang, Q. J., & Su, C.-H. (2022). Temporal disaggregation of daily rainfall measurements using regional reanalysis for hydrological applications. *Journal of Hydrology*, *610*, 127867. https://doi.org/10.1016/j.jhydrol.2022.127867

Adam, J. C., Hamlet, A. F., & Lettenmaier, D. P. (2009). Implications of global climate change for snowmelt hydrology in the twenty-first century. *Hydrological Processes*, *23*(7), 962–972. https://doi.org/10.1002/HYP.7201

Ahmed, N., Wang, G., Booij, M. J., Marhaento, H., Pordhan, F. A., Ali, S., Munir, S., & Hashmi, M. Z. u. R. (2022). Variations in hydrological variables using distributed hydrological model in permafrost environment. *Ecological Indicators*, *145*, 109609. https://doi.org/10.1016/J.ECOLIND.2022.109609

Arguez, A., & Vose, R. S. (2011). The Definition of the Standard WMO Climate Normal: The Key to Deriving Alternative Climate Normals. *Bulletin of the American Meteorological Society*, *92*(6), 699–704. https://doi.org/10.1175/2010BAMS2955.1

Armstrong, R. L., & Brun, E. (2008). *Snow and Climate: Physical Processes, Surface Energy Exchange and Modeling*. Cambridge University Press, 2010.

Armstrong, R. L., Rittger, K., Brodzik, M. J., Racoviteanu, A., Barrett, A. P., Khalsa, S. J. S., Raup, B., Hill, A. F., Khan, A. L., Wilson, A. M., Kayastha, R. B., Fetterer, F., & Armstrong, B. (2019). Runoff from glacier ice and seasonal snow in High Asia: separating melt water sources in river flow. *Regional Environmental Change*, *19*(5), 1249–1261. https://doi.org/10.1007/S10113-018-1429-0/FIGURES/6

Barandun, M., Fiddes, J., Scherler, M., Mathys, T., Saks, T., Petrakov, D., & Hoelzle, M. (2020). The state and future of the cryosphere in Central Asia. *Water Security*, *11*, 100072. https://doi.org/10.1016/J.WASEC.2020.100072

Barandun, M., & Pohl, E. (2023). Central Asia's spatiotemporal glacier response ambiguity due to data inconsistencies and regional simplifications. *Cryosphere*, *17*(3), 1343–1371. https://doi.org/10.5194/TC-17-1343-2023

Beven, K. (2012). Rainfall-Runoff Modelling: The Primer: Second Edition. *Rainfall-Runoff Modelling: The Primer: Second Edition*, 1–457. https://doi.org/10.1002/9781119951001

Beyer, R. A., Alexandrov, O., & McMichael, S. (2018). The Ames Stereo Pipeline: NASA's Open Source Software for Deriving and Processing Terrain Data. *Earth and Space Science*, *5*(9), 537–548. https://doi.org/10.1029/2018EA000409

Botter, M., Zeeman, M., Burlando, P., & Fatichi, S. (2021). Impacts of fertilization on grassland productivity and water quality across the European Alps under current and warming climate: Insights from a mechanistic model. *Biogeosciences*, *18*(6). https://doi.org/10.5194/bg-18-1917-2021

Brock, B. W., Willis, I. C., & Sharp, M. J. (2000). Measurement and parameterization of albedo variations at Haut Glacier d'Arolla, Switzerland. *Journal of Glaciology*, *46*(155), 675–688. https://doi.org/10.3189/172756500781832675

Buchhorn, M., Smets, B., Bertels, L., De Roo, B., Lesiv, M., Tsendbazar, N.-E., Herold, M., & Fritz, S. (2020). Copernicus Global Land Service: Land Cover 100m: collection 3: epoch 2019: Globe (version V3.0.1) [Dataset]. https://doi.org/10.5281/ZENODO.3939050

Buchmann, M., Begert, M., Brönnimann, S., & Marty, C. (2021). Local-scale uncertainty of seasonal mean and extreme values of in-situ snow depth and snow fall measurements. *The Cryosphere*, *15*(10), 4625–4636. https://doi.org/10.5194/tc-2021-125

Buckel, J., Reinosch, E., Hördt, A., Zhang, F., Riedel, B., Gerke, M., Schwalb, A., & Mäusbacher, R. (2021). Insights into a remote cryosphere: A multi-method approach to assess permafrost occurrence at the Qugaqie basin, western Nyainqêntanglha Range, Tibetan Plateau. *Cryosphere*, *15*(1), 149–168. https://doi.org/10.5194/TC-15-149-2021

Buri, P., Fatichi, S., Shaw, T. E., Miles, E. S., McCarthy, M. J., Fyffe, C. L., Fugger, S., Ren, S., Kneib, M., Jouberton, A., Steiner, J., Fujita, K., & Pellicciotti, F. (2023). Land Surface Modeling in the Himalayas: On the Importance of Evaporative Fluxes for the Water Balance of a High-Elevation Catchment. *Water Resources Research*, *59*(10). https://doi.org/10.1029/2022WR033841

Burlando, M., Carassale, L., Georgieva, E., Ratto, C. F., & Solari, G. (2007). A simple and efficient procedure for the numerical simulation of wind fields in complex terrain. *Boundary-Layer Meteorology*, *125*(3), 417–439. https://doi.org/10.1007/S10546-007-9196-3/METRICS

Chen, Y., Li, W., Deng, H., Fang, G., & Li, Z. (2016). Changes in Central Asia's Water Tower: Past, Present and Future. *Scientific Reports 2016 6:1*, *6*(1), 1–12. https://doi.org/10.1038/srep35458

Clark, M. P., Hendrikx, J., Slater, A. G., Kavetski, D., Anderson, B., Cullen, N. J., Kerr, T., Örn Hreinsson, E., Woods, R. A., Hendrikx, J., Slater, A. G., Kavetski, D., Anderson, B., Cullen, N. J., Kerr, T., Hreinsson, r., & Woods, R. A. (2011). Representing spatial variability of snow water equivalent in hydrologic and land-surface models: A review. *Water Resources Research*, *47*(7), 7539. https://doi.org/10.1029/2011WR010745

Crawford, C. J., Manson, S. M., Bauer, M. E., & Hall, D. K. (2013). Multitemporal snow cover mapping in mountainous terrain for Landsat climate data record development. *Remote Sensing of Environment*, *135*, 224–233. https://doi.org/10.1016/J.RSE.2013.04.004

Cucchi, M., P. Weedon, G., Amici, A., Bellouin, N., Lange, S., Müller Schmied, H., Hersbach, H., & Buontempo, C. (2020). WFDE5: Bias-adjusted ERA5 reanalysis data for impact studies. *Earth System Science Data*, *12*(3), 2097–2120. https://doi.org/10.5194/ESSD-12-2097-2020

Cucchi M., Weedon G. P., Amici A., Bellouin N., Lange S., Müller Schmied H., Hersbach H., Cagnazzo, C., & and Buontempo C. (2022). Near surface meteorological variables from 1979 to 2019 derived from bias-corrected reanalysis. https://doi.org/https://doi.org/10.24381/cds.20d54e34

DeBeer, C. M., & Pomeroy, J. W. (2017). Influence of snowpack and melt energy heterogeneity on snow cover depletion and snowmelt runoff simulation in a cold mountain environment. *Journal of Hydrology*, *553*, 199–213. https://doi.org/10.1016/J.JHYDROL.2017.07.051

Dee, D. P., Balmaseda, M., Balsamo, G., Engelen, R., Simmons, A. J., & Thépaut, J. N. (2014). Toward a Consistent Reanalysis of the Climate System. *Bulletin of the American Meteorological Society*, *95*(8), 1235–1248. https://doi.org/10.1175/BAMS-D-13-00043.1

Dice, L. R. (1945). Measures of the Amount of Ecologic Association Between Species. *Ecology*, *26*(3), 297–302. https://doi.org/10.2307/1932409

Doherty, S. J., Warren, S. G., Grenfell, T. C., Clarke, A. D., & Brandt, R. E. (2010). Light-absorbing impurities in Arctic snow. *Atmospheric Chemistry and Physics*, *10*(23), 11647–11680. https://doi.org/10.5194/ACP-10-11647-2010

Donmez, C., Berberoglu, S., Cicekli, S. Y., Cilek, A., & Arslan, A. N. (2021). Mapping snow cover using landsat data: toward a fine-resolution water-resistant snow index. *Meteorology and Atmospheric Physics*, *133*(2), 281–294. https://doi.org/10.1007/S00703-020-00749-Y/FIGURES/8

Dujardin, J., & Lehning, M. (2022). Wind-Topo: Downscaling near-surface wind fields to high-resolution topography in highly complex terrain with deep learning. *Quarterly Journal of the Royal Meteorological Society*, *148*(744), 1368–1388. https://doi.org/10.1002/QJ.4265

Dumont, M., Durand, Y., Arnaud, Y., & Six, D. (2012). Variational assimilation of albedo in a snowpack model and reconstruction of the spatial mass-balance distribution of an alpine glacier. *Journal of Glaciology*, *58*(207), 151–164. https://doi.org/10.3189/2012JOG11J163

Ekström, M., Grose, M. R., & Whetton, P. H. (2015). An appraisal of downscaling methods used in climate change research. *Wiley Interdisciplinary Reviews: Climate Change*, *6*(3), 301–319. https://doi.org/10.1002/WCC.339

Essery, R., Morin, S., Lejeune, Y., & B Ménard, C. (2013). A comparison of 1701 snow models using observations from an alpine site. *Advances in Water Resources*, *55*, 131–148. https://doi.org/10.1016/J.ADVWATRES.2012.07.013

Evin, G., Le Lay, M., Fouchier, C., Penot, D., Colleoni, F., Mas, A., Garambois, P.-A., & Laurantin, O. (2024). Evaluation of hydrological models on small mountainous catchments: impact of the meteorological forcings. *Hydrology and Earth System Sciences*, *28*(1), 261–281. https://doi.org/10.5194/HESS-28-261-2024

Eyring, V., Bony, S., Meehl, G. A., Senior, C. A., Stevens, B., Stouffer, R. J., & Taylor, K. E. (2016). Overview of the Coupled Model Intercomparison Project Phase 6 (CMIP6) experimental design and organization. *Geoscientific Model Development*, *9*(5), 1937–1958. https://doi.org/10.5194/GMD-9-1937-2016

Fan, Y., Clark, M., Lawrence, D. M., Swenson, S., Band, L. E., Brantley, S. L., Brooks, P. D., Dietrich, W. E., Flores, A., Grant, G., Kirchner, J. W., Mackay, D. S., McDonnell, J. J., Milly, P. C., Sullivan, P. L., Tague, C., Ajami, H., Chaney, N., Hartmann, A., … Yamazaki, D. (2019). Hillslope Hydrology in Global Change Research and Earth System Modeling. *Water Resources Research*, *55*(2), 1737–1772. https://doi.org/10.1029/2018WR023903

Farinotti, D., Immerzeel, W. W., de Kok, R. J., Quincey, D. J., & Dehecq, A. (2020). Manifestations and mechanisms of the Karakoram glacier Anomaly. *Nature Geoscience 2020 13:1*, *13*(1), 8–16. https://doi.org/10.1038/s41561-019-0513-5

Fatichi, S., Ivanov, V. Y., & Caporali, E. (2012a). A mechanistic ecohydrological model to investigate complex interactions in cold and warm water-controlled environments: 1. Theoretical framework and plot-scale analysis. *Journal of Advances in Modeling Earth Systems*, *4*(2), 5002. https://doi.org/10.1029/2011MS000086

Fatichi, S., Ivanov, V. Y., & Caporali, E. (2012b). A mechanistic ecohydrological model to investigate complex interactions in cold and warm water-controlled environments: 2. Spatiotemporal analyses. *Journal of Advances in Modeling Earth Systems*, *4*(2), 5003. https://doi.org/10.1029/2011MS000087

Fatichi, S., Ivanov, V. Y., Paschalis, A., Peleg, N., Molnar, P., Rimkus, S., Kim, J., Burlando, P., & Caporali, E. (2016). Uncertainty partition challenges the predictability of vital details of climate change. *Earth's Future*, *4*(5), 240–251. https://doi.org/10.1002/2015EF000336

Fatichi, S., Vivoni, E. R., Ogden, F. L., Ivanov, V. Y., Mirus, B., Gochis, D., Downer, C. W., Camporese, M., Davison, J. H., Ebel, B., Jones, N., Kim, J., Mascaro, G., Niswonger, R., Restrepo, P., Rigon, R., Shen, C., Sulis, M., & Tarboton, D. (2016). An overview of current applications, challenges, and future trends in distributed process-based models in hydrology. *Journal of Hydrology*, *537*, 45–60. https://doi.org/10.1016/J.JHYDROL.2016.03.026

Fiddes, J., Endrizzi, S., & Gruber, S. (2015). Large-area land surface simulations in heterogeneous terrain driven by global data sets: Application to mountain permafrost. *Cryosphere*, *9*(1), 411–426. https://doi.org/10.5194/TC-9-411-2015

Fiddes, J., & Gruber, S. (2012). TopoSUB: A tool for efficient large area numerical modelling in complex topography at sub-grid scales. *Geoscientific Model Development*, *5*(5), 1245–1257. https://doi.org/10.5194/GMD-5-1245-2012

Fiddes, J., & Gruber, S. (2014). TopoSCALE v.1.0: Downscaling gridded climate data in complex terrain. *Geoscientific Model Development*, *7*(1), 387–405. https://doi.org/10.5194/GMD-7-387-2014

Fiddes, J., Aalstad, K., & Lehning, M. (2022). TopoCLIM: rapid topography-based downscaling of regional climate model output in complex terrain v1.1. *Geosci. Model Dev*, *15*, 1753–1768. https://doi.org/10.5194/gmd-15-1753-2022

Fiddes, J., Aalstad, K., & Westermann, S. (2019). Hyper-resolution ensemble-based snow reanalysis in mountain regions using clustering. *Hydrology and Earth System Sciences*, *23*(11), 4717–4736. https://doi.org/10.5194/HESS-23-4717-2019

Filhol, S., Fiddes, J., & Aalstad, K. (2023). TopoPyScale: A Python Package for Hillslope Climate Downscaling. *Journal of Open Source Software*, *8*(86), 5059. https://doi.org/10.21105/JOSS.05059

Förster, K., Hanzer, F., Winter, B., Marke, T., & Strasser, U. (2016). An open-source MEteoroLOgical observation time series DISaggregation Tool (MELODIST v0.1.1). *Geoscientific Model Development*, *9*(7), 2315–2333. https://doi.org/10.5194/GMD-9-2315-2016

Freudiger, D., Kohn, I., Seibert, J., Stahl, K., & Weiler, M. (2017). Snow redistribution for the hydrological modeling of alpine catchments. *Wiley Interdisciplinary Reviews: Water*, *4*(5), e1232. https://doi.org/10.1002/WAT2.1232

Fugger, S., Fyffe, C. L., Fatichi, S., Miles, E., McCarthy, M., Shaw, T. E., Ding, B., Yang, W., Wagnon, P., Immerzeel, W., Liu, Q., & Pellicciotti, F. (2022). Understanding monsoon controls on the energy and mass balance of glaciers in the Central and Eastern Himalaya. *Cryosphere*, *16*(5), 1631–1652. https://doi.org/10.5194/TC-16-1631-2022

Fugger, S., Shaw, T., Miles, E., Jouberton, A., Buri, P., McCarthy, M., Fyffe, C., Fatichi, S., et al. (2024). Hydrological regimes and evaporative flux partitioning at the climatic ends of High Mountain Asia. *Environmental Research Letters*.

Fyffe, C. L., Potter, E., Fugger, S., Orr, A., Fatichi, S., Loarte, E., Medina, K., Hellström, R., Bernat, M., Aubry-Wake, C., Gurgiser, W., Perry, L. B., Suarez, W., Quincey, D. J., & Pellicciotti, F. (2021). The Energy and Mass Balance of Peruvian Glaciers. *Journal of Geophysical Research: Atmospheres*, *126*(23), e2021JD034911. https://doi.org/10.1029/2021JD034911

Gabbi, J., Huss, M., Bauder, A., Cao, F., & Schwikowski, M. (2015). The impact of Saharan dust and black carbon on albedo and long-term mass balance of an Alpine glacier. *Cryosphere*, *9*(4), 1385–1400. https://doi.org/10.5194/TC-9-1385-2015

Gardner, A. S., & Sharp, M. J. (2010). A review of snow and ice albedo and the development of a new physically based broadband albedo parameterization. *Journal of Geophysical Research: Earth Surface*, *115*(F1), 1009. https://doi.org/10.1029/2009JF001444

Gobiet, A., Suklitsch, M., & Heinrich, G. (2015). The effect of empirical-statistical correction of intensity-dependent model errors on the temperature climate change signal. *Hydrology and Earth System Sciences*, *19*(10), 4055–4066. https://doi.org/10.5194/HESS-19-4055-2015

Grünewald, T., Grünewald, G., Schirmer, M., Mott, R., & Lehning, M. (2010). Spatial and temporal variability of snow depth and ablation rates in a small mountain catchment. *The Cryosphere*, *4*, 215–225. https://doi.org/10.5194/tc-4-215-2010

Gudmundsson, L., Bremnes, J. B., Haugen, J. E., & Engen-Skaugen, T. (2012). Technical Note: Downscaling RCM precipitation to the station scale using statistical transformations – A comparison of methods. *Hydrology and Earth System Sciences*, *16*(9), 3383–3390. https://doi.org/10.5194/HESS-16-3383-2012

Gutowski, J., William J., Decker, S. G., Donavon, R. A., Pan, Z., Arritt, R. W., Takle, E. S., Gutowski, J., William J., Decker, S. G., Donavon, R. A., Pan, Z., Arritt, R. W., & Takle, E. S. (2003). Temporal Spatial Scales of Observed and Simulated Precipitation in Central U.S. Climate. *JCli*, *16*(22), 3841–3847. https://doi.org/10.1175/1520-0442(2003)016

Haeberli, W., Noetzli, J., Arenson, L., Delaloye, R., Gärtner-Roer, I., Gruber, S., Isaksen, K., Kneisel, C., Krautblatter, M., & Phillips, M. (2010). Mountain permafrost: development and challenges of a young research field. *Journal of Glaciology*, *56*(200), 1043–1058. https://doi.org/10.3189/002214311796406121

Hagg, W., Hoelzle, M., Wagner, S., Mayr, E., & Klose, Z. (2013). Glacier and runoff changes in the Rukhk catchment, upper Amu-Darya basin until 2050. *Global and Planetary Change*, *110*, 62–73. https://doi.org/10.1016/J.GLOPLACHA.2013.05.005

Hall, D. K., & Riggs, G. A. (2021). MODIS/Terra Snow Cover Daily L3 Global 500m SIN Grid, Version 61 [Dataset]. https://doi.org/https://doi.org/10.5067/MODIS/MOD10A1.061

Hartigan, J. A., & Wong, M. A. (1979). A K-Means Clustering Algorithm. *Journal of the Royal Statistical Society: Series C (Applied Statistics)*, *28*(1), 100–108. https://doi.org/10.2307/2346830

Hersbach, H., Bell, B., Berrisford, P., Biavati, G., Horányi, A., Muñoz Sabater, J., Nicolas, J., Peubey, C., Radu, R., Rozum, I., Schepers, D., Simmons, A., Soci, C., Dee, D., & Thépaut, J.-N. (2023a). ERA5 hourly data on pressure levels from 1940 to present. https://doi.org/10.24381/cds.bd0915c6

Hersbach, H., Bell, B., Berrisford, P., Biavati, G., Horányi, A., Muñoz Sabater, J., Nicolas, J., Peubey, C., Radu, R., Rozum, I., Schepers, D., Simmons, A., Soci, C., Dee, D., & Thépaut, J.-N. (2023b). ERA5 hourly data on single levels from 1940 to present. https://doi.org/10.24381/cds.adbb2d47

Hersbach, H., Bell, B., Berrisford, P., Hirahara, S., Horányi, A., Muñoz-Sabater, J., Nicolas, J., Peubey, C., Radu, R., Schepers, D., Simmons, A., Soci, C., Abdalla, S., Abellan, X., Balsamo, G., Bechtold, P., Biavati, G., Bidlot, J., Bonavita, M., … Thépaut, J. N. (2020). The ERA5 global reanalysis. *Quarterly Journal of the Royal Meteorological Society*, *146*(730), 1999–2049. https://doi.org/10.1002/QJ.3803

Hong, S. Y., & Kanamitsu, M. (2014). Dynamical downscaling: Fundamental issues from an NWP point of view and recommendations. *Asia-Pacific Journal of Atmospheric Sciences*, *50*(1), 83–104. https://doi.org/10.1007/S13143-014-0029-2/METRICS

Huang, J., Su, F., Yao, T., & Sun, H. (2022). Runoff Regime, Change, and Attribution in the Upper Syr Darya and Amu Darya, Central Asia. *Journal of Hydrometeorology*, *23*(10), 1563–1585. https://doi.org/10.1175/JHM-D-22-0036.1

Huang, L., Hock, R., Li, X., Bolch, T., Yang, K., Wang, N., Yao, T., Zhou, J., Dou, C., & Li, Z. (2022). Winter accumulation drives the spatial variations in glacier mass balance in High Mountain Asia. *Z. Li). Science Bulletin*, *67*, 1967–1970. https://doi.org/10.1016/j.scib.2022.08.019

Huang, Y., Bárdossy, A., & Zhang, K. (2019). Sensitivity of hydrological models to temporal and spatial resolutions of rainfall data. *Hydrology and Earth System Sciences*, *23*(6), 2647–2663. https://doi.org/10.5194/HESS-23-2647-2019

Hugonnet, R., McNabb, R., Berthier, E., Menounos, B., Nuth, C., Girod, L., Farinotti, D., Huss, M., Dussaillant, I., Brun, F., & Kääb, A. (2021). Accelerated global glacier mass loss in the early twenty-first century. *Nature*, *592*(7856), 726–731. https://doi.org/10.1038/s41586-021-03436-z

Immerzeel, W. W., Droogers, P., de Jong, S. M., & Bierkens, M. F. (2009). Large-scale monitoring of snow cover and runoff simulation in Himalayan river basins using remote sensing. *Remote Sensing of Environment*, *113*(1), 40–49. https://doi.org/10.1016/J.RSE.2008.08.010

Immerzeel, W. W., Lutz, A. F., Andrade, M., Bahl, A., Biemans, H., Bolch, T., Hyde, S., Brumby, S., Davies, B. J., Elmore, A. C., Emmer, A., Feng, M., Fernández, A., Haritashya, U., Kargel, J. S., Koppes, M., Kraaijenbrink, P. D., Kulkarni, A. V., Mayewski, P. A., … Baillie, J. E. (2019). Importance and vulnerability of the world's water towers. *Nature 2019 577:7790*, *577*(7790), 364–369. https://doi.org/10.1038/s41586-019-1822-y

Ivanov, M. A., Luterbacher, J., & Kotlarski, S. (2018). Climate Model Biases and Modification of the Climate Change Signal by Intensity-Dependent Bias Correction. *Journal of Climate*, *31*(16), 6591–6610. https://doi.org/10.1175/JCLI-D-17-0765.1

Jiang, H., Zheng, G., Yi, Y., Chen, D., Zhang, W., Yang, K., & Miller, C. E. (2020). Progress and Challenges in Studying Regional Permafrost in the Tibetan Plateau Using Satellite Remote Sensing and Models. *Frontiers in Earth Science*, *8*, 560403. https://doi.org/10.3389/FEART.2020.560403/BIBTEX

Jiang Jie, Zhou Tianjun, Chen Xiaolong, Zhang Lixia, & Lixia Zhang. (2020). Future changes in precipitation over Central Asia based on CMIP6 projections. *Environmental Research Letters*, *15*(5). https://doi.org/10.1088/1748-9326/AB7D03

Johnson, E., & Rupper, S. (2020). An Examination of Physical Processes That Trigger the Albedo-Feedback on Glacier Surfaces and Implications for Regional Glacier Mass Balance Across High Mountain Asia. *Frontiers in Earth Science*, *8*, 469367. https://doi.org/10.3389/FEART.2020.00129/BIBTEX

Kendall, M. (1975). Rank Correlation Measures.

Krajčí, P., Holko, L., Perdigão, R. A., & Parajka, J. (2014). Estimation of regional snowline elevation (RSLE) from MODIS images for seasonally snow covered mountain basins. *Journal of Hydrology*, *519*(PB), 1769–1778. https://doi.org/10.1016/J.JHYDROL.2014.08.064

Lavers, D. A., Simmons, A., Vamborg, F., & Rodwell, M. J. (2022). An evaluation of ERA5 precipitation for climate monitoring. *Quarterly Journal of the Royal Meteorological Society*, *148*(748), 3152–3165. https://doi.org/10.1002/QJ.4351

Li, W., Yan, D., Weng, B., & Zhu, L. (2023). Research progress on hydrological effects of permafrost degradation in the Northern Hemisphere. *Geoderma*, *438*, 116629. https://doi.org/10.1016/J.GEODERMA.2023.116629

Li, X., Ji, Y., Zhou, G., Zhou, L., Li, X., He, X., & Tian, Z. (2023). A New Method for Bare Permafrost Extraction on the Tibetan Plateau by Integrating Machine Learning and Multi-Source Information. *Remote Sensing 2023, Vol. 15, Page 5328*, *15*(22), 5328. https://doi.org/10.3390/RS15225328

Liang, S. (2001). Narrowband to broadband conversions of land surface albedo I: Algorithms. *Remote Sensing of Environment*, *76*(2), 213–238. https://doi.org/10.1016/S0034-4257(00)00205-4

Liston, G. E., & Elder, K. (2006). A Meteorological Distribution System for High-Resolution Terrestrial Modeling (MicroMet). *Journal of Hydrometeorology*, *7*(2), 217–234. https://doi.org/10.1175/JHM486.1

Luo, Y., Wang, X., Piao, S., Sun, L., Ciais, P., Zhang, Y., Ma, C., Gan, R., & He, C. (2018). Contrasting streamflow regimes induced by melting glaciers across the Tien Shan – Pamir – North Karakoram. *Scientific Reports 2018 8:1*, *8*(1), 1–9. https://doi.org/10.1038/s41598-018-34829-2

Machguth, H., Paul, F., Kotlarski, S., & Hoelzle, M. (2009). Calculating distributed glacier mass balance for the Swiss Alps from regional climate model output: A methodical description and interpretation of the results. *Journal of Geophysical Research: Atmospheres*, *114*(D19), 19106. https://doi.org/10.1029/2009JD011775

Mann, H. B. (1945). Nonparametric Tests Against Trend. *Econometrica*, *13*(3), 245. https://doi.org/10.2307/1907187

Manoli, G., Ivanov, V. Y., & Fatichi, S. (2018). Dry-Season Greening and Water Stress in Amazonia: The Role of Modeling Leaf Phenology. *Journal of Geophysical Research: Biogeosciences*, *123*(6), 1909–1926. https://doi.org/10.1029/2017JG004282

Marty, C., Philipona, R., Frøhlich, C., & Ohmura, A. (2002). Altitude dependence of surface radiation fluxes and cloud forcing in the alps: Results from the alpine surface radiation budget network. *Theoretical and Applied Climatology*, *72*(3-4), 137–155. https://doi.org/10.1007/S007040200019/METRICS

Masek, J., Ju, J., Roger, J., Skakun, S., Vermote E., Claverie, M., Dungan, J., Yin, Z., Freitag, B., & Justice, C. (2021). HLS Operational Land Imager Surface Reflectance and TOA Brightness Daily Global 30m v2.0 [Dataset]. https://doi.org/https://doi.org/10.5067/HLS/HLSL30.002

Mastrotheodoros, T., Pappas, C., Molnar, P., Burlando, P., Hadjidoukas, P., & Fatichi, S. (2019). Ecohydrological dynamics in the Alps: Insights from a modelling analysis of the spatial variability. *Ecohydrology*, *12*(1), e2054. https://doi.org/10.1002/ECO.2054

Mastrotheodoros, T., Pappas, C., Molnar, P., Burlando, P., Manoli, G., Parajka, J., Rigon, R., Szeles, B., Bottazzi, M., Hadjidoukas, P., & Fatichi, S. (2020). More green and less blue water in the Alps during warmer summers. *Nature Climate Change*, *10*(2). https://doi.org/10.1038/s41558-019-0676-5

Masuda, M., Yatagai, A., Kamiguchi, K., & Tanaka, K. (2019). Daily Adjustment for Wind-Induced Precipitation Undercatch of Daily Gridded Precipitation in Japan. *Earth and Space Science*, *6*(8), 1469–1479. https://doi.org/10.1029/2019EA000659

Melton, J. R., Verseghy, D. L., Sospedra-Alfonso, R., & Gruber, S. (2019). Improving permafrost physics in the coupled Canadian Land Surface Scheme (v.3.6.2) and Canadian Terrestrial Ecosystem Model (v.2.1) (CLASS-CTEM). *Geoscientific Model Development*, *12*(10), 4443–4467. https://doi.org/10.5194/GMD-12-4443-2019

Michel, A., Sharma, V., Lehning, M., & Huwald, H. (2021). Climate change scenarios at hourly time-step over Switzerland from an enhanced temporal downscaling approach. *International Journal of Climatology*, *41*(6), 3503–3522. https://doi.org/10.1002/JOC.7032

Miles, E., McCarthy, M., Dehecq, A., Kneib, M., Fugger, S., & Pellicciotti, F. (2021). Health and sustainability of glaciers in High Mountain Asia. *Nature Communications 2021 12:1*, *12*(1), 1–10. https://doi.org/10.1038/s41467-021-23073-4

Mott, R., Schirmer, M., & Lehning, M. (2011). Scaling properties of wind and snow depth distribution in an Alpine catchment. *Journal of Geophysical Research: Atmospheres*, *116*(D6), 6106. https://doi.org/10.1029/2010JD014886

Muñoz-Sabater, J. (2019). ERA5-Land hourly data from 1950 to present. https://doi.org/10.24381/cds.e2161bac

Muñoz-Sabater, J., Dutra, E., Agustí-Panareda, A., Albergel, C., Arduini, G., Balsamo, G., Boussetta, S., Choulga, M., Harrigan, S., Hersbach, H., Martens, B., Miralles, D. G., Piles, M., Rodríguez-Fernández, N. J., Zsoter, E., Buontempo, C., & Thépaut, J.-N. (2021). ERA5-Land: a state-of-the-art global reanalysis dataset for land applications. *Earth Syst. Sci. Data*, *13*, 4349–4383. https://doi.org/10.5194/essd-13-4349-2021

Murphy, D. M., & Koop, T. (2005). Review of the vapour pressures of ice and supercooled water for atmospheric applications. *Quarterly Journal of the Royal Meteorological Society*, *131*(608), 1539–1565. https://doi.org/10.1256/QJ.04.94

Naegeli, K., & Huss, M. (2017). Sensitivity of mountain glacier mass balance to changes in bare-ice albedo. *Annals of Glaciology*, *58*(75pt2), 119–129. https://doi.org/10.1017/AOG.2017.25

Naegeli, K., Huss, M., & Hoelzle, M. (2019). Change detection of bare-ice albedo in the Swiss Alps. *Cryosphere*, *13*(1), 397–412. https://doi.org/10.5194/TC-13-397-2019

Niwano, M., Aoki, T., Hashimoto, A., Matoba, S., Yamaguchi, S., Tanikawa, T., Fujita, K., Tsushima, A., Iizuka, Y., Shimada, R., & Hori, M. (2018). NHM-SMAP: Spatially and temporally high-resolution nonhydrostatic atmospheric model coupled with detailed snow process model for Greenland Ice Sheet. *Cryosphere*, *12*(2), 635–655. https://doi.org/10.5194/TC-12-635-2018

Normatov, I., & Normatov, P. (2020). Climate change impact on hydrological characteristics and water availability of the Mountain Pamir Rivers. *Proceedings of the International Association of Hydrological Sciences*, *383*, 31–41. https://doi.org/10.5194/PIAHS-383-31-2020

Obu, J., Westermann, S., Bartsch, A., Berdnikov, N., Christiansen, H. H., Dashtseren, A., Delaloye, R., Elberling, B., Etzelmüller, B., Kholodov, A., Khomutov, A., Kääb, A., Leibman, M. O., Lewkowicz, A. G., Panda, S. K., Romanovsky, V., Way, R. G., Westergaard-Nielsen, A., Wu, T., . . . Zou, D. (2019). Northern Hemisphere permafrost map based on TTOP modelling for 2000–2016 at 1km2 scale. *Earth-Science Reviews*, *193*, 299–316. https://doi.org/10.1016/J.EARSCIREV.2019.04.023

Obu, J., Westermann, S., Vieira, G., Abramov, A., Balks, M. R., Bartsch, A., Hrbáček, F., Kääb, A., & Ramos, M. (2020). Pan-Antarctic map of near-surface permafrost temperatures at 1 km 2 scale. *The Cryosphere*, *14*, 497–519. https://doi.org/10.5194/tc-14-497-2020

O'Neill, B. C., Kriegler, E., Ebi, K. L., Kemp-Benedict, E., Riahi, K., Rothman, D. S., van Ruijven, B. J., van Vuuren, D. P., Birkmann, J., Kok, K., Levy, M., & Solecki, W. (2017). The roads ahead: Narratives for shared socioeconomic pathways describing world futures in the 21st century. *Global Environmental Change*, *42*, 169–180. https://doi.org/10.1016/J.GLOENVCHA.2015.01.004

O'Neill, B. C., Tebaldi, C., Van Vuuren, D. P., Eyring, V., Friedlingstein, P., Hurtt, G., Knutti, R., Kriegler, E., Lamarque, J. F., Lowe, J., Meehl, G. A., Moss, R., Riahi, K., & Sanderson, B. M. (2016). The Scenario Model Intercomparison Project (ScenarioMIP) for CMIP6. *Geoscientific Model Development*, *9*(9), 3461–3482. https://doi.org/10.5194/GMD-9-3461-2016

Östrem, G. (1959). Ice Melting under a Thin Layer of Moraine, and the Existence of Ice Cores in Moraine Ridges. *Geografiska Annaler*, *41*(4), 228–230. https://doi.org/10.1080/20014422.1959.11907953

Otsu, N. (1979). A Threshold Selection Method from Gray-Level Histograms. *IEEE Trans Syst Man Cybern*, *SMC-9*(1), 62–66. https://doi.org/10.1109/TSMC.1979.4310076

Parker, W. S. (2016). Reanalyses and Observations: What's the Difference? *Bulletin of the American Meteorological Society*, *97*(9), 1565–1572. https://doi.org/10.1175/BAMS-D-14-00226.1

Paschalis, A., Bonetti, S., Guo, Y., & Fatichi, S. (2022). On the Uncertainty Induced by Pedotransfer Functions in Terrestrial Biosphere Modeling. *Water Resources Research*, *58*(9), e2021WR031871. https://doi.org/10.1029/2021WR031871

Peleg, N., Fatichi, S., Paschalis, A., Molnar, P., & Burlando, P. (2017). An advanced stochastic weather generator for simulating 2-D high-resolution climate variables. *Journal of Advances in Modeling Earth Systems*, *9*(3), 1595–1627. https://doi.org/10.1002/2016MS000854

Pohl, E., Gloaguen, R., Andermann, C., & Knoche, M. (2017). Glacier melt buffers river runoff in the Pamir Mountains. *Water Resources Research*, *53*(3), 2467–2489. https://doi.org/10.1002/2016WR019431

Reichert, P., Ammann, L., & Fenicia, F. (2021). Potential and Challenges of Investigating Intrinsic Uncertainty of Hydrological Models With Stochastic, Time-Dependent Parameters. *Water Resources Research*, *57*(3), e2020WR028400. https://doi.org/10.1029/2020WR028400

Renard, B., Kavetski, D., Kuczera, G., Thyer, M., & Franks, S. W. (2010). Understanding predictive uncertainty in hydrologic modeling: The challenge of identifying input and structural errors. *Water Resources Research*, *46*(5), 5521. https://doi.org/10.1029/2009WR008328

Reyer, C. P., Otto, I. M., Adams, S., Albrecht, T., Baarsch, F., Cartsburg, M., Coumou, D., Eden, A., Ludi, E., Marcus, R., Mengel, M., Mosello, B., Robinson, A., Schleussner, C. F., Serdeczny, O., & Stagl, J. (2017). Climate change impacts in Central Asia and their implications for development. *Regional Environmental Change*, *17*(6), 1639–1650. https://doi.org/10.1007/S10113-015-0893-Z/FIGURES/3

Reynolds, D., Gutmann, E., Kruyt, B., Haugeneder, M., Jonas, T., Gerber, F., Lehning, M., & Mott, R. (2023). The High-resolution Intermediate Complexity Atmospheric Research (HICAR v1.1) model enables fast dynamic downscaling to the hectometer scale. *Geoscientific Model Development*, *16*(17), 5049–5068. https://doi.org/10.5194/GMD-16-5049-2023

RGI Consortium. (2017). Randolph Glacier Inventory - A Dataset of Global Glacier Outlines, Version 6. https://doi.org/https://doi.org/10.7265/4m1f-gd79

Rye, C. J., Arnold, N. S., Willis, I. C., & Kohler, J. (2010). Modeling the surface mass balance of a high Arctic glacier using the ERA-40 reanalysis. *Journal of Geophysical Research: Earth Surface*, *115*(F2), 2014. https://doi.org/10.1029/2009JF001364

Scher, S., & Peßenteiner, S. (2021). Technical Note: Temporal disaggregation of spatial rainfall fields with generative adversarial networks. *Hydrol. Earth Syst. Sci*, *25*, 3207–3225. https://doi.org/10.5194/hess-25-3207-2021

Scherler, D., Wulf, H., & Gorelick, N. (2018). Global Assessment of Supraglacial Debris-Cover Extents. *Geophysical Research Letters*, *45*(21), 798–11. https://doi.org/10.1029/2018GL080158

Schuler, T. V., & Østby, T. r. I. (2020). Sval-Imp: A gridded forcing dataset for climate change impact research on Svalbard. *Earth System Science Data*, *12*(2), 875–885. https://doi.org/10.5194/ESSD-12-875-2020

Shaw, T. E., Miles, E. S., Chen, D., Jouberton, A., Kneib, M., Fugger, S., Ou, T., Lai, H. W., Fujita, K., Yang, W., Fatichi, S., & Pellicciotti, F. (2022). Multi-decadal monsoon characteristics and glacier response in High Mountain Asia. *Environmental Research Letters*, *17*(10), 104001. https://doi.org/10.1088/1748-9326/AC9008

Sorensen, T. (1948). *A Method of Establishing Groups of Equal Amplitude in Plant Sociology Based on Similarity of Species and Its Application to Analyses of the Vegetation on Danish Commons*. Kongelige Danske Videnskabernes Selskab. https://www.scirp.org/reference/ReferencesPapers?ReferenceID=2150293

Sorg, A., Bolch, T., Stoffel, M., Solomina, O., & Beniston, M. (2012). Climate change impacts on glaciers and runoff in Tien Shan (Central Asia). *Nature Climate Change 2012 2:10*, *2*(10), 725–731. https://doi.org/10.1038/nclimate1592

Takaku, J., Tadono, T., & Tsutsui, K. (2014). Generation of High Resolution Global DSM from ALOS PRISM. *The International Archives of the Photogrammetry, Remote Sensing and Spatial Information Sciences*, *XL-4*(4), 243–248. https://doi.org/10.5194/ISPRSARCHIVES-XL-4-243-2014

Tapiador, F. J., Navarro, A., Moreno, R., Sánchez, J. L., & García-Ortega, E. (2020). Regional climate models: 30 years of dynamical downscaling. *Atmospheric Research*, *235*, 104785. https://doi.org/10.1016/J.ATMOSRES.2019.104785

Themeßl, M. J., Gobiet, A., & Heinrich, G. (2012). Empirical-statistical downscaling and error correction of regional climate models and its impact on the climate change signal. *Climatic Change*, *112*(2), 449–468. https://doi.org/10.1007/S10584-011-0224-4/FIGURES/14

Themeßl, M. J., Gobiet, A., & Leuprecht, A. (2011). Empirical-statistical downscaling and error correction of daily precipitation from regional climate models. *International Journal of Climatology*, *31*(10), 1530–1544. https://doi.org/10.1002/JOC.2168

USGS EROS Archive. (2020). Landsat 7 ETM Plus Collection 2 Level-2 Science Products [Dataset]. https://doi.org/10.5066/P9C7I13B

van Tiel, M., Stahl, K., Freudiger, D., & Seibert, J. (2020). Glacio-hydrological model calibration and evaluation. *Wiley Interdisciplinary Reviews: Water*, *7*(6), e1483. https://doi.org/10.1002/WAT2.1483

Wang, X., Luo, Y., Sun, L., He, C., Zhang, Y., & Liu, S. (2016). Attribution of Runoff Decline in the Amu Darya River in Central Asia during 1951–2007. *Journal of Hydrometeorology*, *17*(5), 1543–1560. https://doi.org/10.1175/JHM-D-15-0114.1

Wang, X., Tolksdorf, V., Otto, M., & Scherer, D. (2021). WRF-based dynamical downscaling of ERA5 reanalysis data for High Mountain Asia: Towards a new version of the High Asia Refined analysis. *International Journal of Climatology*, *41*(1), 743–762. https://doi.org/10.1002/JOC.6686

Westermann, S., Ostby, T. I., Gisnäs, K., Schuler, T. V., & Etzelmüller, B. (2015). A ground temperature map of the North Atlantic permafrost region based on remote sensing and reanalysis data. *Cryosphere*, *9*(3), 1303–1319. https://doi.org/10.5194/TC-9-1303-2015

White, C. J., Tanton, T. W., & Rycroft, D. W. (2014). The Impact of Climate Change on the Water Resources of the Amu Darya Basin in Central Asia. *Water Resources Management*, *28*(15), 5267–5281. https://doi.org/10.1007/S11269-014-0716-X/FIGURES/5

Wilcke, R. A. I., Mendlik, T., & Gobiet, A. (2013). Multi-variable error correction of regional climate models. *Climatic Change*, *120*(4), 871–887. https://doi.org/10.1007/S10584-013-0845-X/FIGURES/7

Winstral, A., Jonas, T., & Helbig, N. (2017). Statistical Downscaling of Gridded Wind Speed Data Using Local Topography. *Journal of Hydrometeorology*, *18*(2), 335–348. https://doi.org/10.1175/JHM-D-16-0054.1

Yao, J., Gu, L., Yang, C., Chen, H., Wang, J., Ding, Y., Li, R., Zhao, L., Xiao, Y., Qiao, Y., Shi, J., & Chen, C. (2020). Estimation of surface energy fluxes in the permafrost region of the Tibetan Plateau based on in situ measurements and the surface energy balance system model. *International Journal of Climatology*, *40*(13), 5783–5800. https://doi.org/10.1002/JOC.6551

Yokohata, T., Saito, K., Takata, K., Nitta, T., Satoh, Y., Hajima, T., Sueyoshi, T., & Iwahana, G. (2020). Model improvement and future projection of permafrost processes in a global land surface model. *Progress in Earth and Planetary Science*, *7*(1), 1–12. https://doi.org/10.1186/S40645-020-00380-W/FIGURES/12

Zhang, Z., Lin, H., Wang, M., Liu, X., Chen, Q., Wang, C., & Zhang, H. (2022). A Review of Satellite Synthetic Aperture Radar Interferometry Applications in Permafrost Regions: Current status, challenges, and trends. *IEEE Geoscience and Remote Sensing Magazine*, *10*(3), 93–114. https://doi.org/10.1109/MGRS.2022.3170350

Appendix A: Observations

Table A.1: Overview of the available data during the hydrological year 2022 for each measured variable and location.

Location	Variable	Start date	End date
KYZ_AWS	Ta	01.10.2021	21.09.2022
	Rh		
	Sw↓		
	Lw↓		
	Ws		
	Tdeb		21.06.2022
	Sd		13.06.2022
KYZ_AWS_PLU	Ta	01.10.2021	17.09.2022
	Rh		
	Ws		
	Pr		23.09.2022
	Sd		22.06.2022
KYZ_GAUG	Ps	01.10.2021	21.09.2022
KYZ_T_3200	Ta	22.06.2022	22.09.2022
KYZ_T_3500	Ta	01.10.2021	23.09.2022
KYZ_T_3900	Ta	01.10.2021	19.09.2022
SANG_AWS	Ta	19.10.2021	06.09.2022
	Rh		
	Sw↓		
	Lw↓		
	Ws		
	Ts		
	Sd		
SANG_T_1	Ts	01.10.2021	06.09.2022
SANG_T_2	Ts	01.10.2021	17.09.2022
SANG_T_3	Ts	01.10.2021	06.09.2022
SANG_T_4	Ts	01.10.2021	07.09.2022
SANG_T_5	Ts	01.10.2021	07.09.2022
SANG_T_7	Ts	01.10.2021	07.09.2022
SANG_T_8	Ts	01.10.2021	07.09.2022
SANG_T_9	Ts	01.10.2021	06.09.2022
SANG_T_10	Ts	01.10.2021	05.09.2022
SANG_T_11	Ts	01.10.2021	04.09.2022

Appendix B: Methods

B.1 HIMAL-method

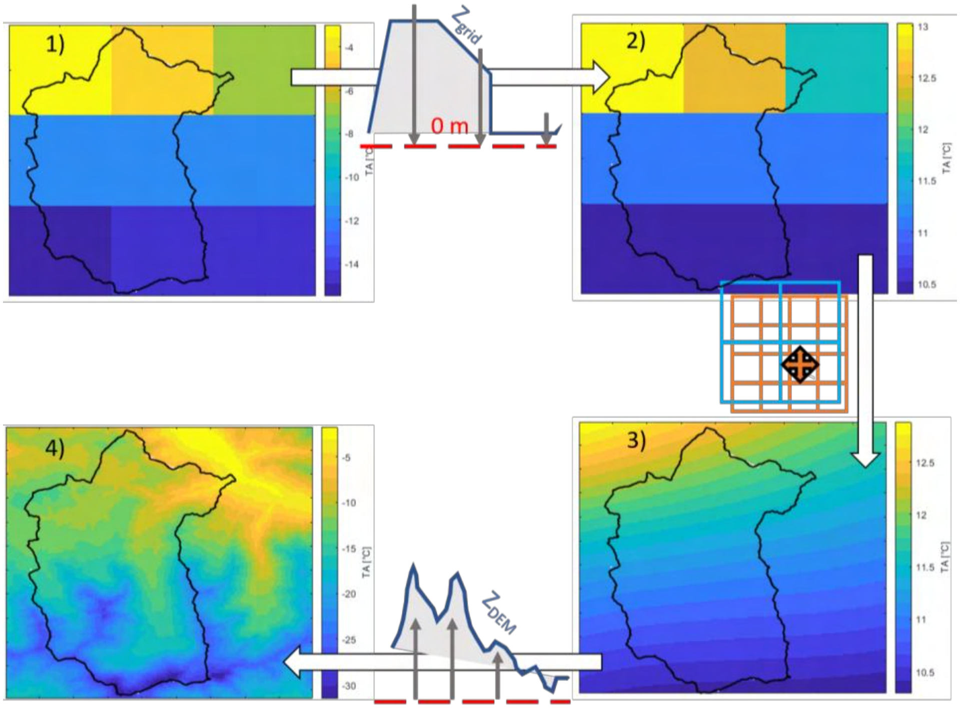

Figure B.1: A schematic figure of the process used to downscale forcing grids following Machguth et al. (2009). The example is taken for the Kyzylsu catchment in Tajikistan using air temperature for the first hour (00:00) of April 2021. Steps 1-4 are described above. Note: colour scales vary between plots. Source: Fugger et al. (2024)

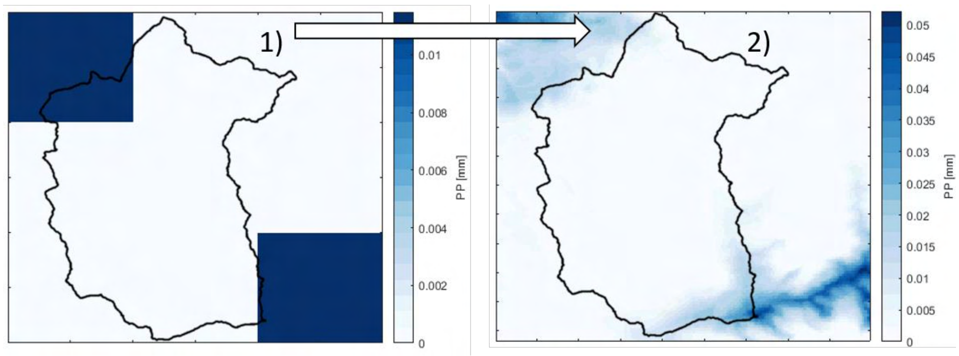

Figure B.2: As Figure B.1, but for the first and final step of precipitation downscaling, where the limits of the precipitation occurrence after-downscaling with a vertical gradient are preserved. Source: Fugger et al. (2024)

B.2 T&C

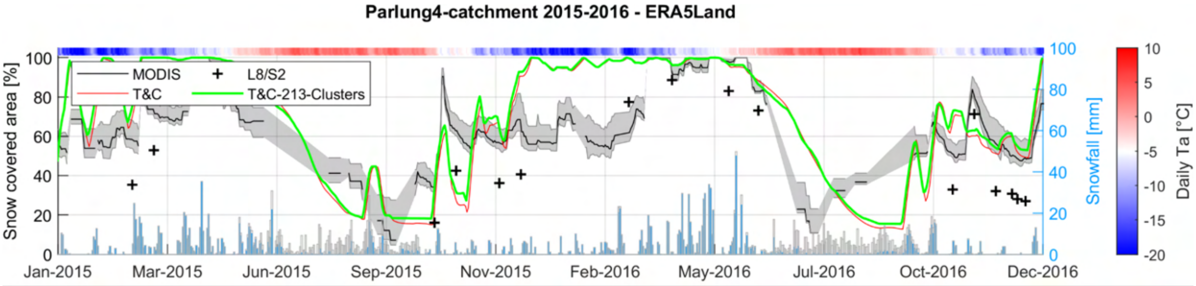

Figure B.3: Comparison of model performances in reproducing snow cover of the fully distributed (red line) and TopoSUB-clustered (green line) model runs in a different catchment, conducted by co-supervisor Achille Jouberton.

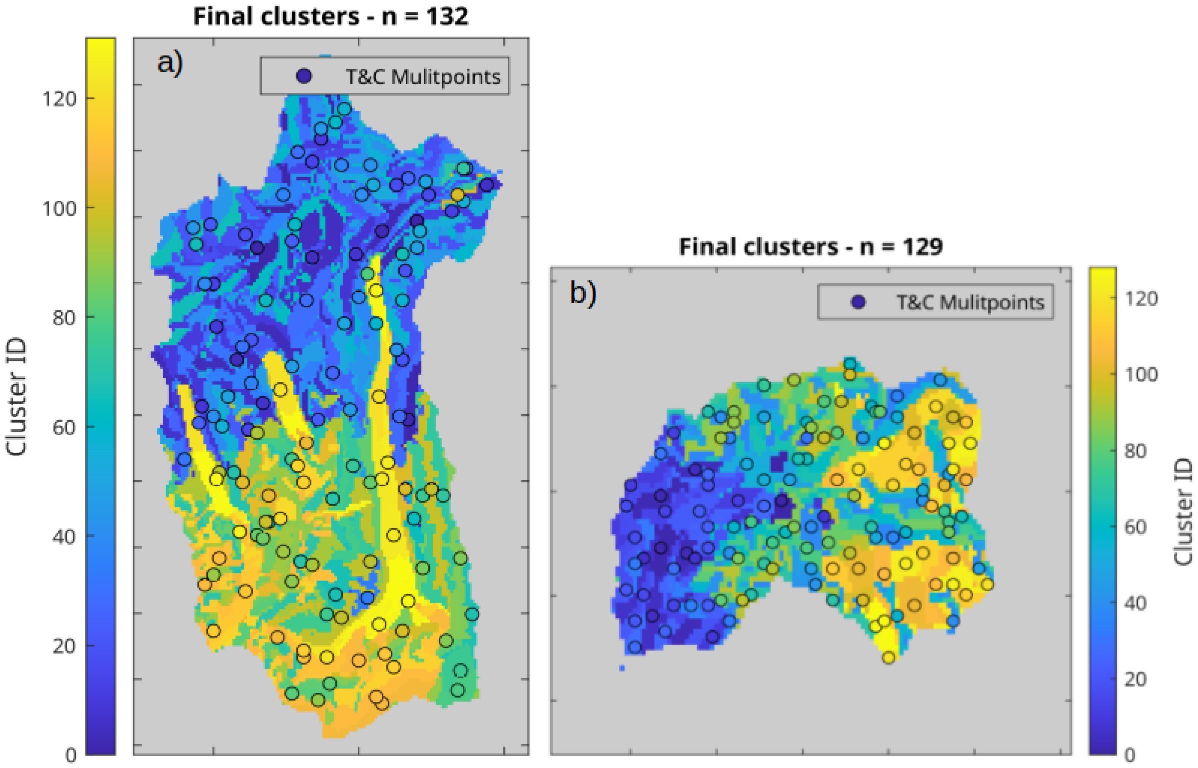

Figure B.4: Map of the TopoSUB clusters used for semi-distributed T&C-modelling in a) Kyzylsu and b) Sangvor. Note: colour scales vary between plots

Appendix C: Downscaled reanalysis

C.1 Evaluation of meteorological forcings

C.1.1 2m air temperature

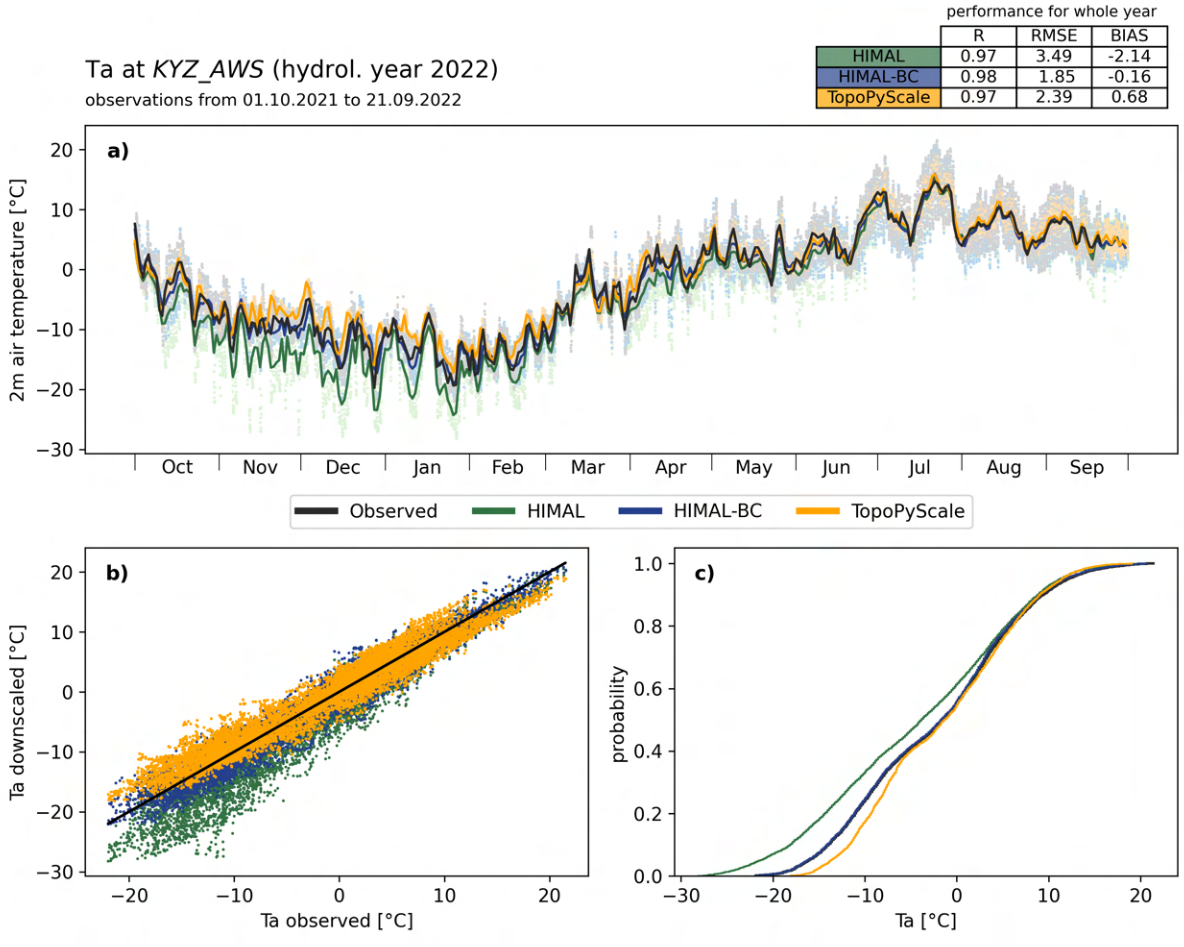

performance for whole year

	R	RMSE	BIAS
HIMAL	0.97	3.49	-2.14
HIMAL-BC	0.98	1.85	-0.16
TopoPyScale	0.97	2.39	0.68

Figure C.1: Evaluation of downscaled 2m air temperature at KYZ_AWS.

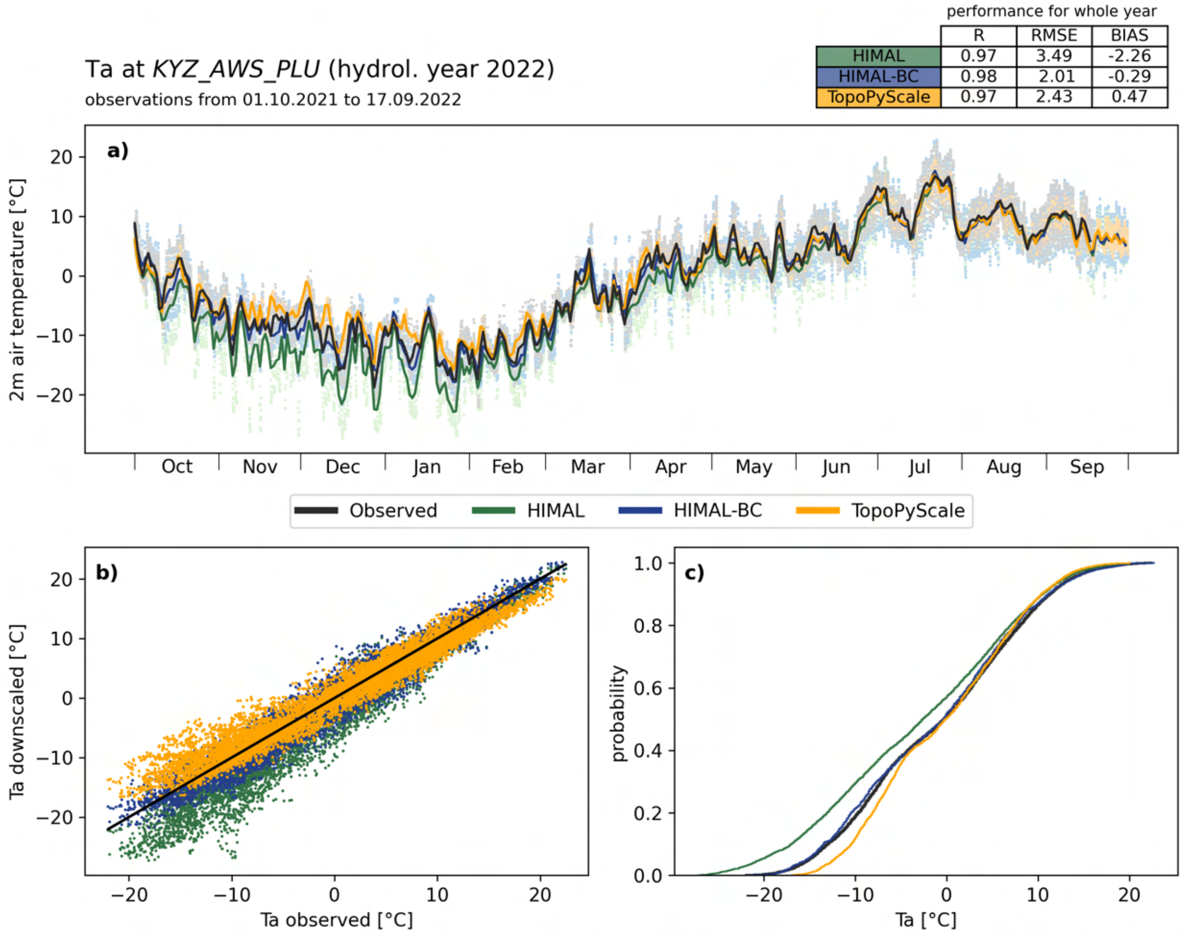

	R	RMSE	BIAS
HIMAL	0.97	3.49	-2.26
HIMAL-BC	0.98	2.01	-0.29
TopoPyScale	0.97	2.43	0.47

Figure C.2: Evaluation of downscaled 2m air temperature at KYZ_AWS_PLU.

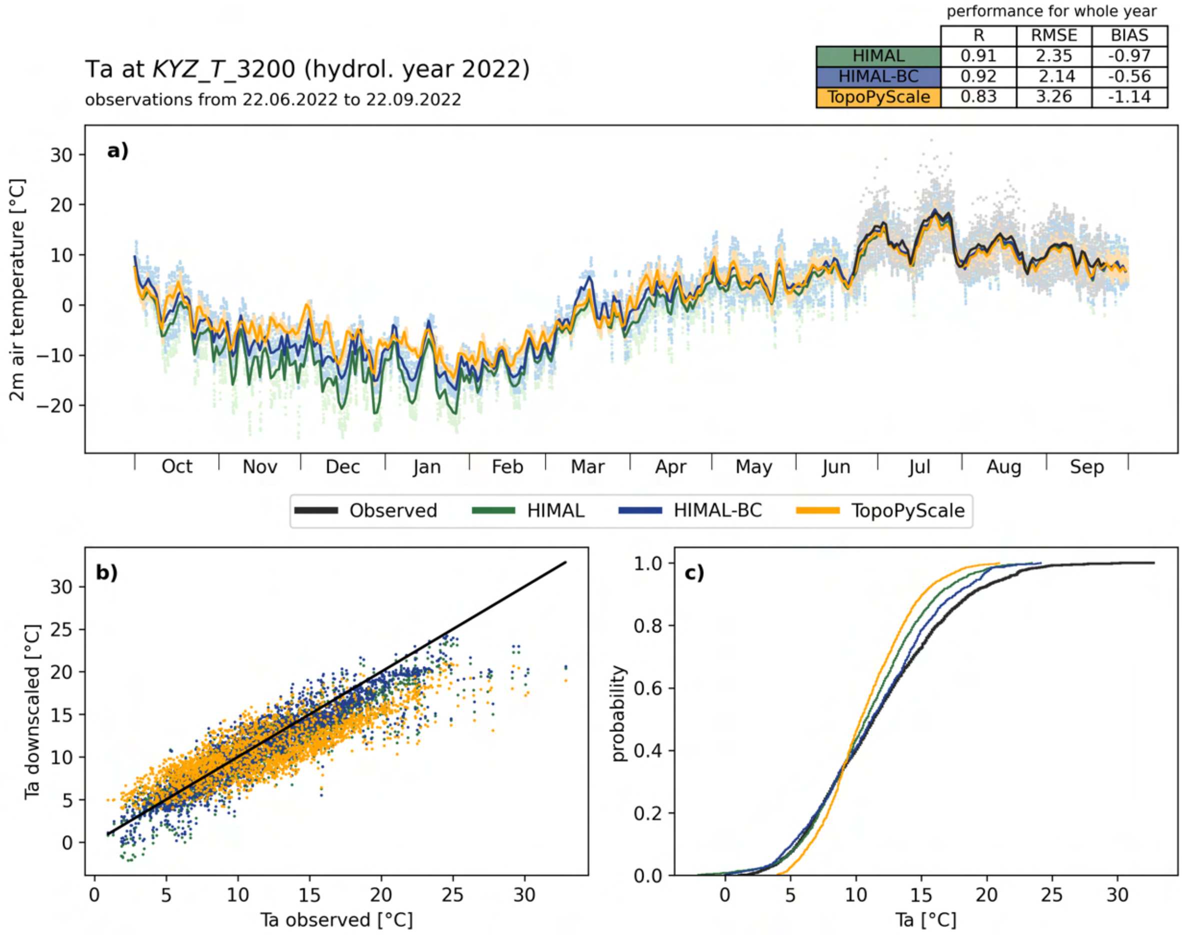

performance for whole year

	R	RMSE	BIAS
HIMAL	0.91	2.35	-0.97
HIMAL-BC	0.92	2.14	-0.56
TopoPyScale	0.83	3.26	-1.14

Figure C.3: Evaluation of downscaled 2m air temperature at KYZ_T_3200.

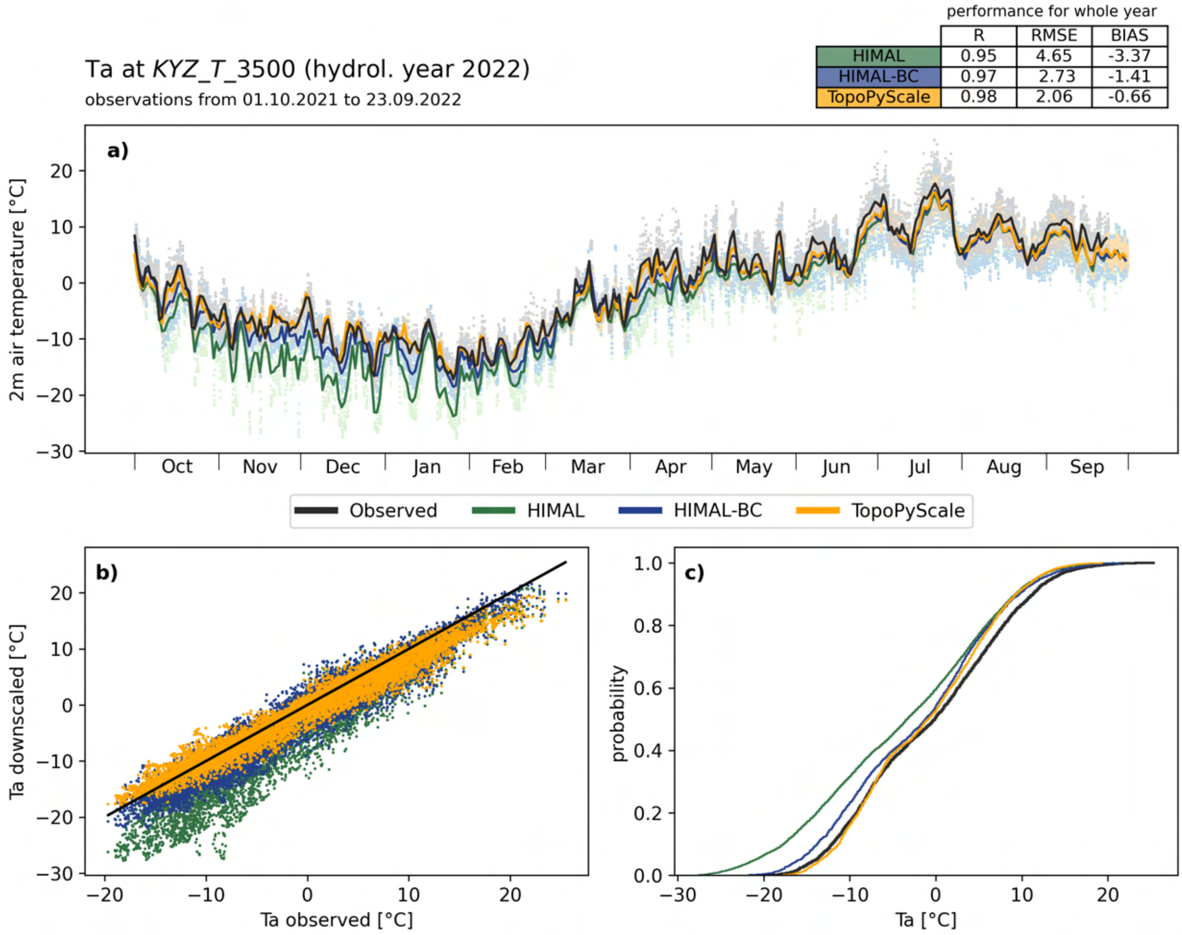

performance for whole year

	R	RMSE	BIAS
HIMAL	0.95	4.65	-3.37
HIMAL-BC	0.97	2.73	-1.41
TopoPyScale	0.98	2.06	-0.66

Figure C.4: Evaluation of downscaled 2m air temperature at KYZ_T_3500.

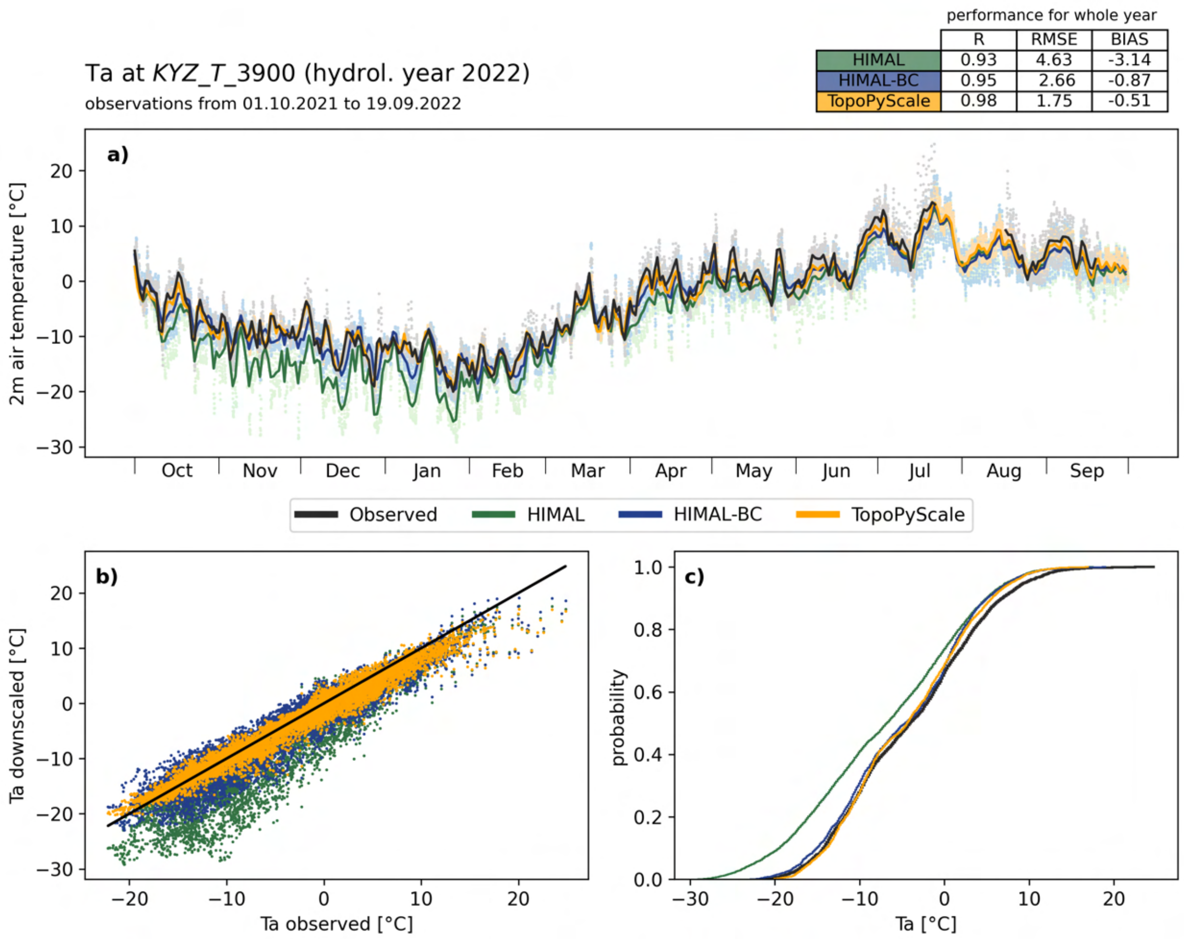

	R	RMSE	BIAS
HIMAL	0.93	4.63	-3.14
HIMAL-BC	0.95	2.66	-0.87
TopoPyScale	0.98	1.75	-0.51

Figure C.5: Evaluation of downscaled 2m air temperature at KYZ_T_3900.

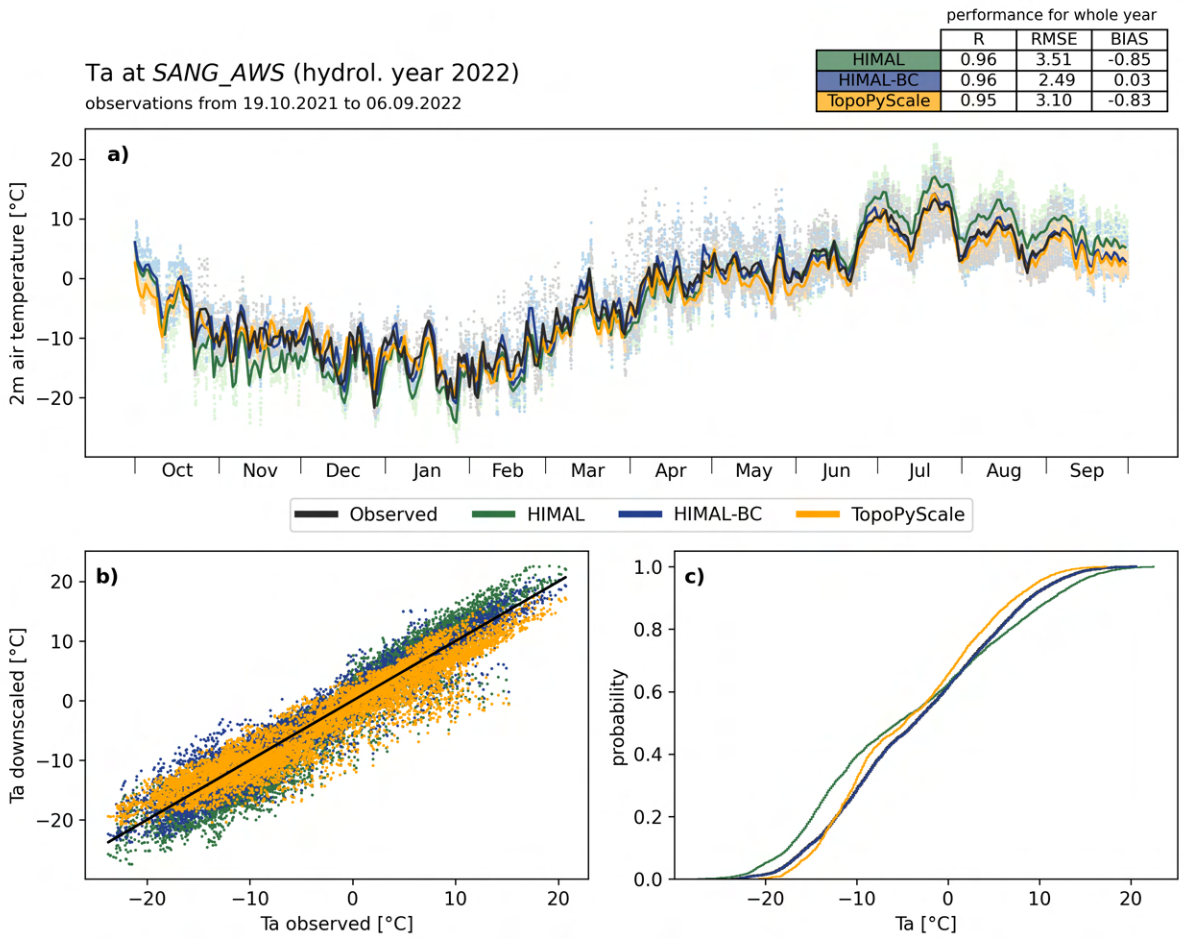

	R	RMSE	BIAS
HIMAL	0.96	3.51	-0.85
HIMAL-BC	0.96	2.49	0.03
TopoPyScale	0.95	3.10	-0.83

Figure C.6: Evaluation of downscaled 2m air temperature at SANG_AWS.

C.1.2 Near-surface relative humidity

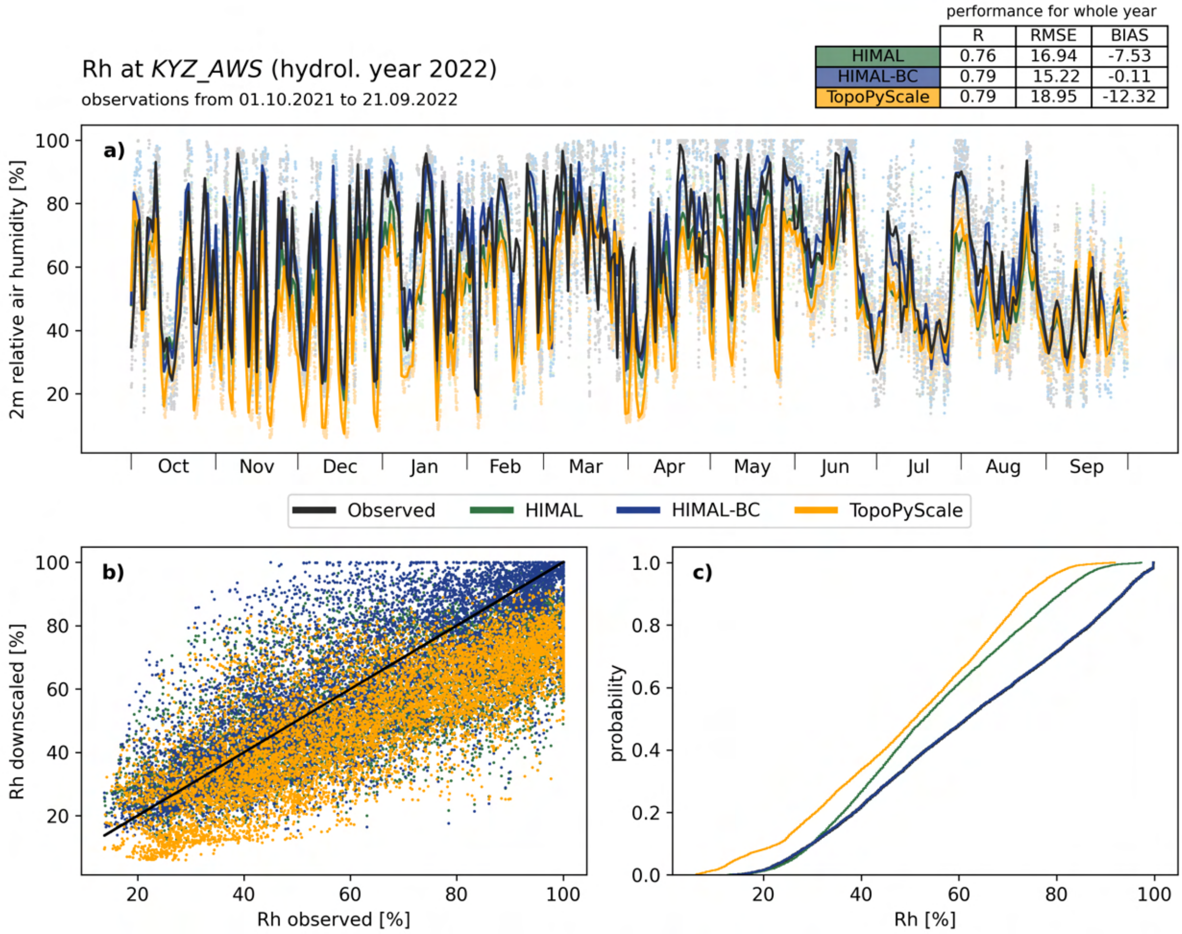

performance for whole year

	R	RMSE	BIAS
HIMAL	0.76	16.94	-7.53
HIMAL-BC	0.79	15.22	-0.11
TopoPyScale	0.79	18.95	-12.32

Figure C.7: Evaluation of downscaled near-surface relative humidity at KYZ_AWS.

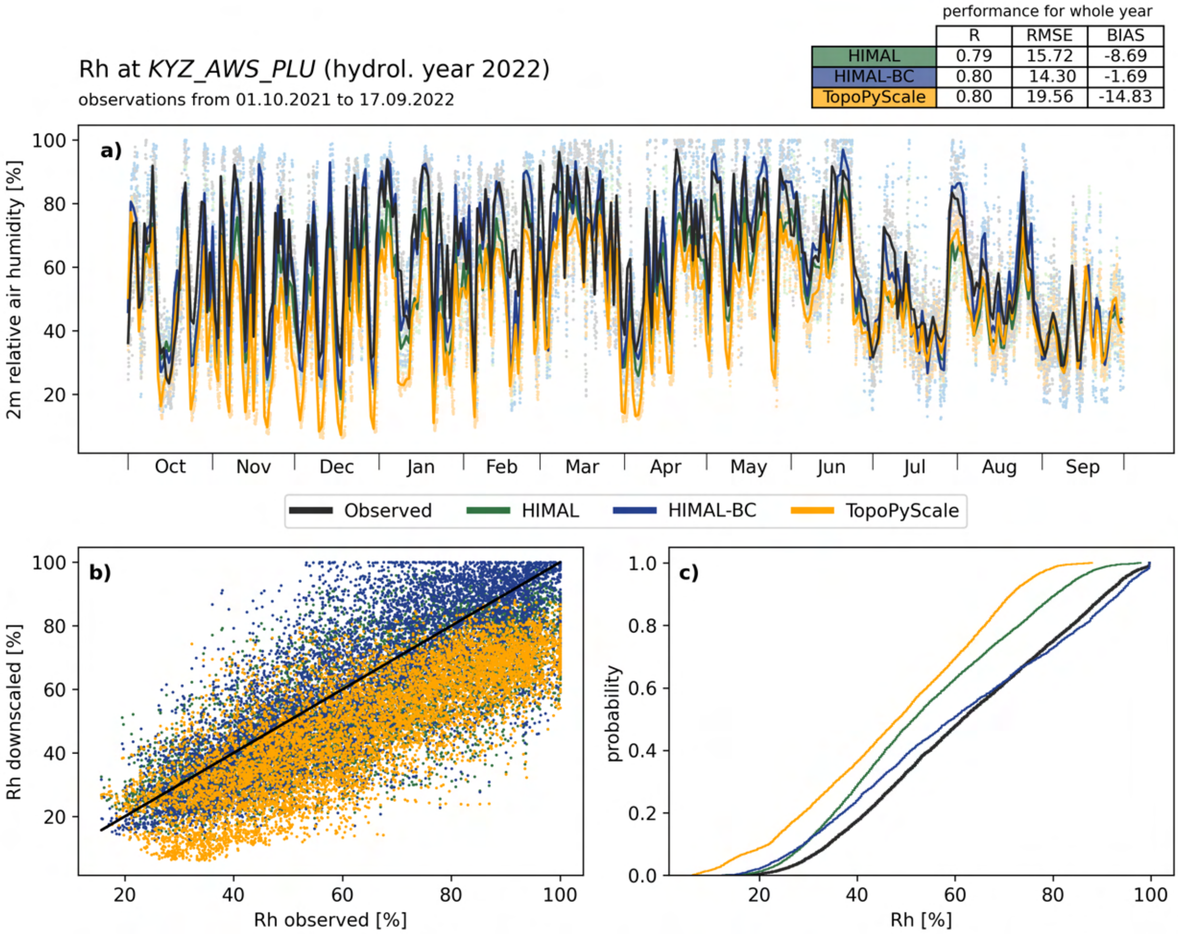

performance for whole year

	R	RMSE	BIAS
HIMAL	0.79	15.72	-8.69
HIMAL-BC	0.80	14.30	-1.69
TopoPyScale	0.80	19.56	-14.83

Figure C.8: Evaluation of downscaled near-surface relative humidity at KYZ_AWS_PLU.

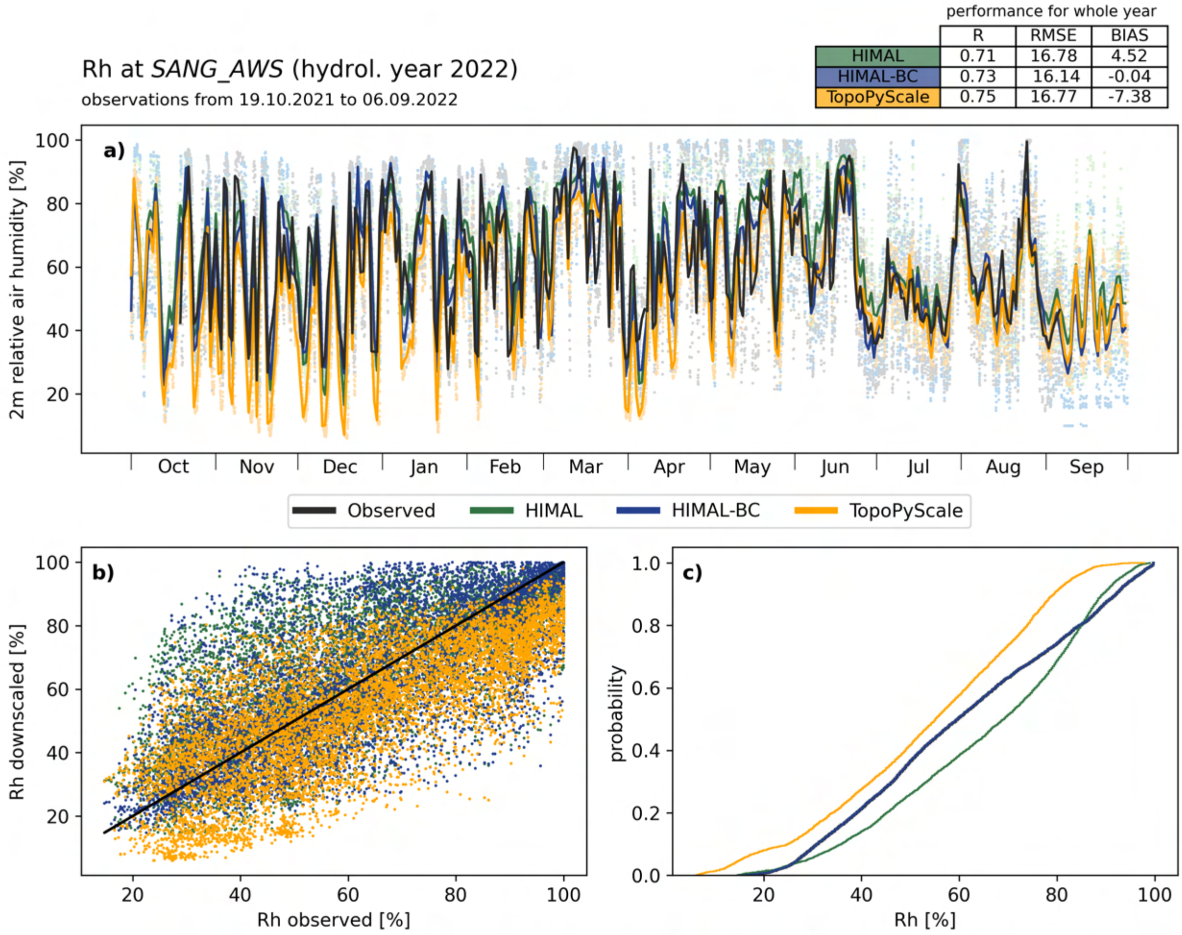

	R	RMSE	BIAS
HIMAL	0.71	16.78	4.52
HIMAL-BC	0.73	16.14	-0.04
TopoPyScale	0.75	16.77	-7.38

Figure C.9: Evaluation of downscaled near-surface relative humidity at SANG_AWS.

C.1.3 Precipitation

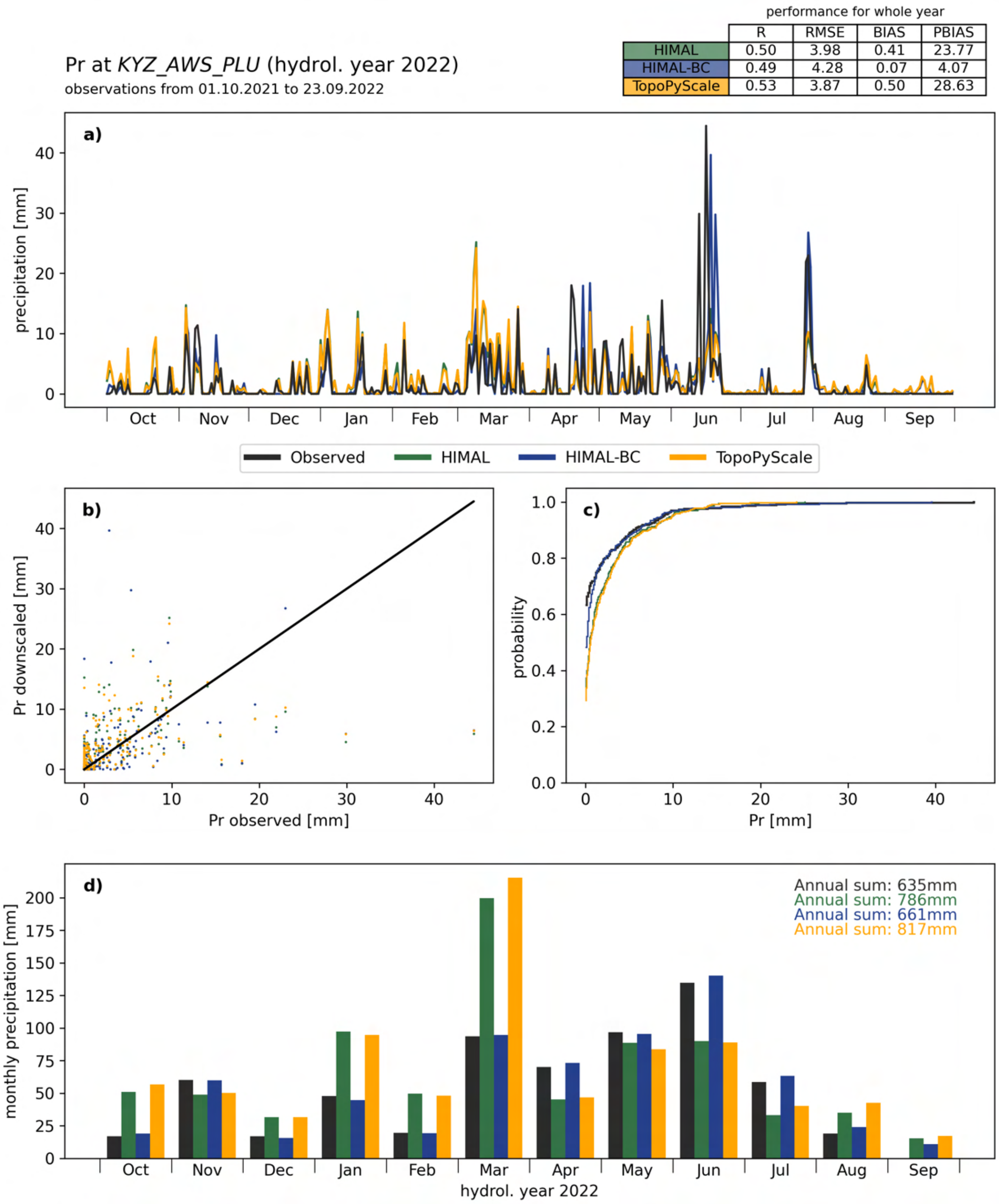

performance for whole year

	R	RMSE	BIAS	PBIAS
HIMAL	0.50	3.98	0.41	23.77
HIMAL-BC	0.49	4.28	0.07	4.07
TopoPyScale	0.53	3.87	0.50	28.63

Figure C.10: Evaluation of downscaled precipitation at KYZ_AWS_PLU. With d) additionally showing the monthly precipitation sums.

C.1.4 Surface air pressure

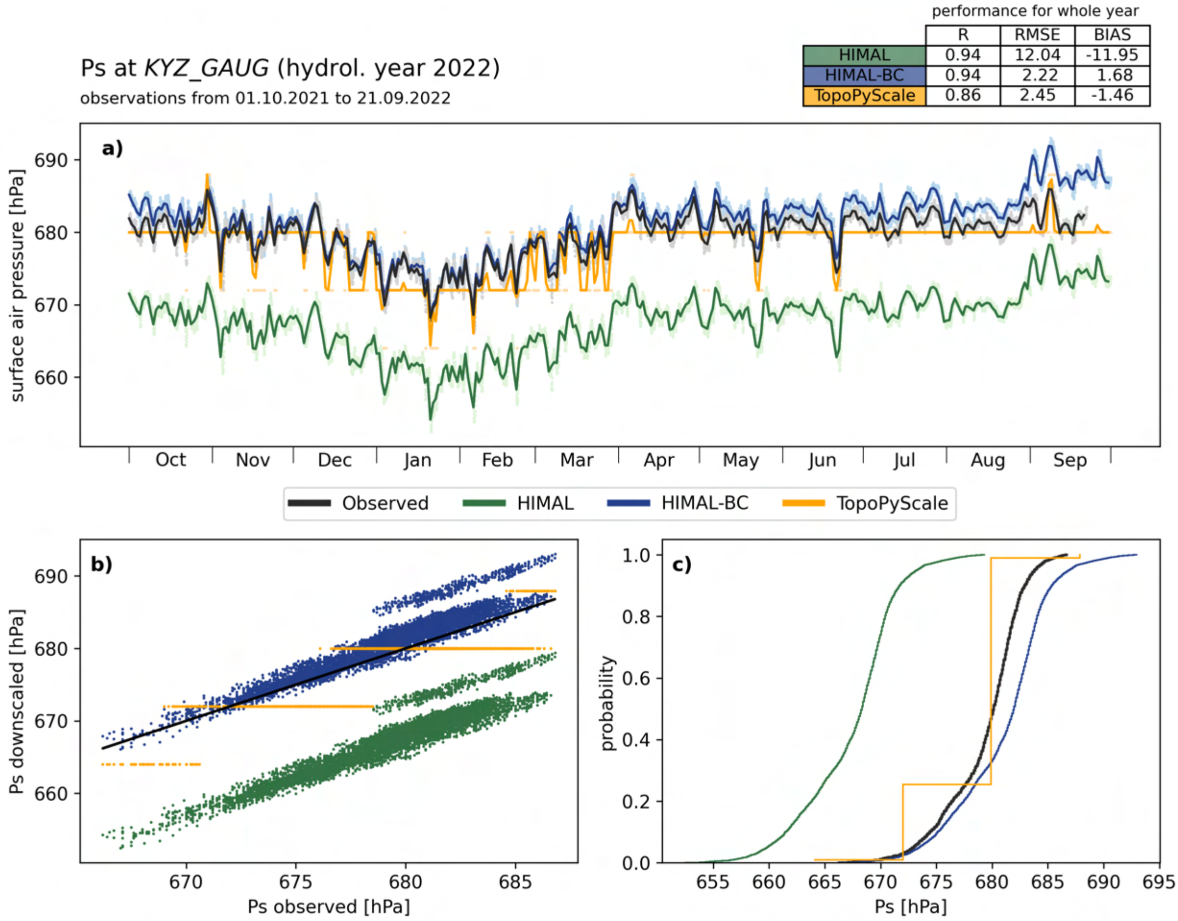

performance for whole year

	R	RMSE	BIAS
HIMAL	0.94	12.04	-11.95
HIMAL-BC	0.94	2.22	1.68
TopoPyScale	0.86	2.45	-1.46

Figure C.11: Evaluation of downscaled surface air pressure at KYZ_GAUG.

C.1.5 Incoming shortwave radiation

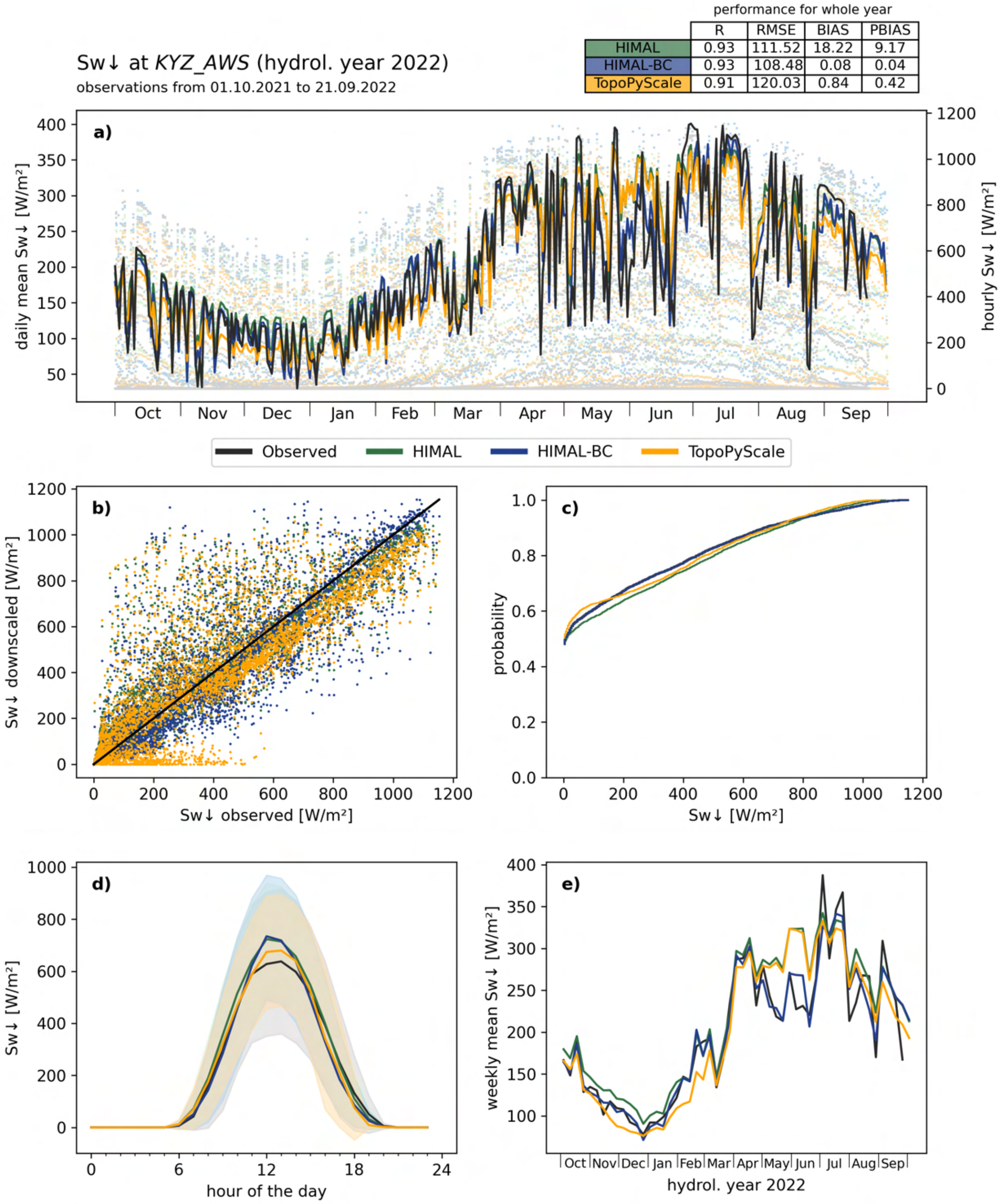

performance for whole year

	R	RMSE	BIAS	PBIAS
HIMAL	0.93	111.52	18.22	9.17
HIMAL-BC	0.93	108.48	0.08	0.04
TopoPyScale	0.91	120.03	0.84	0.42

Figure C.12: Evaluation of downscaled incoming shortwave radiation at KYZ_AWS. With d) additionally indicating the average diurnal cycle (standard deviation as shading) and e) showing the weekly mean radiation.

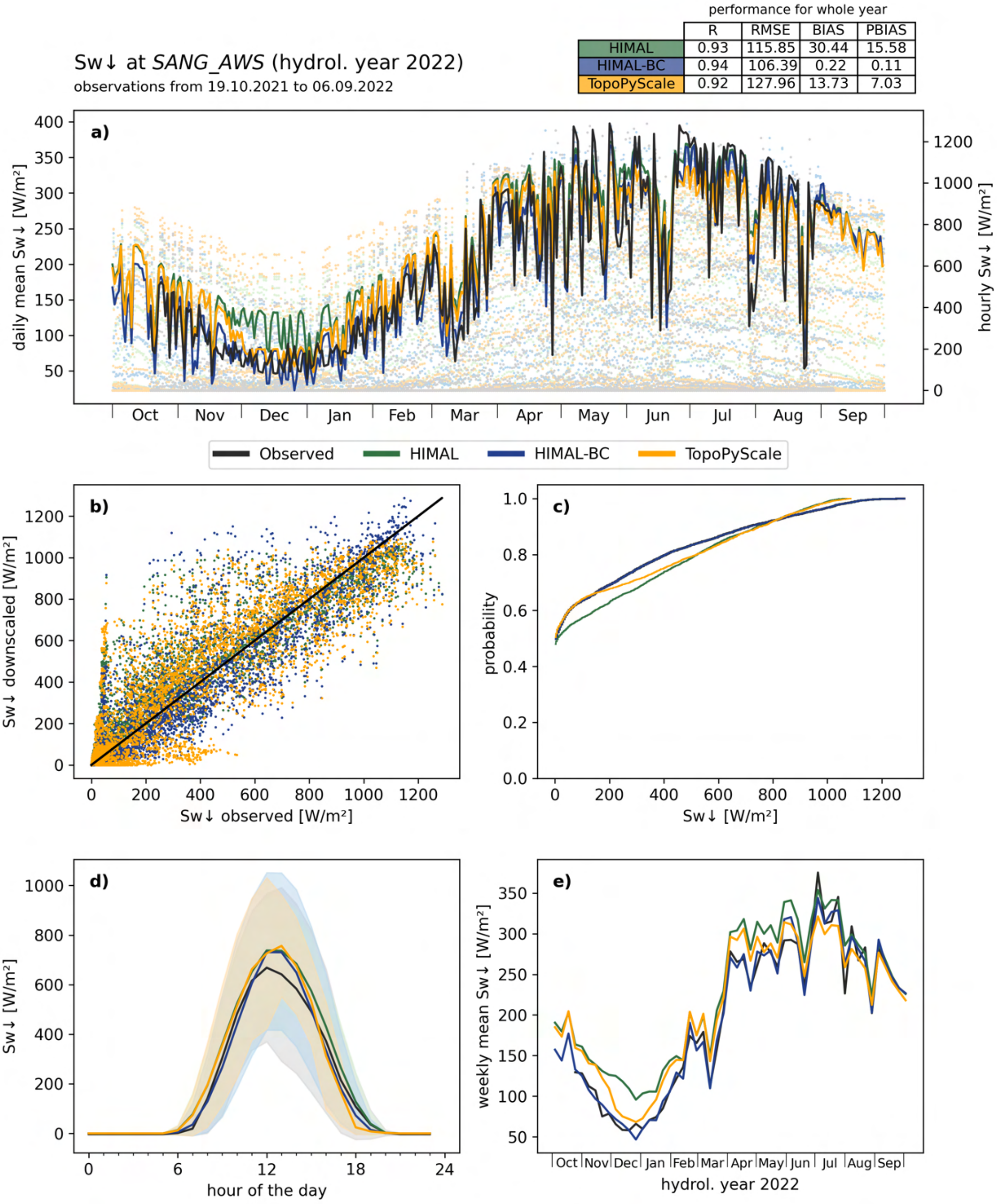

performance for whole year

	R	RMSE	BIAS	PBIAS
HIMAL	0.93	115.85	30.44	15.58
HIMAL-BC	0.94	106.39	0.22	0.11
TopoPyScale	0.92	127.96	13.73	7.03

Figure C.13: Evaluation of downscaled incoming shortwave radiation at SANG_AWS. With d) additionally indicating the average diurnal cycle (standard deviation as shading) and e) showing the weekly mean radiation.

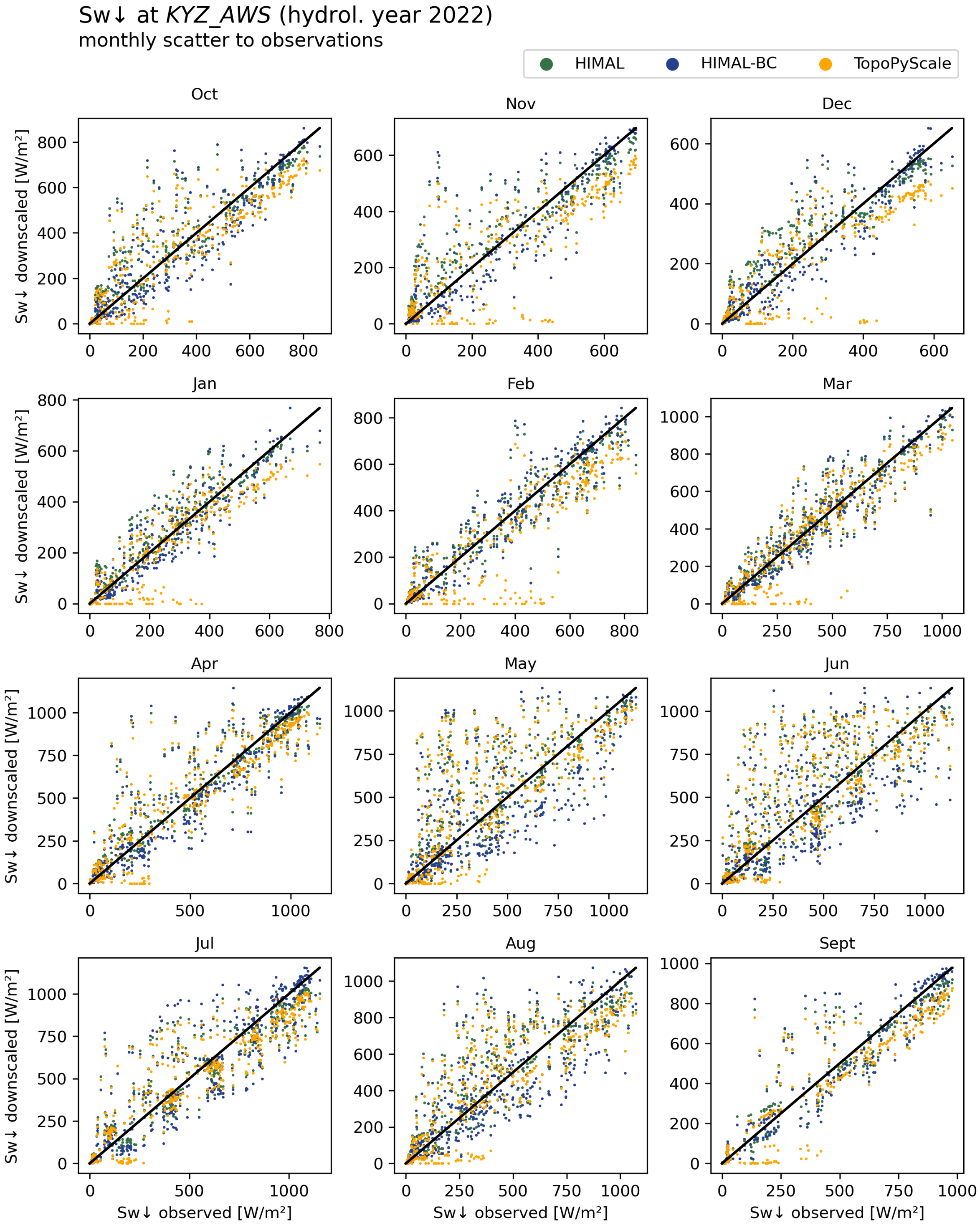

Figure C.14: Supporting figure for evaluating downscaled incoming shortwave radiation: scatter of downscaled values to observations grouped by month at KYZ_AWS.

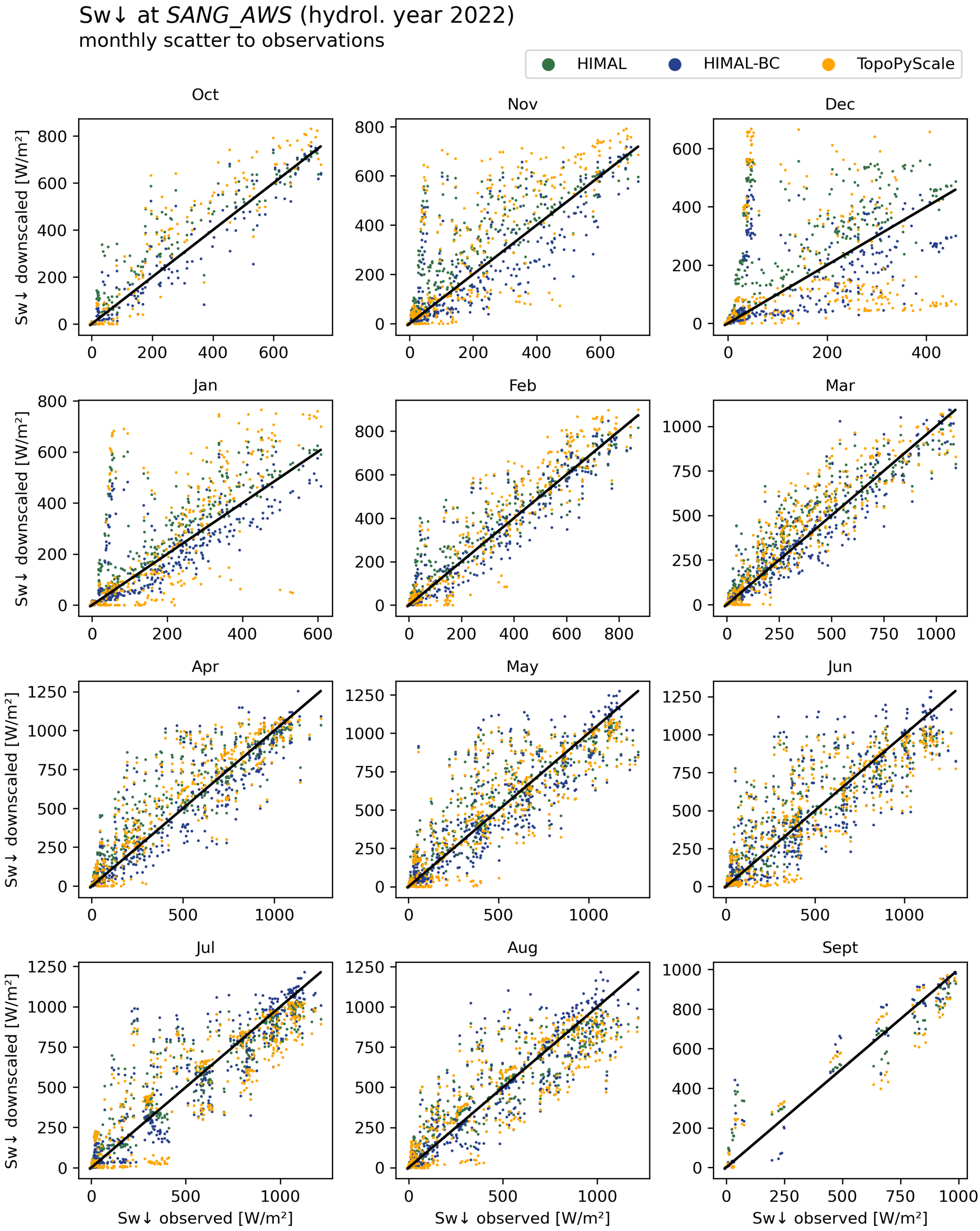

Figure C.15: Supporting figure for evaluating downscaled incoming shortwave radiation: scatter of downscaled values to observations grouped by month at SANG_AWS

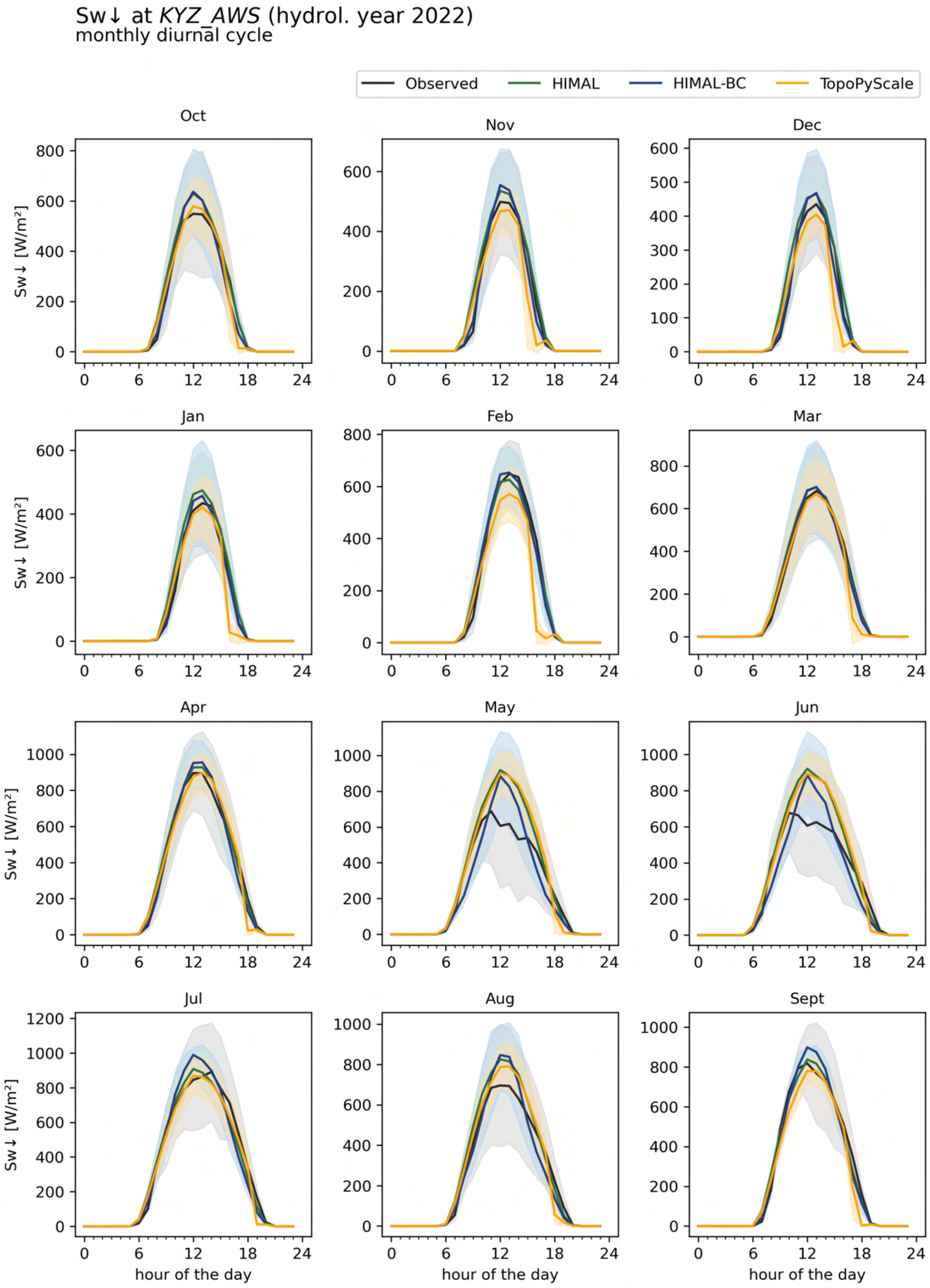

Figure C.16: Supporting figure for evaluating downscaled incoming shortwave radiation: monthly mean diurnal cycle of downscaled values and observations at KYZ_AWS.

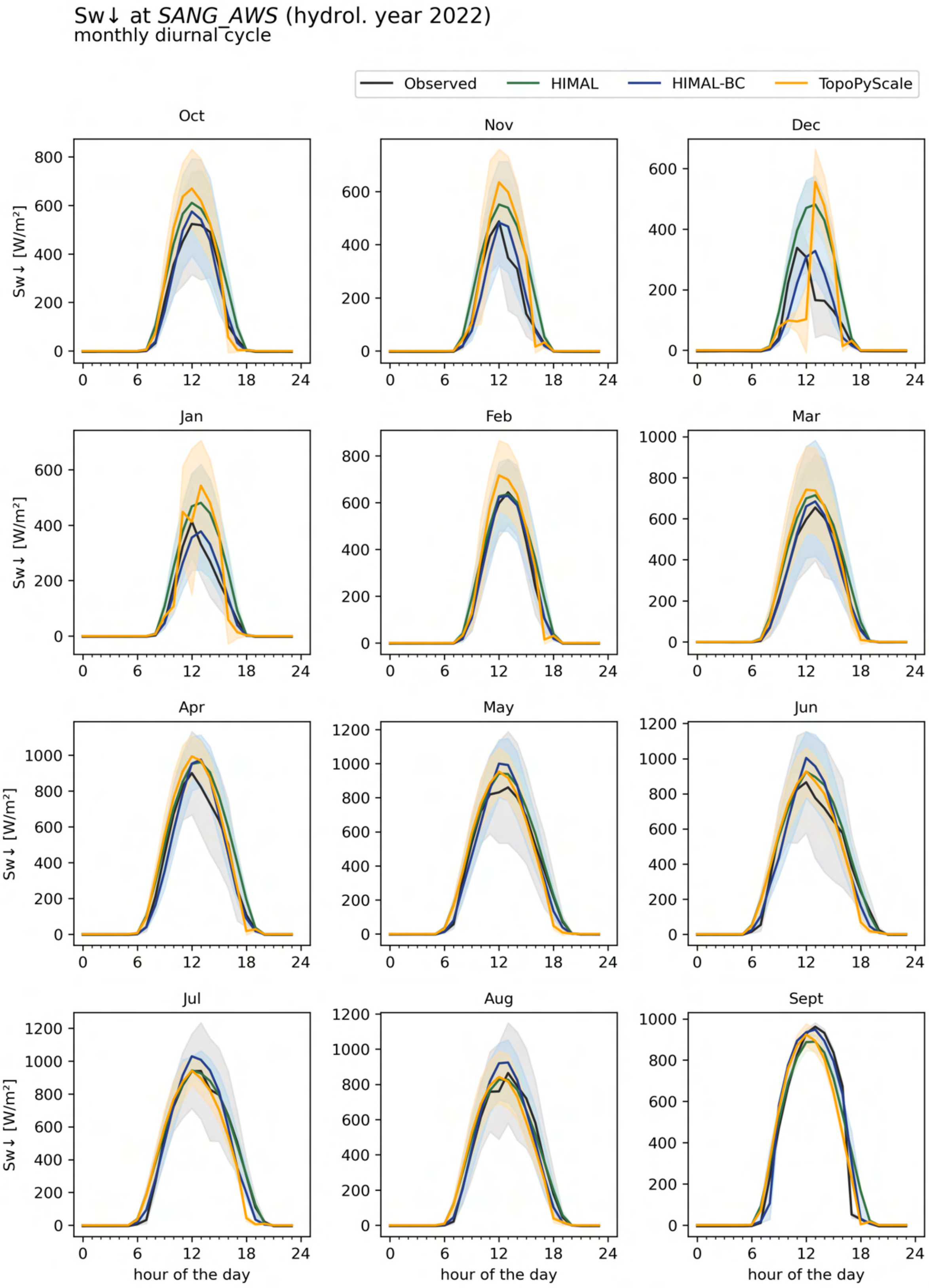

Figure C.17: Supporting figure for evaluating downscaled incoming shortwave radiation: monthly mean diurnal cycle of downscaled values and observations at SANG_AWS

C.1.6 Incoming longwave radiation

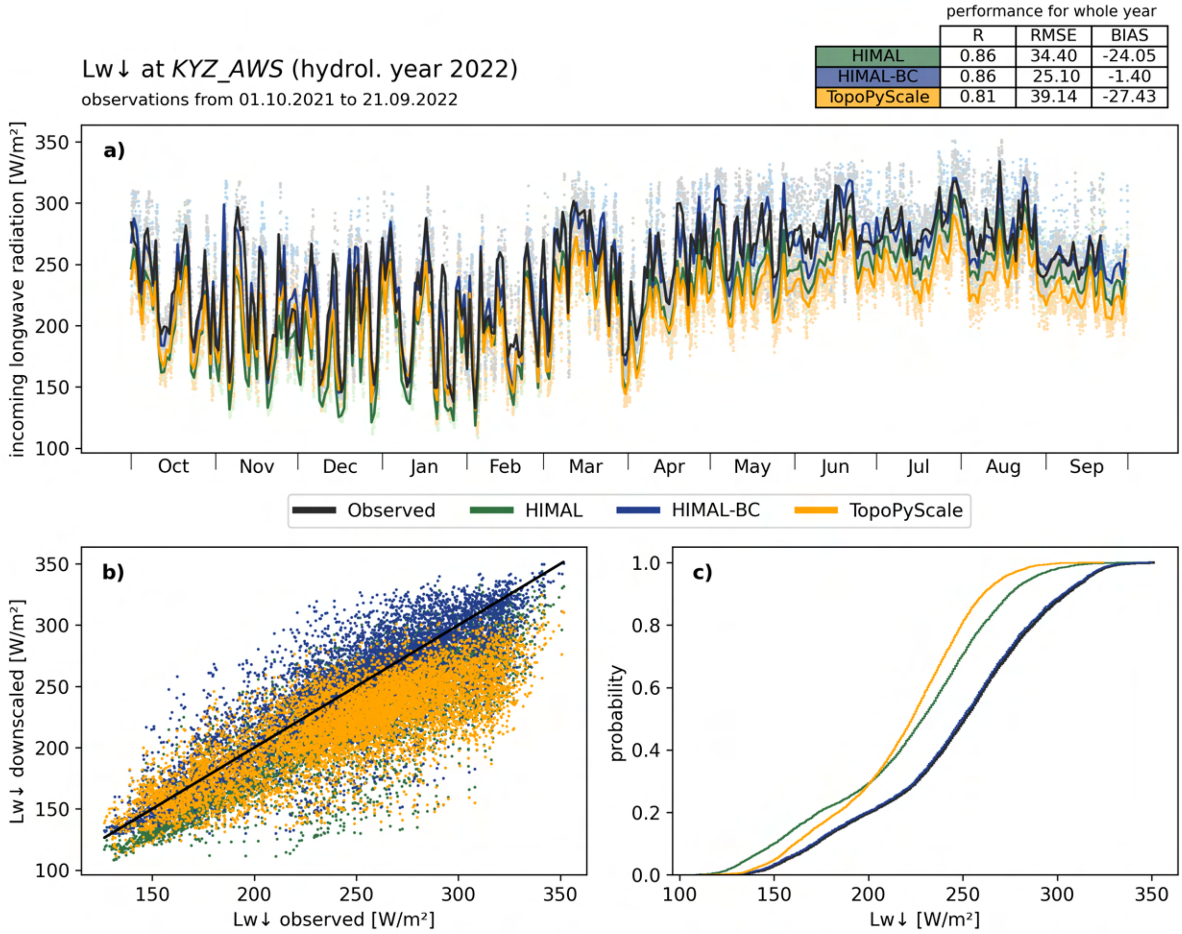

	R	RMSE	BIAS
HIMAL	0.86	34.40	-24.05
HIMAL-BC	0.86	25.10	-1.40
TopoPyScale	0.81	39.14	-27.43

Figure C.18: Evaluation of downscaled incoming longwave radiation at KYZ_AWS.

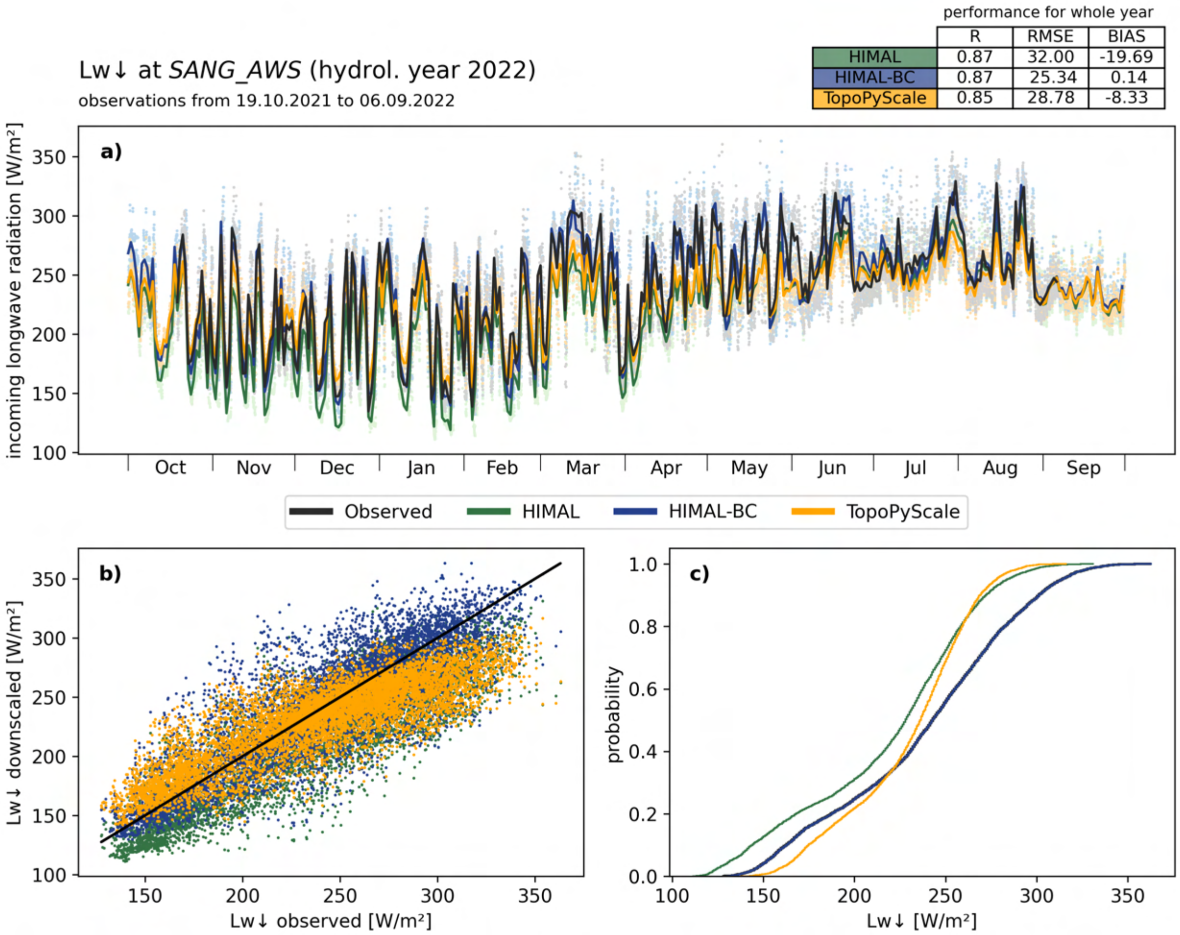

	R	RMSE	BIAS
HIMAL	0.87	32.00	-19.69
HIMAL-BC	0.87	25.34	0.14
TopoPyScale	0.85	28.78	-8.33

Figure C.19: Evaluation of downscaled incoming longwave radiation at SANG_AWS.

C.1.7 Wind speed

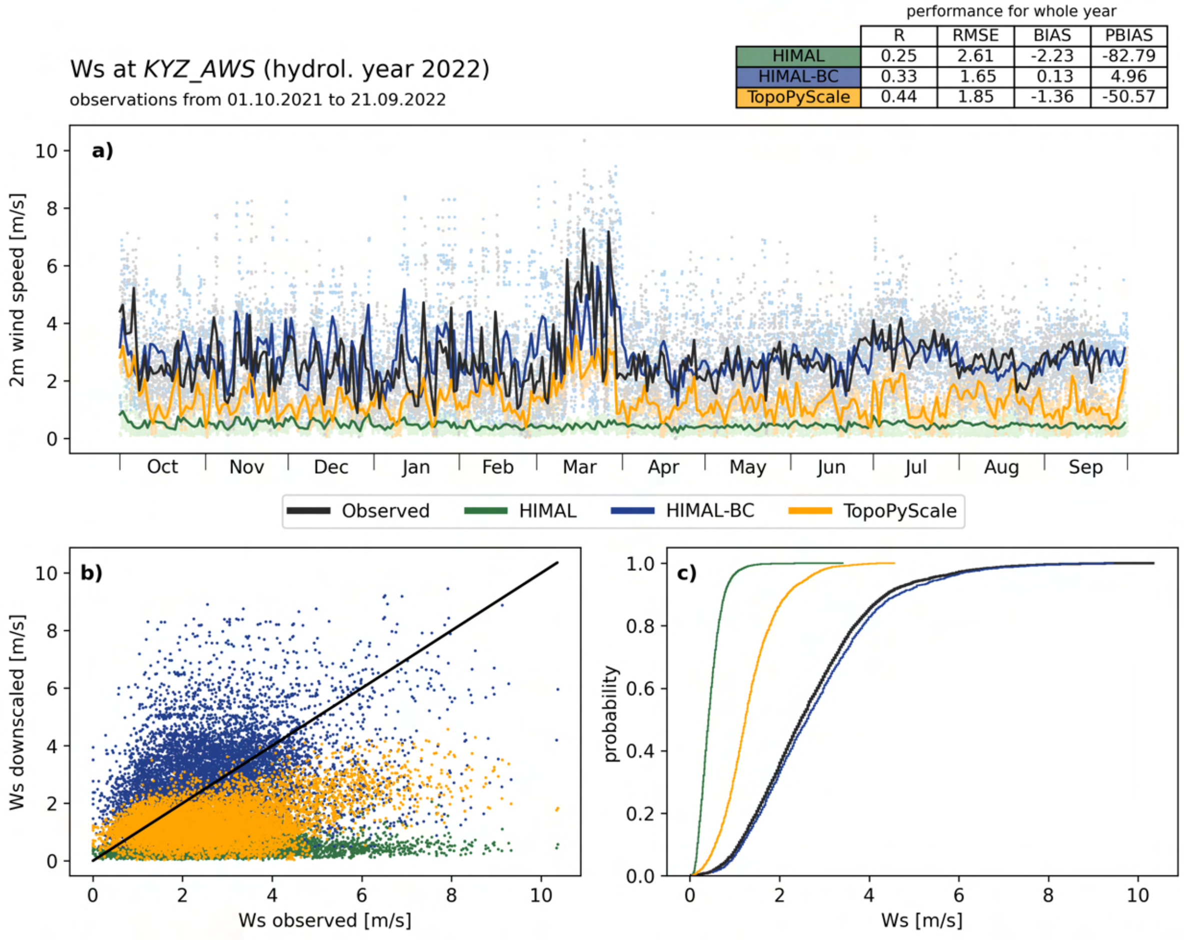

performance for whole year

	R	RMSE	BIAS	PBIAS
HIMAL	0.25	2.61	-2.23	-82.79
HIMAL-BC	0.33	1.65	0.13	4.96
TopoPyScale	0.44	1.85	-1.36	-50.57

Figure C.20: Evaluation of downscaled wind speed at KYZ_AWS.

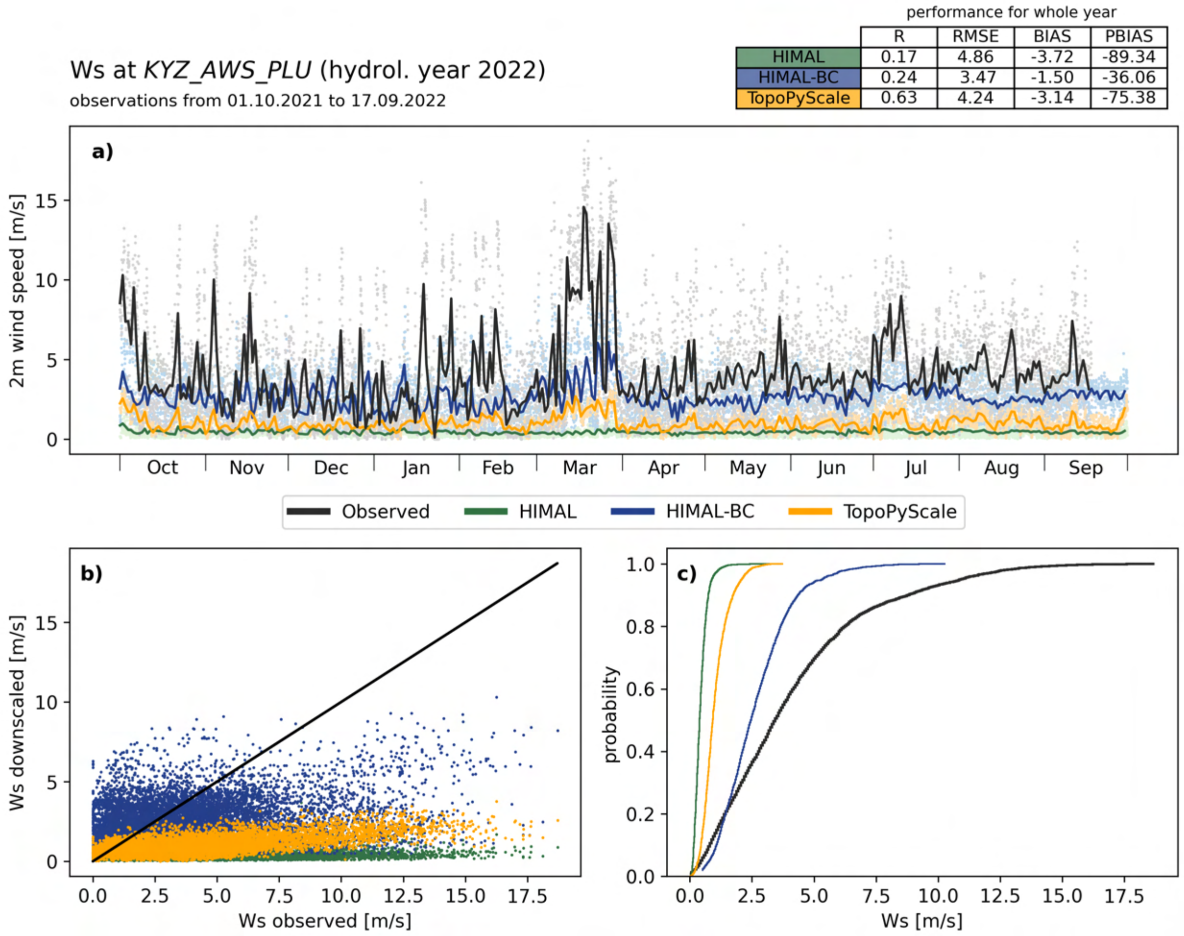

performance for whole year

	R	RMSE	BIAS	PBIAS
HIMAL	0.17	4.86	-3.72	-89.34
HIMAL-BC	0.24	3.47	-1.50	-36.06
TopoPyScale	0.63	4.24	-3.14	-75.38

Figure C.21: Evaluation of downscaled wind speed at KYZ_AWS_PLU.

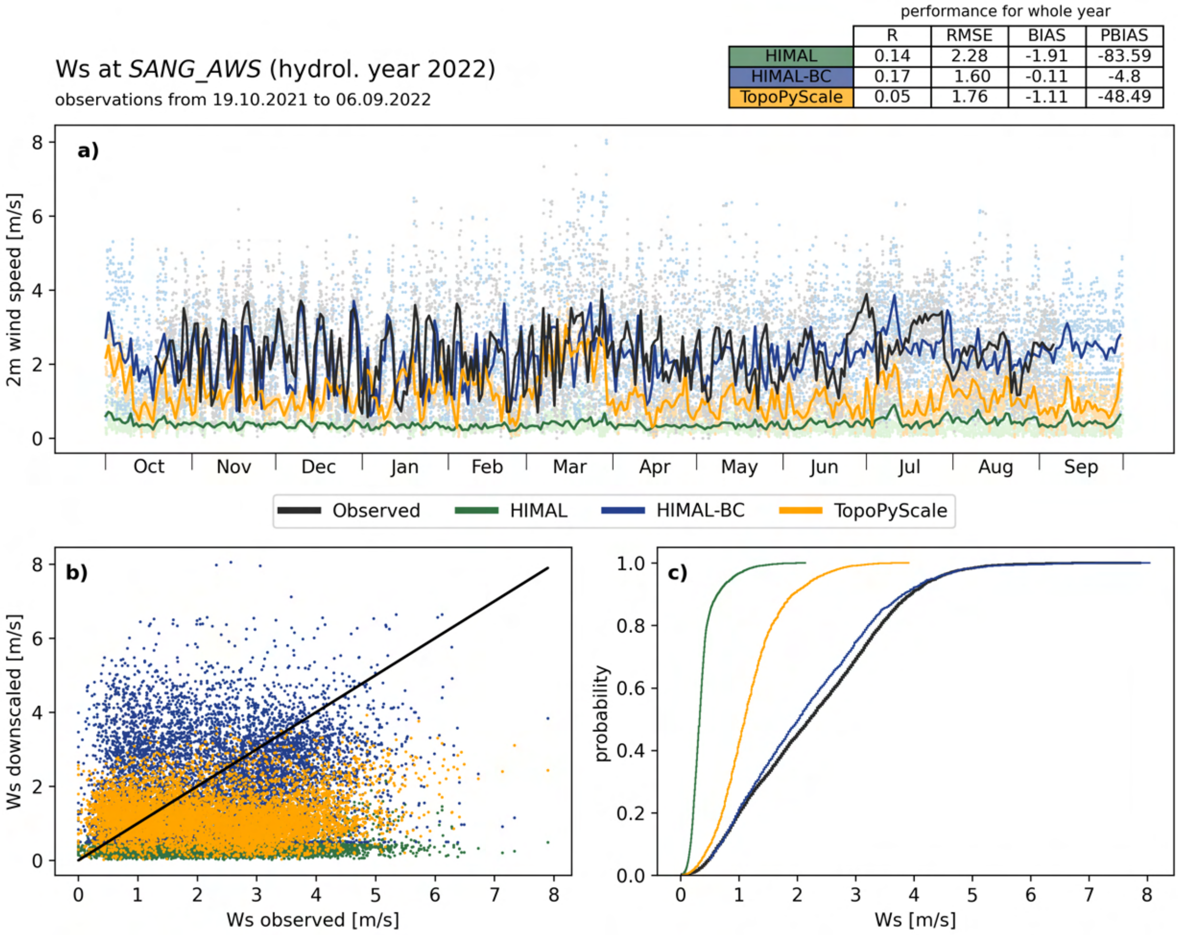

performance for whole year

	R	RMSE	BIAS	PBIAS
HIMAL	0.14	2.28	-1.91	-83.59
HIMAL-BC	0.17	1.60	-0.11	-4.8
TopoPyScale	0.05	1.76	-1.11	-48.49

Figure C.22: Evaluation of downscaled wind speed at SANG_AWS.

C.2 Evaluation of T&C model outputs at plot-scale

C.2.1 Ts

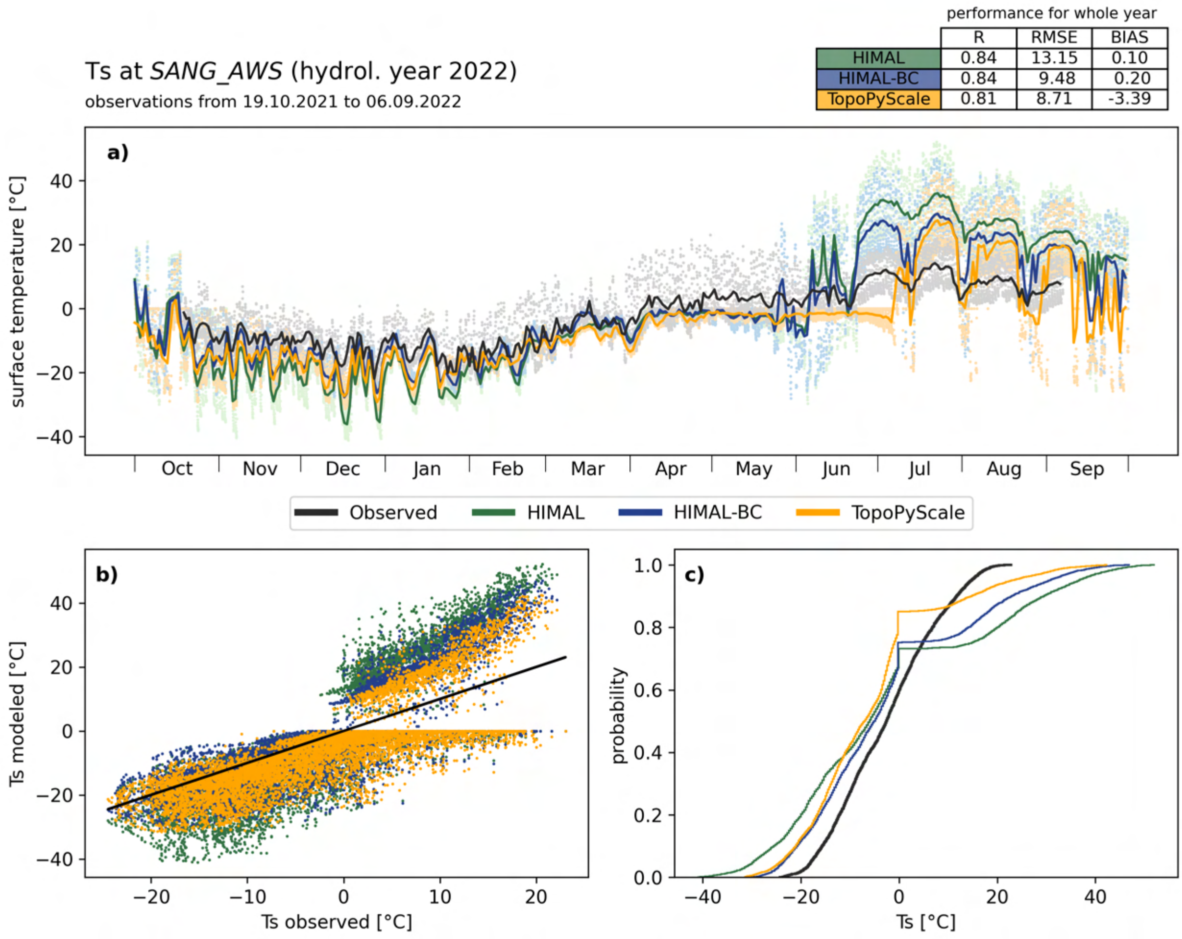

	R	RMSE	BIAS
HIMAL	0.84	13.15	0.10
HIMAL-BC	0.84	9.48	0.20
TopoPyScale	0.81	8.71	-3.39

Figure C.23: Evaluation of simulated surface temperature at SANG_AWS.

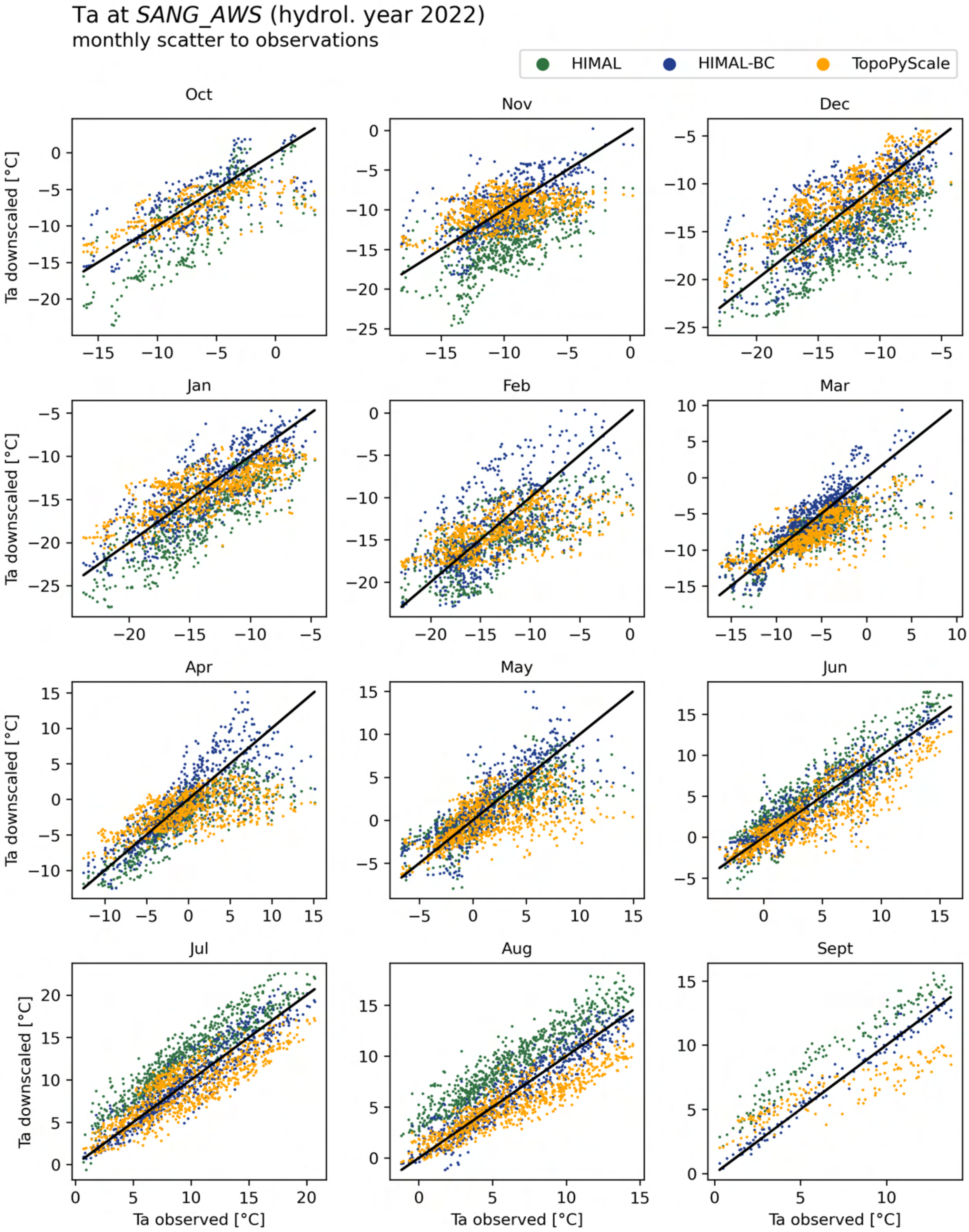

Figure C.24: Supporting figure for evaluating simulated surface temperature: scatter of downscaled to observed 2m air temperature grouped by month at SANG_AWS.

C.2.2 Ts$_{Aug}$

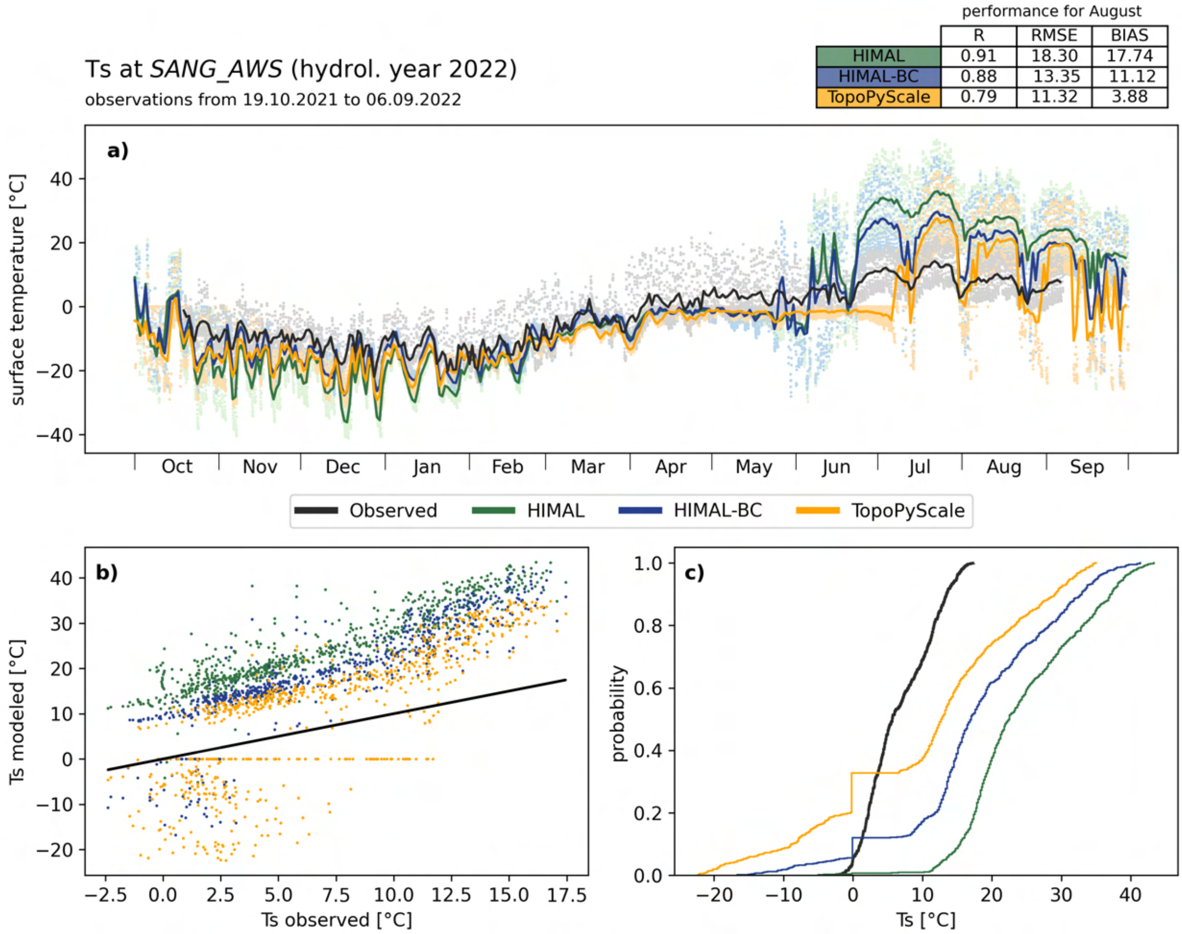
performance for August

	R	RMSE	BIAS
HIMAL	0.91	18.30	17.74
HIMAL-BC	0.88	13.35	11.12
TopoPyScale	0.79	11.32	3.88

Figure C.25: Evaluation of simulated surface temperature in August at SANG_AWS.

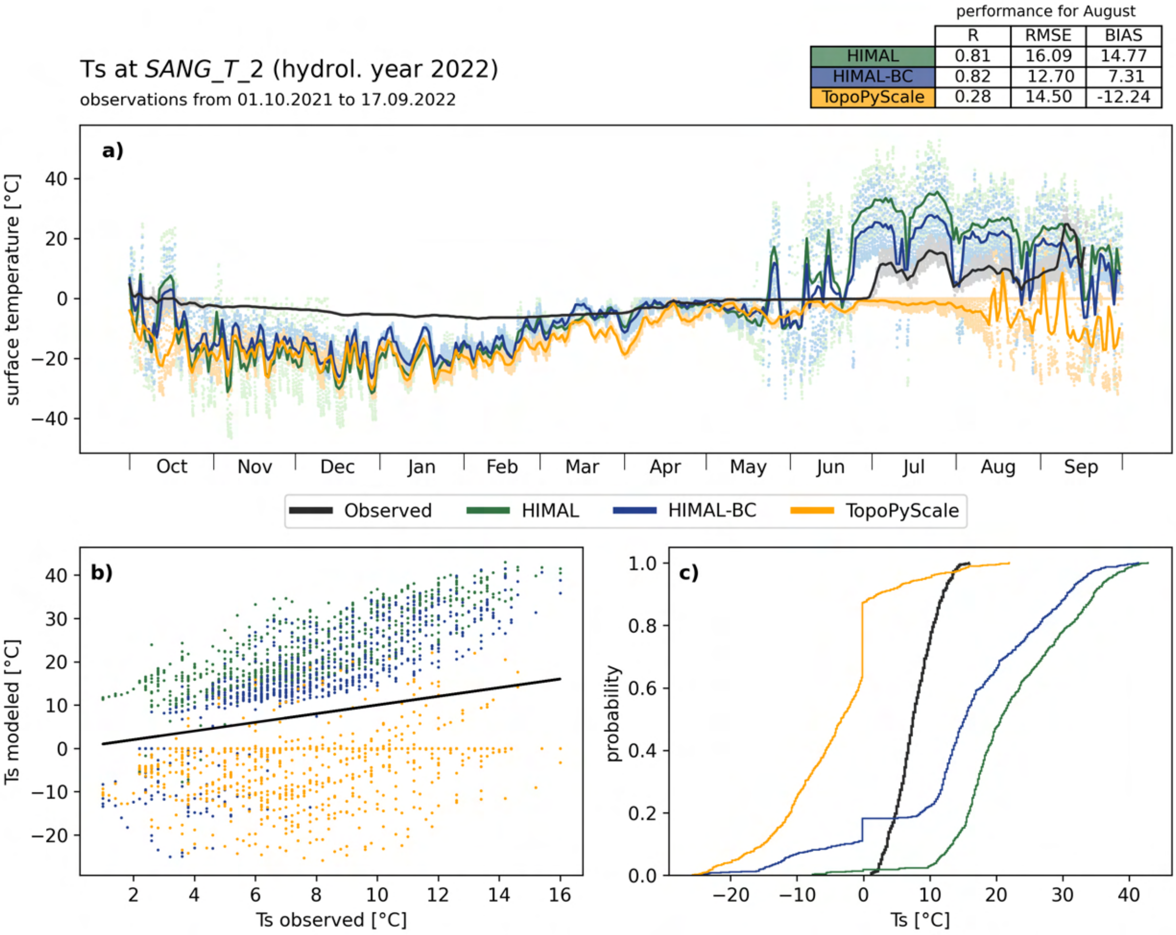

performance for August

	R	RMSE	BIAS
HIMAL	0.81	16.09	14.77
HIMAL-BC	0.82	12.70	7.31
TopoPyScale	0.28	14.50	-12.24

Figure C.26: Evaluation of simulated surface temperature in August at SANG_T_2.

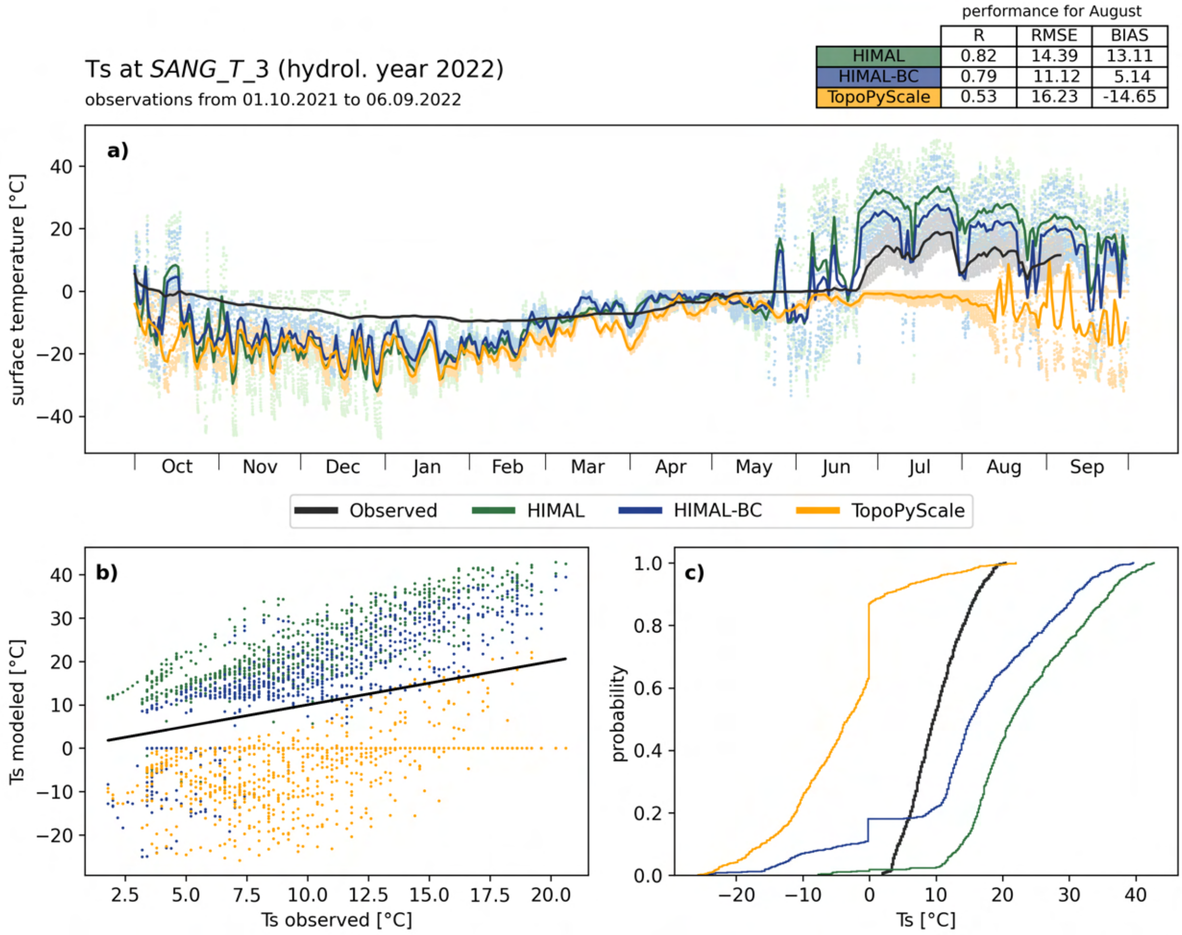

performance for August

	R	RMSE	BIAS
HIMAL	0.82	14.39	13.11
HIMAL-BC	0.79	11.12	5.14
TopoPyScale	0.53	16.23	-14.65

Figure C.27: Evaluation of simulated surface temperature in August at SANG_T_3.

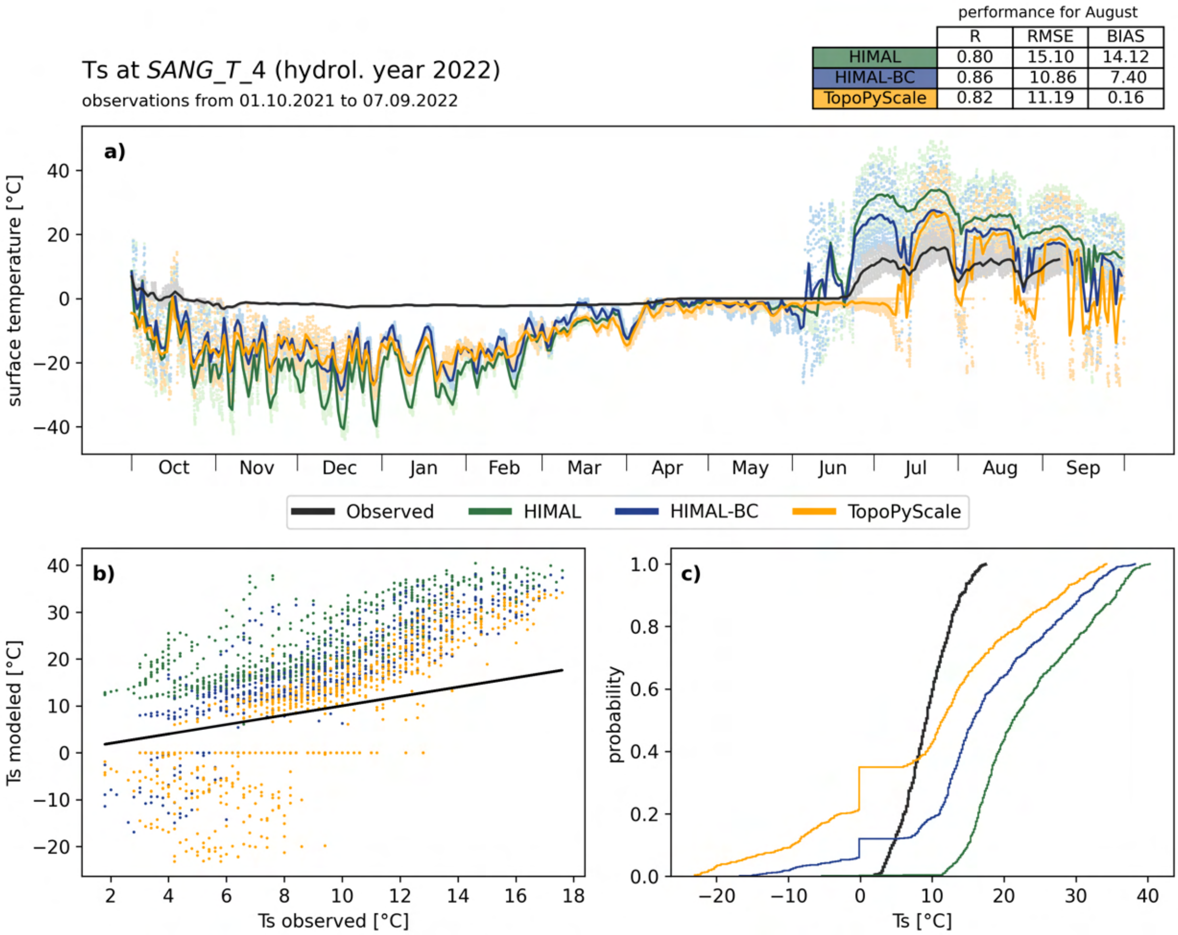

performance for August

	R	RMSE	BIAS
HIMAL	0.80	15.10	14.12
HIMAL-BC	0.86	10.86	7.40
TopoPyScale	0.82	11.19	0.16

Figure C.28: Evaluation of simulated surface temperature in August at SANG_T_4.

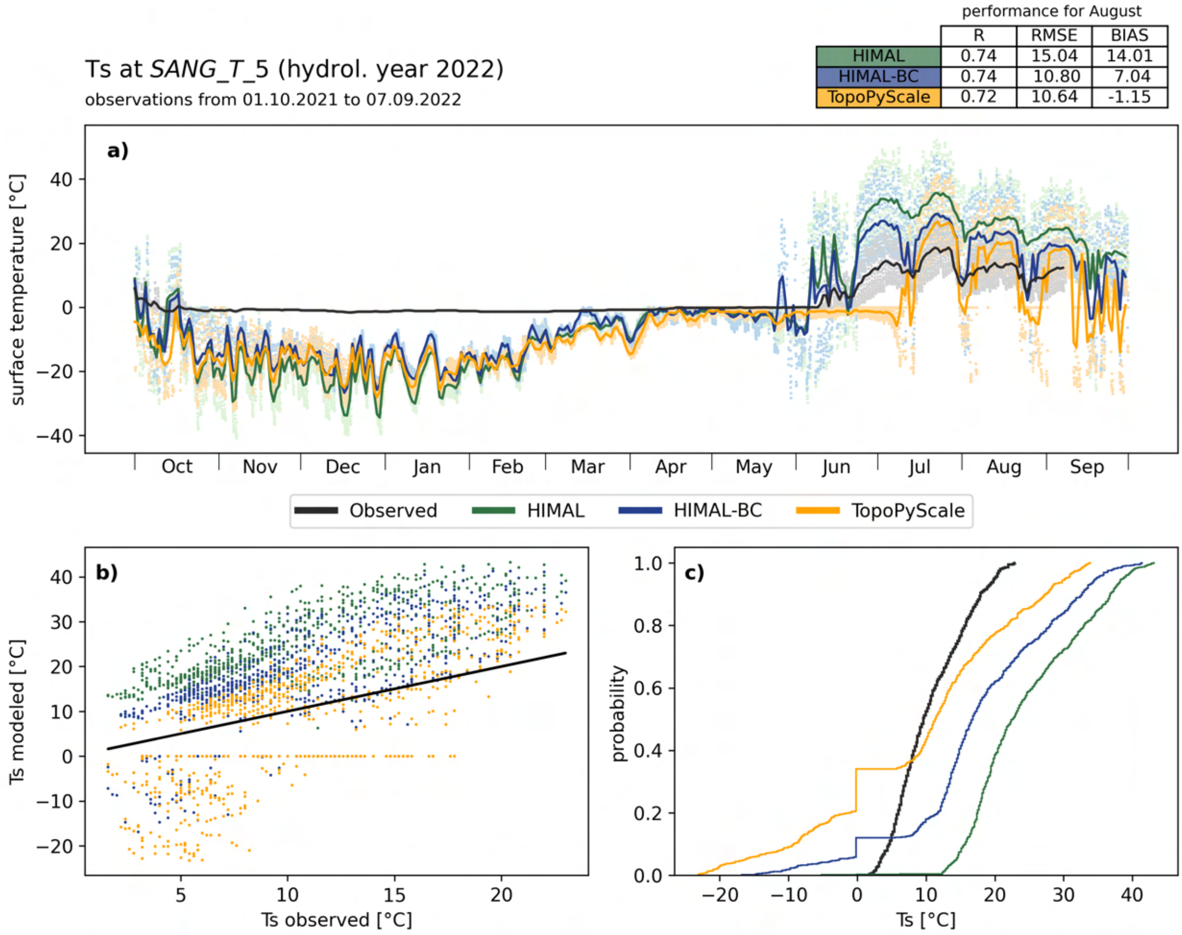

performance for August

	R	RMSE	BIAS
HIMAL	0.74	15.04	14.01
HIMAL-BC	0.74	10.80	7.04
TopoPyScale	0.72	10.64	-1.15

Figure C.29: Evaluation of simulated surface temperature in August at SANG_T_5.

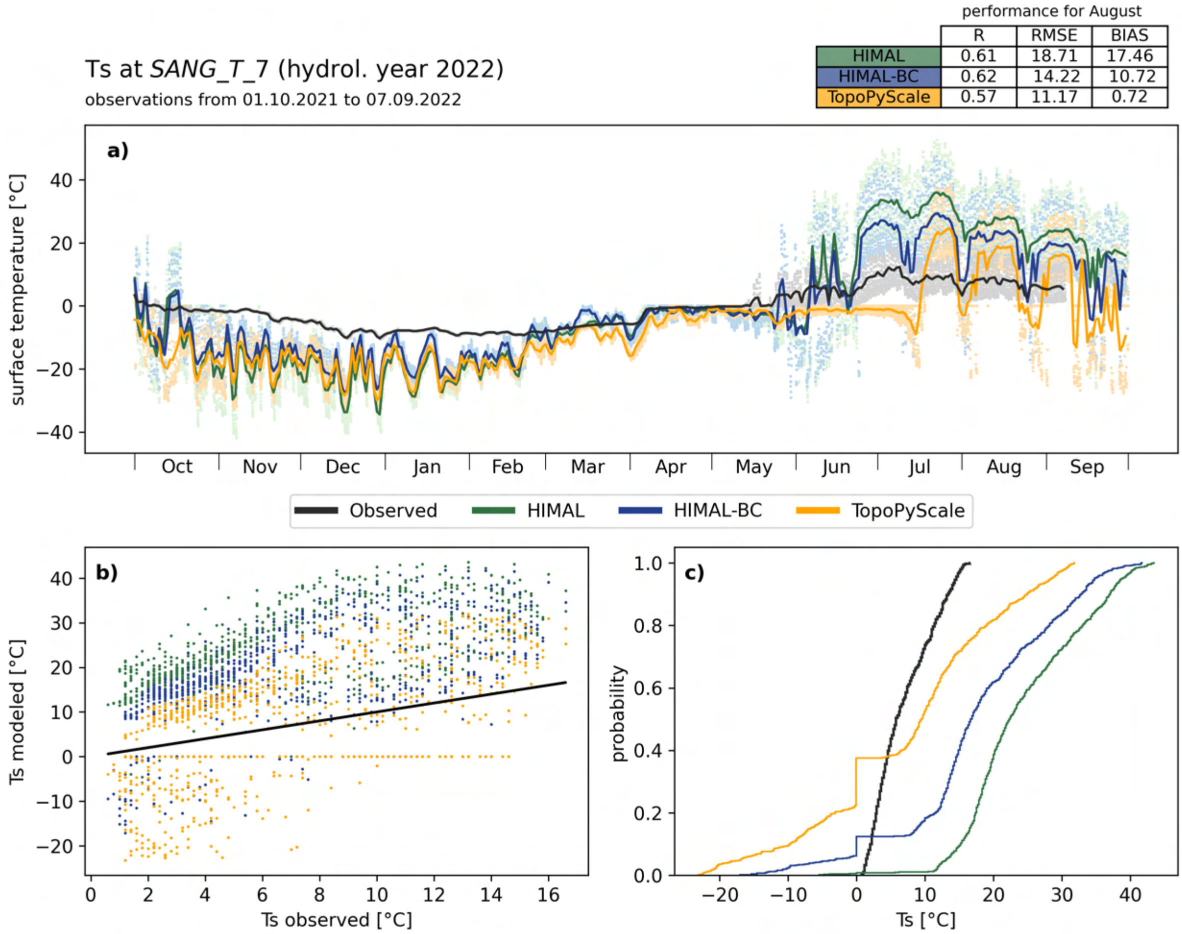

performance for August

	R	RMSE	BIAS
HIMAL	0.61	18.71	17.46
HIMAL-BC	0.62	14.22	10.72
TopoPyScale	0.57	11.17	0.72

Figure C.30: Evaluation of simulated surface temperature in August at SANG_T_7.

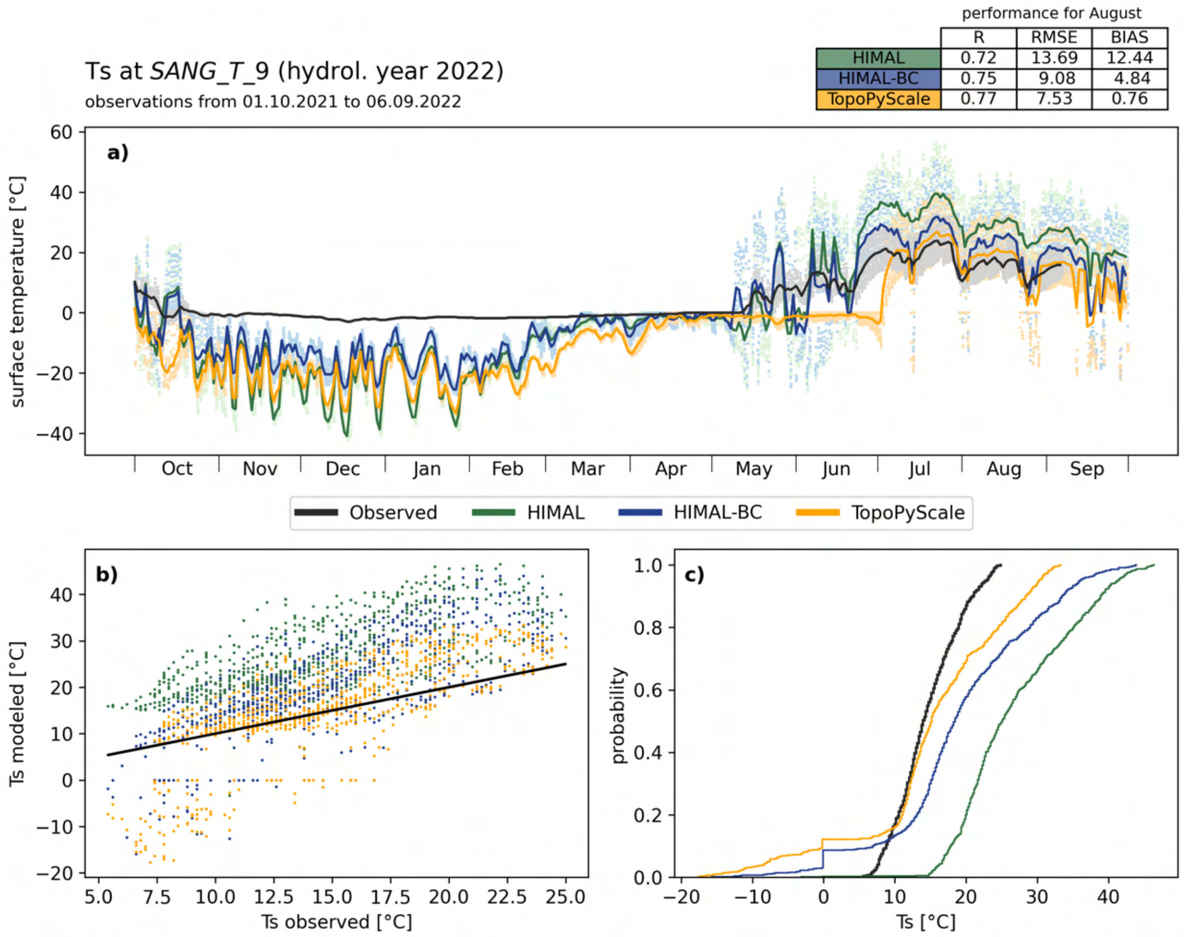

performance for August

	R	RMSE	BIAS
HIMAL	0.72	13.69	12.44
HIMAL-BC	0.75	9.08	4.84
TopoPyScale	0.77	7.53	0.76

Figure C.31: Evaluation of simulated surface temperature in August at SANG_T_9.

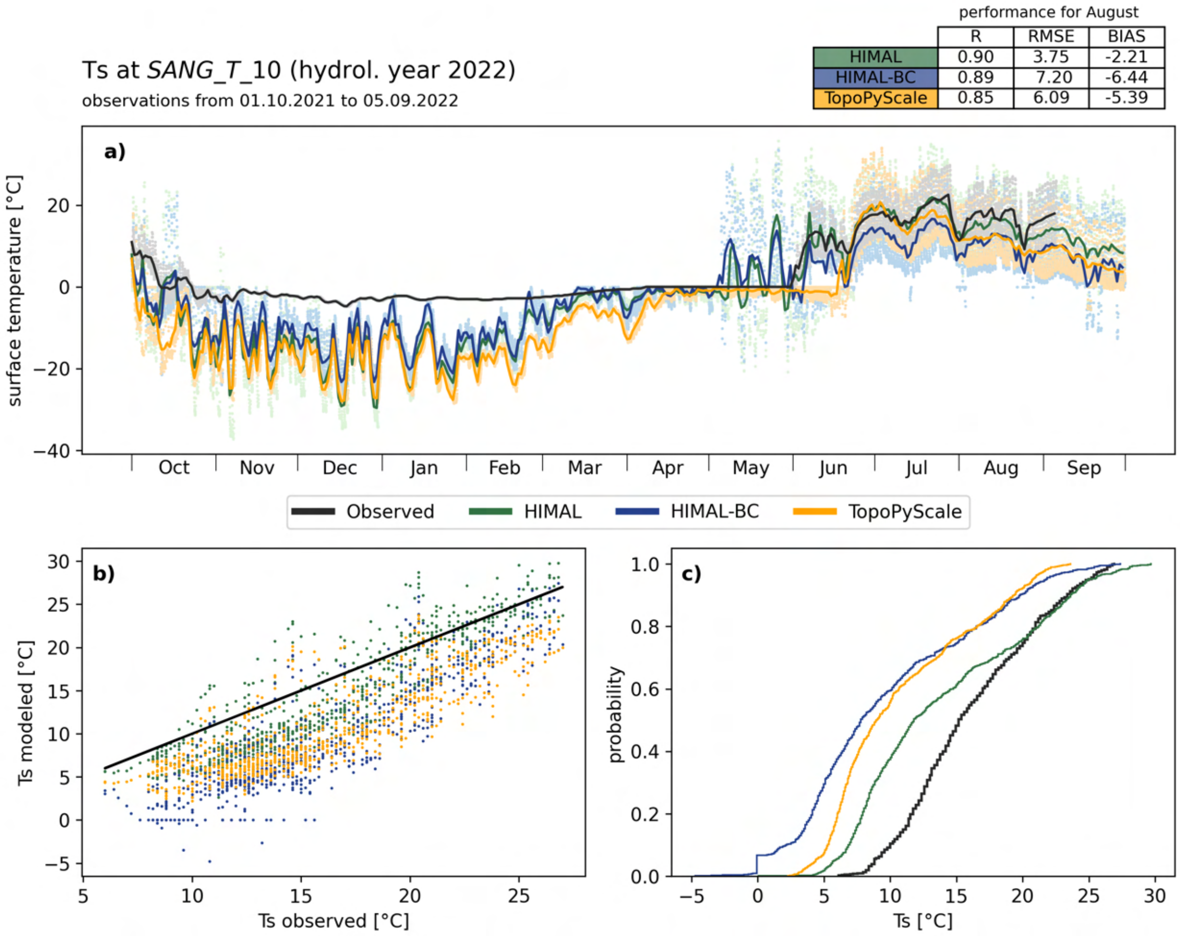

Ts at *SANG_T*_10 (hydrol. year 2022)

observations from 01.10.2021 to 05.09.2022

performance for August

	R	RMSE	BIAS
HIMAL	0.90	3.75	-2.21
HIMAL-BC	0.89	7.20	-6.44
TopoPyScale	0.85	6.09	-5.39

Figure C.32: Evaluation of simulated surface temperature in August at SANG_T_10.

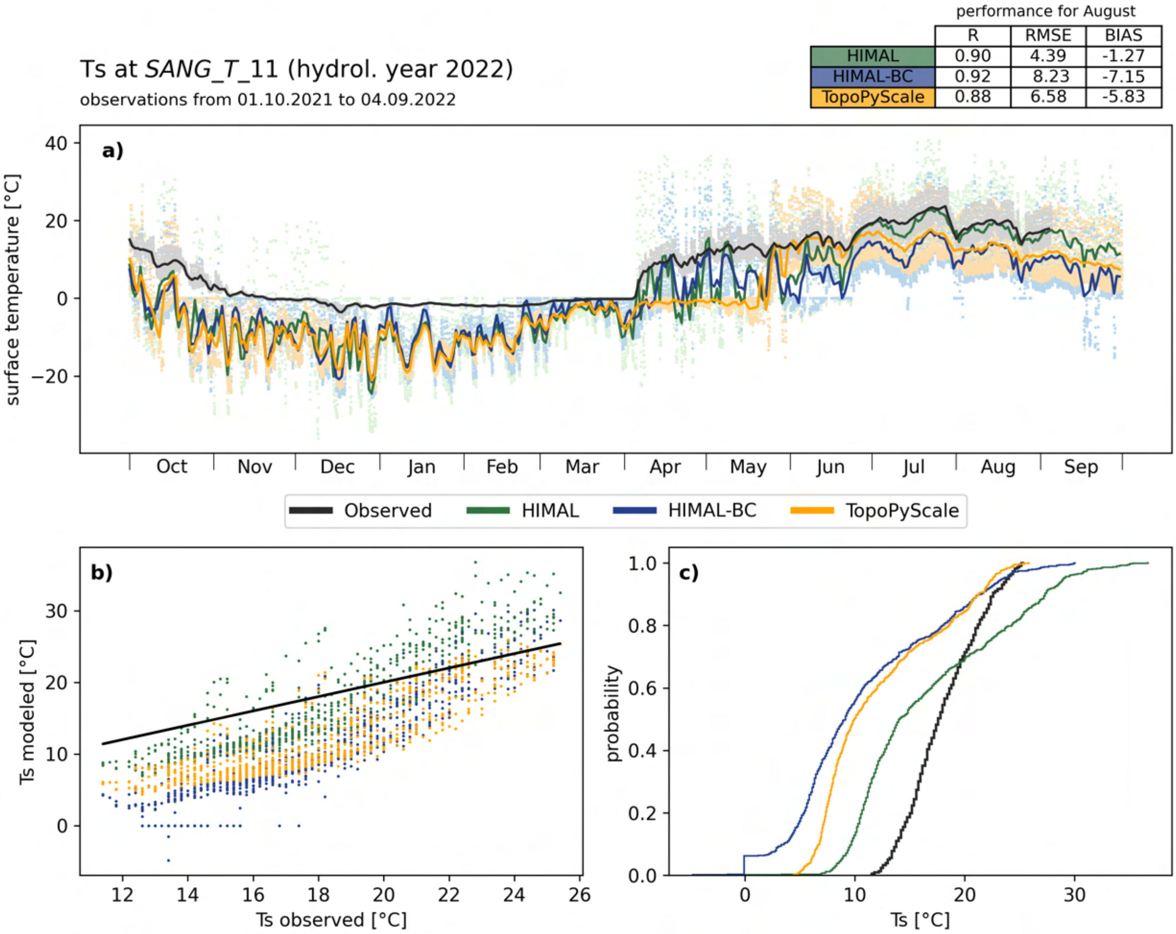

performance for August

	R	RMSE	BIAS
HIMAL	0.90	4.39	-1.27
HIMAL-BC	0.92	8.23	-7.15
TopoPyScale	0.88	6.58	-5.83

Figure C.33: Evaluation of simulated surface temperature in August at SANG_T_11.

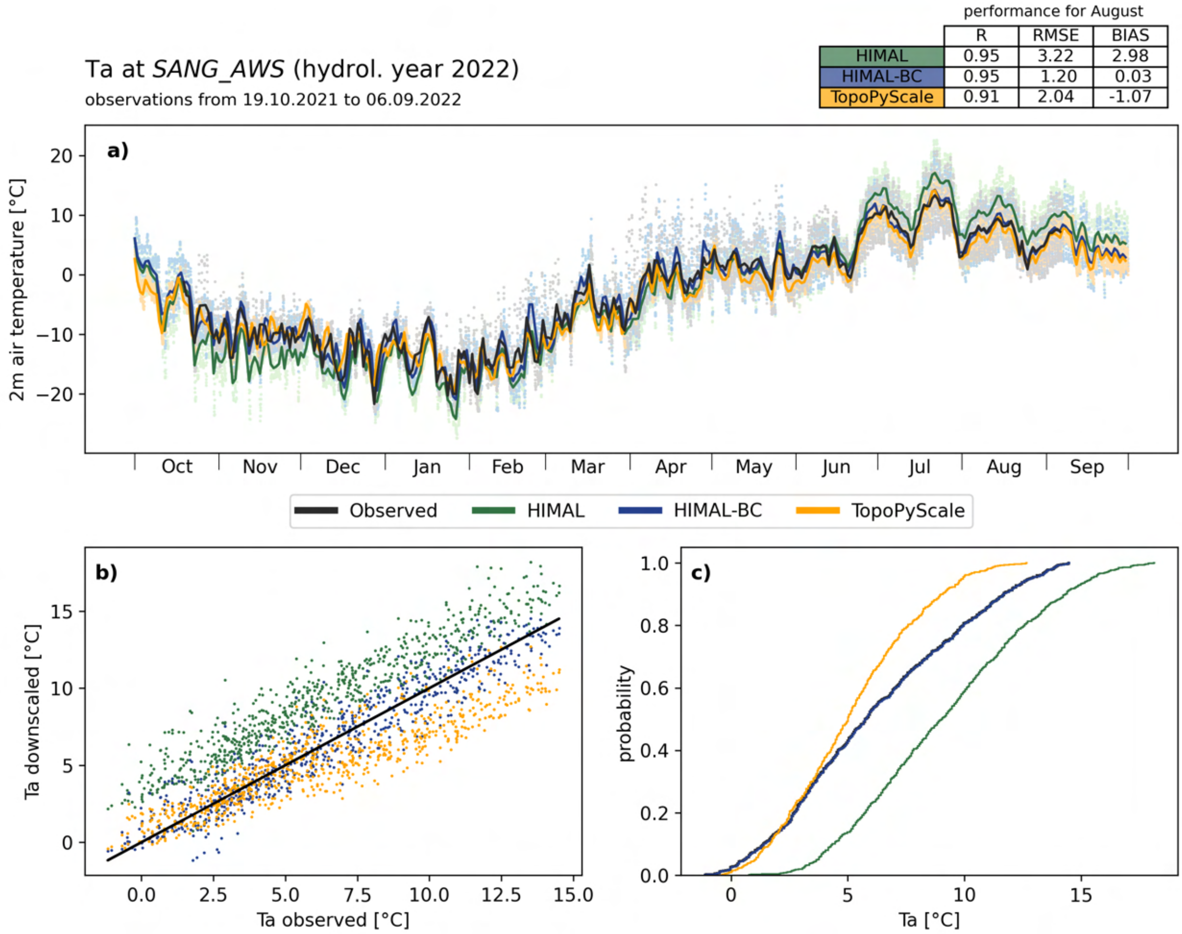

performance for August

	R	RMSE	BIAS
HIMAL	0.95	3.22	2.98
HIMAL-BC	0.95	1.20	0.03
TopoPyScale	0.91	2.04	-1.07

Figure C.34: Supporting figure for evaluating simulated surface temperature in August: performance of downscaled 2m air temperature in August at SANG_AWS.

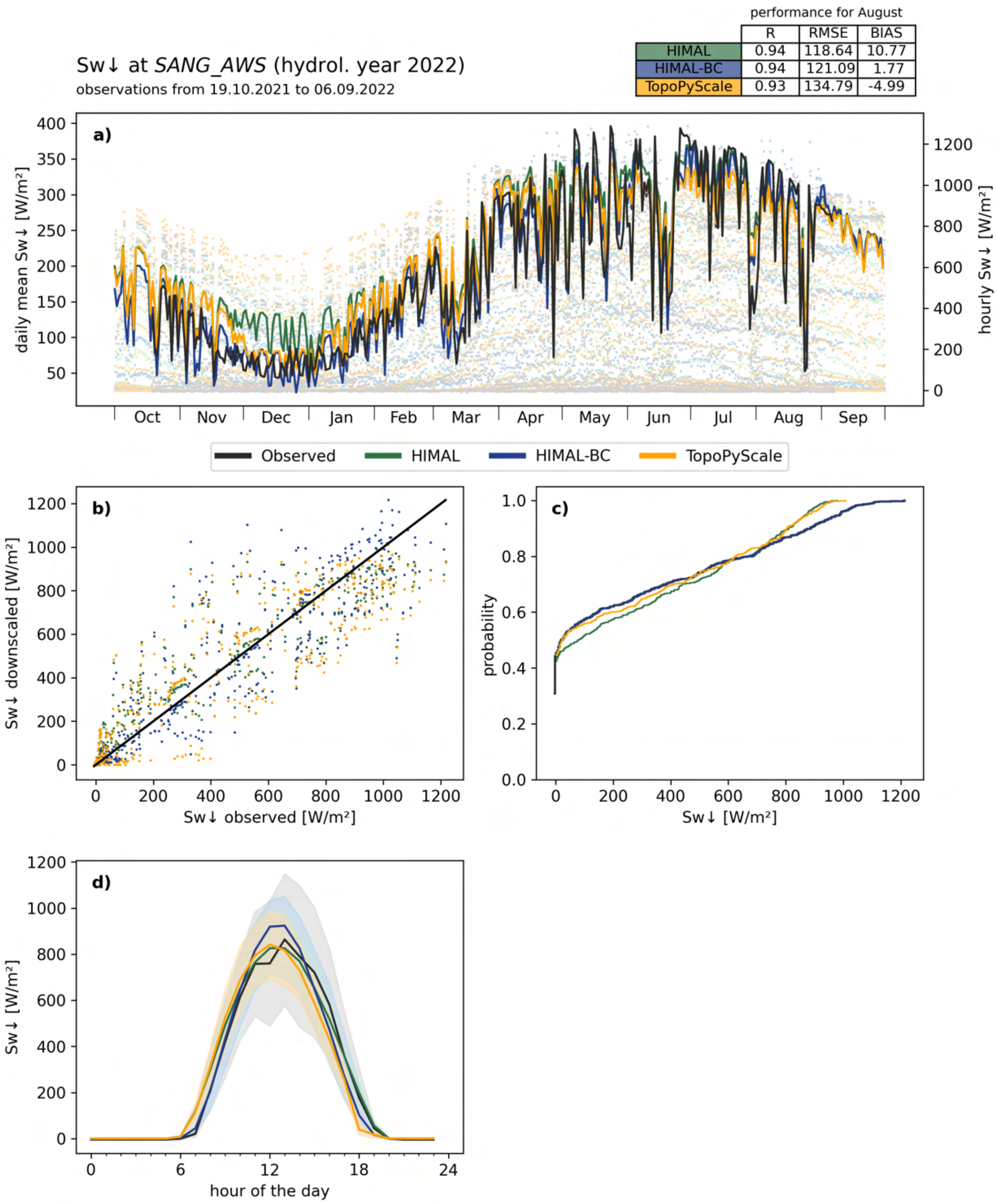

Figure C.35: Supporting figure for evaluating simulated surface temperature in August: performance of downscaled Sw↓ in August at SANG_AWS. With d) additionally indicating the average diurnal cycle (standard deviation as shading).

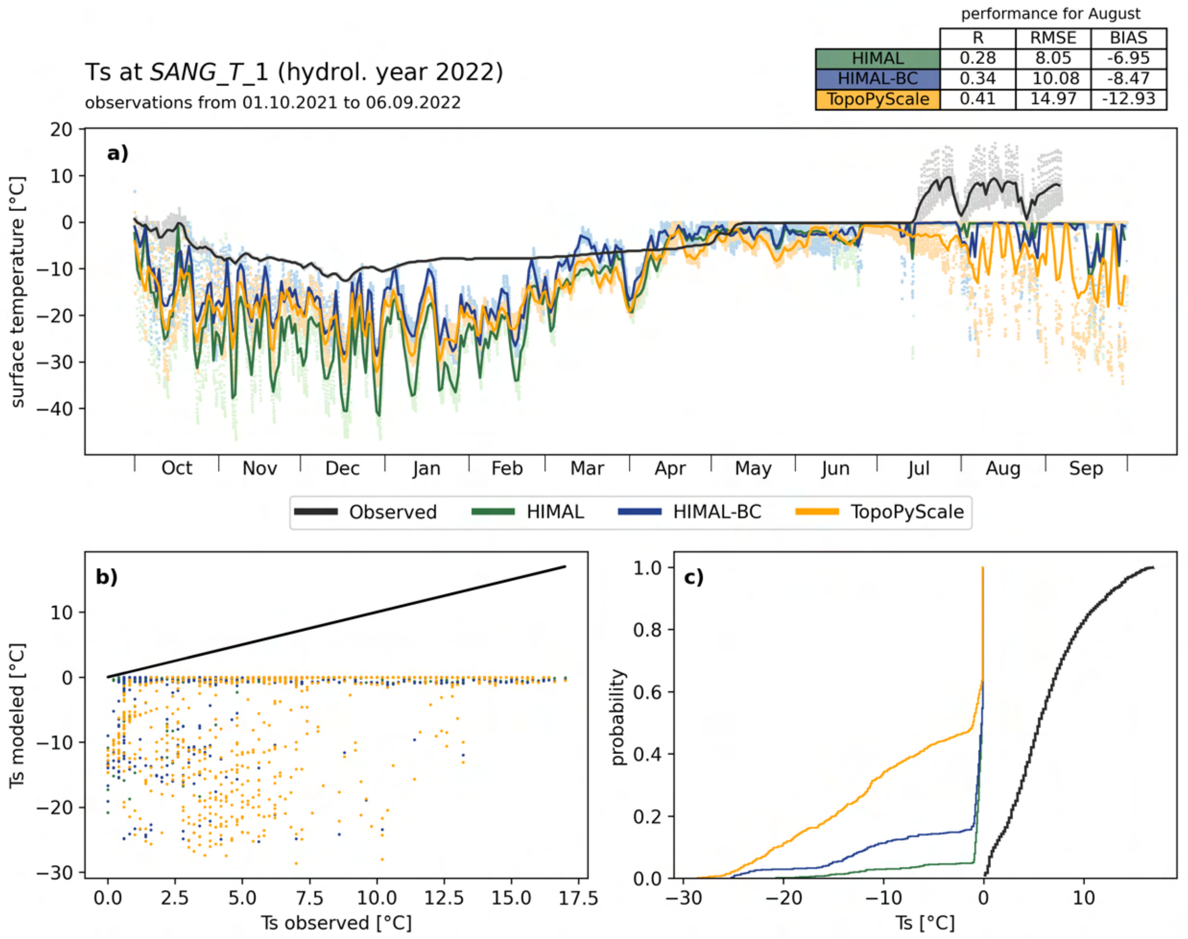

	R	RMSE	BIAS
HIMAL	0.28	8.05	-6.95
HIMAL-BC	0.34	10.08	-8.47
TopoPyScale	0.41	14.97	-12.93

Figure C.36: Overview of simulated surface temperature in August at SANG_T_1. This location is excluded from the evaluation, since the model represents this site as glaciated instead of bare rock. The site is located close to SANG$_{T2}andSANG_{T}3(approximatelytobothlocations)$.

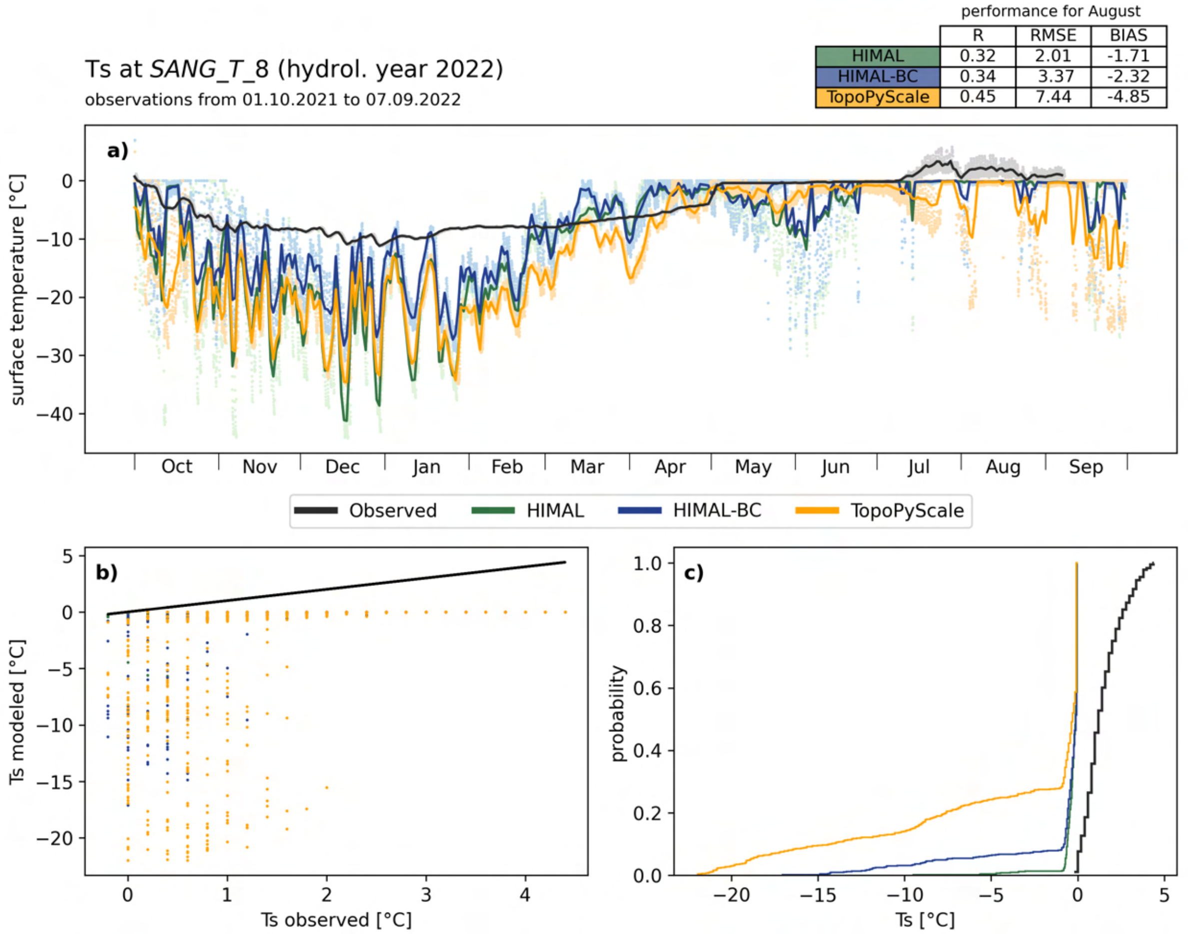

	R	RMSE	BIAS
HIMAL	0.32	2.01	-1.71
HIMAL-BC	0.34	3.37	-2.32
TopoPyScale	0.45	7.44	-4.85

Figure C.37: Overview of simulated surface temperature in August at SANG_T_8. This location is excluded from the evaluation, since the model represents this site as glaciated instead of bare rock.

C.2.3 Sd

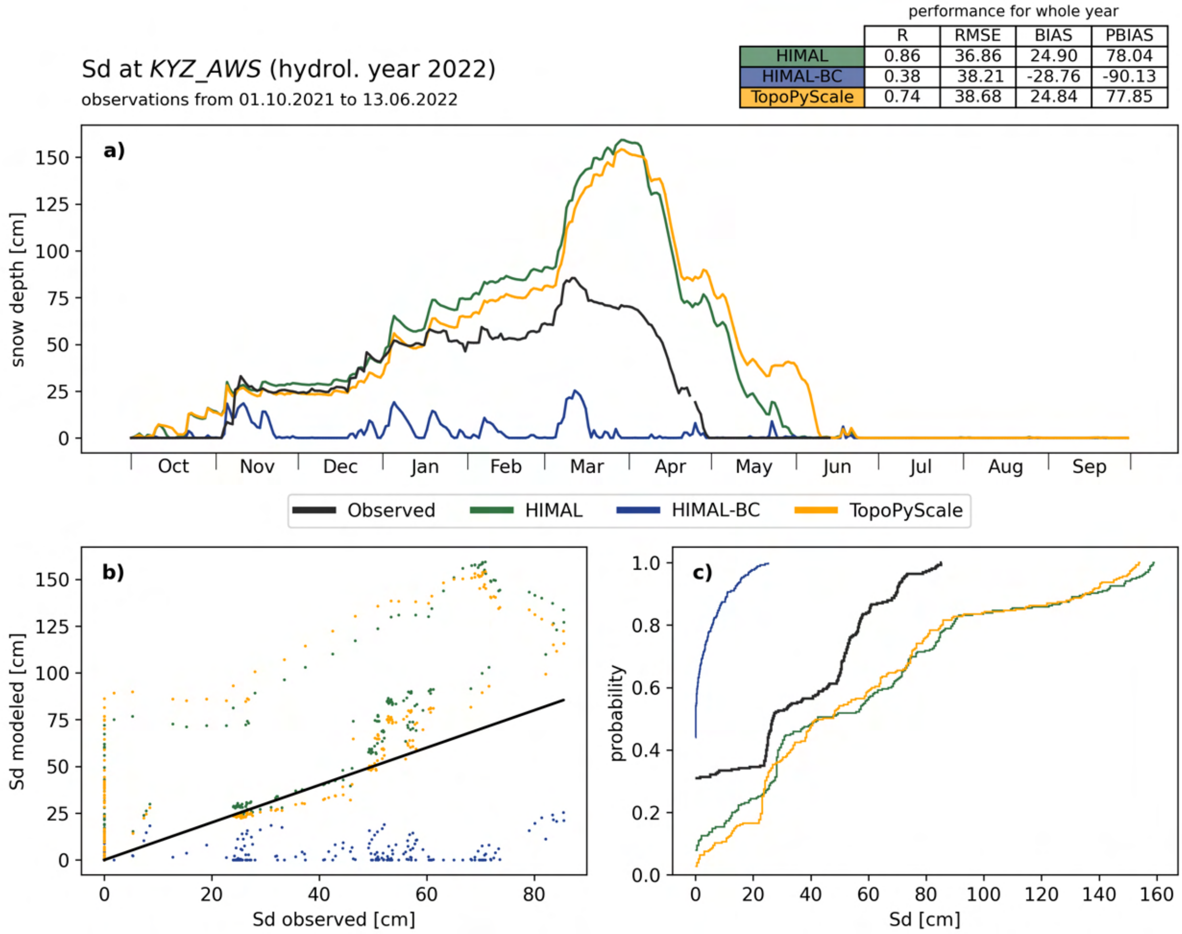

	R	RMSE	BIAS	PBIAS
HIMAL	0.86	36.86	24.90	78.04
HIMAL-BC	0.38	38.21	-28.76	-90.13
TopoPyScale	0.74	38.68	24.84	77.85

Figure C.38: Evaluation of simulated snow depth at KYZ_AWS.

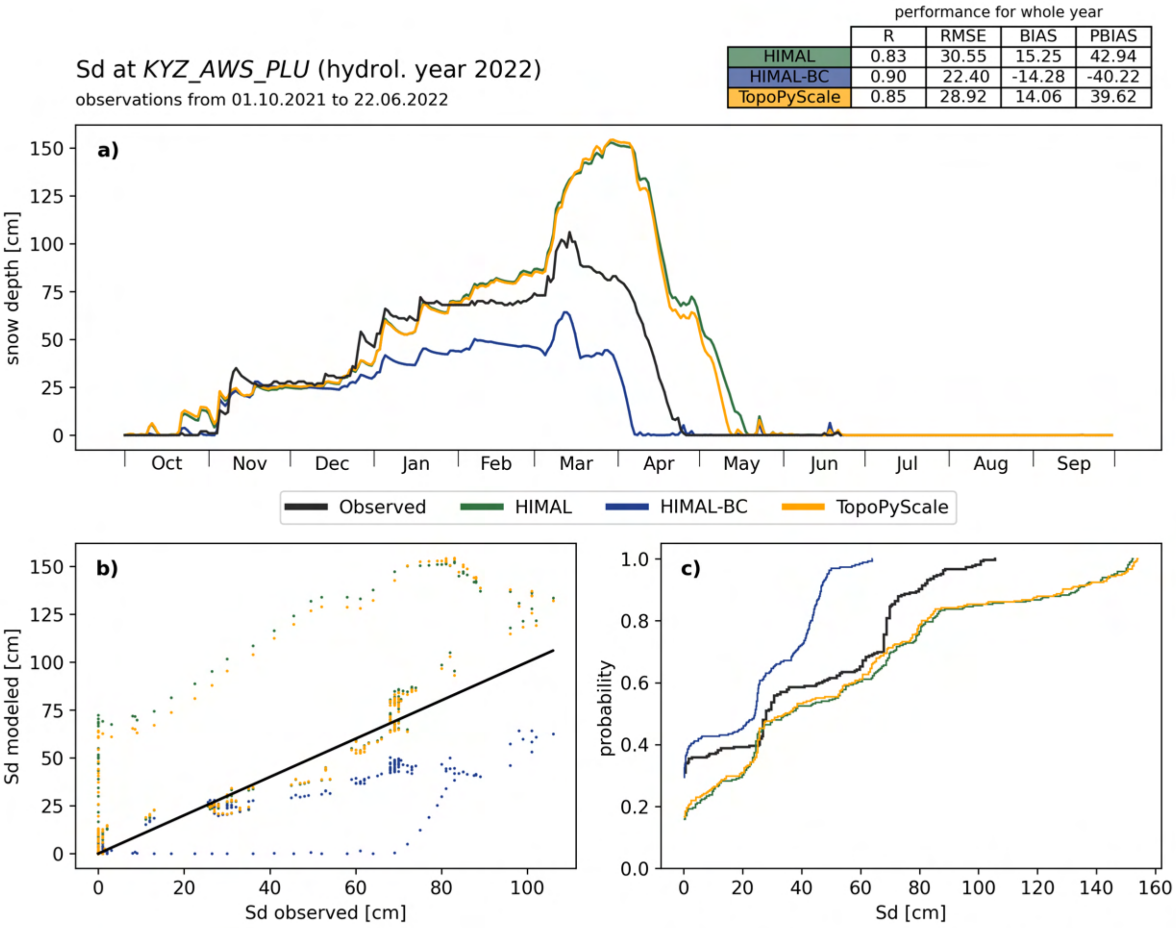

performance for whole year

	R	RMSE	BIAS	PBIAS
HIMAL	0.83	30.55	15.25	42.94
HIMAL-BC	0.90	22.40	-14.28	-40.22
TopoPyScale	0.85	28.92	14.06	39.62

Figure C.39: Evaluation of simulated snow depth at KYZ_AWS_PLU.

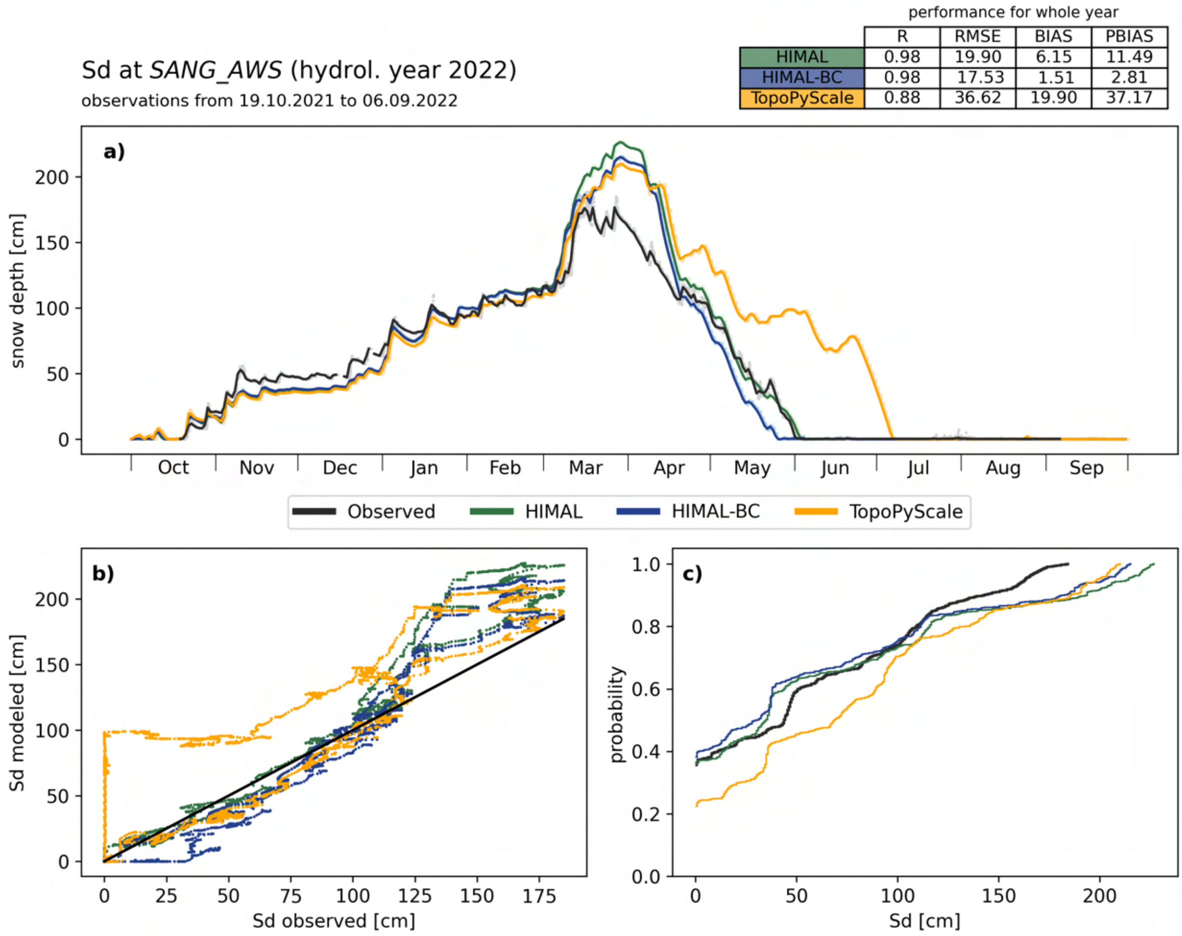

performance for whole year

	R	RMSE	BIAS	PBIAS
HIMAL	0.98	19.90	6.15	11.49
HIMAL-BC	0.98	17.53	1.51	2.81
TopoPyScale	0.88	36.62	19.90	37.17

Figure C.40: Evaluation of simulated snow depth at SANG_AWS.

C.2.4 Tdeb

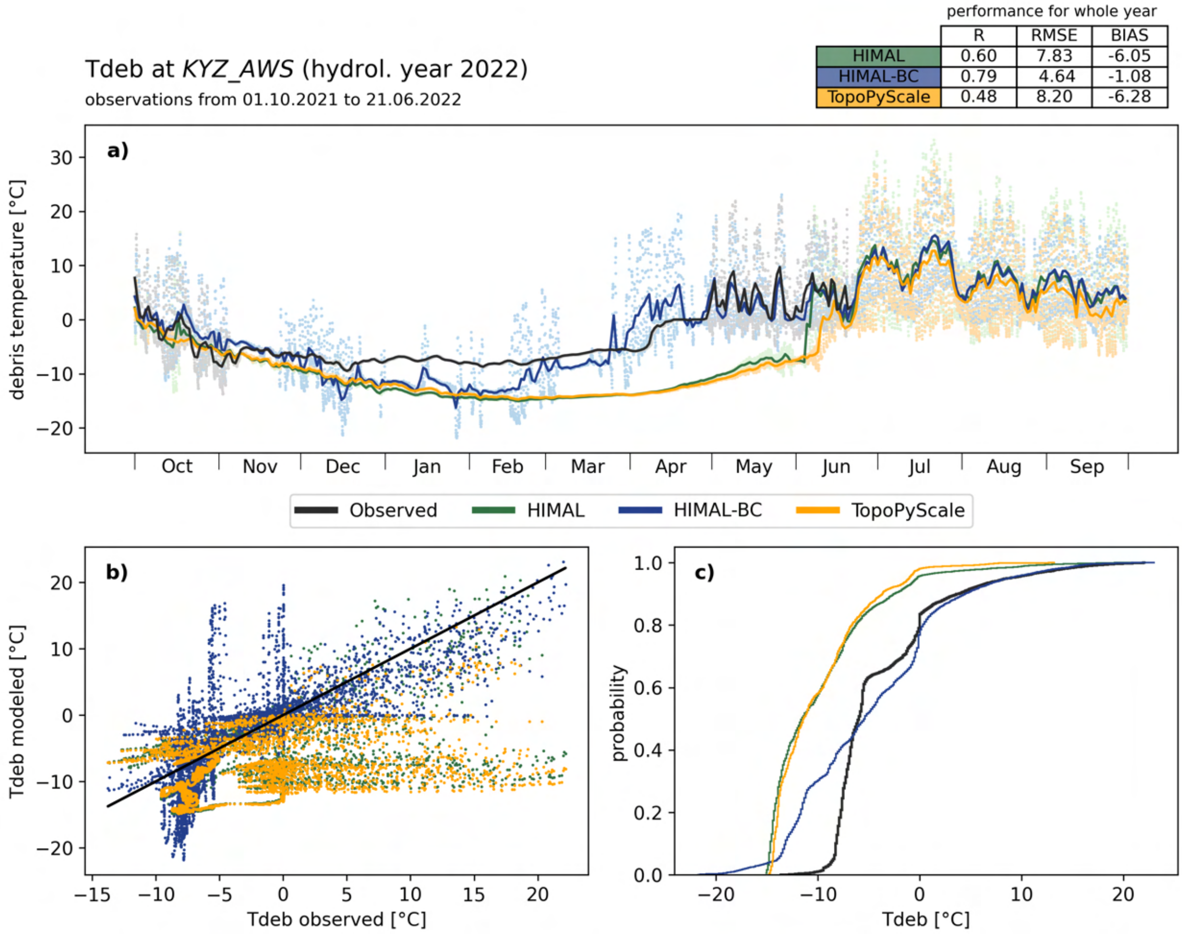

	R	RMSE	BIAS
HIMAL	0.60	7.83	-6.05
HIMAL-BC	0.79	4.64	-1.08
TopoPyScale	0.48	8.20	-6.28

Figure C.41: Evaluation of simulated debris temperature at KYZ_AWS.

Appendix D: Downscaled CMIP6

D.1 Evaluation of meteorological forcings

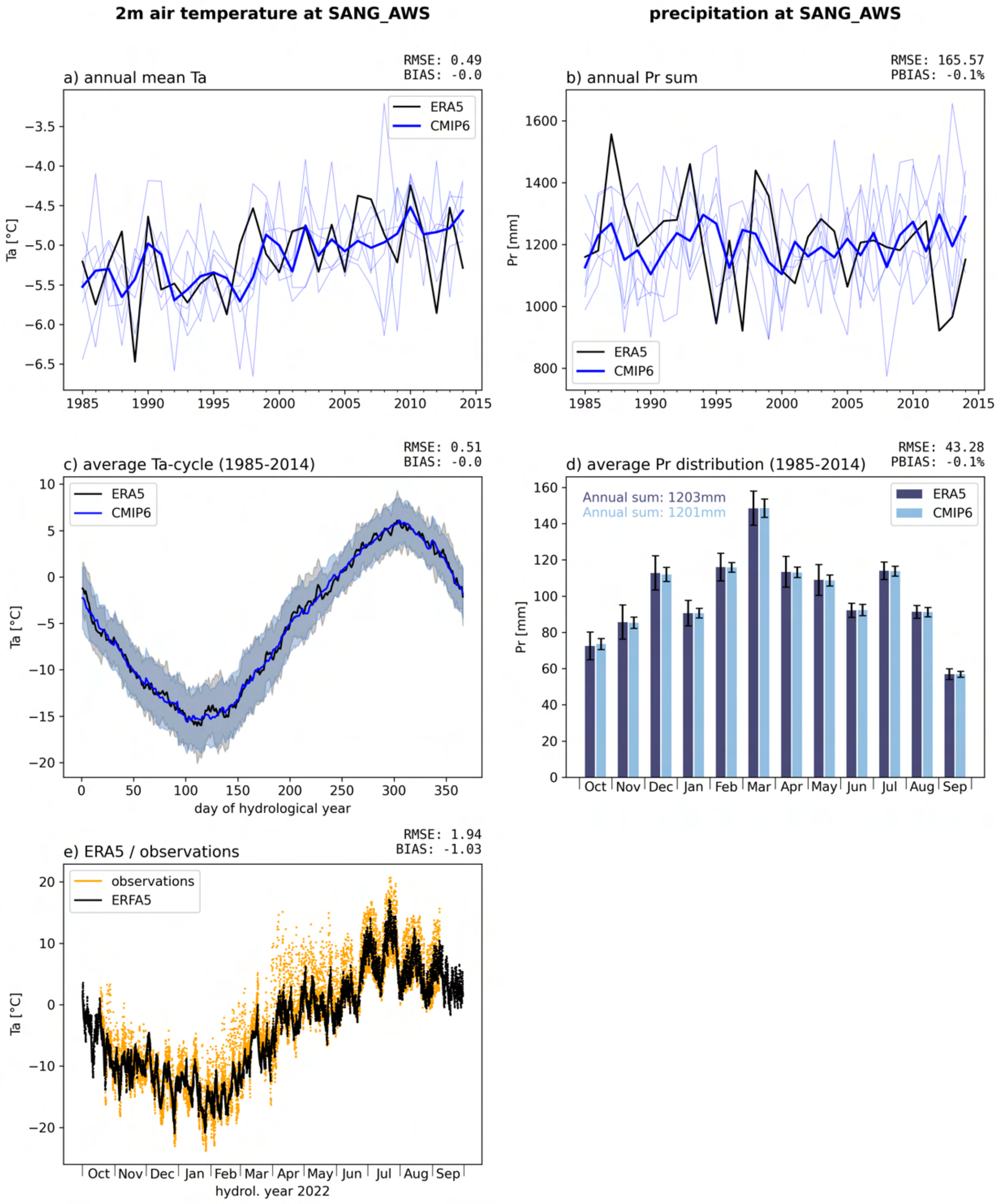

Figure D.1: Evaluation of the CMIP6-downscaling process for 2m air temperature (Ta) and precipitation (Pr) in the Sangvor catchment. Ta at SANG_AWS is presented in the left column and Pr at SANG_AWS in the right column. a) to e) are pendent to Figure 9.

D.2 Evaluation of spatial snow pack dynamics

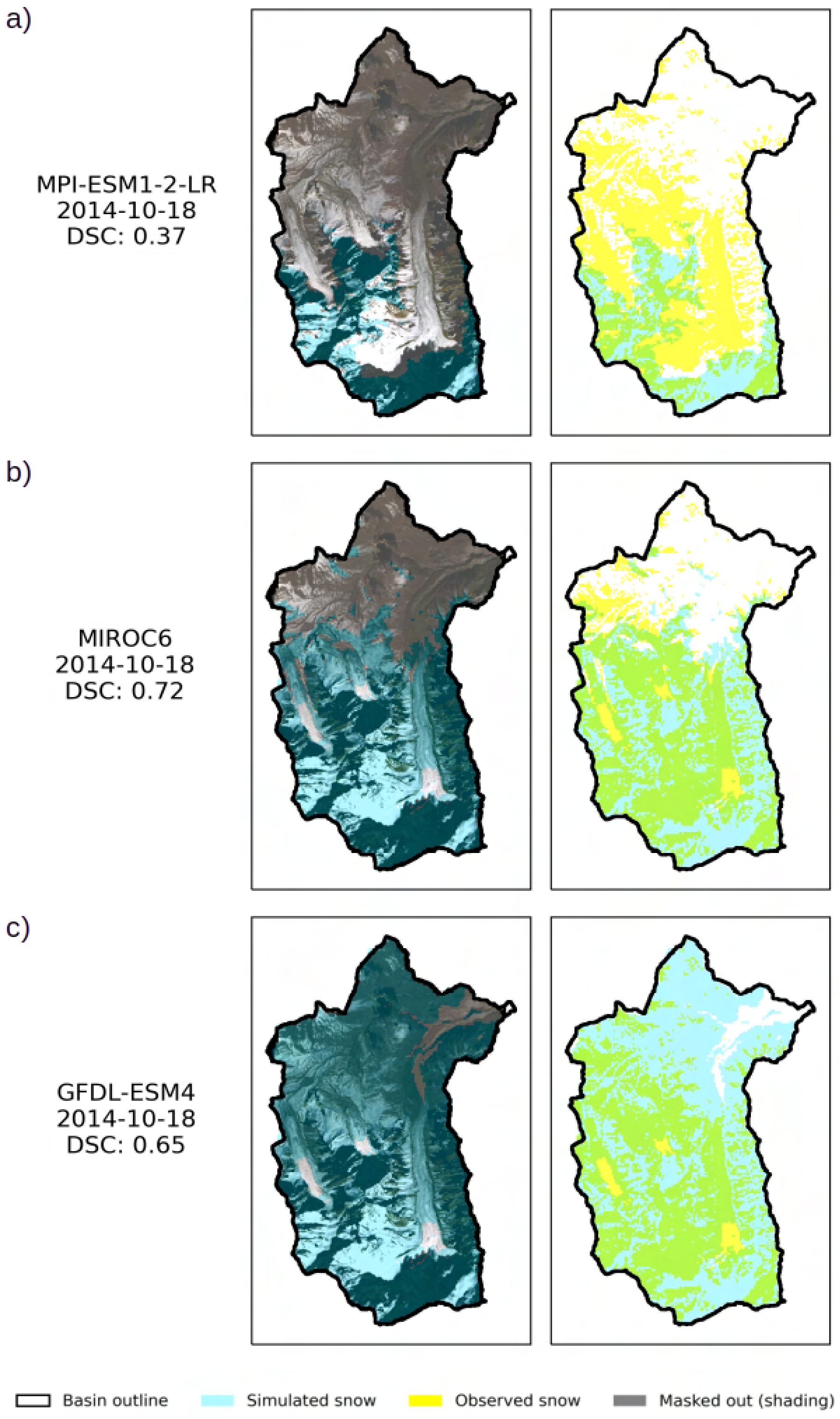

Figure D.2: Different performance in simulating snow cover of three downscaled CMIP6 model chains in the Kyzylsu catchment on the same day (18.10.2014).

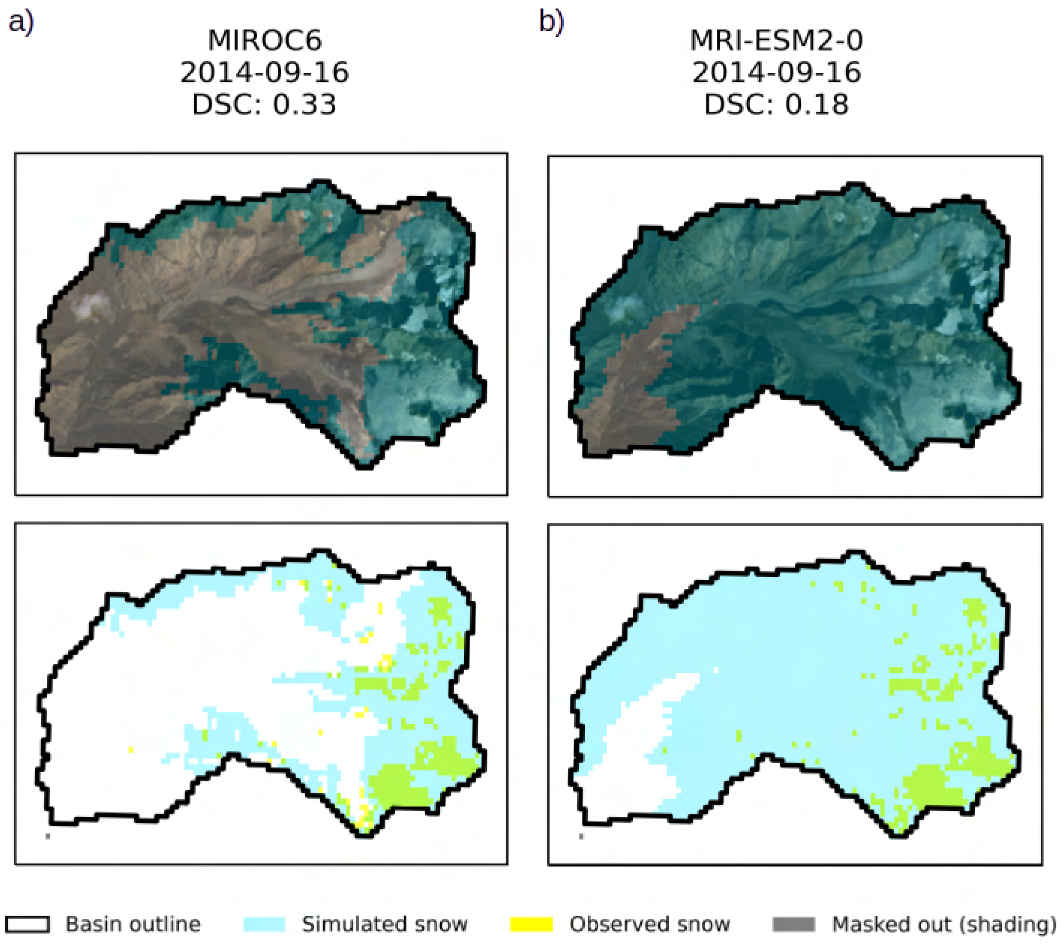

Figure D.3: Scene-by-scene evaluation of simulated snow cover against Landsat-7/Landsat-8 in the Sangvor catchment on a day with low performance (16.09.2014), for two different model chains.

Appendix E: Climate change signal

E.1 Kyzylsu

E.1.1 Precipitation

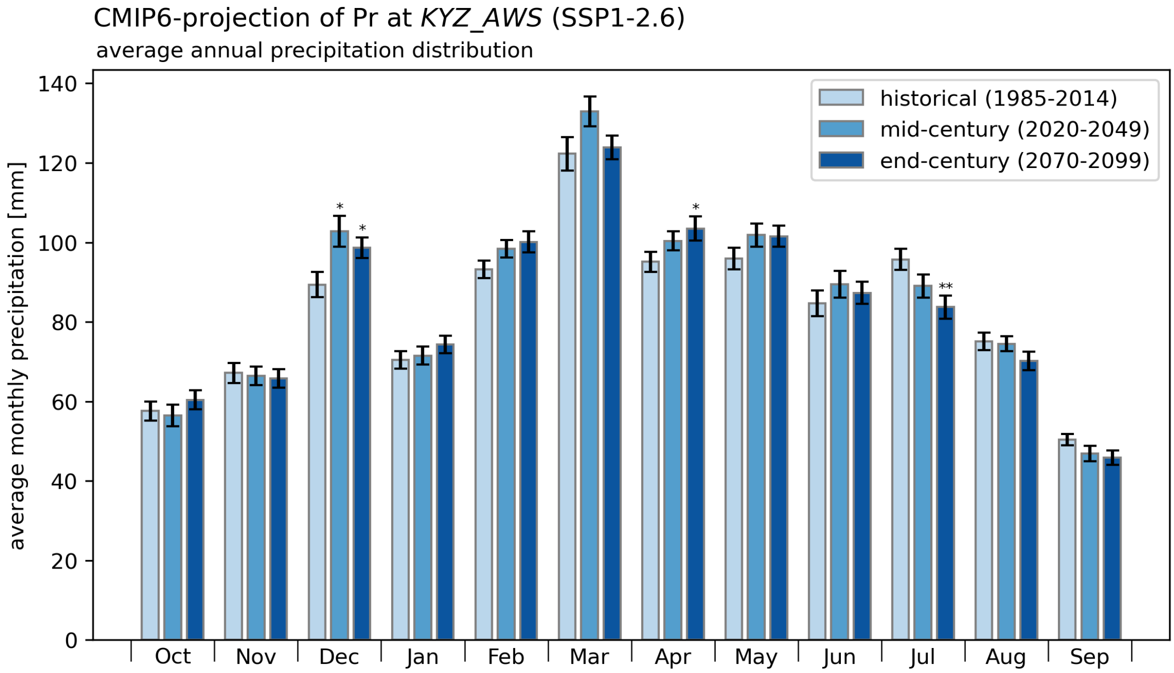

Figure E.1: Average annual precipitation distribution during the historical reference period (1985-2014), mid-century (2020-2049) and end-century (2070-2099) of SSP1-2.6 CMIP6-projections at KYZ_AWS. The significance of change in a certain month is calculated with a T-test and indicated by stars, whereby a change is regarded as significant if it has a confidence interval of at least 95%. The following labels are used for significant changes: *>=95% / **>=99% / ***>=99.9%.

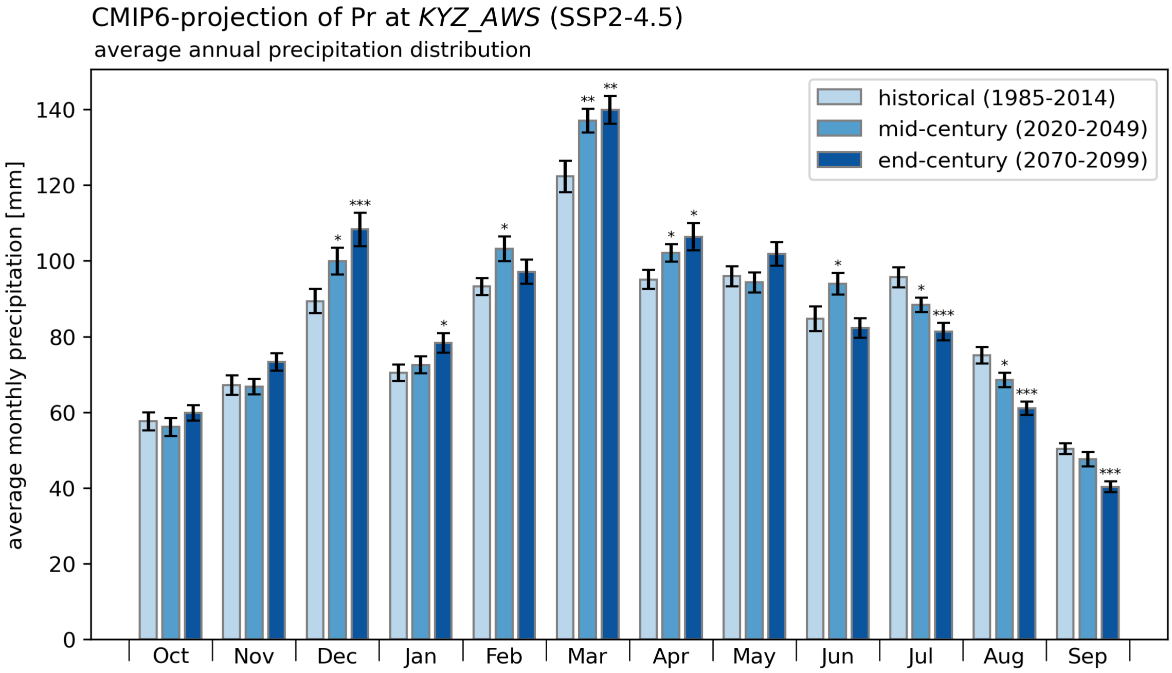

Figure E.2: Average annual precipitation distribution during the historical reference period (1985-2014), mid-century (2020-2049) and end-century (2070-2099) of SSP2-4.5 CMIP6-projections at KYZ_AWS. The significance of change in a certain month is calculated with a T-test and indicated by stars, whereby a change is regarded as significant if it has a confidence interval of at least 95%. The following labels are used for significant changes: *>=95% / **>=99% / ***>=99.9%.

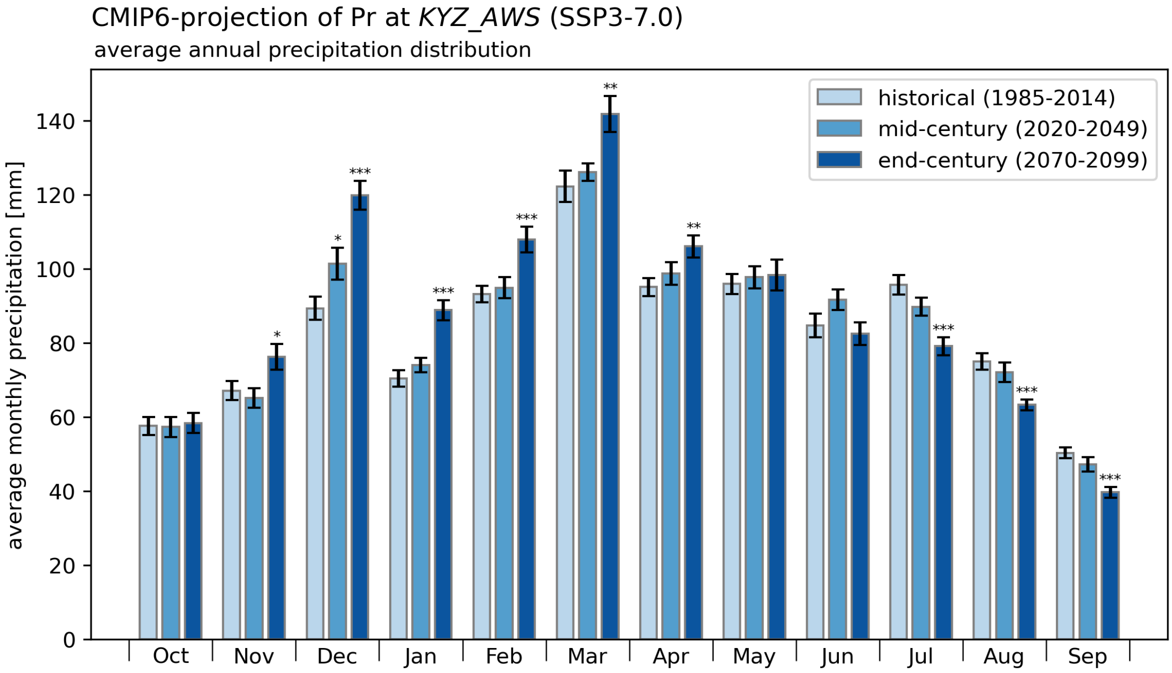

Figure E.3: Average annual precipitation distribution during the historical reference period (1985-2014), mid-century (2020-2049) and end-century (2070-2099) of SSP3-7.0 CMIP6-projections at KYZ_AWS. The significance of change in a certain month is calculated with a T-test and indicated by stars, whereby a change is regarded as significant if it has a confidence interval of at least 95%. The following labels are used for significant changes: *>=95% / **>=99% / ***>=99.9%.

E.1.2 Surface air pressure

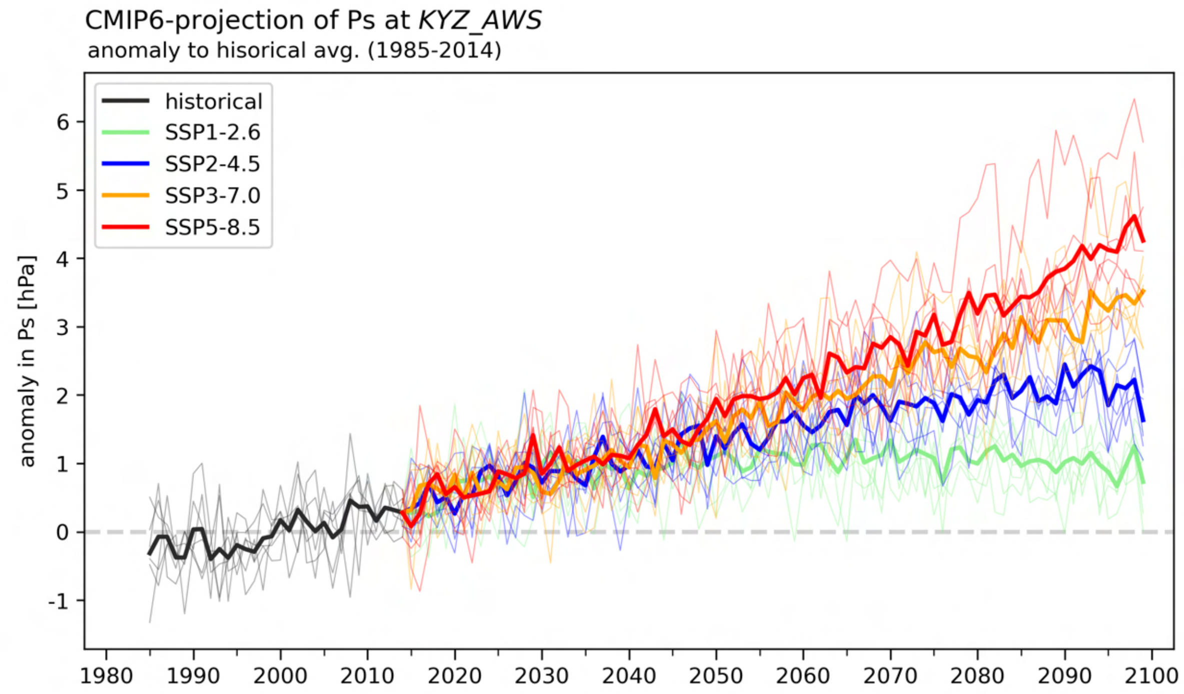

Figure E.4: Anomaly in surface air pressure in CMIP6-projections to historical average at KYZ_AWS. The average of the historical reference period (1985-2014) is thereby indicated as a grey, dashed line, representing zero-change. The CMIP6 ensemble means are plotted in the colours presented in the legend, with its individual members (model chains) indicated by thinner lines in the same colour.

E.1.3 Incoming shortwave radiation

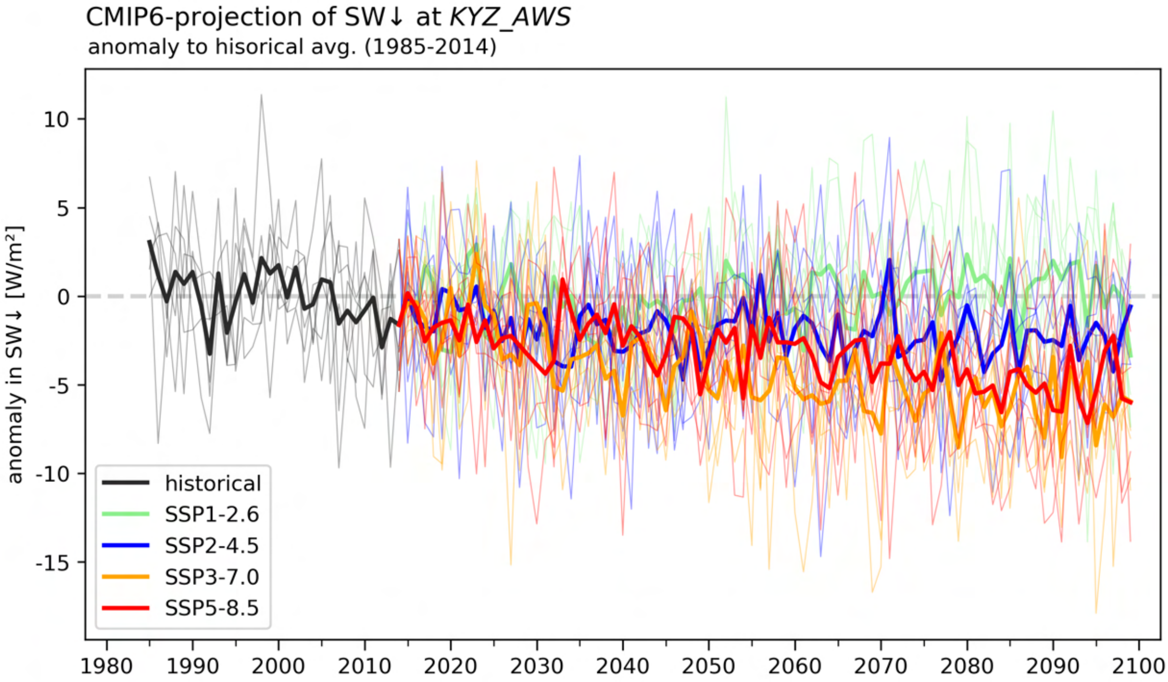

Figure E.5: Anomaly in incoming shortwave radiation in CMIP6-projections to historical average at KYZ_AWS. The average of the historical reference period (1985-2014) is thereby indicated as a grey, dashed line, representing zero-change. The CMIP6 ensemble means are plotted in the colours presented in the legend, with its individual members (model chains) indicated by thinner lines in the same colour.

E.1.4 Incoming longwave radiation

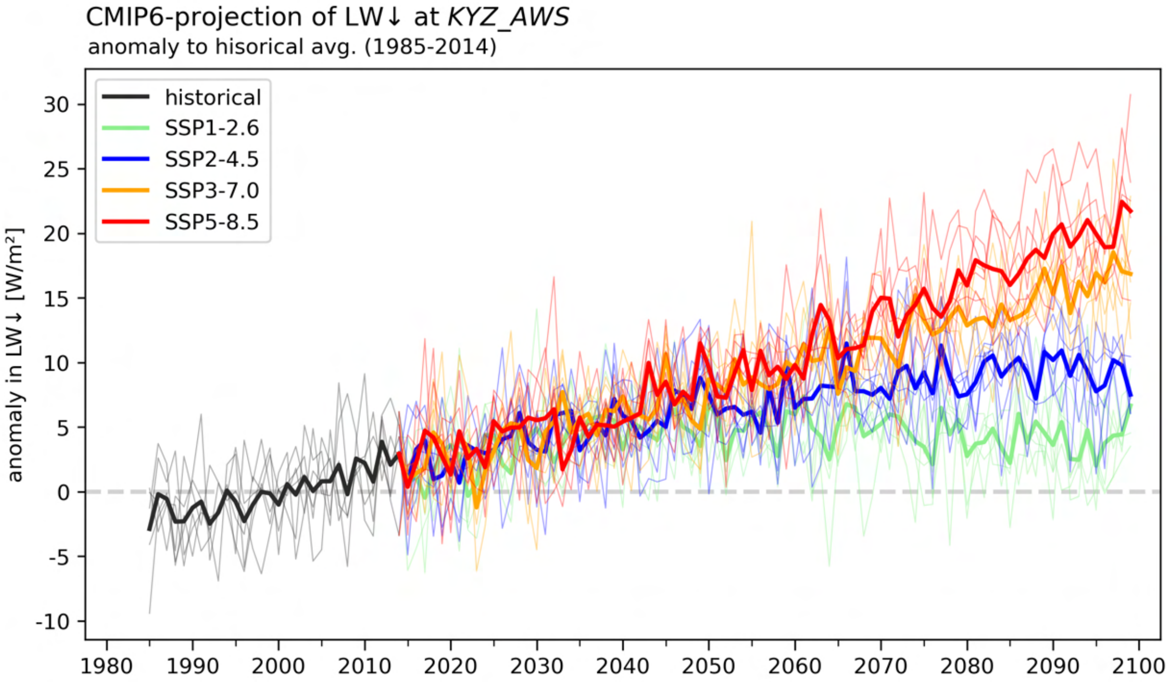

Figure E.6: Anomaly in incoming longwave radiation in CMIP6-projections to historical average at KYZ_AWS. The average of the historical reference period (1985-2014) is thereby indicated as a grey, dashed line, representing zero-change. The CMIP6 ensemble means are plotted in the colours presented in the legend, with its individual members (model chains) indicated by thinner lines in the same colour.

E.1.5 Wind speed

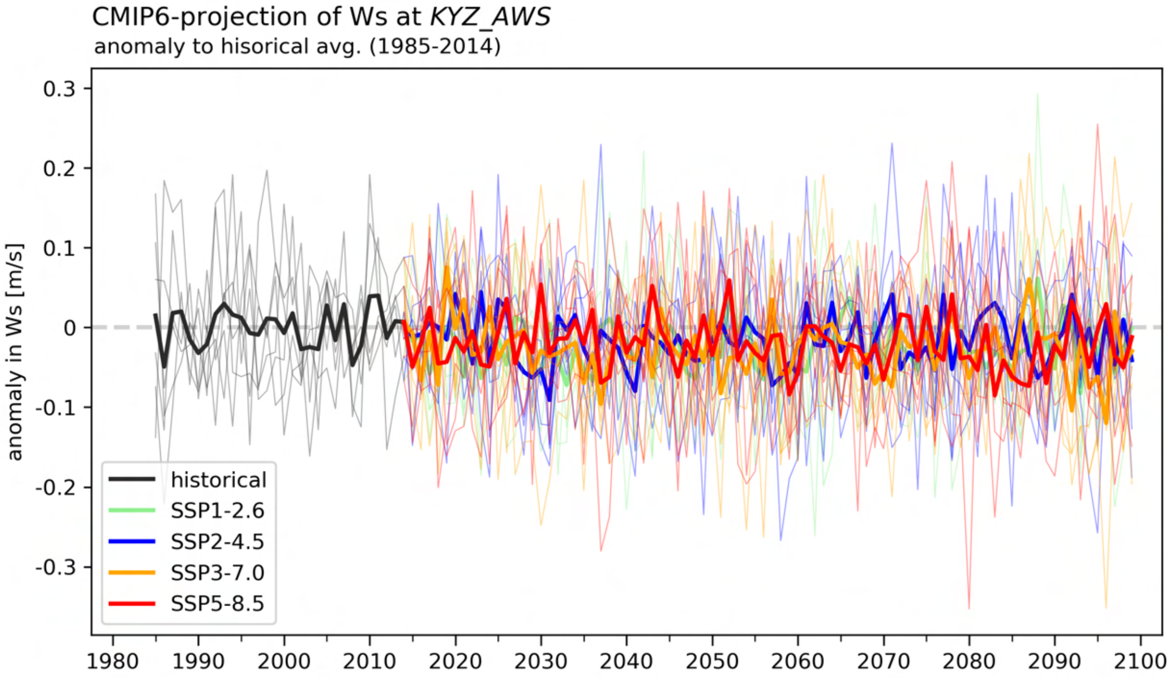

Figure E.7: Anomaly in wind speed in CMIP6-projections to historical average at KYZ_AWS. The average of the historical reference period (1985-2014) is thereby indicated as a grey, dashed line, representing zero-change. The CMIP6 ensemble means are plotted in the colours presented in the legend, with its individual members (model chains) indicated by thinner lines in the same colour.

E.2 Sangvor

Table E.1: Overview of the Mann-Kendall trend analysis for all downscaled meteorological CMIP6 variables in the Sangvor catchment. The trend analysis is carried out for all Tier 1 Scenarios at mid century and end century. Significant trends are indicated in the column *trend* of the corresponding period, whereby a '$-$' indicates a negative trend and '$+$' a positive trend. A trend is considered as significant at the confidence interval of 95% and higher. The significance level of the observed trend is further indicated by stars with the following confident intervals:*>=95% / **>=99% / ***>=99.9%. Further, the average change of the ensemble mean is indicated, as well as the lowest and highest trend of its members (model chains). All units refer to the yearly mean (sum for precipitation) and are relative to the historical reference period.

				Mid-century (2020-2049)				End-century (2070-2099)			
Variable	Unit	Station	Scenario	Trend	Avg. change	Lower bound	Upper bound	Trend	Avg. change	Lower bound	Upper bound
Ta	°C	SANG_AWS	SSP1-2.6	$+^{**}$	+1.00	+0.80	+1.45	$+^{***}$	+1.28	+0.94	+1.88
			SSP2-4.5	$+^{***}$	+1.15	+0.87	+1.60	$+^{***}$	+2.42	+1.99	+3.01
			SSP3-7.0	$+^{***}$	+1.14	+0.95	+1.37	$+^{***}$	+3.59	+3.20	+3.99
			SSP5-8.5	$+^{***}$	+1.30	+0.89	+1.74	$+^{***}$	+4.58	+3.96	+5.45
Rh	%	SANG_AWS	SSP1-2.6		-1.09	-1.74	-0.56	$-^{***}$	-2.01	-6.47	-0.29
			SSP2-4.5	$-^{*}$	-1.34	-4.65	-0.58	$-^{***}$	-3.08	-7.97	-0.74
			SSP3-7.0		-1.18	-3.02	-0.37	$-^{***}$	-3.58	-7.26	-1.04
			SSP5-8.5	$-^{**}$	-1.42	-3.81	-0.25	$-^{***}$	-4.85	-12.05	-0.78
Pr	mm	SANG_AWS	SSP1-2.6		+29.34	-25.21	+83.53		+12.37	-61.49	+95.52
			SSP2-4.5		+30.89	-16.70	+69.02		+30.83	-50.16	+154.04
			SSP3-7.0		+12.94	-23.53	+73.88	$+^{*}$	+66.59	-99.72	+206.98
			SSP5-8.5		+29.06	-16.15	+117.82		+74.68	-77.85	+298.21
Ps	hPa	SANG_AWS	SSP1-2.6	$+^{***}$	+0.89	+0.65	+1.13	$+^{***}$	+1.07	+0.80	+1.33
			SSP2-4.5	$+^{***}$	+0.97	+0.67	+1.16	$+^{***}$	+2.09	+1.72	+2.56
			SSP3-7.0	$+^{***}$	+0.98	+0.71	+1.11	$+^{***}$	+2.99	+2.36	+3.79
			SSP5-8.5	$+^{***}$	+1.10	+0.78	+1.32	$+^{***}$	+3.64	+3.00	+4.89
Sw↓	W/m^2	SANG_AWS	SSP1-2.6		-0.98	-2.37	+1.22		+0.31	-1.83	+2.82
			SSP2-4.5		-2.34	-3.27	-1.76		-2.69	-5.44	-0.76
			SSP3-7.0		-3.17	-4.18	-2.43	$-^{*}$	-7.02	-9.74	-5.58
			SSP5-8.5		-2.53	-4.40	-0.83		-5.59	-11.00	-1.16
Lw↓	W/m^2	SANG_AWS	SSP1-2.6	$+^{***}$	+3.73	+2.14	+5.55	$+^{***}$	+3.93	+2.67	+5.11
			SSP2-4.5	$+^{***}$	+4.47	+3.09	+6.23	$+^{***}$	+8.33	+5.21	+9.63
			SSP3-7.0	$+^{***}$	+4.60	+2.88	+6.09	$+^{***}$	+13.17	+10.45	+15.23
			SSP5-8.5	$+^{***}$	+5.01	+2.99	+7.81	$+^{***}$	+16.03	+10.01	+20.27
Ws	m/s	SANG_AWS	SSP1-2.6		-0.02	-0.05	-0.00		-0.02	-0.06	+0.00
			SSP2-4.5		-0.02	-0.03	+0.01		-0.01	-0.05	+0.01
			SSP3-7.0		-0.02	-0.06	+0.00		-0.03	-0.07	+0.04
			SSP5-8.5		-0.01	-0.03	+0.01		-0.03	-0.08	+0.02

E.2.1 2m air temperature

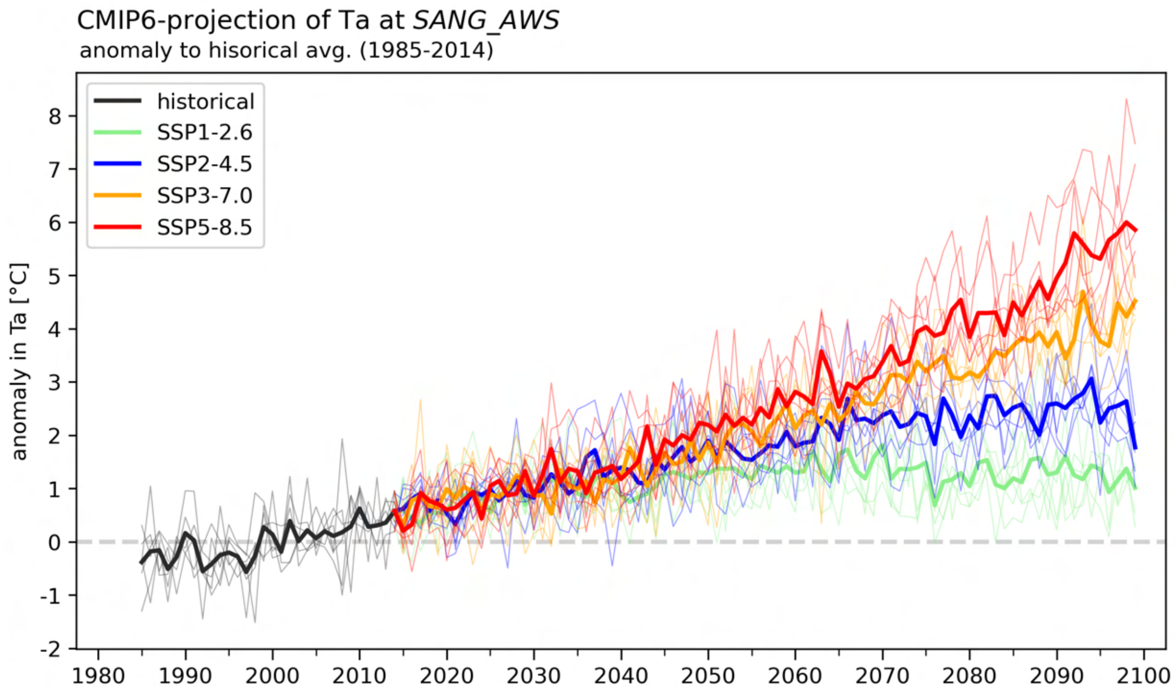

Figure E.8: Anomaly in 2m air temperature in CMIP6-projections to historical average at SANG_AWS. The average of the historical reference period (1985-2014) is thereby indicated as a grey, dashed line, representing zero-change. The CMIP6 ensemble means are plotted in the colours presented in the legend, with its individual members (model chains) indicated by thinner lines in the same colour.

E.2.2 Near-surface relative humidity

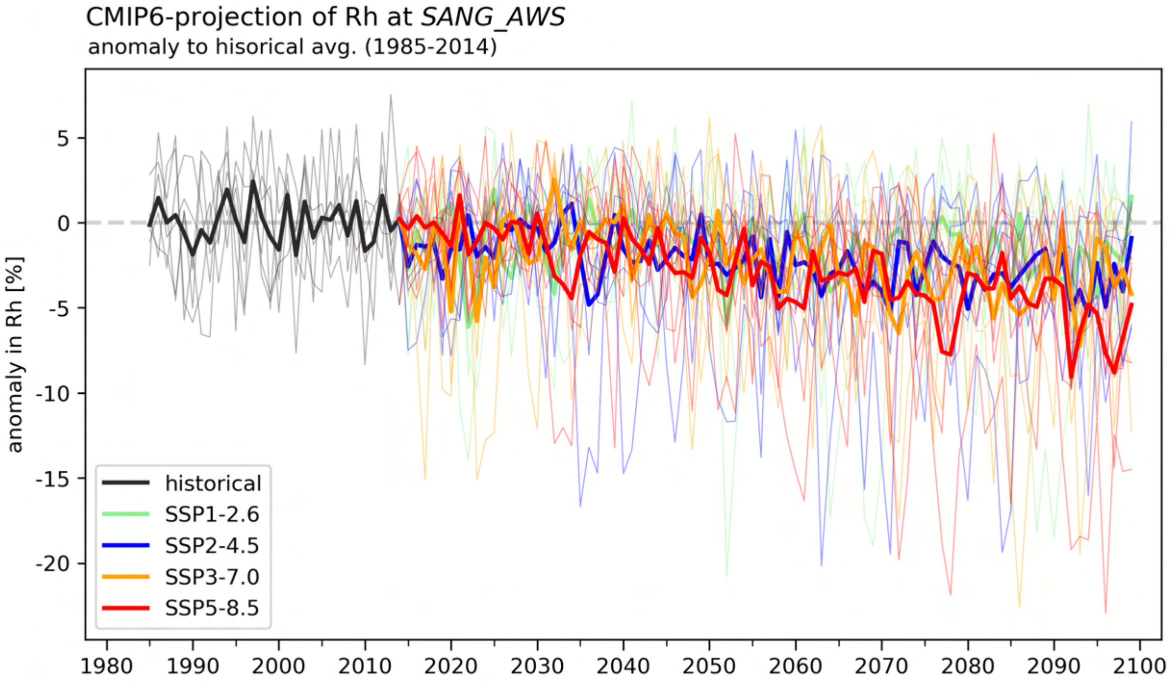

Figure E.9: Anomaly in relative humidity in CMIP6-projections to historical average at SANG_AWS. The average of the historical reference period (1985-2014) is thereby indicated as a grey, dashed line, representing zero-change. The CMIP6 ensemble means are plotted in the colours presented in the legend, with its individual members (model chains) indicated by thinner lines in the same colour.

E.2.3 Precipitation

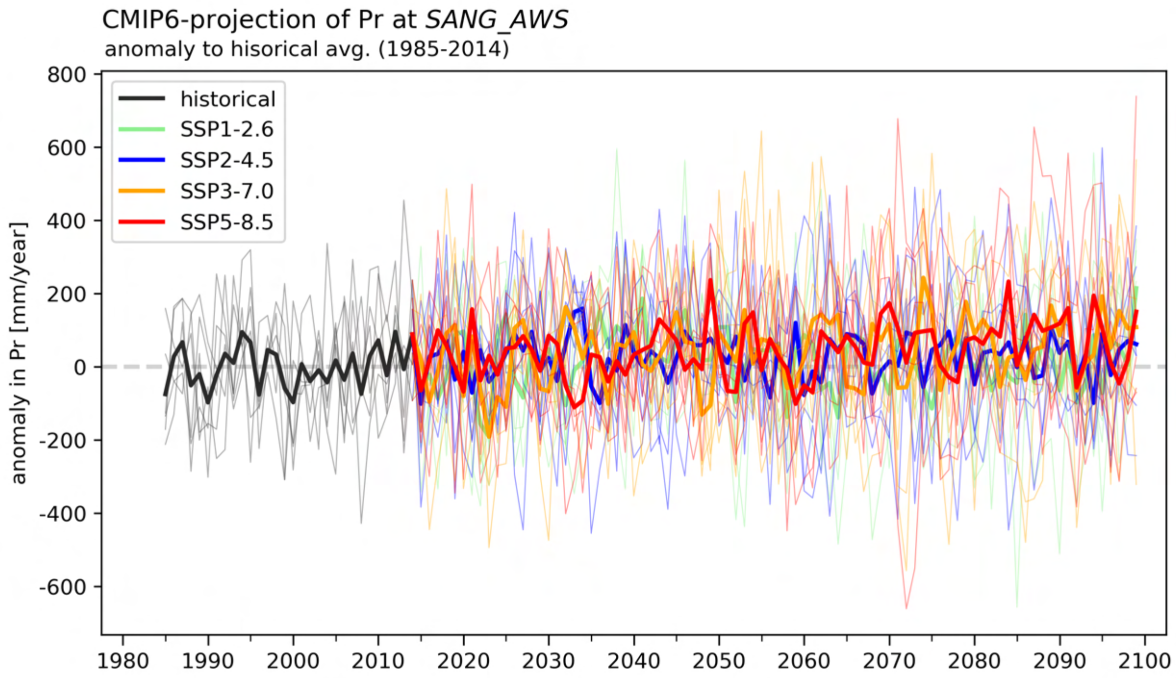

Figure E.10:]

Anomaly in precipitation in CMIP6-projections to historical average at SANG_AWS. The average of the historical reference period (1985-2014) is thereby indicated as a grey, dashed line, representing zero-change. The CMIP6 ensemble means are plotted in the colours presented in the legend, with its individual members (model chains) indicated by thinner lines in the same colour.

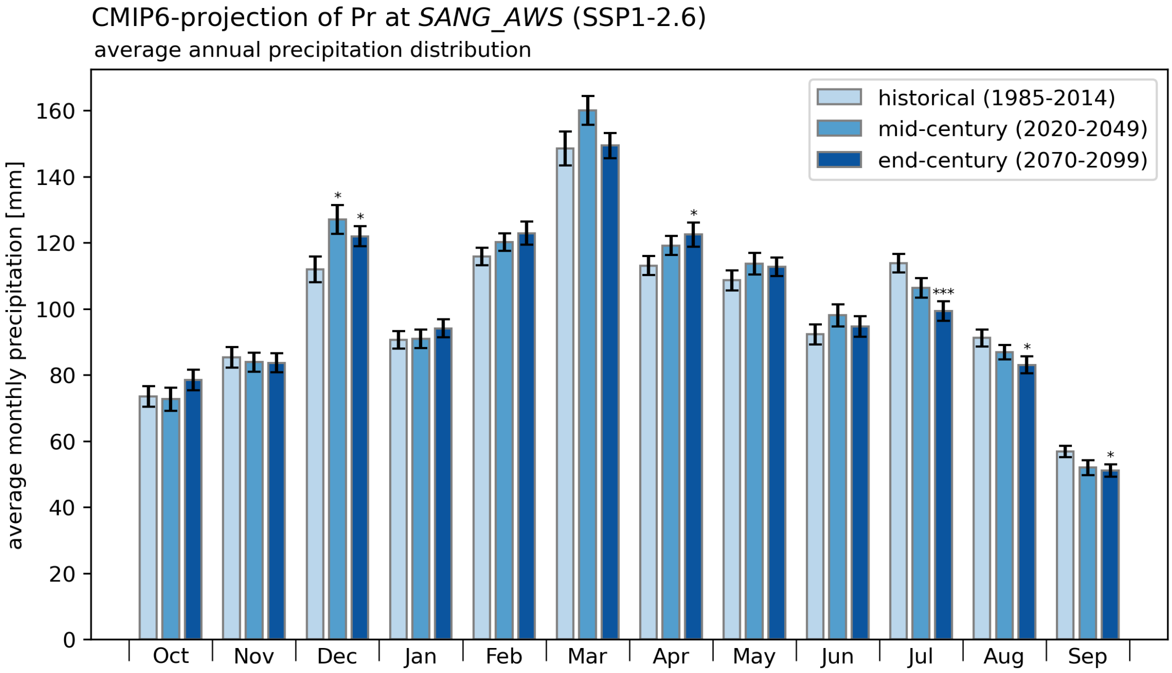

Figure E.11: Average annual precipitation distribution during the historical reference period (1985-2014), mid-century (2020-2049) and end-century (2070-2099) of SSP1-2.6 CMIP6-projections at SANG_AWS. The significance of change in a certain month is calculated with a T-test and indicated by stars, whereby a change is regarded as significant if it has a confidence interval of at least 95%. The following labels are used for significant changes: *>=95% / **>=99% / ***>=99.9%.

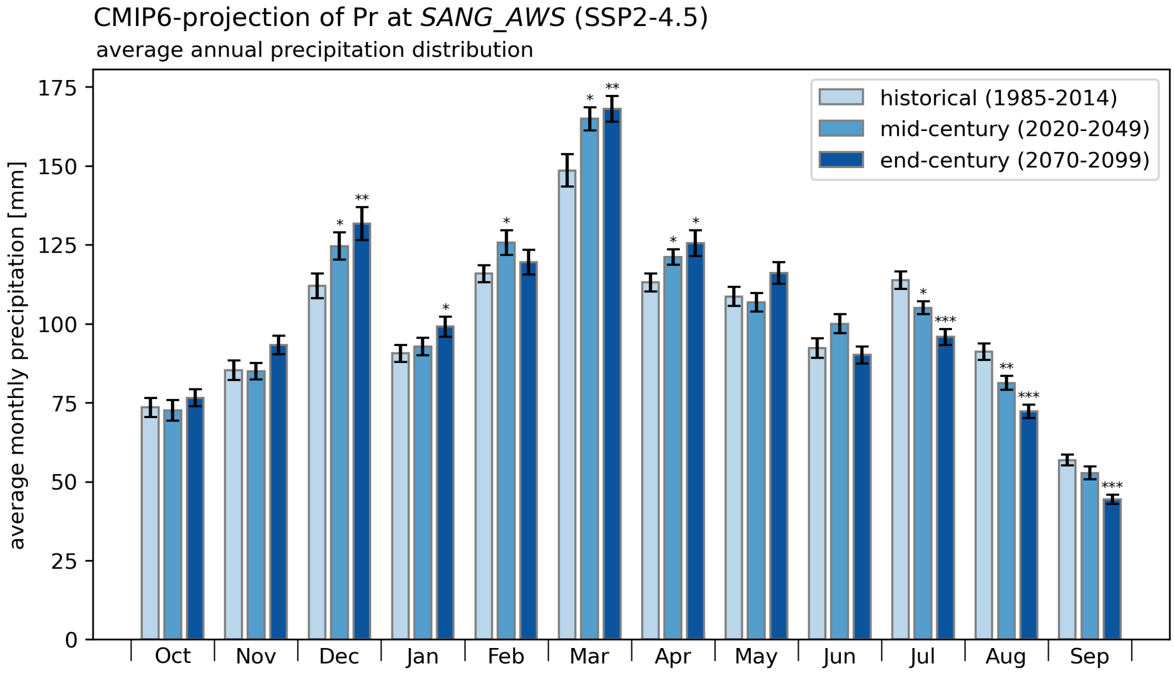

Figure E.12: Average annual precipitation distribution during the historical reference period (1985-2014), mid-century (2020-2049) and end-century (2070-2099) of SSP2-4.5 CMIP6-projections at SANG_AWS. The significance of change in a certain month is calculated with a T-test and indicated by stars, whereby a change is regarded as significant if it has a confidence interval of at least 95%. The following labels are used for significant changes: *>=95% / **>=99% / ***>=99.9%.

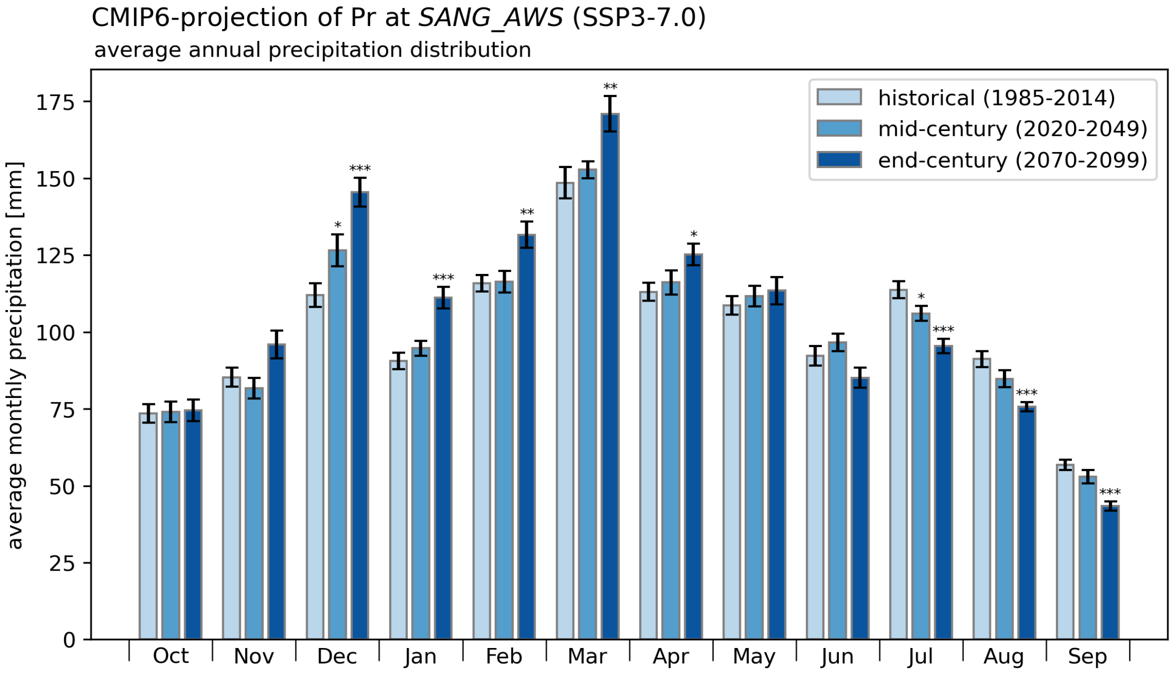

Figure E.13: Average annual precipitation distribution during the historical reference period (1985-2014), mid-century (2020-2049) and end-century (2070-2099) of SSP3-7.0 CMIP6-projections at SANG_AWS. The significance of change in a certain month is calculated with a T-test and indicated by stars, whereby a change is regarded as significant if it has a confidence interval of at least 95%. The following labels are used for significant changes: *>=95% / **>=99% / ***>=99.9%.

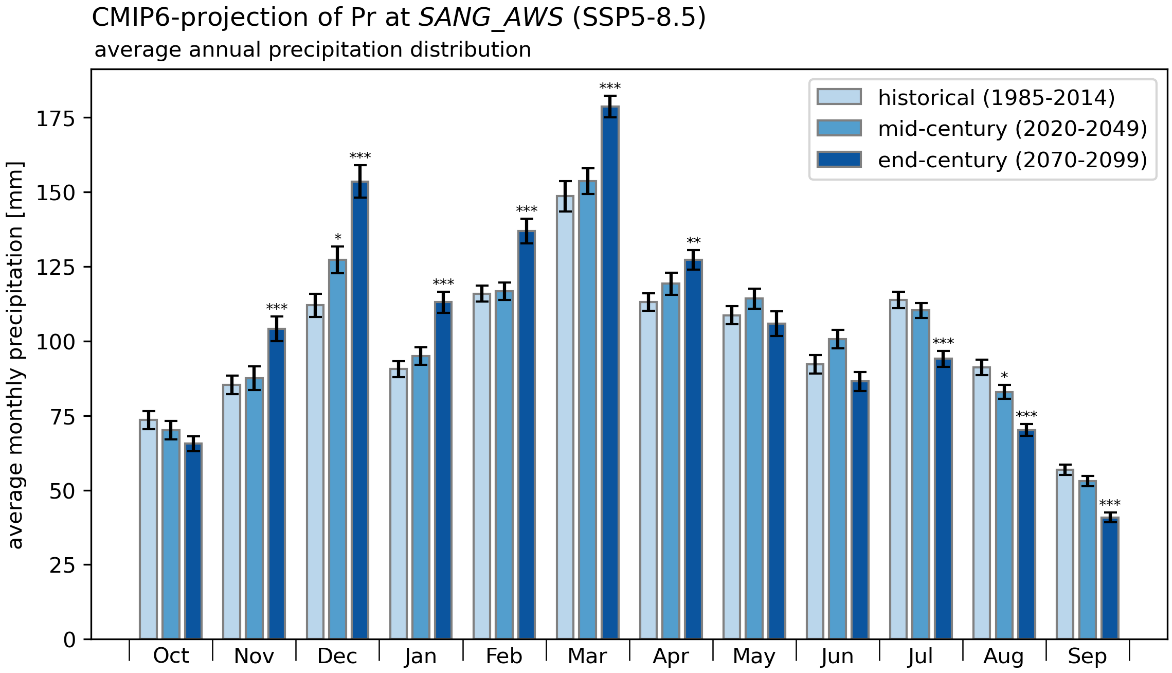

Figure E.14: Average annual precipitation distribution during the historical reference period (1985-2014), mid-century (2020-2049) and end-century (2070-2099) of SSP5-8.5 CMIP6-projections at SANG_AWS. The significance of change in a certain month is calculated with a T-test and indicated by stars, whereby a change is regarded as significant if it has a confidence interval of at least 95%. The following labels are used for significant changes: *>=95% / **>=99% / ***>=99.9%.

E.2.4 Surface air pressure

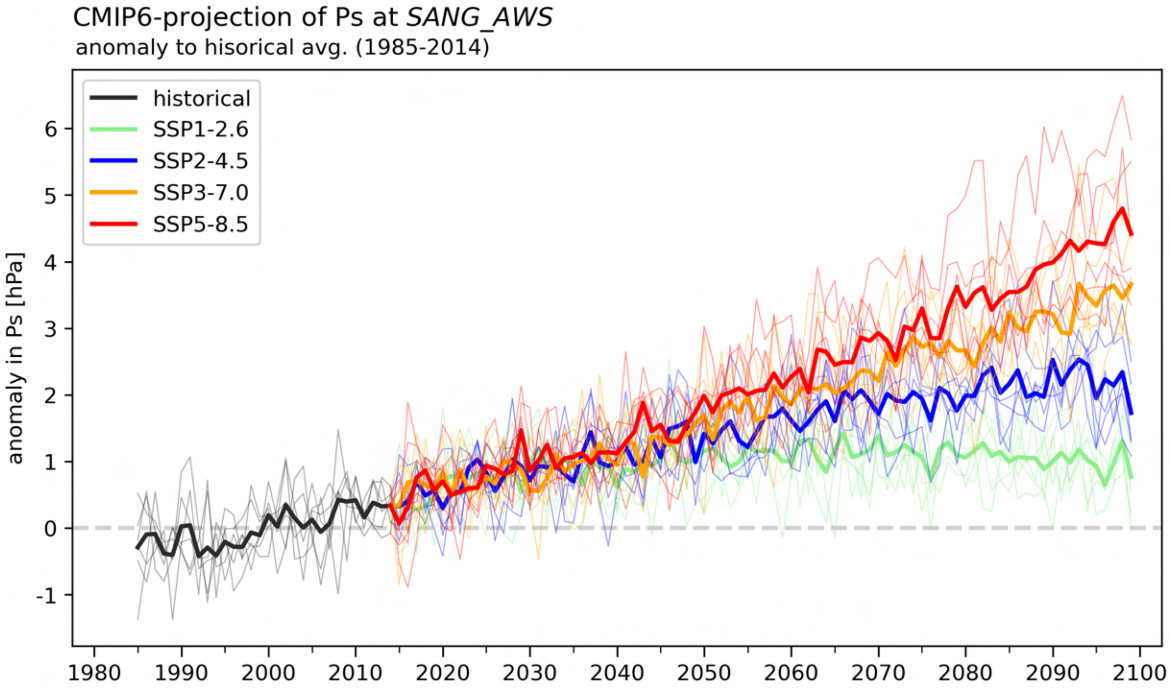

Figure E.15: Anomaly in surface air pressure in CMIP6-projections to historical average at SANG_AWS. The average of the historical reference period (1985-2014) is thereby indicated as a grey, dashed line, representing zero-change. The CMIP6 ensemble means are plotted in the colours presented in the legend, with its individual members (model chains) indicated by thinner lines in the same colour.

E.2.5 Incoming shortwave radiation

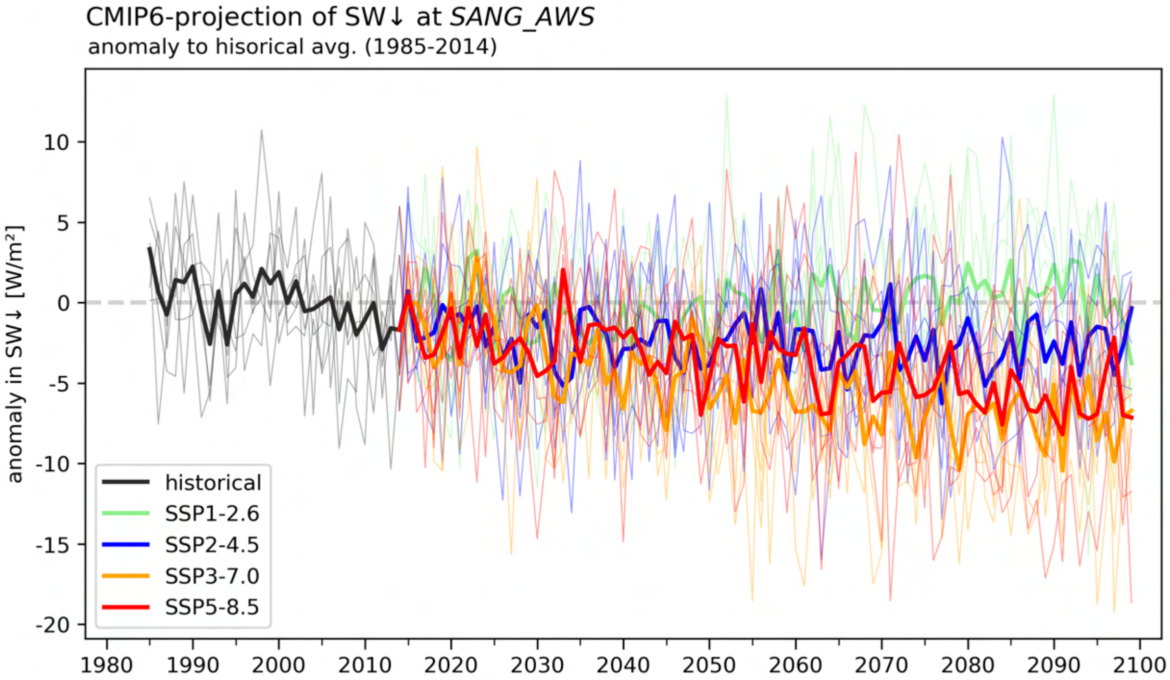

Figure E.16: Anomaly in incoming shortwave radiation in CMIP6-projections to historical average at SANG_AWS. The average of the historical reference period (1985-2014) is thereby indicated as a grey, dashed line, representing zero-change. The CMIP6 ensemble means are plotted in the colours presented in the legend, with its individual members (model chains) indicated by thinner lines in the same colour.

E.2.6 Incoming longwave radiation

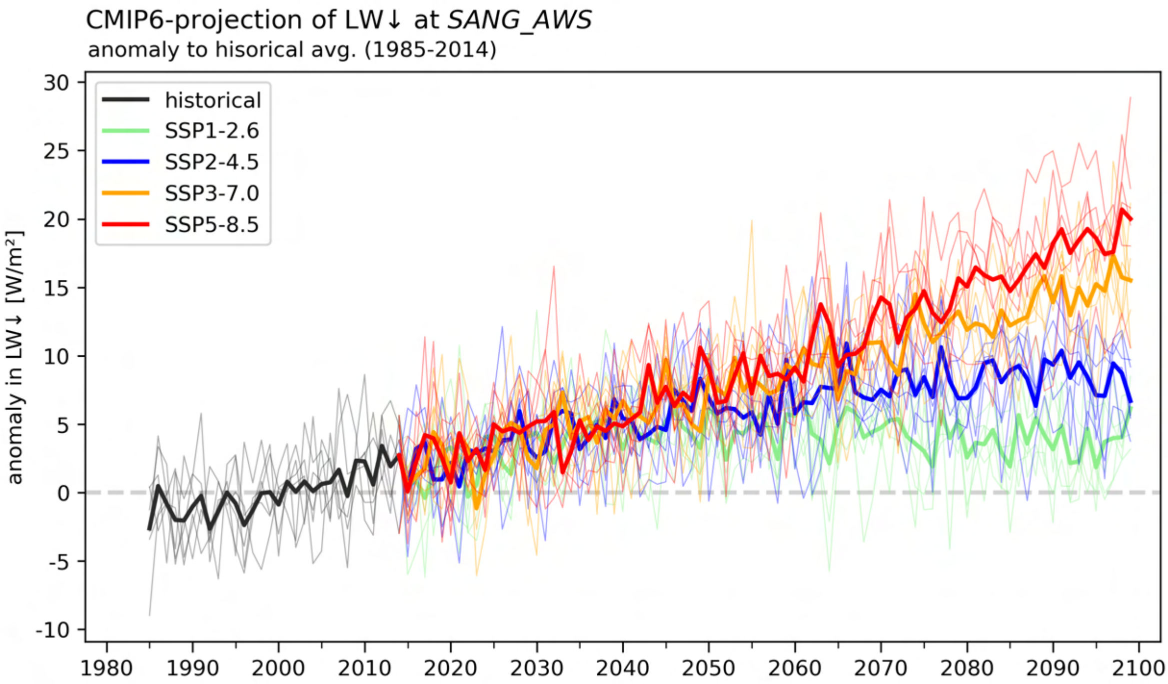

Figure E.17: Anomaly in incoming longwave radiation in CMIP6-projections to historical average at SANG_AWS. The average of the historical reference period (1985-2014) is thereby indicated as a grey, dashed line, representing zero-change. The CMIP6 ensemble means are plotted in the colours presented in the legend, with its individual members (model chains) indicated by thinner lines in the same colour.

E.2.7 Wind speed

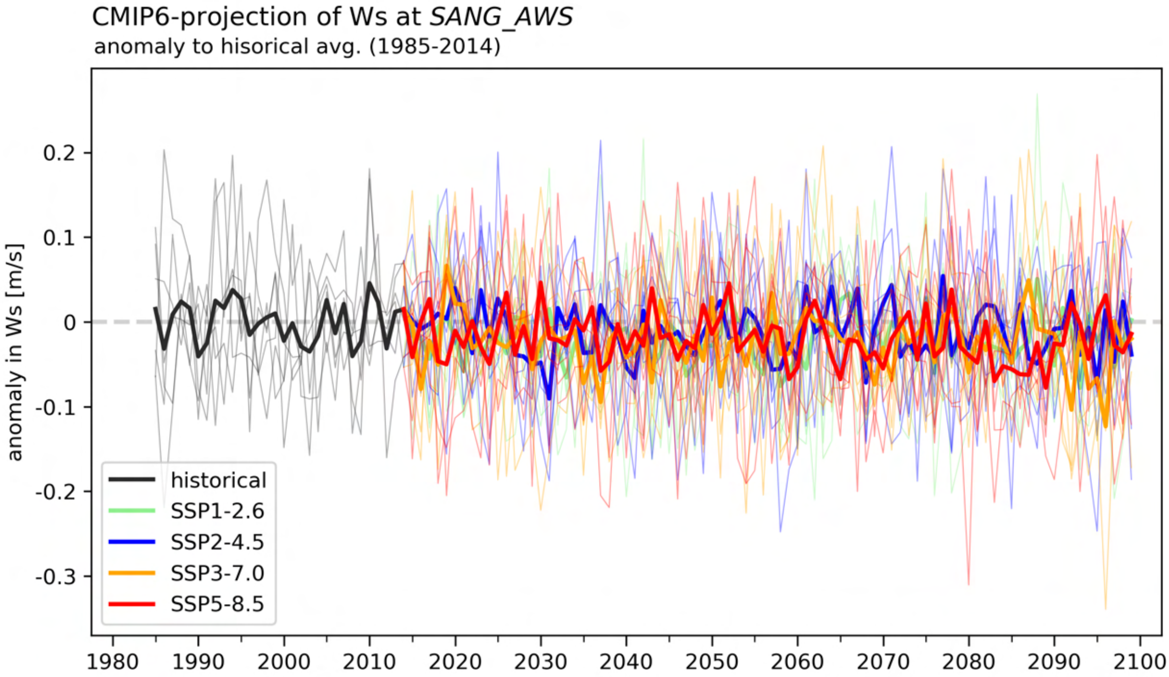

Figure E.18: Anomaly in wind speed in CMIP6-projections to historical average at SANG_AWS. The average of the historical reference period (1985-2014) is thereby indicated as a grey, dashed line, representing zero-change. The CMIP6 ensemble means are plotted in the colours presented in the legend, with its individual members (model chains) indicated by thinner lines in the same colour.

Personal declaration

I hereby declare that the submitted thesis is the result of my own, independent work. All external sources are explicitly acknowledged in the thesis.

Bern, 31 January 2024

P. Wyss

Pascal Wyss